

Molecular Theory of Solute-Pump/Solvent-Probe Spectroscopy and Application to Preferential Solvation Dynamics

by

Xiang Sun

M. A., Brown University, 2010

B. Sc., University of Science and Technology of China, 2008

A Dissertation submitted in partial fulfillment of the
requirements for the Degree of Doctor of Philosophy
in the Department of Chemistry at Brown University

Providence, Rhode Island

May 2014

© Copyright 2014 by Xiang Sun

This dissertation by Xiang Sun is accepted in its present form
by the Department of Chemistry as satisfying the dissertation
requirement for the degree of Doctor of Philosophy.

Date _____

Richard M. Stratt, Director

Recommended to the Graduate Council

Date _____

Jimmie D. Doll, Reader

Date _____

Christoph Rose-Petruck, Reader

Approved by the Graduate Council

Date _____

Peter M. Weber, Dean of the Graduate School

Curriculum Vitæ

Born November 3, 1987, Xinxiang, Henan, China.

Education

Ph. D., Theoretical Chemistry, Brown University, Providence, RI, 2013.

M. A., Chemistry, Brown University, Providence, RI, 2010.

B. Sc., Chemical Physics, University of Science and Technology of China, China, 2008.

Publications

1. X. Sun, R. M. Strat, “How a solute-pump/solvent-probe spectroscopy can reveal structural dynamics: Polarizability response spectra as a two-dimensional solvation spectroscopy”, *J. Chem. Phys.* **139**, 044506 (2013).
2. X. Sun, R. M. Strat, “The molecular underpinnings of a solute-pump/solvent-probe spectroscopy: The theory of polarizability response spectra and an application to preferential solvation”, *Phys. Chem. Chem. Phys.* **14**, 6320 (2012).
3. S. X. Tian, X. Sun, R. Cao, J. Yang, “Thermal Stabilities of the Microhydrated Zwitterionic Glycine: A Kinetics and Dynamics Study”, *J. Phys. Chem. A* **113**, 480 (2009).

Presentations

1. Invited talk, School of Chemistry and Materials Science, University of Science and Technology of China, Hefei, China, March 27, 2013.
2. Xiang Sun and Richard M. Strat, “Theory of solute-pump/solvent-probe spectroscopy and an application to preferential solvation”, Symposium on solvent dynamics at biomolecular interfaces: experiment and theory, the 244th ACS national meeting, Philadelphia, PA, August 19-23, 2012.

Honors and Awards

Sigma Xi Award for Excellence in Research, Brown University, 2013.

Dissertation Fellowship, Brown University, 2012.

University Fellowship for First-year Students, Brown University, 2009.

Excellent Graduate of University of Science and Technology of China, 2008.

MEDY Scholarship, University of Science and Technology of China, 2007.

Professional Affiliations

American Chemical Society

Sigma Xi

Dedicated to my parents

Acknowledgements

This dissertation would never have come to fruition without the support of many people. It is with happiness and gratitude that I acknowledge those who were instrumental in all kinds of ways to the success of this study and because of whom my graduate experience has been a great treasure that I will cherish forever.

Foremost, I would like to express the utmost appreciation to my advisor, Richard Strat, for his guidance, encouragement, patience and care during the entire course of my Ph.D. education. I feel fortunate to have such an opportunity of working with him. Rich is truly a role model as well as a great mentor for young scientists like myself. I have been amazed by his broad knowledge, enlightening insights and systematic investigating styles. Rich showed me how to think in a logical manor, how to grasp the point of an idea, how to ask right questions and how to present in a clear and enjoyable way. In addition, he has always been there when I have questions or problems. This work would not have been possible without his help, and I have to mention that he kindly read the thesis draft line by line and offered valuable revision suggestions including the use of articles.

It gives me immense pleasure to declare gratitude to my thesis committee, Jimmie Doll and Christoph Rose-Petruck for reading through my thesis and providing thoughtful comments. I really appreciate that Jimmie considerately took part in the telephone meeting of my defense when he is off sick. I am extremely grateful to Jimmie for his constant interest in my research and constructive suggestions for all the years I spend here at Brown. I also would like to thank Christoph for his invaluable questions and scientific merits. I

would like to extend my gratitude especially to Matthew Zimmt for serving on my original research propositional committee. He has always been very supportive, enthusiastic and willing to help me to learn new things.

I gratefully acknowledge Norbert Scherer, David Blank and their co-workers for implementing the idea of solute-pump/solvent-probe spectroscopy experimentally, and especially I would like to thank Margaret Hershberger for sharing her experience and knowledge of the spectroscopy and much more beyond. I am also deeply grateful to Graham Fleming, Nancy Levinger, Richard Saykally, Kevin Kubarych and David Birch for their brilliant comments and helpful remarks from experimentalists' perspective. My sincere gratitude and warm appreciation goes to distinguished theorist Branka Ladanyi who collaborated with our group long termly and recently hosted my visit to the beautiful Colorado State University. I was impressed by the progress that we made on our molecular liquid simulation in such a limited time, and I believe that is due to the fact that Branka always put herself in my place and hence gave me spot-on advice. I must say a big thank you to Guoqing Zhang for inviting Rich and me to deliver lectures at my *Alma Mater*, University of Science and Technology of China, early this year. I appreciate very much his lasting inspiration, encouragement and friendship in the past decade.

My acknowledgement will never be complete without the special mention of our group seniors who have introduced me the basic skill set for theoretical chemists. I am especially indebted to Crystal Nguyen for her helps on my first molecular dynamics simulation and furthermore the insights on preferential solvation and Baofeng Zhang for bouncing ideas with me. I also would like to thank our group members, Xiao Liang, Qingqing Ma, Beth Shimmyo, Joe Isaacson, Dan Jacobson, Vale Cofer-Shabica and Gengqi Wang for their intriguing discussions on research and stuff.

It has been a great privilege to spend best several years in the Department of Chemistry at Brown University. Its members will always remain dear to me. Besides those I have already mentioned above, I would like to extend my appreciation to Margaret Doll for

maintaining our computing resources. I also want to thank James Baird for teaching me quantum mechanics and lending me books. I benefited from the Edward Mason collection of books in room GC246 as well. I am truly grateful to our librarian Lee Pedersen who helped me finding books and journal articles that I needed, particularly for purchasing a copy of Shaul Mukamel's nonlinear spectroscopy book on my request.

Life would not have been as colorful without the many wonderful friends I met in this pretty little state of Rhode Island. Special thanks also go to my lifelong friends scattered all over the world. No amount of word is enough to express my regards to them who make me understand the truth of life. I feel blessed to have such friends. With you, I share some lyrics from song "I was here" by Beyoncé:

I was here. I lived, I loved.

Above and beyond all, my heartfelt gratitude goes to my parents for their much unwavering supports and understanding in every possible way. Their endless love and everything made all this possible.

Xiang Sun
December 2013
Providence, RI

Contents

List of Tables	xiii
List of Figures	xviii
List of Symbols	xxii
List of Abbreviations	xxiv
1 Introduction	1
1.1 Liquid Dynamics	1
1.2 Theoretical Methods	2
1.2.1 Instantaneous-normal-mode theory	3
1.2.2 Time correlation function	6
1.2.3 Statistical mechanics and spectroscopy	7
1.2.4 Langevin equation and generalized Langevin equation	9
1.2.5 Linear response theory	13
1.2.6 Computer simulations	19
1.3 Experimental Methods	21
1.3.1 Time-dependent fluorescence spectroscopy	23
1.3.2 Transient absorption	24
1.3.3 Scattering experiments	26
1.3.4 Coherent nonlinear spectroscopy	29
1.4 Design of Solute-Pump/Solvent-Probe Spectroscopy	42
2 Linear Response Theory	48
2.1 Preparations	48
2.2 Traditional Linear Response Theory	52
2.2.1 Average on excited state	53

2.2.2	Average on ground state (Schrödinger picture)	55
2.2.3	Average on ground state (Heisenberg picture)	58
2.2.4	Application to four-wave-mixing light scattering	60
2.3	Gaussian Statistics and Linear Response Theory	62
2.3.1	Gaussian distribution	63
2.3.2	Generating function	64
2.3.3	Linear response	66
2.4	Application to Solute-Pump/Solvent-Probe Spectroscopy	67
3	Preferential Solvation Dynamics and Optical Kerr Effect Spectroscopy	77
3.1	Preferential Solvation Dynamics	77
3.2	Molecular Dynamics Simulation	80
3.3	Optical Kerr Effect (OKE) Spectroscopy	86
3.3.1	OKE experiment	86
3.3.2	Many-body polarizability (dipole-induced-dipole model)	93
3.3.3	OKE spectra for our model	100
3.3.4	Difference spectra	105
3.4	Projection Operator Analysis of Molecular Contributions	112
3.5	Discussions	132
4	Nonequilibrium Two-Dimensional Solute-Pump/Solvent-Probe Spectroscopy	139
4.1	Introduction	139
4.2	Instantaneous-Normal-Mode (INM) Theory	141
4.2.1	Mass-weighted INM	142
4.2.2	INM density of states in liquid argon	145
4.2.3	INM influence spectrum	154
4.2.4	INM approach to OKE spectra	156
4.2.5	INM solvation influence spectrum	167
4.3	Evaluation of Solute-Pump/Solvent-Probe Response	167
4.3.1	Hybrid INM/MD method	169
4.3.2	SHO-like approximation	172
4.3.3	Non-INM numerical evaluation	177
4.4	Short-time Expansion of Solute-Pump/Solvent-Probe Response	179
4.4.1	Exact expansion	180
4.4.2	INM approximation	182

4.4.3	SHO-like approximation	186
4.5	2D Solute-Pump/Solvent-Probe Spectra for Our Model	187
4.6	Structural Information in Preferential Solvation	192
4.6.1	First-shell population dynamics	192
4.6.2	Bond-angle distribution	195
4.7	Discussions on Analytical Approximations for 2D Spectroscopic Responses	219
5	Concluding Remarks	224
5.1	Future Studies	230
Appendix A	Poisson Bracket	234
Appendix B	Derivation of Linear Contribution to $\exp(\hat{A} + \hat{B})$	237
Appendix C	Rotational Average	240
Appendix D	Simulation Details	246
Appendix E	Spatial Derivative of the Many-body Polarizability	253
Appendix F	Snapshot of Initial OKE Response	261
	Bibliography	266
	Index	281

List of Tables

1.1	Light–matter interaction Hamiltonian $H_{int} = -\hat{V} \cdot F(\mathbf{r}, t)$ with different choices of external field $F(\mathbf{r}, t)$ and coupling molecular property \hat{V}	41
3.1	Molecular polarizability and dipole of common solvents.	79
3.2	Averaged first shell population and $1/e$ relaxation time (ps).	86
3.3	Fitting results for the long-time diffusive portion of the OKE response function in 10% S and 50% S mixtures on the equilibrium ground and excited state. The OKE response function is calculated by averaging 10^7 <i>infinite order</i> DID polarizabilities, sampled every 5 time steps.	103
3.4	Fitting results for the long-time diffusive portion of the OKE response function in 10% S and 50% S mixtures on the equilibrium ground and excited state. The OKE response function is calculated by averaging 10^8 <i>first order</i> DID polarizabilities, sampled every 10 time steps.	105
3.5	Summary of single snapshot analysis of $k_B TR(0)$ and its largest term(s) (unit in $\sigma^5 \cdot (\epsilon/m)^{1/2}$) of each category with “u” for the solute, “v” for a solvent. s and w stand for strong solvent and weak solvent with subscripts j, k, l to distinguish different solvent atoms. The same ground state equilibrium configuration is used in both 10% S and 50% S, and different excited equilibrium configurations are used in 10% S and 50% S. Details are included in Appendix F.	130
4.1	Compositions of first-shell/first-shell, first-shell/second-shell and second-shell/second-shell contributions to fcc and hcp lattice bond-angles $\cos \theta=0.5$ and 0.87 with strong solvent percentage $p = 0.1, 0.5$ and 1	215

List of Figures

1.1	Instantaneous-normal-mode spectrum (density of states) of liquid argon, simulated at temperature $k_B T / \epsilon = 1.00$ and density $\rho \sigma^3 = 0.80$	5
1.2	Schematic illustration of time-dependent fluorescence spectroscopy (time-resolved fluorescence Stokes shift).	16
1.3	Experimental $S_V(t)$ and simulated $C_{\Delta E}(t)$ solvation response functions for Coumarin 343 in water.	17
1.4	Rotational energy relaxation of CN in liquid Ar.	18
1.5	Time scales relevant to physical, chemical and biological processes.	22
1.6	Molecular structure of coumarin 153.	23
1.7	Solvation response functions of coumarin 153 in acetonitrile/benzene mixture measured by time-dependent fluorescence spectroscopy.	25
1.8	Double-sided Feynman diagrams for time-domain four-wave mixing in a two-level system.	34
1.9	(a) Comparison of experimental and calculated 3-pulse photon echo peak shift for tricyanocyanine dye IR144 in acetonitrile at 297K; (b) Comparison of the instantaneous normal mode solvation spectrum of acetonitrile, and the rescaled inertial spectral density calculated with parameters fitting experimental result.	39
1.10	Illustration of solute-pump/solvent-probe spectroscopy for preferential solvation.	43
1.11	Experimental sequence of laser pulses in resonant-pump polarizability-response spectroscopy (RP-PORS).	44
1.12	(a) Two-dimensional anisotropic resonant-pump polarizability-response spectrum (RP-PORS) response function for coumarin 153 in acetonitrile; (b) Anisotropic transient solvation polarizability measurement for coumarin 153 in acetonitrile, which is the derivative of RP-PORS spectrum with respect to solvation time T	45
2.1	Preparation of nonequilibrium state in response to an external perturbation.	53
2.2	Sequence of polarizability interactions in four-wave mixing.	61
2.3	Sequence of excitations in solute-pump/solvent-probe spectroscopy.	69
2.4	Schematic illustration of pulse sequence and liquid structural evolution in solute-pump/solvent-probe spectroscopy.	72

3.1	Solute–solvent radial distribution function in atomic liquid with ground-state solute, 10% S system with excited-state solute, and 50% S system with excited-state solute.	81
3.2	Velocity autocorrelation function for Lennard–Jones liquid at density $\rho\sigma^3 = 0.8$ and temperature $k_B T/\varepsilon = 1.00$	83
3.3	Solvation responses for the atomic liquid preferential solvation model in a range of solvent compositions. Shown here are both the equilibrium solvation correlation function $C(t)$ and the nonequilibrium solvation relaxation function $S(t)$, with the detailed view of subpicosecond relaxations in the inset.	84
3.4	Time evolution of the first shell population in 10% S solvent mixture after solute excitation.	85
3.5	Schematic illustration of optical Kerr effect (OKE) spectroscopy.	88
3.6	Optical Kerr effect spectra for 2,4,6-trifluoropyridine at 306 K.	92
3.7	Anisotropic and isotropic OKE responses in 10% S and 50% S systems on equilibrated ground and excited states.	101
3.8	Time-domain OKE response functions for two different solvent mixtures, 10% S and 50% S systems in the equilibrated ground state and excited state.	102
3.9	Frequency-domain OKE spectra for 10% S and 50% S systems. For each system, shown are the results with equilibrated ground-state (g) solute, excited-state (e) solute and the difference between the two (e-g).	104
3.10	Comparison of the OKE reduced spectral densities for 10% S and 50% S solvent mixtures with ground-state solute (g), excited-state solute (e) and their difference spectrum (e-g).	106
3.11	Comparison of the long waiting time limit anisotropic RP-PORS spectra for 10% S and 50% S solvent mixtures.	107
3.12	Comparison of OKE spectra in 10% S system, (a) infinite order DID approximation and full solute polarizability, (b) infinite order DID approximation with the solute’s polarizability set to zero and (c) first order DID approximation with full solute polarizability.	108
3.13	Comparison of OKE spectra in 50% S system, (a) infinite order DID approximation and full solute polarizability, (b) infinite order DID approximation with the solute’s polarizability set to zero and (c) first order DID approximation with full solute polarizability.	109
3.14	Comparison of different polarizability contributions to the long waiting limit anisotropic RP-PORS spectra for 10% S and 50% S solvent mixtures.	111
3.15	Polarizability-velocity correlation function $G(t)$ projected to first shell and everything else contributions.	117
3.16	Polarizability-velocity correlation function $G(t)$ projected to first shell, second shell and everything else contributions.	118
3.17	Projection of the OKE responses for 10% S and 50% S solvent mixtures into first-shell, outer-shells and cross contributions.	121
3.18	Projection of the OKE spectral densities for 10% S and 50% S solvent mixtures into first-shell, outer-shells and cross contributions.	122

3.19	Projection of the e–g difference in spectral densities for 10% S and 50% S solvent mixtures into first-shell, outer-shells and cross contributions.	123
3.20	Projection of the OKE reduced spectral densities for 10% S and 50% S solvent mixtures into first-shell and outer-shells.	124
3.21	Projection of the long waiting time limit anisotropic solute-pump/solvent-probe spectra for 10% S and 50% S solvent mixtures into first-shell and outer-shells contributions.	125
3.22	Projection of the OKE spectral densities for 10% S and 50% S solvent mixtures into first-shell, second-shell and outer-shells contributions.	127
3.23	Projection of the e–g difference in spectral densities for 10% S and 50% S solvent mixtures into first-shell, second-shell and outer-shells contributions.	128
3.24	Illustration of how interaction-induced polarizabilities are affected by number of spectroscopic bright solvent, leading to sign changes in the solute-pump/solvent-probe spectra.	135
3.25	Rotational averaging of a solute–solvent–solvent equilateral triangle.	137
4.1	Instantaneous-normal-mode spectrum (density of states) of liquid Ar at temperature $k_B T / \varepsilon = 1.00$ and density $\rho \sigma^3 = 0.80$	147
4.2	Instantaneous-normal-mode spectrum (density of states) of liquid Ar at temperature $k_B T / \varepsilon = 1.00$ and density $\rho \sigma^3 = 0.80$ with and without zero frequencies removed.	148
4.3	Distribution of eigenvalues of the dynamical matrix for liquid Ar at temperature $k_B T / \varepsilon = 1.00$ and density $\rho \sigma^3 = 0.80$	149
4.4	Comparison of the instantaneous-normal-mode spectra of liquid Ar using frequency histogram and eigenvalue histogram.	150
4.5	Instantaneous-normal-mode spectra (density of states) of (a) liquid argon, 10% S on the ground and the excited state, and (b) 10% S vs 50% S on the ground and the excited state.	153
4.6	Instantaneous-normal-mode polarizability influence spectra of (a) 10% S and (b) 50% S on the ground state and on the excited state at temperature $k_B T / \varepsilon = 1.00$ and density $\rho \sigma^3 = 0.80$	157
4.7	Instantaneous-normal-mode OKE influence spectra of (a) 10% S and (b) 50% S on the ground state and on the excited state at temperature $k_B T / \varepsilon = 1.00$ and density $\rho \sigma^3 = 0.80$	162
4.8	Comparison of instantaneous-normal-mode and exact molecular-dynamics predictions of OKE spectra for the 10% S solvent mixture.	163
4.9	Comparison of e-g difference of the OKE spectra using instantaneous-normal-mode approximation and exact molecular dynamics results for 10% S and 50% S solvent mixtures.	164
4.10	Comparison of instantaneous-normal-mode and exact molecular-dynamics predictions of OKE spectra for the 10% S solvent mixture. The upper panel is the OKE spectrum of the system with an excited-state solute and the lower panel is the difference spectrum between the excited- and ground-state-solute OKE spectra.	165

4.11	Comparison of instantaneous-normal-mode and exact molecular-dynamics predictions of e–g difference of OKE spectra for the 10% S solvent mixture with an atomic solute. Different system sizes and numbers of configurations for averaging are compared.	166
4.12	Instantaneous-normal-mode polarizability influence spectrum vs. solvation influence spectrum of 10% S solvent mixture with an excited-state solute. .	168
4.13	Comparison of response functions using SHO-like approximation at $T = 0$ ps, $T = 50$ ps, long T with the equilibrium excited state OKE response function.	176
4.14	Comparison of full DID and first order DID response functions using SHO-like approximation at $T = 0$ ps.	177
4.15	Two-dimensional solute-pump/solvent-probe spectra for our preferential solvation system 10% S solvent mixtures.	189
4.16	Two-dimensional solute-pump/solvent-probe spectra for our preferential solvation system 50% S solvent mixtures.	190
4.17	Comparison of the fluctuations of solute-pump/solvent-probe responses at a finite waiting time T with that of the equilibrium e–g difference in INM OKE influence spectra for our preferential solvation systems 10% S and 50% S.	191
4.18	The principal result of this chapter: two-dimensional solute-pump/solvent-probe spectra for our 10% S preferential solvation system. The 2D spectra show how the solution’s intermolecular vibrational spectrum evolves with increasing delay time T after the solute excitation.	196
4.19	Most revealing analysis of this chapter: comparison of the relaxation profile observed by solute-pump/solvent-probe spectra with structure- and potential-energy-sensitive equilibrium solvation correlation functions for our 10% S preferential solvation system.	197
4.20	Evolution of strong solvent population distributions in the first solvation shell and in the second solvation shell for both 10% S solvent mixture and 50% S solvent mixture following the resonant solute excitation.	198
4.21	Comparison of the structure- and potential-energy-sensitive equilibrium solvation correlation functions for our 50% S preferential solvation system.	199
4.22	Two-dimensional solute-pump/solvent-probe spectra for our <i>polarizability-switched</i> 10% S preferential solvation system.	200
4.23	Illustration of the bond angle between strong solvent pair and the solute.	201
4.24	T -dependent angular distributions of strong solvent (a) in the first shell, (b) in the second shell and (c) in the first and second shells of 10% S solvent mixture.	203
4.25	T -dependent angular distributions of strong solvent (a) in the first shell and (b) in the first and second shell of 50% S solvent mixture.	204
4.26	Comparison of first-shell population relaxation, solvation energy relaxation and the bond-angle relaxations in the 10% S system.	205
4.27	Illustration of the <i>fcc</i> and <i>hcp</i> close packing.	206

4.28	Angular distributions for liquid-equivalent <i>fcc</i> lattices for atoms (a) in the first shell, (b) in the second shell and (c) in the first and second shells taken together.	208
4.29	Angular distributions for liquid-equivalent <i>hcp</i> lattices for atoms (a) in the first shell, (b) in the second shell and (c) in the first and second shells taken together.	209
4.30	Angular distributions for liquid-equivalent <i>fcc</i> lattices for atoms (a) in the first shell, (b) in the second shell and (c) in the first and second shells with varying bright solvent percentages $p = 0.1, 0.5$ and 1	211
4.31	Angular distributions for liquid-equivalent <i>hcp</i> lattices for atoms (a) in the first shell, (b) in the second shell and (c) in the first and second shells with varying bright solvent percentages $p = 0.1, 0.5$ and 1	212
4.32	Comparison of T -dependent angular distributions in 10% S solvent mixture and angular distributions of liquid-equivalent <i>fcc</i> and <i>hcp</i> lattices in the first shell and in the second shell.	214
4.33	Comparison of T -dependent angular distributions in 10% S solvent mixture and angular distributions of liquid-equivalent <i>fcc</i> and <i>hcp</i> lattices in the first and second shells.	215
4.34	Enlarged view of comparison of T -dependent angular distributions in 10% S mixture and angular distributions of liquid-equivalent <i>fcc</i> and <i>hcp</i> lattices in the first shell, in the second shell and in the first and second shells.	216
4.35	Comparison of T -dependent angular distributions in 50% S mixture and angular distribution of liquid-equivalent <i>fcc</i> and <i>hcp</i> lattices in the first shell and in the first and second shells.	217
4.36	Schematic illustration of the solvent structural change induced by the solute excitation in a preferential solvation system.	218
C.1	Euler angle ϕ, θ, χ relating the space-fixed XYZ and molecule-fixed xyz frames. $\phi = 0 \sim 2\pi, \theta = 0 \sim \pi, \chi = 0 \sim 2\pi$	241
D.1	Order parameter of the ground-state simulated Lennard-Jones liquid ($N = 256$).	248
E.1	Comparison of numerical and analytical OKE response functions for the ground-state 50% S mixture.	259
E.2	Comparison of numerical and analytical OKE response functions for the ground-state 50% S mixture. Both first order and infinite order DID approximations used to calculate the many-body polarizability and the spatial derivative of the many-body polarizability are compared in the same plot.	260

List of Symbols

<i>Symbol</i>	<i>Meaning</i>
i, j, k, \dots	molecule indices
$\mu, \nu, \gamma, \delta, \dots$	Cartesian coordinate indices x, y, z
$\mathbf{A}, \mathbf{B}, \mathbf{C}, \dots$	vectors, matrices, or tensors
N	number of particles
\mathbf{R}	coordinate, liquid configuration
\mathbf{r}	single molecular/atomic position
\mathbf{P}	momentum or polarization
\mathbf{v}	single molecular/atomic velocity
\mathbf{X}	phase space point = (\mathbf{R}, \mathbf{P})
$A(\mathbf{X}(t))$	dynamical variable
$\rho(\mathbf{X}, t)$	phase space distribution
$\langle A \rangle$	ensemble average of A
\bar{A}	nonequilibrium average or rotational average
\hat{A}	operator
\dot{A}	time derivative of A
$\{A, B\}$	classical Poisson bracket
$[A, B]$	quantum commutator
δA	fluctuation of A
$\sigma(A)$	standard deviation of A
β	$(k_B T)^{-1}$
H	Hamiltonian
V	potential energy
$\boldsymbol{\mu}$	molecular dipole moment
α	isolated molecular polarizability

α	isotropic molecular polarizability
γ	anisotropy of molecular polarizability
π	effective molecular polarizability
Π	many-body polarizability
Π	element of many-body polarizability
m	mass of atom or molecule
ε	energy well depth of Lennard-Jones potential
σ	length parameter of Lennard-Jones potential
$\hat{\Omega}$	molecular orientational unit vector
$\hat{\mathbf{P}}_{\mathbf{X}}$	projection operator
\mathbf{Z}	mass-weighted coordinate
$\mathbf{D}(\mathbf{R})$	dynamical matrix
$D(\omega)$	density of states or Fourier transform of OKE response function
$R(t, \dots)$	response function
$G(t)$	spectroscopic “velocity” autocorrelation function
$C(t)$	equilibrium solvation relaxation or correlation function
$S(t)$	nonequilibrium solvation relaxation
$\Delta R(0, T, T + t)$	solute-pump/solvent-probe response
$\Delta R(\omega, T)$	solute-pump/solvent-probe spectra
$S(T; \omega)$	solute-pump/solvent-probe spectral relaxation
q_{α}	the α -th instantaneous normal mode (INM)
p_{α}	the conjugate momentum of the α -th INM
$\rho_A(\omega)$	influence spectrum
c_{α}	coupling coefficient with respect to the α -th INM
$\chi(t_1, t_2)$	fundamental Poisson bracket
$\mathbf{E}(\mathbf{r}, t)$	electric field
$\chi^{(n)}$	n th-order electric susceptibility
\mathbf{k}	wave vector
ω	light frequency or vibrational frequency
$\rho(t)$	density matrix
$\rho(\cos \theta)$	bond-angle distribution
$\rho(\mathbf{k})$	translational order parameter

$g(r)$	radial distribution function
\mathcal{L}	Liouville operator
\mathcal{F}	Fourier transform
ΔV	potential energy gap = $V_e - V_g$
$F(t)$	external perturbing field
\mathbf{x}	n-dimensional Gaussian variable
δt	MD time step
g	ground state of the solute
e	excited state of the solute
u	solute
v	solvent
S	strong solvent
W	weak solvent

List of Abbreviations

<i>Abbreviation</i>	<i>Meaning</i>	<i>Introduced page</i>
2D IR	two-dimensional infrared spectroscopy	41
3PEPS	3-pulse photon echo peak shift	38
C153	coumarin 153	23
DID	dipole-induced-dipole	93
DMSO	dimethyl sulfoxide	79
DRSK	DeVane-Ridley-Space-Keys approximation	222
FWHM	full width at half maximum	231
FWM	four-wave mixing	30
GLE	generalized Langevin equation	11
INM	instantaneous normal mode	3
LJ	Lennard-Jones	80
LO	local oscillator	89
LRT	linear response theory	9
MC	Monte Carlo	20
MD	molecular dynamics	20
OHD	optical heterodyne detection	36
OKE	optical Kerr effect spectroscopy	30
RaPTORS	resonant-pump third-order Raman spectroscopy	228
RIKES	Raman-induced Kerr effect spectroscopy	37
RP-PORS	resonant-pump polarizability response spectroscopy	44
RSD	reduced spectral density	91
SD	spectral density	7
SHO	simple harmonic oscillator	172
TCF	time-correlation function	6

TDF	time-dependent fluorescence	6
TG	transient grating	30
TRFSS	time-resolved fluorescence Stokes shift	15
TSP	transient solvation polarizability spectrum	46

Abstract of “Molecular Theory of Solute-Pump/Solvent-Probe Spectroscopy and Application to Preferential Solvation Dynamics” by Xiang Sun, Ph.D., Brown University, May 2014

Common resonant spectroscopic methods used to study dynamics in solutions, such as time-dependent fluorescence, share a feature of probing the solute directly, or more precisely the solute-solvent interaction energy. One has to infer how the solvents move from the solute’s time-dependent information. By contrast, nonresonant light scattering experiments report on the dynamics of a liquid as a whole, but cannot concentrate on dynamics of any local portion of the solution. A recently demonstrated two-dimensional solute-pump/solvent-probe spectroscopy, a combination of the two approaches mentioned above, enables us to follow the nonequilibrium dynamics of solvents after the solute’s electronic excitation. This dissertation is a theoretical attempt at understanding the molecular information behind this kind of spectroscopy. After developing the general linear response theory for these spectra using classical statistical mechanics, I apply the resulting formalism to a preferential solvation model system consisting of an atomic solute dissolved in an atomic-liquid mixture. In the experimentally interesting limit of long solute-pump/solvent-probe delays, the spectra become the differences in light-scattering spectra between solutions with equilibrated ground- and excited-state solutes. The drastically distinctive spectra for various solvents in this limit suggest how changing liquid structure affects intermolecular liquid dynamics and how local a portion of the solvent dynamics can be accessed by the spectra. For the more general nonequilibrium case of the spectra with finite solute-pump/solvent-probe delays, a practical hybrid calculation method combining instantaneous-normal-mode theory with molecular dynamics shows a great advantage in dealing with two-dimensional spectroscopies especially with separated time scales. The full two-dimensional spectra can serve as a solvation spectroscopy capable of distinguishing the structural and energetic solvation dynamics. Calculations of our preferential solvation model indicate that the spectra indeed display the same relaxation

profile as the local solvent population changes, which is measurably different from the solute-solvent interaction energetic relaxation measured by time-dependent fluorescence. Thus the two-dimensional spectroscopy effectively singles out structural dynamics of local solvents around the solute.

Chapter 1

Introduction

1.1 Liquid Dynamics

From glassware in the laboratory to warm and wet interior of living cells, a tremendous number of important chemical reactions take place in liquid phases. Like all condensed-matter phases, the structure and dynamics of a liquid are drastically different from the gas phase — in the gas phase, each molecule is nearly isolated and moves freely most of the time and only collides with another molecule much more infrequently than in a condensed phase. Unlike other condensed phases, liquids possess the highest translational and rotational symmetries,¹ i.e. homogeneity and isotropy. In other words, a liquid is so random that any direction or any location is equally important. These non-broken symmetries might make one believe that liquids are simple at first glance. As a matter of fact, liquid dynamics could be complicated especially from a microscopic perspective.

Liquids are highly disordered and dense, so we cannot investigate liquid dynamics with the established approaches that are used to treat gases and solids. For example, molecular motions in crystals are only small oscillations about their equilibrium positions. Oscillations in solids can be described as combinations of collective motions of the entire crystal. These collective motions are called phonons and are independent from each other:

they can be just as simple as individual molecules in the gas phase. Furthermore, the structure of a liquid can vary over a broad range of temporal and spatial scales, which makes the problem of liquid dynamics more intricate.

Molecules in liquids constantly interact with one another through translation, rotation and vibration. These elementary motions are necessary for a chemical reaction to occur. The ultimate question that one would ask is exactly how these microscopic processes take place. In particular, how is the dynamics of these degrees of freedom affected by the interactions between molecules, the liquid structures and external perturbations? For example in a solution, there are two typical fundamental processes arising between a molecule and its surroundings: molecules exchange energy and rearrange their positions.² The particular form of energy exchange relevant to how a vibrationally hot species dissipates its excess energy to other molecules or to other degrees of freedom within itself is called vibrational relaxation. An essential concept in reaction dynamics named Intramolecular Vibrational-energy Redistribution (IVR)^{3,4} describes energy transfers from the initially populated vibrational state to other vibrational states inside a polyatomic molecule. The second of the two fundamental processes is known as solvation, during which a group of ambient solvent molecules reorganize their positions in order to accommodate a newly excited solute. Solvation is primarily related to the energetics of solute-solvent interaction and the intermolecular motions involving both solute and solvent. We will get back to the topic of solvation later in this thesis, but now let us have an overview of theoretical and experimental methods that have been applied to the field of liquid dynamics.

1.2 Theoretical Methods

Owing to the complexity of liquid dynamics on different spatial and temporal scales, there is no universal theory that can solve all the problems related to the dynamics of liquid. Yet a number of theories have flourished in the last few decades intended to tackle

different aspects of liquid dynamics. An excellent example is the Instantaneous-Normal-Mode (INM) theory, which is developed in the early 1990s by Stratt⁵⁻⁹ and Keyes^{10,11} independently. This theory offers an accurate picture of the short-time dynamics of liquid at the molecular level. The notion of INM originates from the phonon concept of solid-state matter.⁹ Phonons are well defined in solid — independent collective oscillations of the entire crystal — that require the intermolecular forces are harmonic, in other words, atoms can be regarded as being held together by springs. But the spring analogy does not apply to liquid in that the arrangement of atoms or molecules in liquid is not stable. In a stable arrangement like solid, only small oscillations of atoms around some fixed positions are allowed. Atoms in liquid diffuse and the whole liquid flow, so in conventional sense, phonons do not exist in liquid, at least persistently. Nevertheless when looking at a time scale that is so short during which atoms do not move far from its original positions, comparable to the displacements of atoms in solid, the normal-mode concept is still applicable in dealing with liquid dynamics.

1.2.1 Instantaneous-normal-mode theory

The instantaneous-normal-mode approach is based on the normal-mode analysis on an instantaneous liquid configuration \mathbf{R}_0 (a $3N$ -dimensional coordinate vector in an N -atom system, for example).⁹ Suppose one would like to know what is the configuration at a short time t later, \mathbf{R}_t . We can expand the total potential energy $V(\mathbf{R})$ as a function of the configurational difference between two times to the second order (harmonic approximation).

$$V(\mathbf{R}_t) = V(\mathbf{R}_0) + \nabla V(\mathbf{R}_0) \cdot (\mathbf{R}_t - \mathbf{R}_0) + \frac{1}{2} (\mathbf{R}_t - \mathbf{R}_0) \cdot \nabla \nabla V(\mathbf{R}_0) \cdot (\mathbf{R}_t - \mathbf{R}_0), \quad (1.1)$$

where gradient operator $\nabla \equiv \frac{\partial}{\partial \mathbf{R}}$. Although the first derivative of the potential energy does not vanish like in the solid case, one can still perform the normal-mode analysis by diagonalizing the $3N \times 3N$ dynamical Hessian matrix $\nabla \nabla V(\mathbf{R}_0)$.

$$\mathbf{U}(\mathbf{R}_0) \cdot \nabla \nabla V(\mathbf{R}_0) \cdot \mathbf{U}^T(\mathbf{R}_0) = m \cdot \text{diag}\{\omega_1^2, \dots, \omega_{3N}^2\}. \quad (1.2)$$

In the equation above, m is the mass of an atom, $\mathbf{U}(\mathbf{R}_0)$ is the unitary matrix that diagonalizes the dynamical Hessian matrix and ω_α ($\alpha = 1, \dots, 3N$) are frequencies corresponding to every INM. Now the instantaneous normal modes are

$$q_\alpha(t; \mathbf{R}_0) = [\mathbf{U}(\mathbf{R}_0) \cdot (\mathbf{R}_t - \mathbf{R}_0)]_\alpha, \quad (\alpha = 1, \dots, 3N). \quad (1.3)$$

Among $3N$ instantaneous normal modes, each mode corresponds to an independent collective harmonic motion. The independency warrants a limpid physical picture of liquid dynamics, a collection of uncoupled harmonic oscillators. By rewriting the above relation, it gets clearer that the dynamics of a liquid at short times is determined by these harmonic modes and their initial conditions which include the initial instantaneous forces and initial velocities. In other words, the time evolution of the whole liquid can be predicted based on the dynamical information at time 0 alone, as long as the time interval is short enough. It is worth noting that most of the harmonic modes barely finish a single cycle within such a short time, so full oscillations especially low-frequency ones are rare in liquid.

$$\mathbf{R}_t = \mathbf{R}_0 + \mathbf{U}^T(\mathbf{R}_0) \cdot \mathbf{q}(t; \mathbf{R}_0). \quad (1.4)$$

The instantaneous-normal-mode spectrum is defined as the distribution of INM frequencies. For example, in an atomic liquid with total N atoms, the density of states

$$D(\omega) = \left\langle \frac{1}{3N} \sum_{\alpha=1}^{3N} \delta(\omega - \omega_\alpha) \right\rangle. \quad (1.5)$$

Figure 1.1 shows the density of states of liquid argon simulated by molecular dynamics, in which the imaginary frequencies are plotted on the negative frequency axis. These imaginary frequencies corresponds to unstable instantaneous normal modes. And it is these

modes with imaginary frequencies that differentiate liquids from solids — no imaginary frequency in solids. An imaginary-frequency INM implies a negative local curvature on the potential energy surface,⁵ or a local maximum along the direction of this INM. By contrast, a real-frequency INM indicates a positive local curvature on the potential energy surface (consider a local minimum).

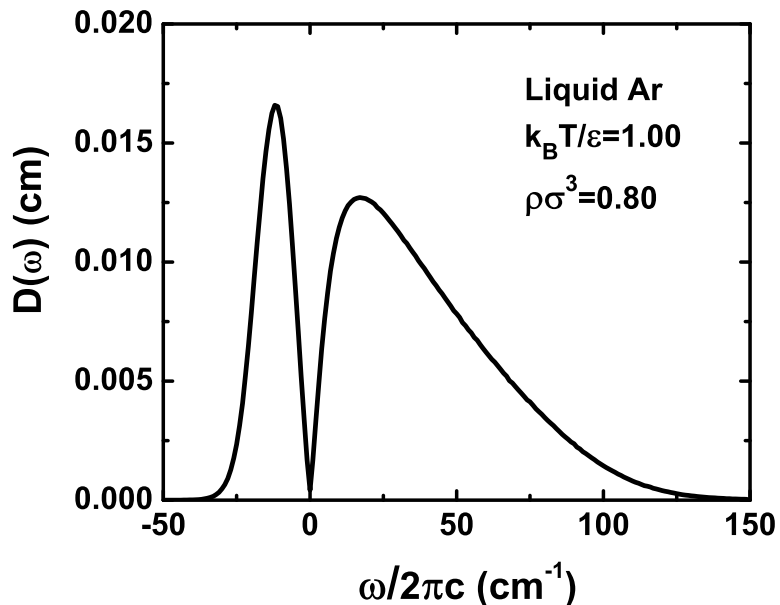


Figure 1.1 Instantaneous-normal-mode spectrum (density of states) of liquid argon. Molecular dynamics simulation with 256 atoms is performed at temperature $k_B T/\epsilon = 1.00$, density $\rho\sigma^3 = 0.80$. 20,000 instantaneous liquid configurations are sampled. The imaginary frequencies are plotted on the negative frequency axis. Three translational modes with zero frequencies are removed.

The real power of the instantaneous-normal-mode theory is not merely an extrapolation of liquid dynamics from any instant to an immediate future, but a new statistical mechanical point of view to inspect the dynamics in liquids. An instantaneous-normal-mode analysis on a single liquid configuration will not tell too much about a macroscopic system, but what is more practical is the ensemble average through sampling an equilibrium distribution. And the ensemble average connects the most microscopic events with macroscopic measurable quantities. Besides the density of states spectrum, instantaneous-normal-mode

theory enables one to calculate ensemble-averaged time correlation functions (TCFs).

1.2.2 Time correlation function

Time correlation functions play a central role in nonequilibrium statistical mechanics, as the partition function does in equilibrium statistical mechanics.¹² Many properties of systems out of equilibrium are determined by various time correlation functions. For example, diffusion, viscosity and thermal conductivity can be described by time correlation functions. Suppose we look at some time-dependent quantity $A(t)$, and the time correlation function of this quantity is $\langle A(0)A(t) \rangle$, ($\langle \dots \rangle$ denotes the ensemble average)

$$\langle A(0)A(t) \rangle \equiv \frac{\int d\mathbf{X} A(\mathbf{X})A(\mathbf{X}(t))e^{-\beta H(\mathbf{X})}}{\int d\mathbf{X} e^{-\beta H(\mathbf{X})}}, \quad (1.6)$$

where $\mathbf{X} = (\mathbf{R}, \mathbf{P})$ is the phase space point, \mathbf{R} is the position coordinate and \mathbf{P} is the conjugate momentum. The time-dependent quantity A is often termed a *dynamical variable*¹³ that is a function of the phase space, $A(\mathbf{X})$. A dynamical variable A with initial condition at phase space point \mathbf{X} is written as $A = A(0) = A(\mathbf{X}) = A(\mathbf{X}(0))$. And $A(t) = A(\mathbf{X}(t))$ denotes the value of the dynamical variable at time t , evolved from the initial state \mathbf{X} . The integration $\int d\mathbf{X}$ is over the whole of phase space. In addition, $\beta = 1/k_B T$ and $H(\mathbf{X})$ is the Hamiltonian of the system equal to the total energy, which governs the time evolution of the whole system. The equations of motion of a classical system are the Hamilton's equations:¹⁴(the overdot denotes time derivative d/dt throughout the thesis.)

$$\dot{\mathbf{R}} = \frac{\partial H}{\partial \mathbf{P}}, \quad \text{and} \quad \dot{\mathbf{P}} = -\frac{\partial H}{\partial \mathbf{R}}. \quad (1.7)$$

The probability density of finding the system at state around phase point \mathbf{X} is

$$\rho_{eq}(\mathbf{X}) = \frac{e^{-\beta H(\mathbf{X})}}{\int d\mathbf{X} e^{-\beta H(\mathbf{X})}}. \quad (1.8)$$

Then Equation 1.6 can be rewritten as

$$\langle A(0)A(t) \rangle = \int d\mathbf{X} A(\mathbf{X})A(\mathbf{X}(t))\rho_{eq}(\mathbf{X}). \quad (1.9)$$

The most general assumption that serves as the foundation of statistical mechanics is ergodicity. This ergodic hypothesis states that the ensemble average is equivalent to the time average, e.g. for a time correlation function,¹²

$$\langle A(0)A(t) \rangle = \lim_{\tau \rightarrow \infty} \frac{1}{\tau} \int_0^\tau ds A(s)A(t+s). \quad (1.10)$$

Time correlation functions with the form $\langle A(0)A(t) \rangle$ are called autocorrelation function. Another form of time correlation function is called a cross-correlation function with a general expression $\langle A(0)B(t) \rangle$ (sometimes when discussing general properties of correlation functions, this form is preferred.). Physically, time correlation functions describe how a given property of a system affects the same property (or other property) at another time under statistical averaging, in other words, how much is left of the memory of a property at time 0 that still influences the same property (or other property) at time t . Because the correlation function is an ensemble average, this memory tends to be averaged out by interactions. A classic example is the velocity correlation function which determines the diffusion coefficient,

$$D = \frac{1}{3} \int_0^\infty dt \langle \mathbf{v}(0) \cdot \mathbf{v}(t) \rangle. \quad (1.11)$$

1.2.3 Statistical mechanics and spectroscopy

The Fourier transform converts the time correlation function $C(t) = \langle A(0)A(t) \rangle$ from time domain to frequency domain. The frequency-domain counterpart of the response function is generally called spectra density (SD) or power spectrum,

$$C(\omega) = \int_{-\infty}^{\infty} dt e^{-i\omega t} C(t). \quad (1.12)$$

The above relation is essential because it gives us a unified view of dynamics and its spectrum with a time–frequency correspondence. For example, in infrared spectroscopy (IR), the absorption lineshape is the Fourier transform of dipole-dipole correlation function,¹⁵

$$I(\omega) = \frac{1}{2\pi} \int_{-\infty}^{\infty} dt e^{-i\omega t} \langle \mathbf{M}(0) \cdot \mathbf{M}(t) \rangle, \quad (1.13)$$

where \mathbf{M} is the total dipole moment of the system.

It would be wise to keep the time-domain/frequency-domain Fourier transformation in mind whenever looking at a time correlation function or a spectrum. Useful conversion between time and frequency is that 1 ps (=10⁻¹² s) time scale corresponds to a frequency of 33 cm⁻¹ (or 1 terahertz, THz) and 0.33 ps corresponds to 100 cm⁻¹. Most of many-body dynamics in liquid falls into the picosecond and sub-picosecond regime, which in frequency domain means a few wave numbers to hundreds of wave numbers.

Now we go back to the topic of the instantaneous-normal-mode theory. The theory enables one to calculate the so-called *influence spectrum*^{9, 16, 17} that is defined as follows,

$$\rho_A(\omega) = \left\langle \sum_{\alpha} c_{\alpha}^2 \delta(\omega - \omega_{\alpha}) \right\rangle, \quad (1.14)$$

where the sensitivity of variable A with respect to α -th INM is

$$c_{\alpha} = \frac{\partial A}{\partial q_{\alpha}}. \quad (1.15)$$

The influence spectrum is the Fourier transform of a “velocity” correlation function $G_{AA}(t) = \langle \dot{A}(0)\dot{A}(t) \rangle = -\frac{d^2}{dt^2} \langle A(0)A(t) \rangle$,

$$\langle \dot{A}(0)\dot{A}(t) \rangle = k_B T \int \rho_A(\omega) \cos \omega t d\omega. \quad (1.16)$$

The time correlation function $\langle A(0)A(t) \rangle$ can be derived by double time-integration of the

“velocity” correlation function $G_{AA}(t)$. So far, the solvation energy autocorrelation,^{16,18} friction–force autocorrelation,^{17,19} polarizability autocorrelation²⁰ have been studied with the instantaneous-normal-mode approach. We will discuss the instantaneous-normal-mode theory and its application to nonlinear spectroscopy in detail in Chapter 4.

1.2.4 Langevin equation and generalized Langevin equation

The fluctuation–dissipation theorem^{21,22} has many a profound implication in statistical mechanics, one of which is the linear response theory (LRT). The connotations of the theorem can be understood with a Brownian motion model. The equation of motion for the random motion of a heavy particle like a dust particle immersed in a liquid bath, the Brownian motion, is called the Langevin equation. Generally speaking, Brownian motion refers to random motion of a particle or a mode in a macroscopic dynamical system caused by a large number of small particles or degrees of freedom. It is a basic model connecting macroscopic measurable random motion with thermal motion of microscopic degrees of freedom, which has wider applications besides heavy dust in liquid, for example, molecular simulations and nonlinear spectroscopy. The Langevin equation incorporates both frictional force and random noise. In one dimension,

$$m \frac{dv}{dt} = -\zeta v + F(t), \quad (1.17)$$

where v is the velocity of the particle and ζ is the friction coefficient. The negative sign in the first term on the right side of the equation is determined by the fact that the friction drags the particle in the opposite direction of its velocity. In this equation, the frictional force is only dependent on the present velocity, which has no memory on the history of velocity. This amnesic process is often called Markovian. The last term $F(t)$ is the random

noise (fluctuating force) satisfying the condition

$$\langle F(t) \rangle = 0, \quad \langle F(t_1)F(t_2) \rangle = 2B\delta(t_1 - t_2), \quad (1.18)$$

where constant B is the strength of the noise and $\delta(t)$ is the Dirac delta function. The condition indicates that the fluctuating force has no correlation between any distinct time instants, or is “white” — the Fourier transform of the correlation function of the noise is independent of frequency. Although the random term makes the Langevin equation a stochastic differential equation, the first-order linear inhomogeneous differential equation has a general formal solution

$$v(t) = v(0)e^{-\zeta t/m} + \frac{1}{m} \int_0^t dt' F(t') e^{-\zeta(t-t')/m}. \quad (1.19)$$

The velocity has an exponential decay of the initial velocity (first term) but the random noise produces extra velocity (second term). If we consider the mean squared value of velocity,

$$\langle v(t)^2 \rangle = \langle v(0)^2 \rangle e^{-2\zeta t/m} + \frac{B}{\zeta m} (1 - e^{-2\zeta t/m}). \quad (1.20)$$

In the long time limit, the first pure frictional term dies out, whereas the random noise keeps the system alive. Eventually, the mean squared value of velocity approaches the equipartition value $k_B T/m$. Thus,

$$B = \zeta k_B T. \quad (1.21)$$

The above result relates the fluctuating random noise B with the friction ζ (energy dissipation), and is a version of the fluctuation–dissipation theorem.²¹ This theorem is one of most fundamental cornerstones in nonequilibrium statistical mechanics, and its intrinsic connection to the linear response theory will be discussed in the next section.

The mean squared displacement of Brownian particle at long times $\langle \Delta x(t)^2 \rangle \rightarrow 2k_B T t / \zeta$

gives the diffusion coefficient

$$D = \frac{k_B T}{\zeta}, \quad (1.22)$$

which is called the Stokes–Einstein formula.²³

The Langevin equation can be only applied to a Markovian process, like the Brownian motion of all kinds, but far-reaching generalizations of the Langevin equation to non-Markovian cases give us more freedom describing complicated yet realistic systems. By adding a time-dependent friction kernel $\zeta(t)$, so-called memory function, we have the generalized Langevin equation (GLE),^{24,25}

$$m \frac{d^2 x(t)}{dt^2} = -\frac{\partial W(x)}{\partial x} - \int_0^t dt' \zeta(t') \cdot \dot{x}(t-t') + F(t), \quad (1.23)$$

where $x(t)$ is the special coordinate or any degrees of freedom you are interested in, $W(x)$ is potential of mean force on x coordinate (averaged over all the bath degrees of freedom), and $F(t)$ is again the random noise. The convolution of the memory function $\zeta(t)$ and the velocity $\dot{x}(t)$ associates the evolution of \dot{x} with its earlier history. A GLE can be derived from a harmonic bath Hamiltonian by simply solving Hamilton’s equations of motion.^{26,27}

The corresponding non-Markovian version of the fluctuation–dissipation theorem reads

$$\zeta(t) = \beta \langle F(0)F(t) \rangle. \quad (1.24)$$

The above equation explains the intrinsic equivalence between the friction in liquid and the fluctuations of random forces. The generalized Langevin equation is useful for studying relaxation processes. One can deduce the rate of vibrational energy relaxation from the microscopic friction by the Landau–Teller relation,²⁸

$$\frac{1}{T_1} = \frac{\zeta_R(\omega)}{\mu}. \quad (1.25)$$

The $\zeta_R(\omega)$ is the real part of the Fourier transform of the friction kernel, $\zeta_R(\omega) =$

$\int_0^\infty dt \cos \omega t \zeta(t)$, and T_1 is the energy relaxation time for vibrational mode at frequency ω and reduced mass μ . The fluctuating force in the correlation function in particular is the solvent force on the vibrational mode of the solute. In an absorption spectroscopy, for instance, the homogeneous lineshape broadening results from the lifetime of a vibrational population relaxation T_1 and the pure dephasing time T_2^* that is the time scale for losing phase information within a given vibrational state due to fluctuations of the environment. The pure dephasing rate can be calculated using the equation below

$$\frac{1}{T_2^*} = \int_0^\infty dt \langle \delta\omega(0)\delta\omega(t) \rangle, \quad (1.26)$$

where $\delta\omega(t)$ is the fluctuation of vibrational frequency.²⁹ Then the following relation gives us the total dephasing time T_2 that is directly related to homogeneous line width,

$$\frac{1}{T_2} = \frac{1}{2T_1} + \frac{1}{T_2^*}. \quad (1.27)$$

The key term in generalized Langevin equation is the memory function.³⁰ For some systems, there is no exact form for the memory function, so we need an approximated form. For example, the instantaneous-normal-mode theory provides a route to calculate the memory function as well as a microscopic perspective on what specific molecular mechanisms contribute to the vibrational friction. The solvent force correlation function that is equivalent to the friction kernel has a corresponding INM influence spectrum for vibrational relaxation.¹⁹ The influence spectrum is the solvent INM frequency distribution weighted by the sensitivity of the solvent force to each solvent mode. Theoretical calculations enable one to isolate typical liquid configurations and project out of the influence spectrum the contributions of a selected subset of solvent molecules or degrees of freedom. Simulation of simple liquids showed that the most effective modes during vibrational relaxation involve solute/nearest-single-solvent pairs, especially at high frequencies. This idea is called the instantaneous-pair (IP) theory.³¹

The choice of dynamical variable in the generalized Langevin equation is not limited to some peculiar particle positions and velocities; the generalized Langevin equation can be applied to any dynamical variable.^{32,33} And there is more than one derivation of the generalized Langevin equation, such as that using the Zwanzig–Mori projection operator formalism.^{34–38}

1.2.5 Linear response theory

The most essential and fundamental connection between equilibrium and nonequilibrium statistical mechanics is the linear response theory. The fundamental idea of the linear response theory is first enunciated in 1931 by Onsager’s regression hypothesis: the relaxation of a macroscopic nonequilibrium disturbance will obey the same laws as the regression of spontaneous microscopic fluctuations in an equilibrium system.^{39,40} This hypothesis is now viewed as an important consequence of the fluctuation–dissipation theorem proved by Callen and Welton in 1951.⁴¹ The fluctuation–dissipation theorem has many forms, two of which are shown in the previous two subsections, and so does the linear response theory. The significance of the linear response theory is that one will not have to actually perturb the system to get the response, instead all the information needed to predict the response is embedded in the fluctuation of the interested quantity in an equilibrated system.

To put the linear response theory in a statistical mechanical language,⁴² if we observe a dynamical variable A in a system that is subject to an external perturbation $F(t)$, with the perturbation Hamiltonian $H' = -A \cdot F(t)$ that is linear in the perturbation, then in the linear regime the nonequilibrium average value of $\overline{A(t)}$ is can be written as

$$\overline{A(t)} = \int_{-\infty}^t dt' R(t, t') \cdot F(t'), \quad (1.28)$$

where $R(t, t')$ is the response function or the generalized susceptibility which describes how much the influence on the system at time t is left, due to an external perturbation at time t' .

The integration runs from time $-\infty$ to time t , incorporating all the influence of the external perturbation till the observation time t . Generally, the response function has the following properties,

$$(i) \quad R(t, t') = R(t - t'), \quad (\text{stationarity of the unperturbed system}) \quad (1.29)$$

$$(ii) \quad R(t - t') = 0, \quad \text{when } t - t' < 0. \quad (\text{causality}) \quad (1.30)$$

In linear response, the response function is independent of the external field as the response function is a property of the system. It will be shown in the next chapter that the response function has the following form, where $\theta(t)$ is the Heaviside step function.

$$R(t) = -\beta \theta(t) \frac{d}{dt} \langle \delta A(0) \delta A(t) \rangle, \quad (1.31)$$

where $\beta = 1/k_B T$, and $\delta A(t) \equiv A(t) - \langle A \rangle$ is the fluctuation of dynamical variable A at time t .

For convenience, we choose the external perturbation $F(t) = F \cdot \theta(-t)$. One can get that the nonequilibrium average by combining Equation 1.28 and Equation 1.31.

$$\overline{\Delta A(t)} = \overline{A(t)} - \langle A \rangle = \beta F \langle \delta A(0) \delta A(t) \rangle, \quad (1.32)$$

another form of the fluctuation–dissipation theorem: the nonequilibrium quantity $\overline{\Delta A(t)}$, the amount of “dissipation” in A that occurs as equilibrium is approached, has a natural connection to itself’s equilibrium “fluctuation” $\langle \delta A(0) \delta A(t) \rangle$. We define the nonequilibrium relaxation profile by normalizing $\overline{\Delta A(t)}$,

$$S(t) = \frac{\overline{A(t)} - \langle A \rangle}{\overline{A(0)} - \langle A \rangle}. \quad (1.33)$$

This $S(t)$ represents how fast the nonequilibrium quantity approaches its equilibrium value

starting from $S(0) = 1$ and ending up with $S(\infty) = 0$. We can also define the normalized correlation function of the fluctuation in A as

$$C(t) = \frac{\langle \delta A(0) \delta A(t) \rangle}{\langle \delta A(0)^2 \rangle}. \quad (1.34)$$

This normalized correlation function describes how soon the system loses the memory of the fluctuation in A at an equilibrium condition. $C(0) = 1$ corresponds to no memory loss and $C(\infty) = 0$ corresponds to a complete memory loss.

The Onsager regression hypothesis is then expressed in the following equation,

$$S(t) = C(t). \quad (1.35)$$

The above relation is also the criterion for testing if a system or a dynamical variable obeys the linear response theory.

Time-dependent fluorescence spectroscopy (TDF), (which has the alternative name the time-resolved fluorescence Stokes shift (TRFSS)) has become a standard approach to investigate solvation dynamics (see Figure 1.2).² In this measurement, the observable is some time-dependent characteristic fluorescence emission frequency, for example, the peak of fluorescence emission spectrum at time t . The dynamical variable is conventionally chosen as the solute-solvent interaction energy gap between ground and excited states, ΔE that is equivalent to the fluorescence frequency since $\Delta E = h\nu$. The corresponding nonequilibrium solvation response $S(t)$ and the energy-gap time correlation function $C(t)$ are defined as

$$S_{\nu}(t) = \frac{\nu(t) - \nu(\infty)}{\nu(0) - \nu(\infty)}, \quad \text{and} \quad C_{\Delta E}(t) = \frac{\langle \delta \Delta E(t) \delta \Delta E(0) \rangle}{\langle \delta \Delta E(0)^2 \rangle}. \quad (1.36)$$

Figure 1.3 shows remarkable agreement between experimental Stokes shift response $S_{\nu}(t)$ and simulated energy-gap time correlation function $C_{\Delta E}(t)$ for coumarin 343 in water

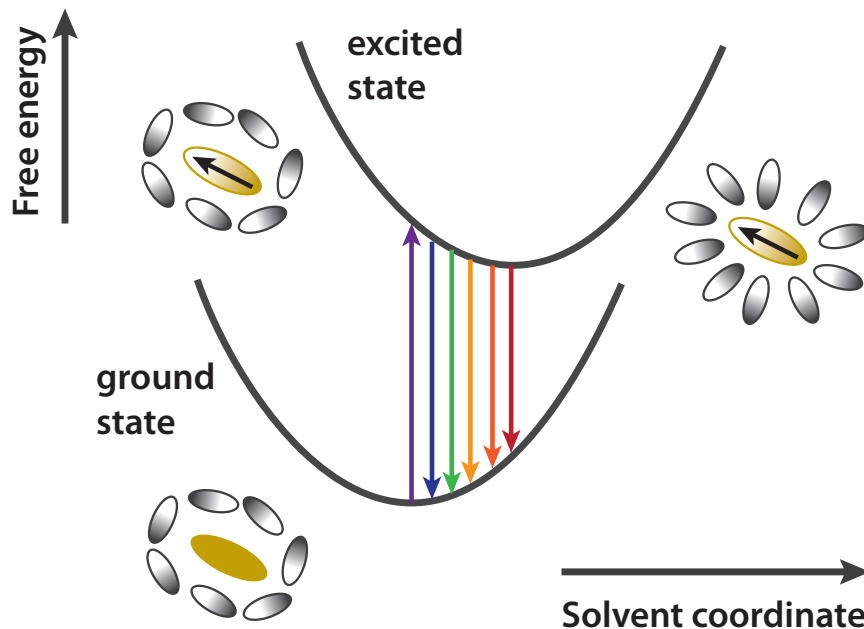


Figure 1.2 Schematic illustration of time-dependent fluorescence spectroscopy (time-resolved fluorescence Stokes shift). Shown here is how an electronic transition in solute can be used to study solvation dynamics. In a polar solvent, a dipole is created in the solute with an ultrafast laser pulse, which brings the solute from the ground state to electronic excited state. The electronic transition is so fast compared with the nuclear motions of solvent that the initially prepared configuration of the excited state is still the same as in equilibrium ground state. As the solvation process happens the solvent rearranges to accommodate the change in the solute and to lower the solvation free energy. The relaxation can be monitored by detecting the emission from the solute as a function of time after excitation. A time-dependent red shift of the emission spectrum as a result of solvation is shown schematically.

solution.⁴³ This agreement validates the linear response theory in the aqueous coumarin solution. The physical content behind is that, if the perturbation is not too large the relaxation of the nonequilibrium system perturbed by electronic transition is intrinsically the same with the relaxation of the spontaneous fluctuations in an unperturbed system at equilibrium. The solvation responses reveal a common bimodal pattern for solvation dynamics, initial ultrafast inertial (mostly librational motions) response followed by a slow diffusive component.

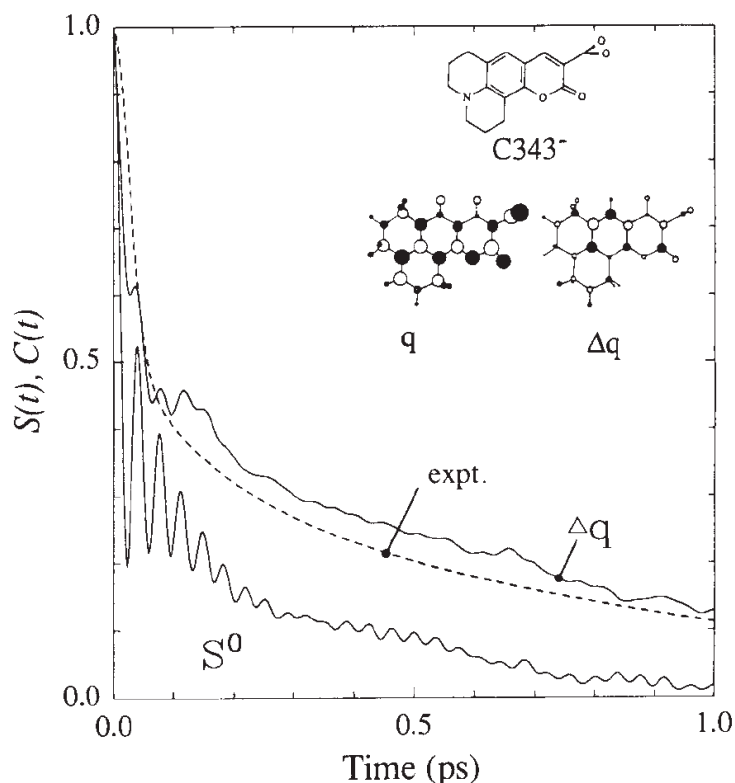


Figure 1.3 Experimental and simulated solvation response functions for Coumarin 343 in water. The experimental nonequilibrium response ($S_V(t)$: “expt.”) is the fluorescence Stokes shift function measured in 10^{-4} M Coumarin 343 sodium salt aqueous solution. The curve marked “ Δq ” is a classical molecular dynamics simulation result $C_{\Delta E}(t)$ using a charge distribution difference between ground and excited states calculated by semi-empirical quantum chemical methods, with SPC/E water potential. Also shown is a simulation for a neutral atomic solute with the Lennard-Jones parameters of the water oxygen atom (S^0). [From R. Jimenez, G. R. Fleming, P. V. Kumar, M. Maroncelli, *Nature* **369**, 471 (1994).]

The traditional linear response theory uses the same approximation as in the fluctuation–

dissipation theorem which assumes the external disturbance is small. But in some cases the disturbance is not small at all. As long as the fluctuation obeys Gaussian statistics, the linear response is still valid.^{2,44,45} The linear response theory with Gaussian statistics will be derived in Chapter 2. The near universality of Gaussian statistics for microscopic quantities is guaranteed by the central limit theorem, because the “microscopic” quantity is usually a statistical average over the order of 10^{23} events. For most cases, the linear response theory can successfully predict the solvation relaxation.^{2,46,47}

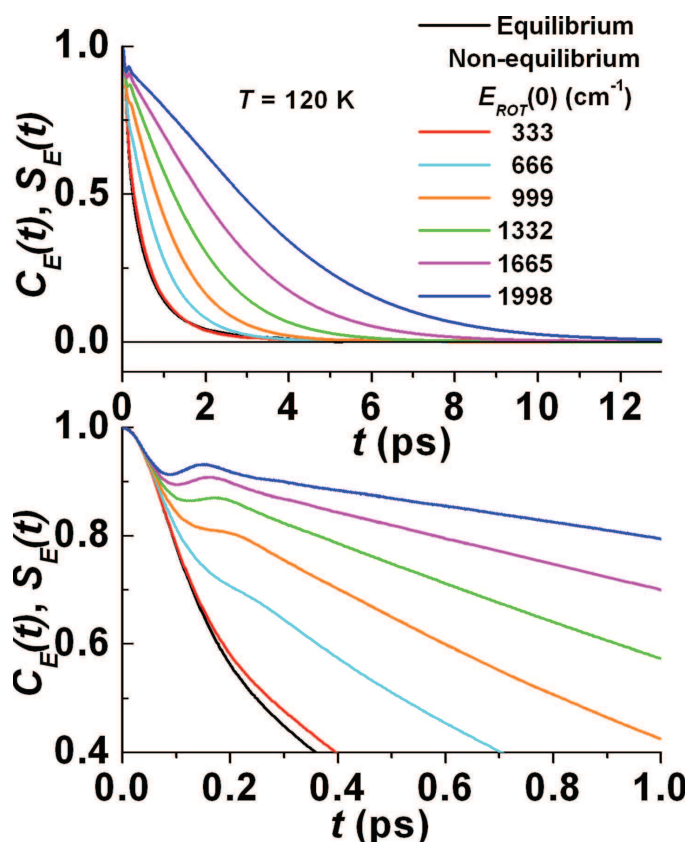


Figure 1.4 Rotational energy relaxation of CN in liquid Ar. The equilibrium linear-response prediction $C_E(t)$ (black curve) is compared with the nonequilibrium response functions $S_E(t)$ (colored curves) calculated for six different choices of the initial CN rotational energy $E_{\text{ROT}}(0)$. The lower panel shows the first picosecond in greater detail, that the initial relaxation (about 100 fs) is given exactly by linear response and that the onset of deviations from linear response is marked by distinguishable wiggles. [From G. Tao, R. M. Stratt, *J. Chem. Phys.* **125**, 114501 (2006).]

However, the breakdown of linear response, in solvation processes for example, often accompanies a large initial disturbance of the the solute that pushes the system far from

equilibrium, and the subsequent relaxation involves a dramatic rearrangement of liquid structure.^{48–50} To make the breakdown happen, a sufficient separation between the solute time scale and that of the solvent geometry evolution is required.^{51,52} Moskun *et al.* reported a linear-response failure in a rotational excited diatomic molecule solution.⁵³ Experimentally, a highly excited CN rotor is generated by photodissociating ICN with an ultrafast deep ultraviolet laser pulse, and found that nearly free rotation lasts for tens of rotational periods (several picoseconds) in solution. Simulation shows that the nonequilibrium rotational relaxation is slower than the equilibrium time correlation function (Figure 1.4). The nonlinear response originates from the fact that the rotationally hot CN solute kicks a nearby solvent out of the innermost solvation shell creating a bubble in solution which makes the solvent structural relaxation time scale much slower than that of the solute.⁵¹ Among a few cases of linear-response breakdown, the nonequilibrium relaxation could be faster than the equilibrium linear-response prediction, with examples like solvated electron in methanol by Turi *et al.*⁵⁴ and solute’s dipole flip in methanol by Ladanyi and co-workers.^{55,56} The electron solvation calculations shows that a rapid decrease in the size of the solute alters the solvent structure, specifically different hydrogen bonding patterns between equilibrium initial and final states. The solvent collapses inwards to accommodate the solute’s transformation, which is easier than a swollen solute, thus faster.

1.2.6 Computer simulations

Computer simulation is nothing but a well-controlled experiment on computer, which serves as a bridge connecting experiment and theory. One can test models by comparing simulation with real experimental results; one can test theories by comparing simulation with theoretical predictions.⁵⁷ Computer simulation provides detailed microscopic information of molecular systems, as well as macroscopic measurable quantities of experimental interest. The flexibility to artificially choose models and selectively turn on or turn off certain contributions enables one to scrutinize molecular mechanisms and unearth hidden

details behind macroscopic measurements. For example, the diffusion coefficient can be determined by integrating velocity autocorrelation function as in Equation 1.11. The two main families of simulation technique are molecular dynamics (MD) and Monte Carlo (MC).

Molecular dynamics simulation provides a direct avenue to real-time motions of individual molecules in many-body systems.⁵⁸ The trajectory, a sequence of positions and momenta of all the particles, is numerically evaluated by integrating classical equations of motion in a step-by-step fashion. The particles interact with each other via inter-/intra-molecular potentials, which is also called the force field. Once the initial condition (positions and momenta of all particles in the system) is given, the trajectory is deterministically set.

A widely used integration method for propagating the classical equations of motion is the velocity Verlet algorithm.⁵⁹ Denote the time-dependent position, velocity and acceleration of a particle as $\mathbf{r}(t)$, $\mathbf{v}(t)$ and $\mathbf{a}(t)$ respectively. The time step is δt , for instance several femtoseconds. The propagation of the position and velocity from time t to time $t + \delta t$ is expressed as follows.

$$\mathbf{a}(t) = -\frac{1}{m}\nabla V(\mathbf{r}(t)), \quad (1.37)$$

$$\mathbf{r}(t + \delta t) = \mathbf{r}(t) + \mathbf{v}(t)\delta t + \frac{1}{2}\mathbf{a}(t)\delta t^2, \quad (1.38)$$

$$\mathbf{v}(t + \delta t) = \mathbf{v}(t) + \frac{1}{2}[\mathbf{a}(t) + \mathbf{a}(t + \delta t)]\delta t. \quad (1.39)$$

Conventional molecular dynamics simulation is essentially a phase-space sampling technique from the microcanonical ensemble — constant NVE (number of particles, volume, energy). The conservation of energy is automatically guaranteed by the nature of classical equations of motion. Although MD in other ensembles, like canonical (constant NVT) and isothermal-isobaric (constant NPT) can be achieved using artificial thermostat

and barostat constraints on system properties with correct equilibrium ensemble averages, some elements of the dynamics might no longer be correct.

The most natural canonical-ensemble sampling method is Monte Carlo⁶⁰ which is a random walk through the configuration space with probability consistent with thermal equilibrium ensemble distribution, in which the temperature is embedded. For example, in Metropolis MC algorithm,⁶¹ the probability accepting a random chosen trial move from \mathbf{R} to \mathbf{R}' is the minimum value between 1 and the canonical Boltzmann factor ratio of the initial and final configuration.

$$P(\mathbf{R}'|\mathbf{R}) = \min \left[1, e^{-\beta[V(\mathbf{R}')-V(\mathbf{R})]} \right], \quad (1.40)$$

which assumes moving downwards on the energy surface is always acceptable, but climbing up the energy surface has to be determined by comparing a uniform distributed random number with the exponential Boltzmann probability. Monte Carlo simulation does not provide true time-dependent dynamical information, the sequence of configurations has no chronological connection, but it has a great number of applications to molecular systems such as statistical mechanics of rare events⁶² and molecular electronic structures.⁶³

1.3 Experimental Methods

The development of laser technology over the past decades has made time-domain observation of molecular structure and interactions in condensed system a reality. A widely-used Ti:Sapphire laser oscillator generates pulse with only a few femtoseconds (1 fs = 10^{-15} s) duration, which is shorter than the time scale of most chemical reactions and molecular motions. Figure 1.5 shows time scales for different kinds of molecular motions and fundamental processes in physics, chemistry and biology.⁶⁴ To date, the shortest laser temporal resolution reaches attosecond regime (1 as = 10^{-18} s) that has been used to investigate electron motions.⁶⁵⁻⁶⁷

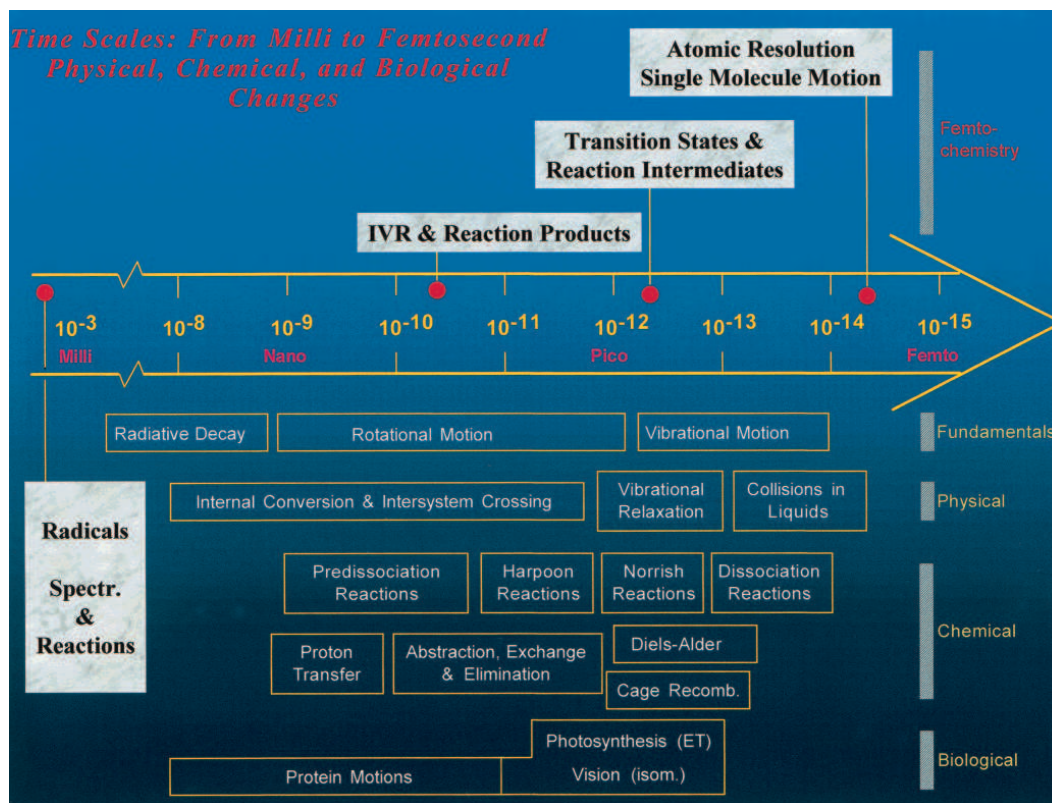


Figure 1.5 Time scales relevant to physical, chemical and biological processes. The fundamental molecular vibrational motion is on femtosecond time scale. [From A. Zewail, *J. Phys. Chem. A* **104**, 5660 (2000).]

Graham Fleming pioneered the field of ultrafast laser spectroscopy⁶⁸ and Ahmed Zewail won the Nobel prize in chemistry in 1999 for building up the field of femtochemistry.⁶⁴

1.3.1 Time-dependent fluorescence spectroscopy

As mentioned in the previous section (Figure 1.2 and Figure 1.3), the time-dependent fluorescence spectroscopy has long been a main tool in understanding the dynamics of solvation.^{2,69–80} A newly excited dye solute with an abrupt change in charge distribution causes the solvent to reposition to lower the solute–solvent interaction energy, leading to a decreasing fluorescence frequency emitted by the solute. By tracking the time evolution of the fluorescence frequency shift (the Stokes shift), one gets the solvation relaxation profile $S_V(t)$. The solvation relaxation reports on how fast the solution find its new optimized organization and the fluorescence frequency is equivalent to the solute–solvent interaction energy which is mostly affected by the interaction between the solute and the solvent in the first shell.⁸¹ This time-dependent-fluorescence idea has been applied to analyze solvation dynamics in simple liquids like chromophore solutions^{82–84} and in complex systems such as proteins,⁷⁴ DNAs^{75–78} and reverse micelles.^{79,80} However, this solute–solvent interaction energetic probe cannot directly tell the structure of the solvent — the dye solute serves as the sole reporter. One can only infer how the solvent structure changes based on the energetic information of the solute–solvent interaction.

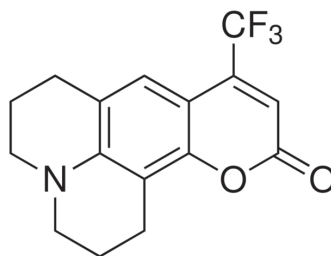


Figure 1.6 Molecular structure of coumarin 153.

Levinger and co-workers studied the solvation response for coumarin 153 (C153) solute (Figure 1.6) in acetonitrile–benzene mixtures using time-dependent fluorescence

technique.⁸⁵ Acetonitrile has a dipole around 4 Debye, and benzene is nonpolar but possesses quadrupole. The solute C153 has a large dipole creation (about 8 Debye) upon photoexcitation, thus the excited C153 favors the dipolar acetonitrile. What they found interesting is that the solvent mixtures relax more slowly than either pure solvent, with the 5% acetonitrile mixture the slowest as shown in Figure 1.7. This phenomenon is called *preferential solvation*,⁸⁶ the solvation process with multiple solvents when the solvating abilities of each solvent are different. The slow-down of solvent mixture has its roots in the time-consuming exchanging process involving both solvents that is absent in a pure-solvent case.⁸⁵⁻⁹⁸ Starting from chapter 3, we will discuss the molecular mechanism of preferential solvation thoroughly and use it as a model system for applying solute-pump/solvent-probe spectroscopy.

1.3.2 Transient absorption

The transient absorption measurement is implemented by a pump-probe configuration of ultrafast laser pulses.⁹⁹ The pump-probe configuration refers to a general description of the set-up of many ultrafast spectroscopies. The time-zero-defining pump laser pulse initiates chemical reactions and the time-delayed probe laser pulse is used to take a snapshot of the molecular behavior (by measuring absorption for example). To study molecular motions, the relative timing of ultrafast laser pulses has to be controlled accurately. The time delay between synchronized pump and probe pulses is varied by diverting the probe pulse through an adjustable optical path length. The numerous choices for wavelengths of pump and probe pulses and specific probing technique lead to different kinds of pump-probe spectroscopies that are sensitive to distinct properties of matter.

Transient IR absorption experiment excels at observing the evolution of molecular vibrations under the influence of ambient chemical environment in real time.¹⁰⁰⁻¹⁰⁶ This technique has been successfully applied to study water dynamics.¹⁰⁷⁻¹⁰⁹ For instance, Fayer and co-workers studied hydrogen bond breaking dynamics through tracking transient

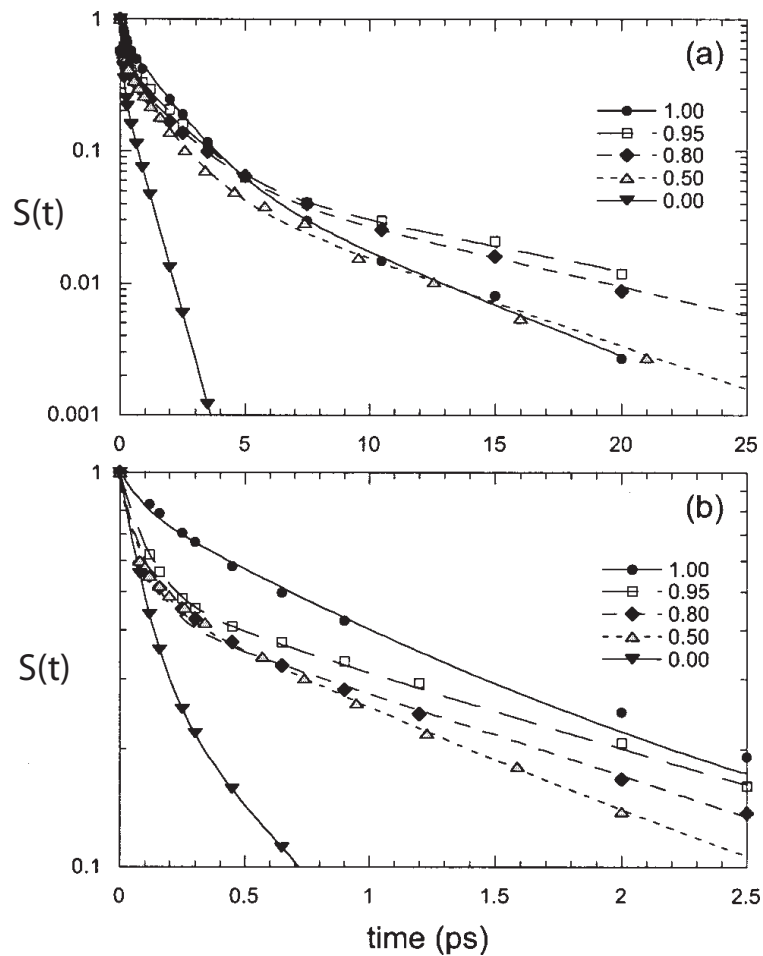


Figure 1.7 Solvation response functions of coumarin 153 in acetonitrile–benzene binary mixtures measured by time-dependent fluorescence spectroscopy. The mole fraction of benzene is shown in the legend. Upper panel (a) depicts the longer-time-scale solvation relaxation; the lower panel (b) shows the initial solvation response in the first 2.5 ps. [From B. M. Luther, J. R. Kimmel, N. E. Levinger, *J. Chem. Phys.* **116**, 3370 (2002).]

absorption of the hydroxyl OD stretching mode of HOD in water at room temperature.¹⁰⁹ In their pump–probe setup, a pump pulse excites a selected vibrational mode(s) followed by a time-delayed probe pulse that detects the instantaneous IR absorption.

Ultrafast X-ray absorption spectroscopy (XAS)^{110–118} is implemented in a laser-pump/X-ray-probe geometry. It measures the difference in X-ray absorption between the laser-excited sample and the unexcited sample. Bressler and Chergui^{111,117} reviewed the time-resolved X-ray absorption spectroscopy and its ability to reveal ultrafast molecular geometrical structures as well as electronic structures in liquids with a typical time resolution of 50–100 ps. Recently, the temporal resolution has been achieved in the sub-picosecond regime¹¹⁹ which makes this technique promising in studying ultrafast chemical dynamics in condensed phases.

1.3.3 Scattering experiments

Scattering experiments offer accurate detection of microscopic structures by impinging elementary particles/waves on matter and watching the scattered particles/waves at all directions. The scattered particle could be a photon, electron or neutron. Photons and electrons are scattered mostly by electrons in the material, whereas neutrons are scattered primarily by nuclei. A popular photon scattering technique is X-ray diffraction (XRD)¹²⁰ which can probe structures at the angstrom scale in bulk samples, primarily solid materials, and is particularly sensitive to lattice dynamics, melting and phase transitions. In light of the million-fold larger scattering cross sections for electrons than X-rays, time-resolved electron scattering has been utilized to study transient structures in dilute gas phase and thin materials.¹¹⁵ Neutron scattering is able to provide complete microscopic information on time-dependent nuclear positions of all atoms, but the neutron source requires a expensive nuclear reactor.^{121,122}

X-ray diffraction provides three-dimensional atomic-scale static structure of lattices with impressive examples like unraveling highly complex structures of proteins and DNA.

Thus usually, X-ray diffraction from solid matter is also called X-ray crystallography. The periodic structures of atoms enhances the diffraction intensity at particular angles, the Bragg angles. Although the well-defined crystalline planes are absent in disordered samples, X-ray diffraction of liquids (diffuse scattering) gives structural information with the form of radial distribution functions.^{123,124}

In X-ray scattering, the key quantity is the momentum transfer $\mathbf{q} = \mathbf{k} - \mathbf{k}_0$, where \mathbf{k}_0 and \mathbf{k} are the incident and the diffracted X-ray wave vectors. The magnitude of momentum transfer obeys $q = 4\pi \sin \theta / \lambda$, where λ is the wavelength of the X-rays and 2θ is the scattering angle. The amplitude of the diffracted electric field is proportional to

$$E(\mathbf{q}) = \int \rho_e(\mathbf{r}) e^{-i\mathbf{q}\cdot\mathbf{r}} d\mathbf{r} = \sum_n f_n(\mathbf{q}) e^{-i\mathbf{q}\cdot\mathbf{r}_n}, \quad (1.41)$$

in which $\rho_e(\mathbf{r})$ is the electron density and $f_n(\mathbf{q})$ is the atomic form factor that is defined as Fourier transform of the electron density of atom n , $f_n(\mathbf{q}) = \int \rho_n(\mathbf{r}) e^{-i\mathbf{q}\cdot\mathbf{r}} d\mathbf{r}$.

So the scattering intensity

$$I(\mathbf{q}) = \left| \sum_n E_n(\mathbf{q}) \right|^2 = \sum_{n,m} f_n(\mathbf{q}) f_m(\mathbf{q}) e^{-i\mathbf{q}\cdot(\mathbf{r}_n - \mathbf{r}_m)} \quad (1.42)$$

and in isotropic medium, the orientational average of the scattering intensity leads to

$$I(q) = \sum_n f_n^2(q) + \sum_{m < n} f_n(q) f_m(q) \frac{\sin q r_{nm}}{q r_{nm}}, \quad (1.43)$$

where r_{nm} is the distance between atom n and atom m .

The connection between the scattering intensity and radial distribution function that is routinely available in simulation is highlighted by the following relation,

$$I(q) = \sum_{\alpha} N_{\alpha} f_{\alpha}^2(q) + \sum_{\alpha < \beta} N_{\alpha} N_{\beta} f_{\alpha}(q) f_{\beta}(q) \int_V \rho_0 [g_{\alpha\beta}(r) - 1] \frac{\sin qr}{qr} dr, \quad (1.44)$$

where α and β are species of atoms, N_α and N_β is the number of α - and β -types of atoms, ρ_0 is the average number density, and $g_{\alpha\beta}(r)$ is the pair distribution function between type α and β ($4\pi r^2 g_{\alpha\beta}(r) dr$ is the probability of finding a β -type atom at the distance r from an α -type atom).

Time-resolved X-ray diffraction has been a fruitful method for investigating ultrafast structural dynamics in condensed matters.^{123–129} For example, Rose-Petruck *et al.* reported time-resolved X-ray diffraction study on fast dynamics in a crystal, a direct observation of coherent acoustic phonon propagation in crystalline gallium arsenide.¹²⁶ Moreover, time-resolved X-ray diffraction is also able to directly probe structural dynamics for chemical reactions in solution.^{123, 124, 127–129} The pump–probe method is used to implement the idea. An ultrafast optical pump pulse initiates a photochemical process, and at a delayed time, an X-ray pulse is sent to the system probing structural dynamics. Through scanning the delay time between the optical pump and X-ray probe, one gets the dynamical information about the solution. The time-resolved difference scattering intensities $\Delta I(q, t)$ are determined by subtracting the unperturbed scattering intensity from the perturbed scattering intensity, and the difference scattering intensities contain the direct structural changes of the solute and solvent. Time-resolved X-ray scattering complements ultrafast optical spectroscopy in that the diffraction signals are sensitive to all atoms simultaneously. It can provide direct structural information that is difficult to detect with ultrafast optical spectroscopy, such as the time evolution of bond lengths and angles of all molecular species including short-lived intermediates over a wide range of times, from picoseconds to milliseconds. But the time resolution of the time-resolved X-ray scattering in liquid is currently limited by the X-ray pulse width available from synchrotron sources (about 100 ps).

For example, Ihee *et al.* investigated the reaction pathways in elimination reaction of $C_2H_4I_2$ and $C_2F_4I_2$ in methanol using a time-resolved X-ray diffraction technique which they term time-resolved X-ray liquidography.¹²³ They show that the reaction pathways are dramatically different for two reactants by comparing experimental radial distributions

with molecular dynamics simulation results. After the reactants dissociate into an iodine atom and a nascent haloethyl radical, C_2H_4I has a bridged triangular structure and C_2F_4I has classic anti/gauche structures. Radical C_2H_4I then binds to an iodine atom forming intermediate C_2H_4I-I before dissociates to C_2H_4 and I_2 eventually. By contrast, fluorine-substituted radical C_2F_4I decays directly into $C_2F_4 + I$.

1.3.4 Coherent nonlinear spectroscopy

Spectroscopies provide copious molecular information in the gas phase and in the condensed phases, especially since the debut of ultrafast laser techniques. Femtosecond-resolution laser systems are routinely available worldwide. Generally speaking, spectroscopic methods have better time resolution than matter-particle diffraction experiments. Photons are sent into molecular systems, and spectroscopy records the property of outgoing photon influenced by light–matter interaction. In the course of light–matter interaction, the incident light induces an oscillating polarization \mathbf{P} in the sample that acts as the source of the emitting radiation, the signal field $\mathbf{E}_s \propto i \mathbf{P}$. The nonlinear optical effects originate from the higher orders in the induced polarization. If we expand the induced polarization into powers of the electric field,¹³⁰

$$\mathbf{P} = \epsilon_0 \left(\boldsymbol{\chi}^{(1)} \cdot \mathbf{E} + \boldsymbol{\chi}^{(2)} : \mathbf{E}\mathbf{E} + \boldsymbol{\chi}^{(3)} : \mathbf{E}\mathbf{E}\mathbf{E} + \dots \right), \quad (1.45)$$

where $\boldsymbol{\chi}^{(n)}$ is the n th-order electric susceptibility which is essentially an $(n + 1)$ th-rank tensor and \mathbf{E} is the external electric field. It is conventional to call an n th-order nonlinear optical process an $(n + 1)$ -wave mixing, counting the signal as the $(n + 1)$ st wave.

In media with inversion symmetry, such as isotropic fluids, even-order susceptibilities vanish, because the polarization must change its sign when the optical electric field is reversed. Therefore, for most bulk samples, the lowest order nonlinear optical phenomenon is the third-order nonlinearity.¹³⁰ In non-centrosymmetric media like surfaces, second-

order nonlinear effects are of great utility, including Second Harmonic Generation (SHG), Sum-Frequency Generation (SFG) and Difference-Frequency Generation (DFG).¹³¹

Four-wave mixing (FWM) is a typical kind of time-domain third-order coherent nonlinear optical process.¹³² The four waves are ascribed to three incident laser fields and one coherent signal field. There are numerous techniques falling into this category, including optical Kerr effect (OKE), transient grating (TG), pump–probe transient absorption, photon echo and coherent anti-Stokes Raman (CARS). In these coherent spectroscopies, the signal has a specific propagating direction — for incoherent spectroscopies like time-dependent fluorescence, spontaneous Raman and light scatterings, there is no specific direction for the signal since the radiating molecules are not driven coherently and thus glow independently. As the molecules are driven coherently, they radiate with constructive interference in a well-defined direction. This special direction is defined by the phase matching condition. The incident electric field with n laser pulses centered at τ_n is given by (we use the scalar form for convenience)¹³³

$$E(\mathbf{r}, t) = \sum_{j=1}^n \left[E_j(\mathbf{r}, t - \tau_j) e^{i\mathbf{k}_j \cdot \mathbf{r} - i\omega_j t} + E_j^*(\mathbf{r}, t - \tau_j) e^{-i\mathbf{k}_j \cdot \mathbf{r} + i\omega_j t} \right]. \quad (1.46)$$

The generated signal has maximum intensity at direction \mathbf{k}_s (by conservation of momentum) and frequency ω_s (by conservation of energy),

$$\mathbf{k}_s = \pm \mathbf{k}_1 \pm \mathbf{k}_2 \cdots \pm \mathbf{k}_n, \quad (1.47)$$

$$\omega_s = \pm \omega_1 \pm \omega_2 \cdots \pm \omega_n. \quad (1.48)$$

In above relations, the choices of sign combinations are consistent for both the wave vectors and the frequencies. Different choices of incoming wave vectors lead to different signal wave vector that is spatially separated from the incident pulses and other signals.

The n th-order induced polarization can be written as the convolution of nonlinear

response function $R^{(n)}$ and the electric fields.

$$P^{(n)}(\mathbf{r}, t) = \int_0^\infty dt_1 \cdots \int_0^\infty dt_n R^{(n)}(t_n, \dots, t_1) E(\mathbf{r}, t - t_n) \cdots E(\mathbf{r}, t - t_1 \cdots - t_n). \quad (1.49)$$

In the quantum mechanical formalism for nonlinear spectroscopy,¹³⁴ the n th-order nonlinear response function is given by

$$R^{(n)}(t_n, \dots, t_1) = \left(\frac{i}{\hbar}\right)^n \theta(t_1) \cdots \theta(t_n) \\ \times \langle [[\cdots [\hat{V}(t_n + \cdots + t_1), \hat{V}(t_{n-1} + \cdots + t_1)], \cdots], \hat{V}(0)] \rho_{eq} \rangle, \quad (1.50)$$

where the dipole operator

$$\hat{V} = \sum_{\alpha} q_{\alpha}(\mathbf{r} - \mathbf{r}_{\alpha}), \quad (1.51)$$

summing over all electrons and nuclei α , with charges q_{α} and positions \mathbf{r}_{α} . It couples with the electric field via the dipole interaction Hamiltonian $\hat{H}_{int} = -E(\mathbf{r}, t) \cdot \hat{V}$, which is the leading term in light-matter interaction. And $\hat{V}(t)$ is the Heisenberg operator with definition

$$\hat{V}(t) = \exp\left(\frac{i}{\hbar} H t\right) \hat{V} \exp\left(-\frac{i}{\hbar} H t\right). \quad (1.52)$$

The equilibrium density matrix $\rho_{eq} = e^{-\beta H} / \text{Tr}[e^{-\beta H}]$, where H is the unperturbed Hamiltonian and Tr stands for trace of a matrix. The concept of density matrix is essential in the quantum approach to nonlinear spectroscopy. We want to understand molecular details in the matter states $|n\rangle$ that are the eigenstates of the (unperturbed) matter Hamiltonian, but what we can observe is the light-matter states $|\psi_k(t)\rangle$ which are the eigenstates of the true Hamiltonian incorporating light-matter interactions. In the matter-state basis, the light-matter states are mixed states. To describe mixed quantum states, the wavefunction language is not enough. For an ensemble of quantum systems, a complete description of a

statistical mixture is provided by the density matrix.¹³⁵ First we define the density operator

$$\rho(t) \equiv \sum_k P_k |\psi_k(t)\rangle \langle \psi_k(t)|, \quad (1.53)$$

where P_k is the classical statistical probability of the system to be in pure state $|\psi_k(t)\rangle$ with constraints $P_k \geq 0$ and $\sum_k P_k = 1$. The system within an ensemble could be on any pure state with probability P_k and there is no quantum interference or coherent phase relations between any members of the ensemble.¹³⁶ If we choose the matter-state basis $|n\rangle$ and apply equality $\mathbf{1} = \sum_n |n\rangle \langle n|$, we have the elements of the density matrix

$$\rho_{nm} = \sum_k P_k \langle n | \psi_k \rangle \langle \psi_k | m \rangle. \quad (1.54)$$

The diagonal elements of density matrix ρ_{nn} are called *populations* that can be viewed as the probability of finding the system in the n th state. By contrast, the off-diagonal elements $\rho_{nm} = \rho_{mn}^*$ are called *coherences* which delineate the superposition of quantum states $|n\rangle$ and $|m\rangle$ with phase information. The quantum coherences in condensed matter often decay rapidly. With density matrix, the ensemble average of any operator \hat{A} at time t is

$$\langle A(t) \rangle = \sum_k P_k \langle \psi_k(t) | \hat{A} | \psi_k(t) \rangle = \sum_n \langle n | \hat{A} \rho(t) | n \rangle = \text{Tr}[\hat{A} \rho(t)]. \quad (1.55)$$

The time evolution (equation of motion) for the density matrix is the quantum Liouville equation,

$$\frac{\partial \rho}{\partial t} = -\frac{i}{\hbar} [H, \rho], \quad (1.56)$$

where H is the Hamiltonian and $[A, B] = AB - BA$ is the quantum commutator whose classical limit is the Poisson bracket,¹³⁷

$$\frac{1}{i\hbar} [A, B] \longrightarrow \{A, B\}. \quad (1.57)$$

Using this framework of density matrices, we can now turn to a useful diagrammatic description of nonlinear optical processes, the double-sided Feynmann diagrams.^{133, 138, 139} As the density matrix has the ket side (left) and the bra side (right), the n th-order response function contains n dipole interactions that can act from the left or the right side of the density matrix, leading to 2^n terms in total, which is consistent with n nested commutators or Poisson brackets in the classical limit. Thus the double-sided Feynmann diagrams portray all the possible interaction sequences with two vertical upward-running lines representing the ket and bra sides of the density matrix and wavy arrows acting from the left or the right side representing the interactions. (Figure 1.8) Any arrow pointing to the right carries a contribution of $E_j \exp(i\mathbf{k}_j \cdot \mathbf{r} - i\omega_j t)$ to the polarization, thus a plus-signed $+\mathbf{k}_j$ and $+\omega_j$ to the phase matching condition; and any arrow pointing to the left corresponds to the complex conjugate of right-pointing arrow, and contributes a minus-signed $-\mathbf{k}_j$ and $-\omega_j$ to the phase matching condition. An arrow pointing inwards excites the system on its corresponding ket/bra side and an outgoing arrow de-excites the system. The last interaction corresponds to the emission of the signal that is originated from the trace $\text{Tr}[\hat{V}\rho(t)]$ and always ends in a population state. It is conventionally chosen to act from the left side; because of the cyclic permutation symmetry of the trace, acting on either side is equivalent. And there is a $(-1)^m$ sign for each diagram with m the number of interactions on the bra side. Mukamel terms the sequence of excited density matrix elements as Liouville-space pathway.¹⁴⁰ With basis size N , the density operator is an $N \times N$ matrix in ordinary Hilbert space and is an $N^2 \times 1$ vector in Liouville space.¹³⁸

Figure 1.8 shows the double-sided Feynman diagram for four-wave mixing in a two-level system. Take pathway R_1 for example, the system is prepared in the ground-state population $|g\rangle\langle g|$, which gets excited on the bra side becoming a coherence $|g\rangle\langle e|$. At a time t_1 after the first interaction, the second excitation on the ket side brings the system to a population on the excited state $|e\rangle\langle e|$ and at a time t_2 later the third incoming electric field de-excites the bra side of the density matrix leading to a coherence $|e\rangle\langle g|$. Finally, at

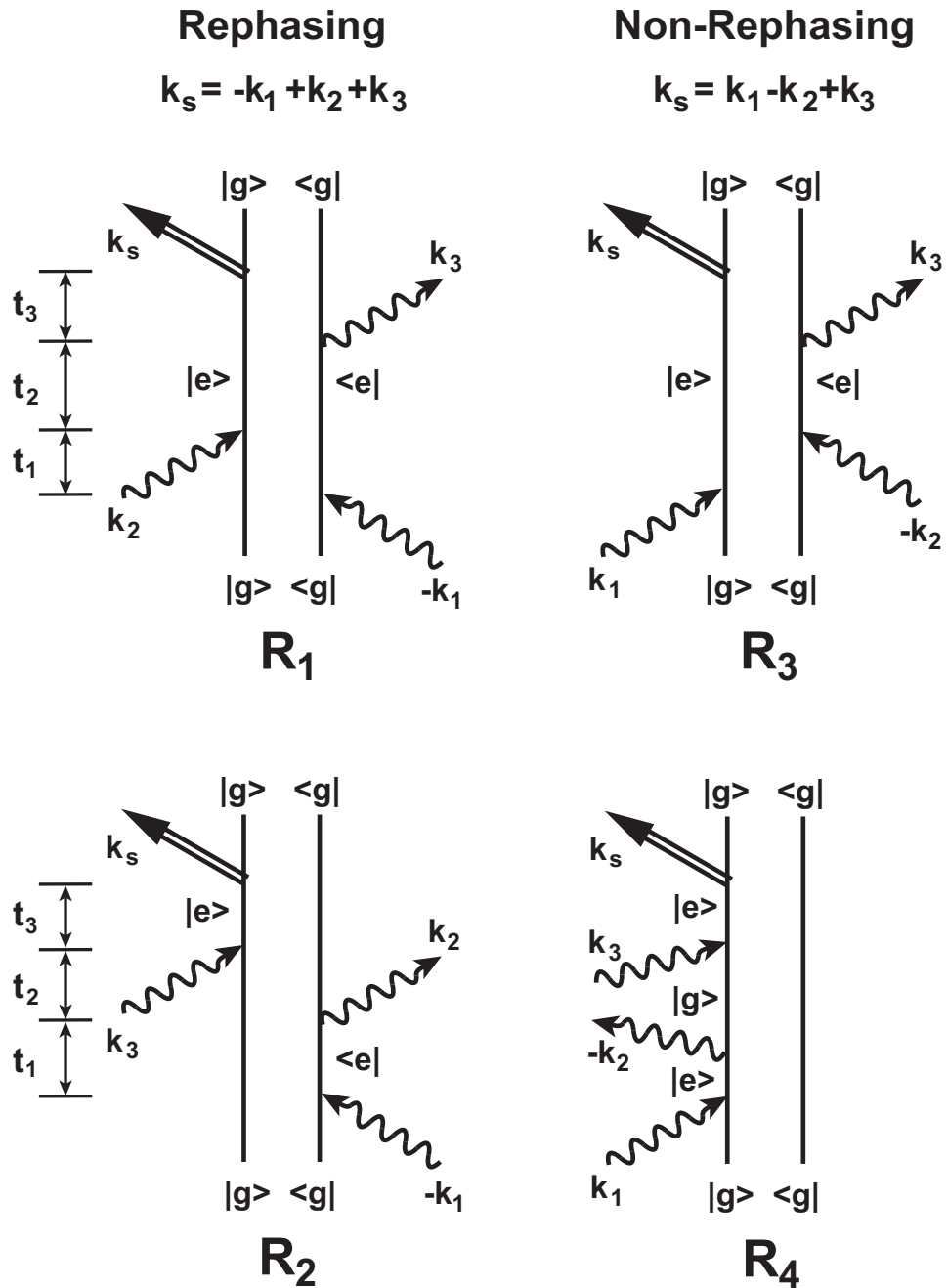


Figure 1.8 Double-sided Feynman diagrams for time-domain four-wave mixing in a two-level system (with $|g\rangle$ the ground state and $|e\rangle$ the excited state) that survive the rotating wave approximation. R_1 and R_2 are rephasing pathways with phase-matching condition $\mathbf{k}_s = -\mathbf{k}_1 + \mathbf{k}_2 + \mathbf{k}_3$; R_3 and R_4 are non-rephasing pathways with phase-matching condition $\mathbf{k}_s = \mathbf{k}_1 - \mathbf{k}_2 + \mathbf{k}_3$. Stimulated emission (SE) pathways R_1 and R_3 have an excited-state population during the second delay time t_2 , whereas ground-state bleaching (GB) pathways R_2 and R_4 have a ground-state population during t_2 .

t_3 after the third interaction, the last interaction generates the signal and the system ends up with a ground state population $|g\rangle\langle g|$. Among the four Liouville-space pathways, R_1 and R_2 are rephasing pathways that can reverse the inhomogeneous dephasing effect due to the opposite-signed frequencies during t_1 and t_3 : the evolution of coherence $|g\rangle\langle e|$ in duration t_1 gives rise to an oscillating factor $e^{-i\omega_{ge}t_1}$ in the nonlinear response and during t_3 the oscillating factor is $e^{-i\omega_{eg}t_3}$ where $\omega_{eg} = -\omega_{ge}$, so the total coherence oscillation factor is $e^{i\omega_{eg}(t_1-t_3)}$ which eliminates the inhomogeneous distribution of ω_{eg} at $t_3 = t_1$.¹³⁸ Inhomogeneous broadening results from ensemble averaging of single molecular responses under different static environments, which is also called ensemble dephasing.¹⁴¹ The rephasing pathways are responsible for the photon echo. The non-rephasing R_3 and R_4 pathways, on the other hand, contribute to other four-wave-mixing processes.

Input pulses with various frequencies, polarizations, wave vectors and time orderings along with specific signal detection give rise to different four-wave-mixing third-order nonlinear spectroscopies, such as optical Kerr effect (OKE), transient grating(TG) and photon echo measurements that are sensitive to distinctive aspects of liquid dynamics.

Optical Kerr effect spectroscopy (OKE)

In 1875, John Kerr discovered a direct-current electric field induced birefringence phenomenon in liquid which is now named after him, the Kerr effect.¹⁴² From a molecular point of view, the electric field induces a degree of net alignment of molecules through dipolar interaction. As long as the molecules are optically anisotropic, this net alignment lead to different indices of refraction parallel and perpendicular to the electric field.

The optical Kerr effect, on the other hand, is a transient birefringence in which the short-lived alignment is caused by fast-oscillating alternating-current electric field. The optical field changes its direction so fast that massive molecules cannot rotate to adjust this change. The optical Kerr effect relies on the polarizability of a liquid molecule because the electrons are light and can respond to an optical electric field quickly. It is the induced

dipole moment originated from the polarizability-electric field interaction that provokes the transient birefringence.^{143, 144}

In optical Kerr effect spectroscopy,^{20, 142, 145–159} a pump–probe laser configuration is employed: a pump laser pulse generate a net alignment of molecules creating a transient birefringence which is detected by a time-delayed probe laser pulse. By scanning the delay time between the pump pulse and the probe pulse, one obtains time-dependent birefringence information of the liquid which reveals the dynamics of liquid. The pump and probe pulses have specially chosen polarized directions and so does the detector. The phase-matching condition is $\mathbf{k}_s = \pm\mathbf{k}_{pu} \mp \mathbf{k}_{pu} + \mathbf{k}_{pr} = \mathbf{k}_{pr}$, where pu and pr denote the pump and the probe respectively. The first two light-matter interactions come from the the pump pulse, and the third interaction is with the probe field. As the time ordering of the first two electric fields are indistinguishable, Liouville-space pathways R_1 through R_4 contribute to the third-order polarization. It is important to mention that the excitations and de-excitations throughout the Liouville-space pathways are not required to be resonant, so the optical-Kerr measurement is essentially a non-resonant technique, which is suited to report intermolecular and intramolecular dynamics in liquids.

The transient birefringence is dispersive, in-phase to the polarization and related to the real part of the susceptibility, like the real part of index of refraction in linear spectroscopy. By comparison, the absorptive response is out-of-phase to the polarization and related to the imaginary part of the susceptibility, (like the imaginary part of the index of refraction describes absorption) and thus gives rise to transient dichroism.^{143, 144} Note that the signal electric field and the polarization have a $\pi/2$ phase shift since $\mathbf{E}_s \propto i \mathbf{P}$. In a word, the dispersive birefringent response represents phase-shifting of the signal field and the absorptive dichroic response represents attenuation of the signal field. Optical heterodyne detection (OHD)^{145, 147, 149, 150, 154} is often utilized to measure the signal electric field with phase information instead of using homodyne detection that measures the intensity of the signal. Detailed description of the experiment will be given in chapter 3. The

optical Kerr effect spectroscopy has an alternative name, the Raman-induced Kerr effect spectroscopy (RIKES).^{160–162} This nomination highlights that it is a (Fourier-transform) Raman spectroscopy in which the fluctuation of polarizability of the whole system serves as the reporter carrying microscopic dynamical information.

Transient grating (TG)

Transient grating measurement^{163–166} is similar to the OKE measurement. The difference is there are two laser pulses crossed at an angle impinging on the sample simultaneously creating a spatial interference fringe, a grating. Then a time-delayed third pulse gets scattered off the grating at the Bragg angle.¹⁶³ The phase-matching condition is $\mathbf{k}_s = \mp \mathbf{k}_1 \pm \mathbf{k}_2 + \mathbf{k}_3$ in which the first two pulses overlap in time (time delay between the first two pulses $t_1=0$). The second time duration t_2 is scanned. And because of the undistinguishable time ordering of the first two pulses, all Liouville-space pathways R_1 through R_4 contribute to the TG response. The transient grating is sensitive to any processes that can wash out the spatial modulation of the grating pattern, including population relaxation, thermal/mass diffusion and heating-induced acoustic waves. If measured with finite pulse durations longer than the electronic dephasing time scale, TG is also sensitive to solvation spectral diffusion, since a coherence can exist during the time between the first and second interactions.^{166,167}

TG, OKE and other non-resonant four-wave-mixing light scattering measurements with the first two time-coincident light-matter interactions, have the same form of response function yet with special choices of polarizations.

$$R_{\mu\nu\delta\gamma}^{(3)}(t) = -\beta \frac{d}{dt} \langle \delta\Pi_{\mu\nu}(0) \delta\Pi_{\delta\gamma}(t) \rangle, \quad (1.58)$$

where $\Pi_{\mu\nu}$ is the element of the many-body polarizability and the Greek letters denote polarization directions.

Three-pulse photon echo peak shift (3PEPS)

Photon echo spectroscopy has been used to eliminate the inhomogeneous contribution to nonlinear response in media close to the static inhomogeneous limit, taking advantage of the rephasing of the optical coherence which generates the echo field.^{141, 168–173} The decay of the integrated echo represents the homogeneous dephasing due to the fluctuation of system-bath interaction. Dephasing denotes the process during which the system loses coherence phase information due to the system-environment interaction, and this dephasing process is closely related to quantum decoherence.¹⁷⁴

The rephasing pathways responsible for the echo are R_1 and R_2 shown in Figure 1.8 with phase-matching condition $\mathbf{k}_s = -\mathbf{k}_1 + \mathbf{k}_2 + \mathbf{k}_3$. The first two time delays t_1 and t_2 are scanned in a three-pulse photon echo (3PE) experiment, and the integrated intensity of the echo field after the third interaction (integrated over t_3) is measured. There is another type of photon echo experiment, two-pulse photon echo (2PE), in which the second and the third interacting fields come from the same laser pulse and thus $\mathbf{k}_s = -\mathbf{k}_1 + 2\mathbf{k}_2$. Only time duration t_1 is scanned in a two-pulse photon echo measurement and there is no population period in 2PE since $t_2=0$, whereas in 3PE, during t_2 , the system evolves on the ground or the excited state surface, so 3PE can be used to investigate solvation. During the population time t_2 , the molecules start to explore new range of available system-bath interaction energies. This is spectral diffusion that reflects the influence of fluctuating bath on the system that brings about the irreversible pure dephasing. In other words, the spectral diffusion process destroys the rephasing ability. So as t_2 increases, the rephasing photon echo becomes eventually the same with the nonrephasing photon echo. By determining the peak shift between the rephasing echo and the nonrephasing echo along the population time t_2 , one knows the time-dependence of spectral diffusion, thus the solvation dynamics.^{141, 175}

Fleming and Cho and co-workers demonstrated the 3-pulse photon echo peak shift (3PEPS)^{141, 167, 172, 175–188} is linearly proportional to the time-dependent fluorescence solvation response for times longer than the bath correlation time.^{141, 169, 176} They were able

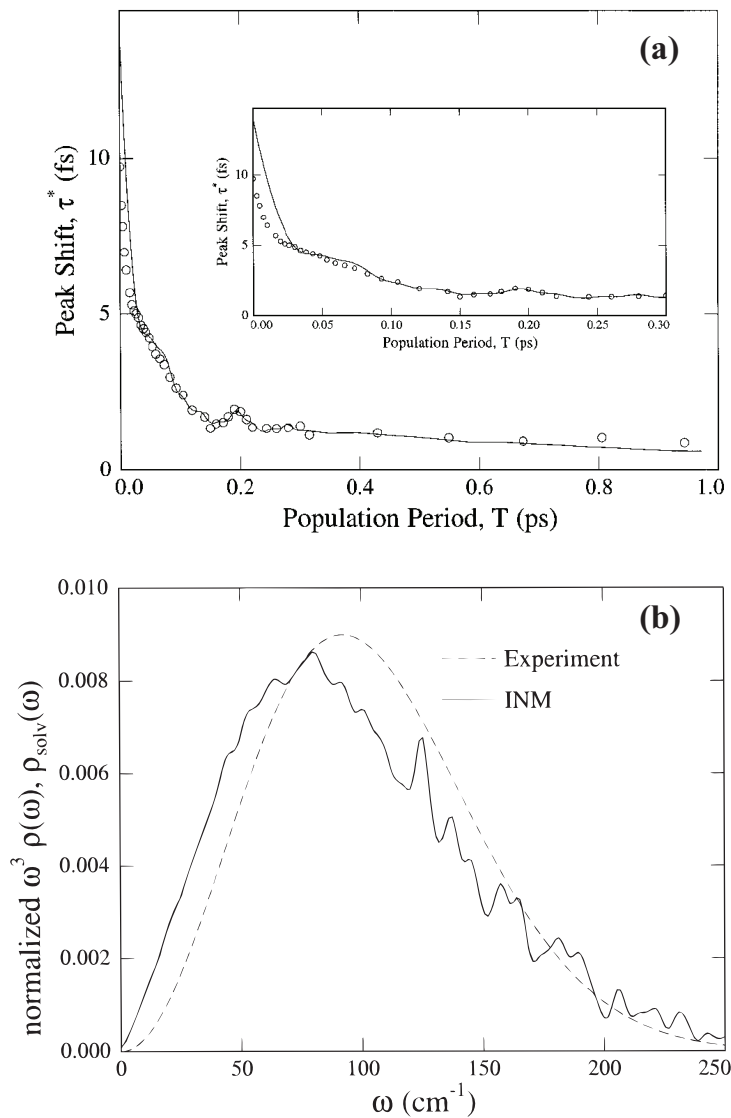


Figure 1.9 (a) Comparison of experimental (circle) and calculated (solid line) 3-pulse photon echo peak shift for tricarbocyanine dye IR144 in acetonitrile at 297K; (b) Comparison of the instantaneous normal mode solvation spectrum of acetonitrile $\rho_{solv}(\omega)$ (solid line) calculated by Ladanyi and Stratt and the rescaled inertial spectral density $\omega^3\rho(\omega)$ (dashed line) calculated with parameters fitting experimental result. [From S. A. Passino, Y. Nagasawa, T. Joo, G. R. Fleming, *J. Phys. Chem. A* **101**, 725 (1997).]

to connect the line-shape function and the fluorescence Stokes shift via (solvation) spectral density, which is defined as¹⁷⁶

$$\rho(\omega) = \frac{2}{\pi\hbar} \frac{\text{Im}[\tilde{G}(\omega)]}{\omega^2}, \quad (1.59)$$

where $\tilde{G}(\omega)$ is the Fourier transform of $G(t) = (i/\hbar)\langle[\delta V_{SB}(t), \delta V_{SB}(0)]\rangle$, with $\delta V_{SB}(t)$ the Heisenberg operator of the fluctuation of system-bath interaction δV_{SB} . The line-shape function bears the form

$$g(t) = \frac{1}{\hbar^2} \int_0^t d\tau \int_0^\tau d\tau' \langle \delta V_{SB}(\tau') \delta V_{SB}(0) \rangle. \quad (1.60)$$

Note that in the linear response regime, the fluorescence Stokes shift is equal to autocorrelation function $\langle \delta V_{SB}(t) \delta V_{SB}(0) \rangle / \langle \delta V_{SB}^2 \rangle$.

Figure 1.9 shows comparison of experimental and theoretical 3PEPS measurements for tricyanocyanine dye IR144 in acetonitrile at 297K as well as the spectral densities calculated using the instantaneous normal mode (INM) theory compared with experiment.¹⁷⁷ The excellent consistency between 3-pulse photon echo peak shift experiment and INM theory proves that the INM theory is accurate.

Light–matter interactions

The leading light–matter interaction is described by Hamiltonian $H_{int} = -\hat{V} \cdot F(\mathbf{r}, t)$, where the operator V is usually the dipole operator, and the field $F(\mathbf{r}, t)$ is accordingly the electric field.¹³⁴ But this combination of choices is not unique. Table 1.1 shows various choices of the interaction Hamiltonian.

The polarizability is coupled to the square of electric field, which is responsible for Raman and Rayleigh scatterings and two photon absorption. The pair of magnetic dipole and magnetic field is related to linear and nonlinear optical activity spectroscopy, such as circular dichroism and Raman optical activity. And the interaction between quadrupole

and the gradient of electric field is important when molecular size is comparable to the wavelength of the radiation.

Molecular properties	\hat{V}	\bullet	$F(\mathbf{r}, t)$
dipole	$\boldsymbol{\mu}$	\bullet	$\mathbf{E}(\mathbf{r}, t)$
quadrupole	\mathbf{Q}	\bullet	$(1/2)\nabla\mathbf{E}(\mathbf{r}, t)$
polarizability	$\boldsymbol{\alpha}$	\bullet	$(1/2)\mathbf{E}^2(\mathbf{r}, t)$
hyper-polarizability	$\boldsymbol{\beta}$	\bullet	$\mathbf{E}^3(\mathbf{r}, t)$
magnetic dipole	\mathbf{m}	\bullet	$\mathbf{B}(\mathbf{r}, t)$

Table 1.1 Light–matter interaction Hamiltonian $H_{int} = -\hat{V} \cdot F(\mathbf{r}, t)$ with different choices of external field $F(\mathbf{r}, t)$ and coupling molecular property \hat{V} .

Among many four-wave-mixing third-order spectroscopies, the two-dimensional infrared spectroscopy (2D IR)^{189–193} provides a route to molecular structures and dynamics in condensed phase by watching the dynamics of the coupling between vibrations of different chemical groups, such as the secondary structural sensitive amide I vibrations in proteins.¹⁹⁴ Three IR laser pulses impinge the system at different times by dipole–electric field interactions and the last detection is also a dipole interaction. We have the response function of 2D IR, which is a combination of four-time correlation functions,^{189, 195}

$$R^{(3)}(t_3, t_2, t_1) = \left(\frac{i}{\hbar}\right)^3 \langle[[[\boldsymbol{\mu}(t_3 + t_2 + t_1), \boldsymbol{\mu}(t_2 + t_1)], \boldsymbol{\mu}(t_1)], \boldsymbol{\mu}(0)]\rho_{eq}]\rangle. \quad (1.61)$$

By contrast, in the fifth-order Raman spectroscopy,^{196–217} the first two light–matter interactions are molecular polarizability with squared field ($\boldsymbol{\alpha}\mathbf{E}_1\mathbf{E}_2^*$ at time 0 and $\boldsymbol{\alpha}\mathbf{E}_3\mathbf{E}_4^*$ at time t_1), and at last what is detected is the polarizability with one incoming field $\boldsymbol{\alpha}\mathbf{E}_5$ at time t_2 . The response function for the fifth-order Raman is as follows,

$$R^{(5)}(t_2, t_1) = \left(\frac{i}{\hbar}\right)^2 \langle[[\boldsymbol{\alpha}(t_2 + t_1), \boldsymbol{\alpha}(t_1)], \boldsymbol{\alpha}(0)]\rho_{eq}]\rangle. \quad (1.62)$$

This two-dimensional Raman is called a fifth-order spectroscopy since there are five effective incident dipole–electric field interactions. One polarizability interaction equals two simultaneous dipole interactions. The following relation between the polarizability

operator and the dipole operator makes it clear: the electronic ground-state polarizability operator²¹⁸

$$\alpha(\omega) = \frac{1}{\hbar} \sum_{e \neq g} \frac{\boldsymbol{\mu}|e\rangle\langle e|\boldsymbol{\mu}}{\omega_{eg} + \omega} + \frac{\boldsymbol{\mu}|e\rangle\langle e|\boldsymbol{\mu}}{\omega_{eg} - \omega}, \quad (1.63)$$

where ω_{eg} is the transition frequency between e - and g -states.

1.4 Design of Solute-Pump/Solvent-Probe Spectroscopy

As briefly discussed in the previous section, ultrafast spectroscopic approaches to liquid dynamics seem to be limited to two diametrically opposite routes: nonresonant and resonant. Nonresonant four-wave-mixing light scattering techniques such as optical Kerr effect and transient grating spectroscopies probe the many-body polarizability of the entire liquid, thereby report on the collective intermolecular dynamics of the liquid as a whole. Although extensive progress has been made in arriving at molecular underpinnings of optical Kerr spectra,^{20, 142, 145–159, 219} their nonresonant nature prevents us from seeing any localized structural information in a solution. Experiments such as time-dependent fluorescence, transient absorption and 3-pulse photon echo peak shift, on the other hand, are resonant studies involving electronic transitions of some molecular probe, which is usually the solute. It is the solute-solvent interaction energy or the energy gap between excited-state-solute and ground-state-solute surfaces that is monitored in these resonant experiments. The solute probe serves as the sole reporter of the solvation dynamics. Thus the resonant approaches cannot provide any direct structural evidence on the solvent dynamics.

The idea of directly probing the solvent structure following an electronic excitation of a solute can be achieved by combining resonant and nonresonant avenues to ultrafast spectra, which we shall call *solute-pump/solvent-probe spectroscopy*.^{220, 221} The resonant solute pump creates a nonequilibrium liquid state from which the system starts to relax, and some nonresonant probe looks at the ultrafast solvent dynamics. In such an experiment, the resonant pump defines a local region around the excited solute, and the nonresonant

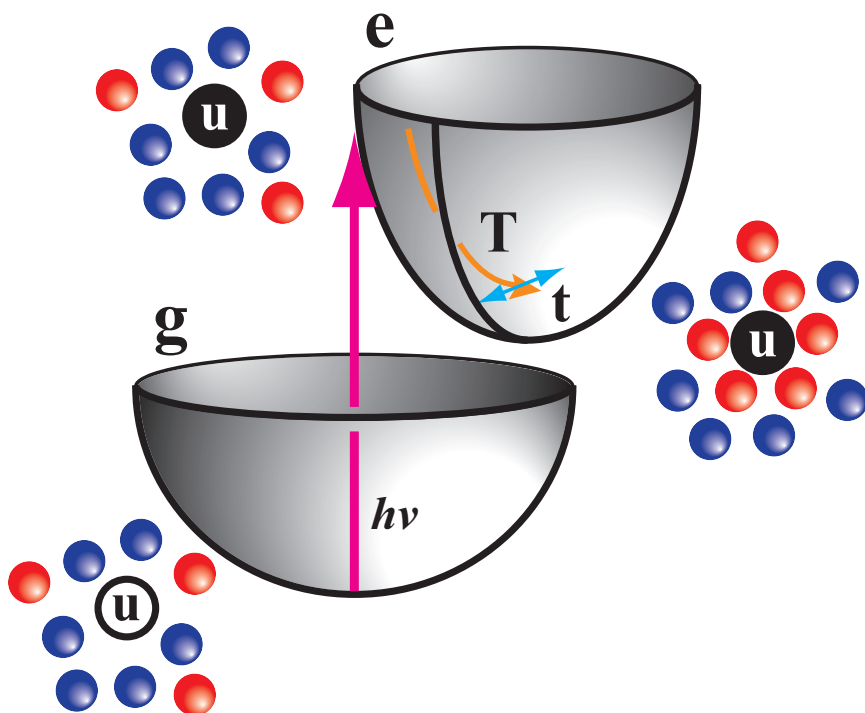


Figure 1.10 Illustration of solute-pump/solvent-probe spectroscopy for preferential solvation. The solute (u) undergoes a transition from its ground electronic state (g, open black circle) to an excited electronic state (e, filled black circle) included by a resonant solute-pump laser pulse. After the photo-excitation of the solute, the structure of the surrounding liquid mixture starts to reorganize, drawing in the solvents towards the first solvation shell and exchanging solvent molecules. At each step T along this structural relaxation process, a nonresonant light scattering probes the ultrafast intermolecular vibrational dynamics as a function of t .

probe reports on the dynamics of solvent in that region. Figure 1.10 portrays this notion. A sudden electronic excitation of the solute puts the system on the excited-state surface that also marks the time zero of the solvation process. As the resonant solute excitation is prompt compared with the nuclear motions, the newly excited molecular system still possesses the equilibrated ground-state liquid structure which is no longer the most stable one. The surrounding solvent molecules begin to rearrange their positions and orientations so as to accommodate the change in the solute's redistributed charge distribution. The solution is allowed to relax for a time T , before the nonresonant-solvent-probe is applied. The solvent probe offers the possibility of looking at the ultrafast intermolecular dynamics on another time scale t that is much shorter than the solvation relaxation time scale T . These two time variables will be used throughout this thesis with T the solvation-related structural relaxation time and t the ultrafast intermolecular dynamical time.

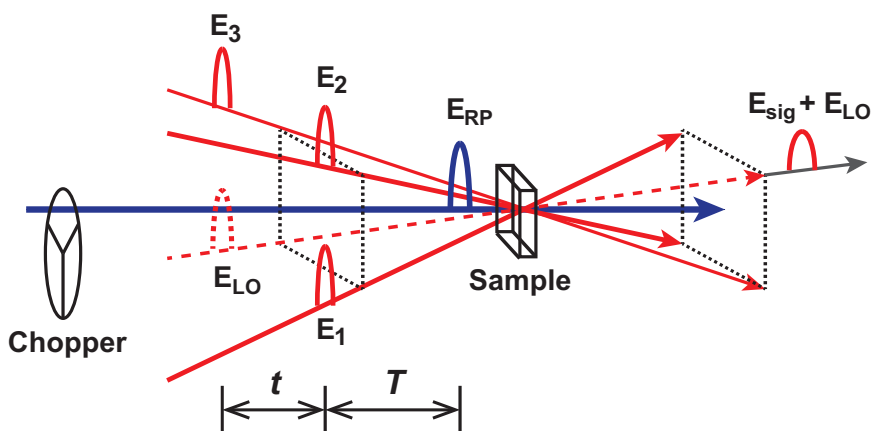


Figure 1.11 Experimental sequence of laser pulses in resonant-pump polarizability-response spectroscopy (RP-PORS).

Choosing four-wave-mixing light scattering as the nonresonant solvent probe, the Scherer group^{222–227} and the Blank group^{228–231} implemented the idea of solute-pump/solvent-probe spectra experimentally. Scherer and co-workers named their version as resonant-pump polarizability-response spectroscopy (RP-PORS). In the latest version of RP-PORS,²²⁶ that light scattering probe is a transient grating measurement carried out by crossing two visible laser pulses at time T after the original solute excitation and watching the scattered

signal field at time $T + t$ later (Figure 1.11). As mentioned before, transient grating as a four-wave-mixing light scattering measures the fluctuation of polarizability on the t time scale, which makes it essentially a Raman spectrum of the liquid's intermolecular librations and vibrations. These ultrafast intermolecular dynamics depends on the gross geometrical features of liquid. Thus, whenever exciting the solute launches a noticeable evolution of the solvent's spatial arrangement around the solute, watching the t -dependent polarizability response as a function of the structural-evolution times T will track precisely how the solution's intermolecular vibrational dynamics evolves with changes in its geometry.

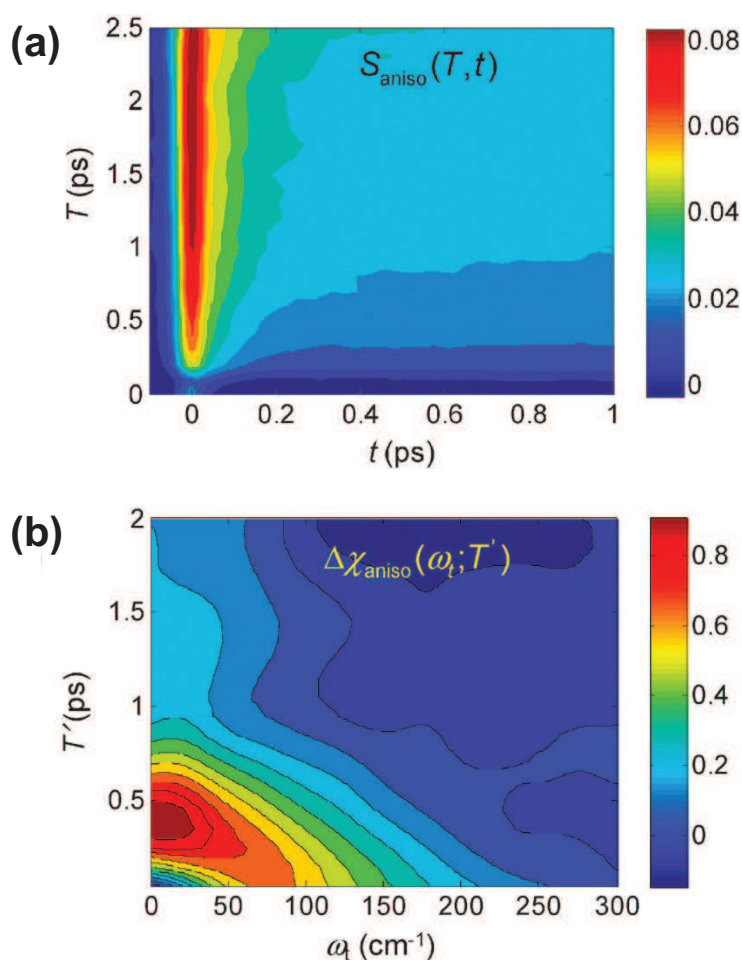


Figure 1.12 (a) Two-dimensional anisotropic resonant-pump polarizability-response spectrum (RP-PORS) response function for coumarin 153 in acetonitrile; (b) Anisotropic transient solvation polarizability measurement for coumarin 153 in acetonitrile, which is the derivative of RP-PORS spectrum with respect to solvation time T . [From S. Park, J. Kim, N. F. Scherer, *Phys. Chem. Chem. Phys.* **14**, 8116 (2012).]

The first two-dimensional RP-PORS measurement for a classic chromophore–dipolar solvent system, coumarin 153 in acetonitrile²²⁷ is shown in Figure 1.12. The time-domain RP-PORS response shown in Figure 1.12(a) is the difference between the light-scattering responses with the resonant-solute-pump on and off, which corresponds to the difference in the nonequilibrium four-wave-mixing response and the equilibrium ground-state four-wave-mixing response. The time-domain RP-PORS response displays a clear separation between two time variables, solvation axis T and ultrafast dynamical axis t . The two-dimensional transient solvation polarizability (TSP) spectrum shown in Figure 1.12(b) is defined as the first derivative of the frequency-domain RP-PORS spectrum with respect to the solvation time T . It indicates that high-frequency inertial solvent modes responds to the electronic excitation of the solute sooner than the low-frequency diffusive solvent modes and the most intriguing details of solvation is the first 2 ps.

However, the microscopic information behind the two-dimensional RP-PORS spectrum is still unclear. For example, questions that one might raise include: Which region of molecules contributes to the RP-PORS spectra, and are they in the first solvation shell? Which kinds of molecule and molecular motion are this spectroscopy sensitive to? For example, how much does translational motion account for the change in spectra and how much does the librational motion? Do the second and higher solvation shells participate in the detailed structural reorganization process, and what is the time scale for different solvation-shell structural rearrangements? Is the polarizability structural probe fundamentally different from the time-dependent fluorescence energy-gap probe, and how much does the nonresonant polarizability report the molecular structure differently than the solute-solvent interaction energy does?

To understand the origins and potential utility of solute-pump/solvent-probe spectroscopy, a molecular theory is necessary. Although some basic phenomenologic theoretic efforts based on a oscillator system-bath model have been made,²²⁴ a genuine microscopic interpretation of this experiment is still needed. To this end, the remainder of this thesis is

organized as follows: chapter 2 shows the development of a classical statistical mechanical linear-response theory for solute-pump/solvent-probe spectra. Chapter 3 describes a long- T -limit application of the theory to preferential solvation dynamics using molecular dynamics simulation with an atomic liquid mixture model. Chapter 4 presents the computation of the full two-dimensional spectra for the preferential solvation problem with a new instantaneous-normal-mode/molecular dynamics hybrid method and unveils what local structural information can be extracted from the spectra. In the end, chapter 5 offers some concluding remarks and outlooks.

Chapter 2

Linear Response Theory

2.1 Preparations

As mentioned in the previous chapter, the linear response theory has an innate connection with the fluctuation–dissipation theorem and Onsager’s regression hypothesis. In this chapter, we derive the linear response theory using a classical statistical mechanical formalism. The traditional linear response theory assuming small external disturbance, as well as the linear response theory with Gaussian statistics will be discussed. Our specific aim is to apply the idea of the linear response theory to nonlinear spectroscopies, in particular, four-wave-mixing light scattering and solute-pump/solvent-probe spectroscopy.

Although it is reasonable to have an impression that the linear response theory concerns only those responses linear to the power of the perturbing field, the notion of linear response theory can be extended to nonlinear spectroscopy with multiple input ultrafast pulses, as long as the response is separately linear in every applied perturbation. Besides the perturbing field does not have to be linear in electric field or magnetic field. Table 1.1 shows some common choices of the perturbing field and the coupled matter property. As a matter of fact, in our following development of the solute-pump/solvent-probe response, the resonant-solute-pump is not treated as linear perturbation, although the nonresonant

four-wave mixing is linearized. Here we address the theory that focuses on how a nonequilibrium relaxation is related to equilibrium fluctuations as the linear response theory. The motivation for this chapter is that we would like to interpret the solute-pump/solvent-probe spectra with examples like the RP-PORS measurements done by Scherer and co-workers,^{226,227} and the linear response theory is the best candidate for doing this job.

Before the derivation, some basic concepts in nonequilibrium statistical mechanics have to be introduced. In an N -atom classical system with a $6N$ -dimensional phase space $\mathbf{X} = (\mathbf{R}, \mathbf{P})$, any dynamical variable is a function of the phase space point \mathbf{X} , and the phase space point evolve with time, thus time-dependent dynamical variable A (implicit in t) is written as $A(\mathbf{X}(t))$. By contrast, the phase space distribution that is the probability density in phase space explicitly depends on both phase space point and time, hence can be written as $\rho(\mathbf{X}, t)$. The time evolutions of a dynamical variable and a phase space distribution are different.

The time evolution equation for a phase space distribution can be derived using the conservation of total probability. Since the total probability is conserved in the phase space for all time, the continuity equation for phase space density is¹³

$$\frac{d\rho(\mathbf{X}, t)}{dt} = \frac{\partial\rho(\mathbf{X}, t)}{\partial t} + (\nabla_{\mathbf{X}}\rho(\mathbf{X}, t)) \cdot \frac{d\mathbf{X}}{dt} = 0, \quad (2.1)$$

where $\nabla_{\mathbf{X}} = \frac{\partial}{\partial \mathbf{X}} = \left(\frac{\partial}{\partial \mathbf{R}}, \frac{\partial}{\partial \mathbf{P}} \right)$. Rearranging the above equation, we have the Liouville equation for the phase space distribution — the time rate of change of the phase space density is equal to the negative of the divergence of its flux,

$$\begin{aligned} \frac{\partial\rho(\mathbf{X}, t)}{\partial t} &= -(\nabla_{\mathbf{X}}\rho(\mathbf{X}, t)) \cdot \frac{d\mathbf{X}}{dt} = -\left(\frac{\partial\rho}{\partial \mathbf{R}} \cdot \frac{d\mathbf{R}}{dt} + \frac{\partial\rho}{\partial \mathbf{P}} \cdot \frac{d\mathbf{P}}{dt} \right) \\ &= \left(\frac{\partial H}{\partial \mathbf{R}} \cdot \frac{\partial\rho}{\partial \mathbf{P}} - \frac{\partial H}{\partial \mathbf{P}} \cdot \frac{\partial\rho}{\partial \mathbf{R}} \right) = \{H, \rho\}. \end{aligned} \quad (2.2)$$

In above derivation, the Hamilton's equations (Equation 1.7) are utilized. The definition of the Poisson bracket $\{A(0), B(t)\}$ is as follows

$$\{A(0), B(t)\} = \sum_{k=1}^{3N} \left(\frac{\partial A(0)}{\partial R_k(0)} \frac{\partial B(t)}{\partial P_k(0)} - \frac{\partial A(0)}{\partial P_k(0)} \frac{\partial B(t)}{\partial R_k(0)} \right) = \left(\frac{\partial A}{\partial \mathbf{R}} \cdot \frac{\partial B(t)}{\partial \mathbf{P}} - \frac{\partial A}{\partial \mathbf{P}} \cdot \frac{\partial B(t)}{\partial \mathbf{R}} \right), \quad (2.3)$$

where the sum runs over all $3N$ degrees of freedom, ($k = 1, \dots, 3N$). More properties of the Poisson bracket can be found in Appendix A. With the Poisson bracket notation, the Liouville operator \mathcal{L} that describes the time evolution of the system under Hamiltonian H is defined as *

$$\mathcal{L} \equiv -\{H, \} = \sum_{k=1}^{3N} \left(\frac{\partial H}{\partial P_k} \frac{\partial}{\partial R_k} - \frac{\partial H}{\partial R_k} \frac{\partial}{\partial P_k} \right). \quad (2.4)$$

Now the Liouville equation (Equation 2.2) can be simplified as

$$\frac{\partial \rho}{\partial t} = -\mathcal{L} \rho. \quad (2.5)$$

The Liouville equation has a formal solution which characterizes the propagation of the phase space distribution,

$$\rho(\mathbf{X}, t) = e^{-t\mathcal{L}} \rho(\mathbf{X}, 0). \quad (2.6)$$

The time evolution of a dynamical variable A , on the other hand, follows the Liouville equation for a dynamical variable shown below which has a different sign than the Liouville equation for the phase space distribution.

$$\frac{d}{dt} A(\mathbf{X}(t)) = \mathcal{L} A(\mathbf{X}(t)), \quad (2.7)$$

since

$$\frac{d}{dt} A(\mathbf{X}(t)) = \frac{\partial A}{\partial \mathbf{R}} \cdot \frac{d\mathbf{R}}{dt} + \frac{\partial A}{\partial \mathbf{P}} \cdot \frac{d\mathbf{P}}{dt} = - \left(\frac{\partial H}{\partial \mathbf{R}} \cdot \frac{\partial A}{\partial \mathbf{P}} - \frac{\partial H}{\partial \mathbf{P}} \cdot \frac{\partial A}{\partial \mathbf{R}} \right) = \mathcal{L} A(\mathbf{X}).$$

*In some literature, the Liouville is defined with an imaginary factor as $i\mathcal{L} = -\{H, \}$.

The formal solution for the Liouville equation for a dynamical variable is

$$A(\mathbf{X}(t)) = e^{t\mathcal{L}} A(\mathbf{X}(0)). \quad (2.8)$$

The ensemble average of a dynamical variable $A(t)$ can be expressed as

$$\langle A(t) \rangle = \int d\mathbf{X} A(\mathbf{X}) \rho(\mathbf{X}, t) = \int d\mathbf{X} A(\mathbf{X}) e^{-t\mathcal{L}} \rho(\mathbf{X}, 0) \quad (2.9)$$

$$= \int d\mathbf{X} A(\mathbf{X}(t)) \rho(\mathbf{X}, 0) = \int d\mathbf{X} (e^{t\mathcal{L}} A(\mathbf{X})) \rho(\mathbf{X}, 0). \quad (2.10)$$

(\mathcal{L} is anti-self-adjoint:¹³ acting to the left, changes the sign of t). The above equations make the distinction between classical Schrödinger picture and Heisenberg picture clear — in Schrödinger picture (Equation 2.9), the variable (classical analog of quantum operator) is time-independent and the density (classical analog of wave function) is time-dependent; in Heisenberg picture (Equation 2.10), the variable is time-dependent and the density is time-independent.

In our case, we are interested in observing the time-dependent nonequilibrium average of dynamical variable A , i.e. $\overline{A(t)}$. The nonequilibrium state is prepared in the following way. Before time 0, the system is equilibrated on the ground state (g) with the ground-state Hamiltonian $H_g(\mathbf{X})$, and at time 0, the system is promoted to its excited state (e) on which the time evolution is governed by the excited-state Hamiltonian $H_e(\mathbf{X})$. The system evolves on the excited-state potential surface for time t , and the ensemble average of nonequilibrium value $A(t)_e = e^{t\mathcal{L}_e} A(0)$ is finally observed. Subscripts g and e on time parameters and Liouville operators mark the propagation is on these respective states, and the subscripts on the ensemble average denote sampling from the corresponding equilibrated state.

$$\langle A \rangle_g = \frac{\int d\mathbf{X} A e^{-\beta H_g(\mathbf{X})}}{\int d\mathbf{X} e^{-\beta H_g(\mathbf{X})}}, \quad \langle A \rangle_e = \frac{\int d\mathbf{X} A e^{-\beta H_e(\mathbf{X})}}{\int d\mathbf{X} e^{-\beta H_e(\mathbf{X})}}. \quad (2.11)$$

In brief, the observed nonequilibrium average is the ensemble average with initial conditions sampled from ground state equilibrium distribution and the dynamics of $A(t)$ propagated on the excited state. The energy gap between the excited state and the ground state is $\Delta V \equiv H_e - H_g$ and its fluctuation is $\delta\Delta V = \Delta V - \langle\Delta V\rangle_e$. Thus the nonequilibrium average of A is

$$\overline{A(t)} = \langle A(t) \rangle_g \quad (2.12)$$

$$= \frac{\int d\mathbf{X} e^{-\beta H_g(\mathbf{X})} A(t)_e}{\int d\mathbf{X} e^{-\beta H_g(\mathbf{X})}} \quad (2.13)$$

$$= \frac{\int d\mathbf{X} e^{-\beta H_e(\mathbf{X})} e^{\beta\Delta V} A(t)_e}{\int d\mathbf{X} e^{-\beta H_e(\mathbf{X})} e^{\beta\Delta V}}$$

$$= \frac{\int d\mathbf{X} e^{-\beta H_e(\mathbf{X})} e^{\beta\delta\Delta V} e^{\beta\langle\Delta V\rangle_e} A(t)_e}{\int d\mathbf{X} e^{-\beta H_e(\mathbf{X})} e^{\beta\delta\Delta V} e^{\beta\langle\Delta V\rangle_e}}$$

$$= \frac{\langle e^{\beta\delta\Delta V} A(t)_e \rangle_e}{\langle e^{\beta\delta\Delta V} \rangle_e}, \quad (2.14)$$

where the initial conditions are sampled from the equilibrated excited state and the dynamics also propagates on the excited state. Then the nonequilibrium average fluctuation is

$$\overline{\delta A(t)} = \overline{A(t) - \langle A \rangle_e} = \frac{\langle e^{\beta\delta\Delta V} \delta A(t)_e \rangle_e}{\langle e^{\beta\delta\Delta V} \rangle_e}. \quad (2.15)$$

So far, the nonequilibrium averages, Equation 2.14 and Equation 2.15, are exact.

2.2 Traditional Linear Response Theory

In traditional linear response theory, the approximation of weak perturbing field is necessary in order to make higher order perturbing contributions negligible. However, the time-dependent nonequilibrium average $\overline{A(t)} = \langle A(t) \rangle_g$ requires initial conditions on the

ground state equilibrium distribution and dynamics of $A(t)$ on the excited state. There are two approaches to derive this nonequilibrium average in traditional linear response theory. One is expanding the ground state distribution about the excited state distribution through first order in the energy difference (which ends up looking at both initial conditions and dynamics on excited state), and the other is expanding the excited-state distribution about the ground-state distribution through first order in the energy difference (which ends up looking at both initial conditions and dynamics on ground state).

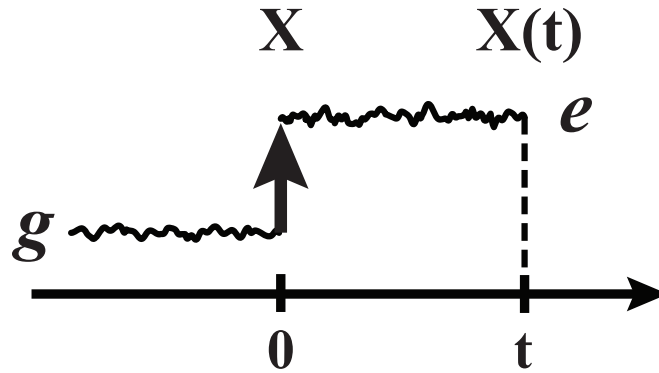


Figure 2.1 Preparation of nonequilibrium state in response to an external perturbation. Before time 0, system is equilibrated on the ground state (g) and at time 0, the system is promoted to its excited state (e). After propagating on the excited-state potential surface for time t , the value of some dynamical variable is observed. The phase space points \mathbf{X} and $\mathbf{X}(t)$ corresponds to the excitation time 0 and observation time t . Note that the ground–excited transition could be a resonant or a nonresonant excitation.

2.2.1 Average on excited state

Assuming the perturbation $\beta \delta \Delta V$ is small, one can expand the following exponential to the linear term

$$e^{\beta \delta \Delta V} = 1 + \beta \delta \Delta V + O(\beta \delta \Delta V)^2 \approx 1 + \beta \delta \Delta V. \quad (2.16)$$

Starting from the exact result for the nonequilibrium average (Equation 2.14), we expand to the linear order in $\beta\delta\Delta V$,

$$\begin{aligned}\overline{A(t)} &= \frac{\langle e^{\beta\delta\Delta V} A(t) \rangle_e}{\langle e^{\beta\delta\Delta V} \rangle_e} \approx \frac{\langle A(t) \rangle_e + \beta \langle \delta\Delta V(0) A(t) \rangle_e}{1 + \beta \langle \delta\Delta V \rangle_e} \\ &\approx \left(\langle A(t) \rangle_e + \beta \langle \delta\Delta V(0) A(t) \rangle_e \right) \cdot \left(1 - \beta \langle \delta\Delta V \rangle_e \right) \\ &= \langle A \rangle_e + \beta \langle \delta\Delta V(0) \delta A(t) \rangle_e + O(\beta\delta\Delta V)^2.\end{aligned}\quad (2.17)$$

In the linear regime, the nonequilibrium average of the fluctuation in A is

$$\overline{\delta A(t)} = \overline{A(t)} - \langle A \rangle_e \approx \beta \langle \delta\Delta V(0) \delta A(t) \rangle_e. \quad (2.18)$$

If we write the perturbation Hamiltonian in the explicit field-coupled property form, $\Delta V = H_e - H_g = -B(\mathbf{X}) \cdot F(t)$, where external weak field $F(t)$ is coupled to a dynamical variable of the system $B(\mathbf{X})$. In the linear regime, $\overline{\delta A(t; \lambda F)} = \lambda \overline{\delta A(t; F)}$ has a general form⁴²

$$\overline{\delta A(t)} = \int_{-\infty}^{\infty} dt' R(t, t') F(t') + O(F^2), \quad (2.19)$$

where $R(t, t')$ is the linear response function that describes how the system respond (time dependence of the external-field-coupled dynamical variable, $\overline{\delta A(t)}$ in this case) at any time after the disturbance of external field $F(t)$. Applying two properties of the response function mentioned in chapter 1 (Equation 1.29 and Equation 1.30) we can write nonequilibrium average of fluctuation of variable $A(t)$ as

$$\overline{\delta A(t)} = \int_{-\infty}^t dt' R(t-t') F(t') = \int_0^{\infty} d\tau R(\tau) F(t-\tau), \quad (\tau = t-t'). \quad (2.20)$$

As the response function is independent of $F(t)$, we are free to choose any convenient form of $F(t)$, for example, $F(t) = F \cdot \theta(-t)$. Applying this external field $F(t)$ to the above

equation and Equation 2.18, one gets

$$\overline{\delta A(t)} = \beta F \langle \delta B(0) \delta A(t)_e \rangle_e = \int_{-\infty}^t dt' R(t-t') F(t') \quad (2.21)$$

$$= F \int_{-\infty}^0 dt' R(t-t') = F \int_t^{\infty} d\tau R(\tau). \quad (2.22)$$

Thus, the linear response function with averaging on the excited state is

$$R(t) = -\theta(t) \beta \frac{d}{dt} \langle \delta B(0) \delta A(t)_e \rangle_e \quad (2.23)$$

$$= -\theta(t) \beta \langle \delta B(0) \delta \dot{A}(t)_e \rangle_e \quad (2.24)$$

$$= \theta(t) \beta \langle \delta \dot{B}(0) \delta A(t)_e \rangle_e. \quad (2.25)$$

In the last equation, the stationarity condition is applied: $\langle B(0)A(t) \rangle = \langle B(-t)A(0) \rangle$.

2.2.2 Average on ground state (Schrödinger picture)

We will derive the linear response theory with average on the ground state. In particular, what is shown in this section is the derivation in Schrödinger picture: the phase-space density is time-dependent, and the dynamical variable is time-independent same as in quantum mechanics. The time dependence of phase space density can be expanded about contributions from ground state (zeroth order) phase space density through first order in the phase space density change due to the perturbation. The physical process of preparing the nonequilibrium state is the same: the system is equilibrated with the unperturbed ground-state Hamiltonian H_g , and later promoted to the excited-state Hamiltonian $H_e = H_g + \Delta V = H_g - B(\mathbf{X})F(\tau)$. The total time-dependent phase space distribution function $\rho(\mathbf{X}, t)$ obeys

the Liouville equation (Equation 2.5)

$$\frac{\partial \rho}{\partial t} = -\mathcal{L}\rho = -\mathcal{L}_0\rho - \mathcal{L}_1\rho, \quad (2.26)$$

$$\text{where } \mathcal{L}_0\rho = -\{H_g(\mathbf{X}), \rho\}, \quad (2.27)$$

$$\mathcal{L}_1\rho = F(t)\{B(\mathbf{X}), \rho\}. \quad (2.28)$$

Expand ρ in powers of external field $F(t)$ to the first order, assuming the external field $F(t)$ is weak,

$$\rho(\mathbf{X}, t) = \rho_0(\mathbf{X}, t) + \rho_1(\mathbf{X}, t) + O(F^2), \quad (2.29)$$

$$\text{zeroth order } \frac{\partial \rho_0}{\partial t} = -\mathcal{L}_0\rho_0, \quad (2.30)$$

$$\text{first order } \frac{\partial \rho_1}{\partial t} = -\mathcal{L}_0\rho_1 - \mathcal{L}_1\rho_0. \quad (2.31)$$

The initial conditions are

$$\rho_0(\mathbf{X}, 0) = \frac{e^{-\beta H_g(\mathbf{X})}}{\int d\mathbf{X} e^{-\beta H_g(\mathbf{X})}}, \quad \text{and } \rho_1(\mathbf{X}, 0) = 0. \quad (2.32)$$

Using $\mathcal{L}_0\rho_0 = 0$, the zeroth order equation has the solution

$$\rho_0(\mathbf{X}, t) = \rho_0(\mathbf{X}) = \rho_0 = \frac{e^{-\beta H_g(\mathbf{X})}}{\int d\mathbf{X} e^{-\beta H_g(\mathbf{X})}}, \quad (\text{all } t). \quad (2.33)$$

The first order equation is an inhomogeneous first order differential equation, so one can use Laplace transform to solve it without changing the order of any operators. As the

initial value vanishes $\rho_1(\mathbf{X}, 0) = 0$, we take Laplace transform [†] on both sides of the first order equation, Equation 2.31

$$s\tilde{\rho}_1(\mathbf{X}, s) = -\mathcal{L}_0\tilde{\rho}_1(\mathbf{X}, s) - \mathbb{L}[\mathcal{L}_1\rho_0(\mathbf{X})],$$

$$\tilde{\rho}_1(\mathbf{X}, s) = -\frac{1}{s + \mathcal{L}_0} \cdot \mathbb{L}[\mathcal{L}_1\rho_0(\mathbf{X})].$$

Then taking the inverse Laplace transform of the above equation, we have

$$\begin{aligned} \rho_1(\mathbf{X}, t) &= -[e^{-t\mathcal{L}_0}] * [\mathcal{L}_1\rho_0(\mathbf{X})] = -\int_0^t dt' e^{-(t-t')\mathcal{L}_0} [\mathcal{L}_1\rho_0]_{t'} \\ &= -\int_0^t dt' e^{-(t-t')\mathcal{L}_0} \{B(\mathbf{X}), \rho_0(\mathbf{X})\} F(t'). \end{aligned} \quad (2.34)$$

By definition of the Poisson bracket and the ground state density (Equation 2.33),

$$\begin{aligned} \{B(\mathbf{X}), \rho_0\} &= -\left(\frac{\partial\rho_0}{\partial\mathbf{P}} \cdot \frac{\partial B}{\partial\mathbf{R}} - \frac{\partial\rho_0}{\partial\mathbf{R}} \cdot \frac{\partial B}{\partial\mathbf{P}}\right) = +\beta\left(\frac{\partial H_g}{\partial\mathbf{P}} \cdot \frac{\partial B}{\partial\mathbf{R}} - \frac{\partial H_g}{\partial\mathbf{R}} \cdot \frac{\partial B}{\partial\mathbf{P}}\right)\rho_0 \\ &= \beta\{H_g, B\}\rho_0 = -\beta(\mathcal{L}_0 B)\rho_0 = -\beta\frac{\partial B(\mathbf{X})}{\partial t}\rho_0 = -\beta\dot{B}(0)\rho_0. \end{aligned} \quad (2.35)$$

Therefore, the first order phase space density

$$\rho_1(\mathbf{X}, t) = \beta \int_0^t dt' F(t') e^{-(t-t')\mathcal{L}_0} \dot{B}(0)\rho_0. \quad (2.36)$$

[†]Laplace transform definition and relevant properties

$$\mathbb{L}[f(t)] = \tilde{F}(s) = \int_0^\infty e^{-st} f(t) dt$$

$$\mathbb{L}[f'(t)] = s\tilde{F}(s) - f(0)$$

$$\mathbb{L}[e^{-\alpha t} \cdot \theta(t)] = \frac{1}{s + \alpha}$$

$$\mathbb{L}^{-1}[F(s) \cdot G(s)] = (f * g)(t) = \int_0^t f(\tau)g(t - \tau) d\tau \quad (* \text{ denotes convolution})$$

Now we apply $\rho(\mathbf{X}, t) \approx \rho_0(\mathbf{X}) + \rho_1(\mathbf{X}, t)$ to calculate time-dependent nonequilibrium average of observable $A(\mathbf{X}(t))$,

$$\begin{aligned}
\overline{A(t)} &\approx \int d\mathbf{X} \rho_0 A(\mathbf{X}) + \int d\mathbf{X} \rho_1(t) A(\mathbf{X}) \\
&= \langle A \rangle_g + \beta \int_0^t dt' F(t') \int d\mathbf{X} A(\mathbf{X}) e^{-(t-t')\mathcal{L}_0} \dot{B}(0) \rho_0 \\
&= \langle A \rangle_g + \beta \int_0^t dt' F(t') \langle A(t-t')_g \dot{B}(0) \rangle_g \\
&= \langle A \rangle_g + \int_0^t dt' F(t') R(t-t').
\end{aligned} \tag{2.37}$$

So the linear response function with average on the ground state is simply

$$R(t) = \theta(t) \beta \langle A(t)_g \dot{B}(0) \rangle_g. \tag{2.38}$$

2.2.3 Average on ground state (Heisenberg picture)

A more practical approach to derive the linear response theory is using the Heisenberg picture. In Heisenberg picture, the density is fixed and the variable is time-dependent, which gives us freedom in dealing with complex nonequilibrium-state preparation process. The key terms involve the exponential of sum of Liouville operators. In this section, we focus on the same nonequilibrium preparation process, and we will see how this approach is applied to more complicated excitation processes later in this chapter. Suppose we still observe $\overline{A(t)}$ after excitation $H_g \rightarrow H_e = H_g - B(\mathbf{X})F(\tau)$,

$$\overline{A(t)} = \int d\mathbf{X} \rho_0(\mathbf{X}) A(\mathbf{X}(t))_e = \int d\mathbf{X} \rho_0(\mathbf{X}) e^{t\mathcal{L}_e} A(\mathbf{X}), \tag{2.39}$$

where the ground state equilibrium distribution is the same as in Equation 2.33 and denote Liouville operators [‡]

$$\mathcal{L}_e = \left(\mathcal{L}_0 + \frac{\partial}{\partial \tau} \right) + \mathcal{L}_1, \quad (2.40)$$

$$\mathcal{L}_0 = -\{H_g, \}, \quad (2.41)$$

$$\mathcal{L}_1 = F(\tau)\{B(\mathbf{X}), \}. \quad (2.42)$$

One can prove the exponential of sum of operators (details are shown in Appendix B) can be written as

$$e^{\hat{A}+\hat{B}} = e^{\hat{A}} + \int_0^1 d\lambda e^{(1-\lambda)\hat{A}} \hat{B} e^{\lambda\hat{A}} + O(\hat{B}^2). \quad (2.43)$$

In our case, we expand the propagator on the excited state:

$$e^{t\mathcal{L}_e} = e^{t(\mathcal{L}_0 + \frac{\partial}{\partial \tau}) + t\mathcal{L}_1} \quad (2.44)$$

$$= e^{t(\mathcal{L}_0 + \frac{\partial}{\partial \tau})} + \int_0^1 d\lambda e^{(1-\lambda)t(\mathcal{L}_0 + \frac{\partial}{\partial \tau})} t\mathcal{L}_1 e^{\lambda t(\mathcal{L}_0 + \frac{\partial}{\partial \tau})} + \dots \quad (2.45)$$

$$= e^{t(\mathcal{L}_0 + \frac{\partial}{\partial \tau})} + \int_0^t dt' e^{(t-t')(\mathcal{L}_0 + \frac{\partial}{\partial \tau})} \mathcal{L}_1 e^{t'(\mathcal{L}_0 + \frac{\partial}{\partial \tau})} + \dots, \quad (2.46)$$

in which $t' = \lambda t$. Truncated after the linear term, the nonequilibrium average of fluctuation

[‡]In the definition of Liouville operator \mathcal{L}_e (Equation 2.40), $\partial/\partial\tau$ acts on any explicit-time variable, such as the external field.

of the observable is

$$\overline{\delta A(t)} = \langle A(t)_e \rangle_g - \langle A \rangle_g \quad (2.47)$$

$$\begin{aligned} &= \int d\mathbf{X} \rho_0(\mathbf{X}) e^{t\mathcal{L}_e} A(\mathbf{X}) - \int d\mathbf{X} \rho_0(\mathbf{X}) e^{t(\mathcal{L}_0 + \frac{\partial}{\partial \tau})} A(\mathbf{X}) \\ &= \int d\mathbf{X} \rho_0(\mathbf{X}) \int_0^t dt' e^{(t-t')(\mathcal{L}_0 + \frac{\partial}{\partial \tau})} F(\tau) \{B(\mathbf{X}), e^{t'(\mathcal{L}_0 + \frac{\partial}{\partial \tau})} A(\mathbf{X})\} \\ &= \int d\mathbf{X} \rho_0(\mathbf{X}) \int_0^t dt' e^{(t-t')(\mathcal{L}_0 + \frac{\partial}{\partial \tau})} F(\tau) \{B(\mathbf{X}), A(\mathbf{X}; t')\}_g \\ &= \int_0^t dt'' \langle \{B(t'')_g, A(t)_g\} \rangle_g F(t'') \quad (\text{using } t'' = t - t') \\ &= \int_0^t dt'' \langle \{B(0), A(t - t'')_g\} \rangle_g F(t'') \end{aligned} \quad (2.48)$$

$$= \beta \int_0^t dt'' \langle \dot{B}(0) A(t - t'')_g \rangle_g F(t''). \quad (2.49)$$

See Appendix A(3) for the proof of last equality. Thus the linear response function

$$R(t) = \theta(t) \beta \langle A(t)_g \dot{B}(0) \rangle_g. \quad (2.50)$$

2.2.4 Application to four-wave-mixing light scattering

In this section, we are going to apply the linear response theory to four-wave-mixing light scattering. Because of the nonresonant feature of four-wave mixing, it makes more sense to use the ground-state averaging version of linear response theory. In a four-wave-mixing measurement, the external perturbation field $F(\tau) = \frac{1}{2} E_\mu(\tau) E_\nu(\tau)$ and its coupled system property is the many-body polarizability $B(\mathbf{X}) = \Pi_{\mu\nu}(\mathbf{X})$. The observable is $A(t) = \Pi_{\gamma\delta}(t)$, which is read out by impinging the third probe field E_γ at time t . The illustration is shown in Figure 2.2.

In particular, the optical Kerr effect spectroscopy has specific choice of electric field polarizations. The time-zero external perturbation field is $E_x E_z$ and at time t later, many-

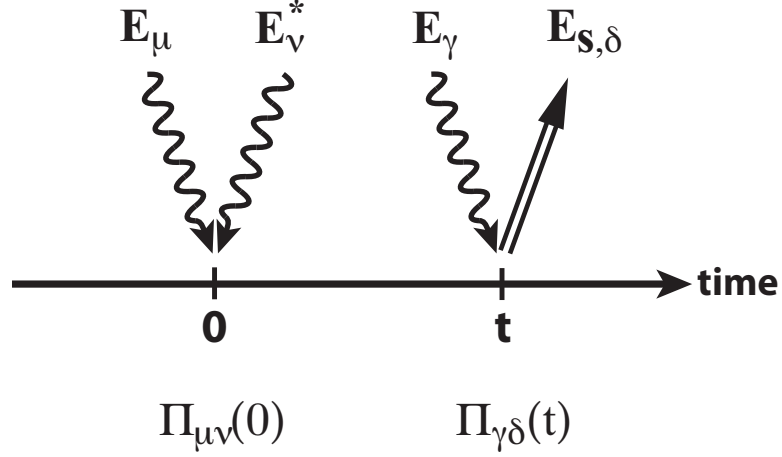


Figure 2.2 Sequence of polarizability interactions in four-wave mixing. At time 0, two “pump” electric fields coupled with the many-body polarizability induce a nonresonant excitation that leads to a transition to a virtual state. Later the many-body polarizability is read out by sending the third “probe” electric field that also defines the delay time t . The polarization directions of electric fields and corresponding polarizability elements are shown on the illustration indicated with Greek letters.

body polarizability element $\Pi_{xz}(t)$ is observed, ($\gamma\delta = \mu\nu = xz$), so the response function of the optical Kerr measurement follows

$$\overline{\delta\Pi_{xz}(t)} = \int_0^t dt' R_{xzxz}(t, t') F_{xz}(t'). \quad (2.51)$$

The OKE response function is given by

$$R_{xzxz}(t_1, t_2) = \langle \{\Pi_{xz}(t_1), \Pi_{xz}(t_2)\} \rangle_g = -\beta \frac{d}{dt} \langle \Pi_{xz}(0) \Pi_{xz}(t) \rangle_g, \quad (t = t_2 - t_1). \quad (2.52)$$

Because of the equality $\langle \delta A(t) \delta B(0) \rangle = \langle A(t) \delta B(0) \rangle = \langle A(t) B(0) \rangle - \langle A \rangle \langle B \rangle$, the time derivative of the polarizability-fluctuation correlation function is equivalent to time derivative of the polarizability correlation function,

$$\frac{d}{dt} \langle \delta A(t) \delta B(0) \rangle = \frac{d}{dt} \langle A(t) \delta B(0) \rangle = \frac{d}{dt} \langle \delta A(t) B(0) \rangle = \frac{d}{dt} \langle A(t) B(0) \rangle. \quad (2.53)$$

Thus, OKE response function can be written as $R(t) = -\beta \frac{d}{dt} \langle \delta \Pi_{xz}(0) \delta \Pi_{xz}(t) \rangle_g$.

As a matter of fact, in practice, we calculate the OKE response function using rotational averaging to get a more efficient averaging since the liquid is isotropic. The rotational average of the anisotropic response R_{xzx} is equivalent to the rotational average of the product of two tensor elements. Appendix C shows that the product of two off-diagonal elements of two matrices has a rotational average,²³² (note that the overbar with a “rotational” subscript here denotes the rotational average, not a nonequilibrium average).

$$\overline{A_{\mu\nu}B_{\mu\nu}}_{\text{rotational}} = \frac{1}{10}\text{PP}(\mathbf{A}, \mathbf{B}) - \frac{1}{30}\text{Tr}(\mathbf{A})\text{Tr}(\mathbf{B}). \quad (2.54)$$

where the pair product and trace of tensors are defined as

$$\text{PP}(\mathbf{A}, \mathbf{B}) = \sum_{\mu, \nu=x,y,z} A_{\mu\nu}B_{\mu\nu}, \quad (2.55)$$

$$\text{Tr}(\mathbf{A}) = \sum_{\mu=x,y,z} A_{\mu\mu}. \quad (2.56)$$

For simplicity, we will omit the rotational average notation in the following parts of the thesis. For convenience, we define the rotational average of the product of off-diagonal elements

$$\mathbf{A} \otimes \mathbf{B} \equiv \frac{1}{10}\text{PP}(\mathbf{A}, \mathbf{B}) - \frac{1}{30}\text{Tr}(\mathbf{A})\text{Tr}(\mathbf{B}). \quad (2.57)$$

So, the OKE response function can be simplified as

$$R(t) = -\beta \frac{d}{dt} \langle \mathbf{\Pi}(0) \otimes \mathbf{\Pi}(t) \rangle_g. \quad (2.58)$$

2.3 Gaussian Statistics and Linear Response Theory

There is a more general approximation other than truncating the nonlinear terms in fields with assumption of small perturbations. This approximation only requires the dynamical variable obeys Gaussian statistics, which leads to the same linear response result.^{2,44,45,219,233}

As a very large number (order of 10^{23}) of events determines macroscopic measurable quantities, the central limit theorem tells us that most of macroscopic variables obey Gaussian statistics. Thus the approximation of Gaussian statistics is a more general one than that in traditional linear response theory. At some situations the linear response holds even when the perturbation is not small at all,⁸³ which reflects the essentiality of the Gaussian statistical version of the linear response theory. For completeness, the derivation of this version is shown below.

2.3.1 Gaussian distribution

Consider a zero-mean Gaussian random variable x or in an n -dimensional case, a vector $\mathbf{x} = (x_1, x_2, \dots, x_n)^T$ with $\langle x \rangle = 0$ or $\langle x_1 \rangle = \dots = \langle x_n \rangle = 0$, whose probability density functions are the following.

$$\text{1-dimensional Gaussian distribution} \quad \rho(x) = \sqrt{\frac{a}{\pi}} e^{-ax^2}, \quad (2.59)$$

$$\text{n-dimensional Gaussian distribution} \quad \rho(\mathbf{x}) = \sqrt{\frac{\det \mathbf{M}}{\pi^n}} e^{-\mathbf{x}^T \mathbf{M} \mathbf{x}}, \quad (2.60)$$

where in the n -dimensional case, the covariance matrix \mathbf{M} whose element is the covariance between two random variables $\mathbf{M}_{ij}^{-1} = 2\langle x_i x_j \rangle$, ($i, j = 1, 2, \dots, n$), is a real symmetric ($\mathbf{M} = \mathbf{M}^T$), positive definite (positive eigenvalues) matrix. Gaussian distribution implies there is no higher order covariances than the quadratic two-variable covariance, i.e. $\langle x_{i_1} x_{i_2} x_{i_3} \rangle = \langle x_{i_1} x_{i_2} \dots x_{i_k} \rangle = 0$ for all $k > 2$. So Gaussian distribution is fully described by the covariance matrix that can be diagonalized by an orthogonal matrix \mathbf{U} ($\mathbf{U}^T = \mathbf{U}^{-1}$) by $\mathbf{M} = \mathbf{U}^T \mathbf{\Lambda} \mathbf{U}$, where the diagonal matrix $\mathbf{\Lambda} = \mathbf{U} \mathbf{M} \mathbf{U}^T = \text{diag}(\lambda_1, \dots, \lambda_n)$.

Define the new basis $\mathbf{q} = \mathbf{U} \mathbf{x}$, we then have

$$\mathbf{x}^T \mathbf{M} \mathbf{x} = (\mathbf{x}^T \mathbf{U}^T) (\mathbf{U} \mathbf{M} \mathbf{U}^T) (\mathbf{U} \mathbf{x}) = \mathbf{q}^T \mathbf{\Lambda} \mathbf{q} = \sum_{\alpha} \lambda_{\alpha} q_{\alpha}^2. \quad (2.61)$$

We test the normalization condition for the distribution,

$$\begin{aligned}\int_{-\infty}^{\infty} \mathbf{dx} \rho(\mathbf{x}) &= \sqrt{\frac{\det \mathbf{M}}{\pi^n}} \int_{-\infty}^{\infty} \mathbf{dx} e^{-\mathbf{x}^T \mathbf{M} \mathbf{x}} = \sqrt{\frac{\det \mathbf{M}}{\pi^n}} \int_{-\infty}^{\infty} \left| \frac{\partial(x_1, \dots, x_n)}{\partial(q_1, \dots, q_n)} \right| \mathbf{dq} e^{-\mathbf{q}^T \boldsymbol{\Lambda} \mathbf{q}} \\ &= \sqrt{\frac{\det \mathbf{M}}{\pi^n}} \int_{-\infty}^{\infty} \dots \int_{-\infty}^{\infty} |\det \mathbf{U}^T| dq_1 \dots dq_n e^{-\sum_{\alpha} \lambda_{\alpha} q_{\alpha}^2}.\end{aligned}\quad (2.62)$$

Using orthogonal matrix property $\det \mathbf{U}^T = \pm 1$, we have

$$\int_{-\infty}^{\infty} \mathbf{dx} \rho(\mathbf{x}) = \sqrt{\frac{\det \mathbf{M}}{\pi^n}} \prod_{\alpha=1}^n \int_{-\infty}^{\infty} dq_{\alpha} e^{-\lambda_{\alpha} q_{\alpha}^2} = \sqrt{\frac{\det \mathbf{M}}{\pi^n}} \prod_{\alpha=1}^n \sqrt{\frac{\pi}{\lambda_{\alpha}}} = 1. \quad (2.63)$$

The average of the square of q_{α} can be calculated as follows,

$$\begin{aligned}\langle q_{\alpha}^2 \rangle &= \sqrt{\frac{\lambda_{\alpha}}{\pi}} \int_{-\infty}^{\infty} q_{\alpha}^2 e^{-\lambda_{\alpha} q_{\alpha}^2} dq_{\alpha} = \sqrt{\frac{\lambda_{\alpha}}{\pi}} \cdot \left(-\frac{\partial}{\partial \lambda_{\alpha}} \int_{-\infty}^{\infty} e^{-\lambda_{\alpha} q_{\alpha}^2} dq_{\alpha} \right) \\ &= \sqrt{\frac{\lambda_{\alpha}}{\pi}} \left(-\frac{\partial}{\partial \lambda_{\alpha}} \sqrt{\frac{\pi}{\lambda_{\alpha}}} \right) = \frac{1}{2\lambda_{\alpha}}.\end{aligned}$$

Arranging the above equation, the relation between the eigenvalues and the average of corresponding basis square is

$$\frac{1}{\lambda_{\alpha}} = 2\langle q_{\alpha}^2 \rangle. \quad (2.64)$$

2.3.2 Generating function

The generating function (or the characteristic function) is defined as $G \equiv \langle e^{\mathbf{F}^T \mathbf{x}} \rangle$, with coefficient vector $\mathbf{F} = (a, b, c, \dots)^T$. The generating function for the n-dimensional Gaussian variable can be derived in the following two ways.

(1) Derivation of basic Gaussian identity by diagonalizing the covariance matrix.

$$\begin{aligned}
G &= \langle e^{\mathbf{F}^T \mathbf{x}} \rangle & (2.65) \\
&= \langle e^{(\mathbf{F}^T \mathbf{U}^T)(\mathbf{U} \mathbf{x})} \rangle = \langle e^{\mathbf{f}^T \mathbf{q}} \rangle \quad (\text{define } \mathbf{f} = \mathbf{U} \mathbf{F}) \\
&= \sqrt{\frac{\det \mathbf{M}}{\pi^n}} \prod_{\alpha=1}^n \int_{-\infty}^{\infty} dq_{\alpha} e^{-\lambda_{\alpha} q_{\alpha}^2 + f_{\alpha} q_{\alpha}} \\
&= \sqrt{\frac{\det \mathbf{M}}{\pi^n}} \prod_{\alpha=1}^n \int_{-\infty}^{\infty} dq_{\alpha} e^{-\lambda_{\alpha} \left(q_{\alpha}^2 - \frac{f_{\alpha}}{\lambda_{\alpha}} q_{\alpha} + \frac{f_{\alpha}^2}{4\lambda_{\alpha}^2} \right)} e^{\frac{f_{\alpha}^2}{4\lambda_{\alpha}}} \\
&= \prod_{\alpha=1}^n e^{\frac{f_{\alpha}^2}{4\lambda_{\alpha}}} = e^{\frac{1}{2} \sum_{\alpha} f_{\alpha}^2 \langle q_{\alpha}^2 \rangle}.
\end{aligned}$$

Since

$$\sum_{\alpha} f_{\alpha} \langle q_{\alpha}^2 \rangle f_{\alpha} = \sum_{\alpha \beta \gamma} f_{\alpha} \delta_{\alpha \beta} \langle q_{\beta} q_{\gamma} \rangle \delta_{\gamma \alpha} f_{\gamma} = \mathbf{f} (\mathbf{U}^T \mathbf{U}) \langle \mathbf{q} \mathbf{q}^T \rangle (\mathbf{U}^T \mathbf{U}) \mathbf{f} = \mathbf{F}^T \langle \mathbf{x} \mathbf{x}^T \rangle \mathbf{F},$$

the generating function can be expressed as

$$G = e^{\frac{1}{2} \mathbf{F}^T \langle \mathbf{x} \mathbf{x}^T \rangle \mathbf{F}}. \quad (2.66)$$

(2) The other way to derive the generating function does not involve diagonalizing the covariance matrix.

$$G = \langle e^{\mathbf{F}^T \mathbf{x}} \rangle = \int_{-\infty}^{\infty} d\mathbf{x} e^{-\mathbf{x}^T \mathbf{M} \mathbf{x} + \mathbf{F}^T \mathbf{x}} / \int_{-\infty}^{\infty} d\mathbf{x} e^{-\mathbf{x}^T \mathbf{M} \mathbf{x}}. \quad (2.67)$$

To complete the square term, we need to obtain a vector \mathbf{c} such that

$$\begin{aligned}\mathbf{x}^T \mathbf{M} \mathbf{x} - \mathbf{F}^T \mathbf{x} &= (\mathbf{x} + \mathbf{c})^T \mathbf{M} (\mathbf{x} + \mathbf{c}) - \mathbf{c}^T \mathbf{M} \mathbf{c}, \\ -\mathbf{F}^T \mathbf{x} &= \mathbf{c}^T \mathbf{M} \mathbf{x} + \mathbf{x}^T \mathbf{M} \mathbf{c} = \mathbf{c}^T \mathbf{M} \mathbf{x} + (\mathbf{M} \mathbf{c})^T \mathbf{x}, \\ -\mathbf{F}^T &= 2\mathbf{c}^T \mathbf{M}.\end{aligned}$$

$$\Rightarrow \mathbf{F} = -2\mathbf{M} \mathbf{c}.$$

$$\Rightarrow \mathbf{c} = -\frac{1}{2} \mathbf{M}^{-1} \mathbf{F}.$$

$$\mathbf{c}^T \mathbf{M} \mathbf{c} = \frac{1}{4} \mathbf{F}^T \mathbf{M}^{-1} \mathbf{M} \mathbf{M}^{-1} \mathbf{F} = \frac{1}{4} \mathbf{F}^T \mathbf{M}^{-1} \mathbf{F}.$$

So,

$$G = \langle e^{\mathbf{F}^T \mathbf{x}} \rangle = e^{\frac{1}{4} \mathbf{F}^T \mathbf{M}^{-1} \mathbf{F}} = \exp \left[\frac{1}{4} \sum_{\mu\nu} F_\mu (\mathbf{M}^{-1})_{\mu\nu} F_\nu \right].$$

Then, the derivative of the generating function

$$\frac{\partial G}{\partial F_\mu} = \frac{G}{4} \left[\sum_\nu (\mathbf{M}^{-1})_{\mu\nu} F_\nu + \sum_\nu F_\nu (\mathbf{M}^{-1})_{\mu\nu} \right].$$

$$\text{So, } \langle \mathbf{x} \mathbf{x}^T \rangle_{\mu\nu} = \frac{\partial^2 G}{\partial F_\mu \partial F_\nu} \Big|_{\mathbf{F}=\mathbf{0}} = \frac{1}{2} \mathbf{M}_{\mu\nu}^{-1}. \quad (2.68)$$

Thus, the generating function

$$G = \langle e^{\mathbf{F}^T \mathbf{x}} \rangle = e^{\frac{1}{4} \mathbf{F}^T \mathbf{M}^{-1} \mathbf{F}} = e^{\frac{1}{2} \mathbf{F}^T \langle \mathbf{x} \mathbf{x}^T \rangle \mathbf{F}}. \quad (2.69)$$

2.3.3 Linear response

From the form of exact result Equation 2.14, we choose $\mathbf{x} = (x, y)$, and $x = \delta A(t)_e$, $y = \delta \Delta V$ and the coefficient $\mathbf{F} = (a, \beta)$. Assuming x and y are Gaussian variables, using

Equation 2.69,

$$\frac{\langle xe^{\beta y} \rangle}{\langle e^{\beta y} \rangle} = \frac{\partial \ln \langle e^{ax + \beta y} \rangle}{\partial a} \Big|_{a=0} = \frac{\partial \ln G}{\partial a} \Big|_{a=0} \quad (2.70)$$

$$\begin{aligned} &= \frac{\partial}{\partial a} \frac{1}{2} (a \ \beta) \begin{pmatrix} \langle x^2 \rangle & \langle xy \rangle \\ \langle xy \rangle & \langle y^2 \rangle \end{pmatrix} \begin{pmatrix} a \\ \beta \end{pmatrix} \Big|_{a=0} \\ &= \frac{1}{2} \frac{\partial}{\partial a} [a^2 \langle x^2 \rangle + 2a\beta \langle xy \rangle + \beta^2 \langle y^2 \rangle]_{a=0} \\ &= \beta \langle xy \rangle, \end{aligned} \quad (2.71)$$

Substituting x and y by $\delta A(t)_e$ and $\delta \Delta V$ respectively, we get

$$\overline{\delta A(t)} = \beta \langle \delta A(t)_e \delta \Delta V(0) \rangle. \quad (2.72)$$

This is the identical to the traditional linear response result. But assuming Gaussian statistics does not require the perturbation $\delta \Delta V$ to be small, and is thus more general.

2.4 Application to Solute-Pump/Solvent-Probe Spectroscopy

So far, we have talked about four approaches to the linear response theory, two of which are particularly useful in the treatment of the solute-pump/solvent-probe spectra. The first one is the linear response with averaging on the excited state (Equation 2.17). This approach is useful since the solute excitation from the solute-pump is a resonant perturbation, although the linearization with respect to the energy gap is optional. The second one is the linear response with averaging on the ground state in the Heisenberg picture. This approach is useful because the solvent excitation from the four-wave-mixing pump is a nonresonant perturbation and it is natural to discuss the evolution of an observable rather than that of a density.

In two-dimensional time-domain solute-pump/solvent-probe spectroscopy, the nonequilibrium state is prepared by one resonant excitation and one nonresonant excitation. At time zero, the equilibrium ground-state system (g) undergoes an electronic transition to its excited state (e) by a resonant solute-pump, and the Hamiltonian changes from H_g to $H_e = H_g + \Delta V$. The excited system evolves on the excited-state potential surface (e) for time T (this e surface is the “ground” state with respect to nonresonant electric field in the previous Heisenberg picture treatment) until a pair of solvent-pump pulses perturb the system with the interaction Hamiltonian

$$H'(\tau) = -B(\mathbf{X})F(\tau) = -\frac{1}{2} \sum_{\mu\nu} E_\mu(\tau) \Pi_{\mu\nu}(\mathbf{X}) E_\nu(\tau), \quad (2.73)$$

then the system starts to propagate on excited state e' with Hamiltonian $H_{e'} = H_e + H'(\tau)$ for another short time t (this e' surface is the “excited” state with respect to nonresonant electric field in the previous Heisenberg picture treatment). Finally at time $T + t$, the many-body polarizability $\Pi_{\gamma\delta}(T + t)$ is observed. This excitation process is depicted in Figure 2.3.

For the sake of generality and simplicity in notation, we still use $A(T + t) = \Pi_{\gamma\delta}(T + t)$ as the observable, and $B(\mathbf{X}) = \Pi_{\mu\nu}(\mathbf{X})$ as the coupled variable with the perturbing field $F(\tau) = \frac{1}{2} E_\mu(\tau) E_\nu(\tau)$. The experiment measures the nonequilibrium average

$$\overline{\delta A(T + t)} = \int d\mathbf{X}_0 \rho_g(\mathbf{X}_0) [A(\mathbf{X}(T + t))|_{e,e'} - \langle A \rangle_e] \quad (2.74)$$

$$= \frac{1}{\langle e^{\beta\delta\Delta V} \rangle_e} \int d\mathbf{X}_0 \rho_e(\mathbf{X}_0) e^{\beta\delta\Delta V(\mathbf{X}_0)} \delta A(\mathbf{X}(T + t))|_{e,e'}. \quad (2.75)$$

The notation $\delta A(\mathbf{X}(T + t))|_{e,e'}$ is essential, which stands for the instantaneous value of fluctuation in dynamical variable A with preparation starting from initial condition \mathbf{X}_0 , evolving on e surface for time T and evolving on e' surface for time t . The two subscripts e, e' indicate which surface the system evolve on (or which Hamiltonian governs the propagation) during time periods T and t . This notation applies to the phase space point as

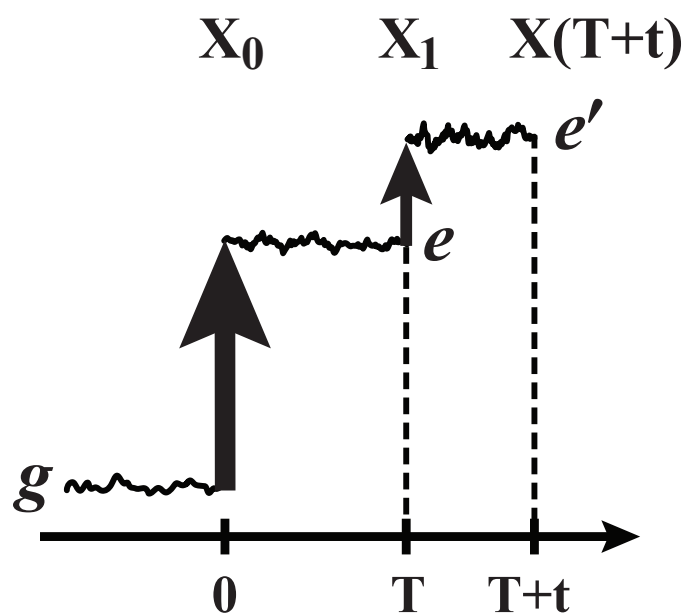


Figure 2.3 Sequence of excitations in solute-pump/solvent-probe spectroscopy. The molecular system is prepared in an equilibrated ground state (g), which gets electronically excited by the resonant solute-pump pulse at time 0, and promoted to the excited state (e). Propagating on the excited-state surface e for time T , the system is then perturbed by the nonresonant solvent-pump pulse that brings the system to excited state e' . After evolving for a short time t on e' surface, the many-body polarizability is observed at time $T + t$. The phase space points \mathbf{X}_0 , \mathbf{X}_1 and $\mathbf{X}(T + t)$ correspond to resonant solute-excitation time 0, nonresonant solvent-excitation time T , and observation time $T + t$.

well. As shown in Figure 2.3, starting from phase space point \mathbf{X}_0 , the system evolves for time T on e surface ending up with phase space point $\mathbf{X}_1 = \mathbf{X}(\mathbf{X}_0; T)|_e$. Then starting from phase space point \mathbf{X}_1 the system evolves on e' surface for time t ending up with phase space point $\mathbf{X}(T+t) = \mathbf{X}(\mathbf{X}_1; t)|_{e'} = \mathbf{X}(\mathbf{X}_0; T, t)|_{e, e'}$. Inside the parenthesis the first argument is the initial phase space point, and separated by a semicolon are propagation durations during which the system evolves on the surface marked by the subscripts in the order written.

We define Liouville operators

$$\mathcal{L}_e = -\{H_e, \}, \quad (2.76)$$

$$\mathcal{L}'_e = \left(\mathcal{L}_e + \frac{\partial}{\partial \tau} \right) + \mathcal{L}_1, \quad (2.77)$$

$$\mathcal{L}_1 = F(\tau)\{B(\mathbf{X}), \}. \quad (2.78)$$

The instantaneous value of dynamical variable A with the above mentioned preparation can be expressed as

$$\begin{aligned} A(\mathbf{X}(t))|_{e, e'} &= e^{t\mathcal{L}'_e} \left[e^{T\mathcal{L}_e} A(\mathbf{X}_0) \right] = e^{t\mathcal{L}'_e} A(\mathbf{X}_1) = A(\mathbf{X}_1; t)|_{e'} \quad (2.79) \\ &= e^{t(\mathcal{L}_e + \frac{\partial}{\partial \tau}) + \mathcal{L}_1} A(\mathbf{X}_1) \\ &\approx \left[e^{t(\mathcal{L}_e + \frac{\partial}{\partial \tau})} + \int_0^t dt' e^{(t-t')(\mathcal{L}_e + \frac{\partial}{\partial \tau})} \mathcal{L}_1 e^{t'(\mathcal{L}_e + \frac{\partial}{\partial \tau})} \right] A(\mathbf{X}_1) \\ &= A(t)_e + \int_0^t dt' F(t-t') \{B(\mathbf{X}_1; t-t'), A(\mathbf{X}_1; t)\}. \quad (2.80) \end{aligned}$$

In above derivation, the exponential of sum of operators, Equation 2.46 is used. The notation $A(\mathbf{X}_1; t)$ means the value of dynamical variable A starting at phase space point

\mathbf{X}_1 and propagating on e surface for time t . The nonequilibrium average observed is

$$\overline{\delta A(T+t)} = \frac{1}{\langle e^{\beta \delta \Delta V} \rangle_e} \int d\mathbf{X}_0 \rho_e(\mathbf{X}_0) e^{\beta \delta \Delta V(\mathbf{X}_0)} \left[\delta A(T+t)_e + \int_0^t dt' F(t-t') \{B(\mathbf{X}_1; t-t'), \delta A(\mathbf{X}_1; t)\} \right] \quad (2.81)$$

$$= \frac{\langle e^{\beta \delta \Delta V(0)} \delta A(T+t)_e \rangle_e}{\langle e^{\beta \delta \Delta V} \rangle_e} + \frac{1}{\langle e^{\beta \delta \Delta V} \rangle_e} \int d\mathbf{X}_0 \rho_e(\mathbf{X}_0) e^{\beta \delta \Delta V(\mathbf{X}_0)} \cdot \int_0^t dt' F(T+t-t') \{B(\mathbf{X}_0; T+t-t'), \delta A(\mathbf{X}_0; T+t)\} \quad (2.82)$$

$$\approx \beta \langle \delta \Delta V(0) \delta A(T+t)_e \rangle_e + \frac{1}{\langle e^{\beta \delta \Delta V} \rangle_e} \int_0^t dt' F(T+t-t') \langle e^{\beta \delta \Delta V(0)} \{B(T+t-t'), \delta A(T+t)\} \rangle_e. \quad (2.83)$$

Now we substitute the physical quantities of solute-pump/solvent-probe spectroscopy into the above result, $A(T+t) = \Pi_{\gamma\delta}(\mathbf{X}; T+t)$, $B(\mathbf{X}) = \Pi_{\mu\nu}(\mathbf{X})$ and $F(\tau) = \frac{1}{2} E_\mu(\tau) E_\nu(\tau)$. The sequence of pulses are shown in Figure 2.4.

$$\overline{\delta \Pi_{\gamma\delta}(T+t)} = \beta \langle \delta \Delta V(0) \delta \Pi_{\gamma\delta}(T+t)_e \rangle_e + \frac{1}{2} \int_0^t dt' E_\mu(T+t-t') E_\nu(T+t-t') \frac{1}{\langle e^{\beta \delta \Delta V} \rangle_e} \langle e^{\beta \delta \Delta V(0)} \{ \Pi_{\mu\nu}(T+t-t'), \delta \Pi_{\gamma\delta}(T+t) \} \rangle_e. \quad (2.84)$$

The first term above can be selected out by choosing particular phase matching condition in the signal detection. Thus, we have the solute-pump/solvent-probe response function that

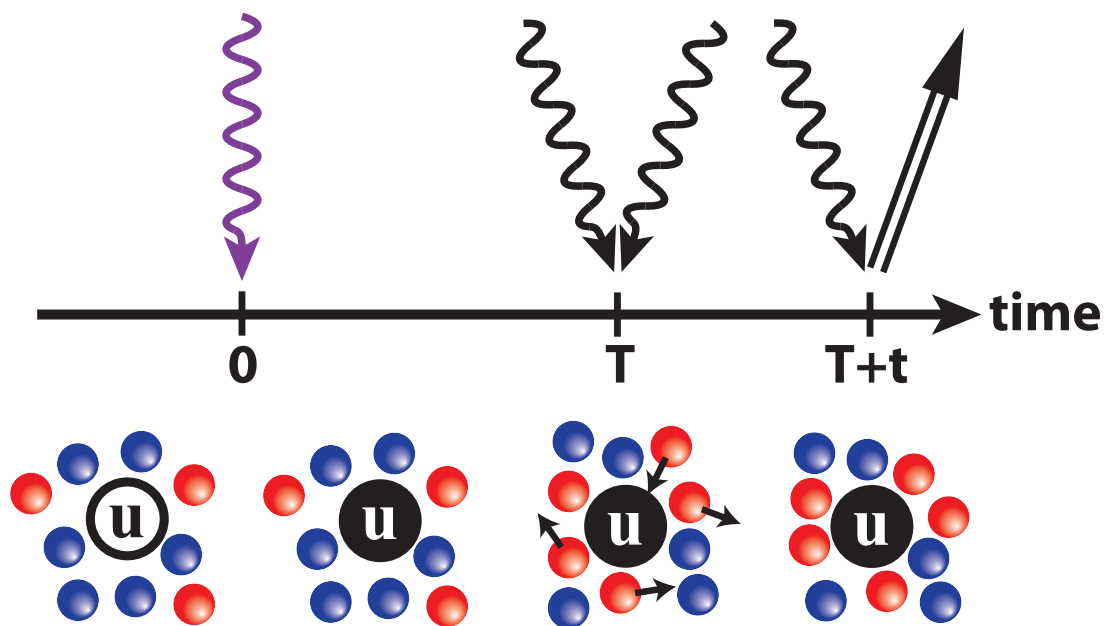


Figure 2.4 Sequence of events in solute-pump/solvent-probe spectroscopy. The molecular system is initially in equilibrium with a ground-state solute (u with open black circle), which gets electronically excited by a resonant solute-pump pulse at time 0, and promoted to the excited state (u with filled black circle). This excitation changes the solute–solvent interactions and leads to structural reorganization in the surrounding solvent (colored circles). After waiting for time T , the experiment measures the ultrafast dynamics by hitting the sample with a pair of nonresonant laser pulses and scattering off the sample with a third nonresonant pulse at a shorter time t later. So the time T reflects the progress of the liquid structural change, and the time duration t corresponds to the ultrafast intermolecular vibrations of the liquid (black arrows) characteristic of the liquid structure at each time T .

is the most important result in this chapter,

$$R(0, T, T+t) = \frac{1}{\langle e^{\beta\delta\Delta V} \rangle_e} \langle e^{\beta\delta\Delta V(0)} \{ \Pi_{\mu\nu}(T), \delta\Pi_{\gamma\delta}(T+t) \} \rangle_e \quad (2.85)$$

$$= \frac{1}{\langle e^{\beta\delta\Delta V} \rangle_e} \langle e^{\beta\delta\Delta V(0)} \{ \delta\Pi_{\mu\nu}(T), \delta\Pi_{\gamma\delta}(T+t) \} \rangle_e \quad (2.86)$$

$$= \frac{1}{\langle e^{\beta\delta\Delta V} \rangle_e} \langle e^{\beta\delta\Delta V(0)} \{ \Pi_{\mu\nu}(T), \Pi_{\gamma\delta}(T+t) \} \rangle_e, \quad (2.87)$$

since $\{B, A\} = \{\delta B, A\} = \{\delta B, \delta A\}$.

The anisotropic response function is practically calculated using the rotational average

$$\begin{aligned} R(0, T, T+t) &= R_{\mu\nu\mu\nu}(0, T, T+t) \\ &= \frac{1}{\langle e^{\beta\delta\Delta V} \rangle_e} \langle e^{\beta\delta\Delta V(0)} \overline{\{ \Pi_{\mu\nu}(t_1), \Pi_{\mu\nu}(t_2) \}}_{\text{rotational}} \rangle_e, \end{aligned} \quad (2.88)$$

but for convenience, the rotational average will not be shown in next chapters.

Until now, we have derived only the solute-pump-on response function (Equation 2.87). However, the solute-pump/solvent-probe experiment looks at the pump-on/pump-off difference,

$$\Delta R_{\mu\nu\gamma\delta}(0, T, T+t) = \frac{1}{\langle e^{\beta\delta\Delta V} \rangle_e} \langle e^{\beta\delta\Delta V(0)} \{ \Pi_{\mu\nu}(T), \Pi_{\gamma\delta}(T+t) \} \rangle_e - \langle \{ \Pi_{\mu\nu}(0), \Pi_{\gamma\delta}(t) \} \rangle_g, \quad (2.89)$$

which is the difference between the solute-pump/solvent-probe response and the four-wave-mixing response equilibrated with a ground-state solute. With optical-Kerr-like xz polarized laser configuration, the RP-PORS response function is

$$\begin{aligned} \Delta R(0, T, T+t) &= \Delta R_{xzxz}(0, T, T+t) \\ &= \frac{1}{\langle e^{\beta\delta\Delta V} \rangle_e} \langle e^{\beta\delta\Delta V(0)} \{ \Pi_{xz}(T), \Pi_{xz}(T+t) \} \rangle_e - \langle \{ \Pi_{xz}(0), \Pi_{xz}(t) \} \rangle_g. \end{aligned} \quad (2.90)$$

To understand this finding, consider the situation when the waiting time T is longer than the typical structural relaxation time in the liquid. Then the RP-PORS response function approaches

$$\begin{aligned}\Delta R(0, T, T+t)|_{T \rightarrow \infty} &= \frac{1}{\langle e^{\beta \delta \Delta V} \rangle_e} \langle e^{\beta \delta \Delta V(0)} \rangle_e \langle \{\Pi_{xz}(T), \Pi_{xz}(T+t)\} \rangle_e - \langle \{\Pi_{xz}(0), \Pi_{xz}(t)\} \rangle_g \\ &= \langle \{\Pi_{xz}(T), \Pi_{xz}(T+t)\} \rangle_e - \langle \{\Pi_{xz}(0), \Pi_{xz}(t)\} \rangle_g\end{aligned}\quad (2.91)$$

$$= -\beta \frac{d}{dt} [\langle \Pi_{xz}(0) \Pi_{xz}(t) \rangle_e - \langle \Pi_{xz}(0) \Pi_{xz}(t) \rangle_g], \quad (2.92)$$

which is simply the difference between four-wave-mixing response functions on two distinct electronic states. At long waiting time limit, the pump-on response is the ordinary OKE response in equilibrium with an excited-state solute. We will concentrate on this large T limit in chapter 3.

By contrast, at the limit of $T = 0$, the pump-on response reflects the light scattering that samples the initial configuration on the equilibrium ground state, with the subsequent dynamics propagating on the excited state. [§]

$$R(0, 0, t) = \int d\mathbf{X}_0 \rho_g(\mathbf{X}_0) \{\Pi(0), \Pi(t)_e\} = \langle \{\Pi(0), \Pi(t)_e\} \rangle_g = \beta \langle \dot{\Pi}(0) \Pi(t)_e \rangle_g. \quad (2.93)$$

The corresponding solute-pump/solvent-probe response function is

$$\Delta R(0, 0, t) = \beta [\langle \dot{\Pi}(0) \Pi(t)_e \rangle_g - \langle \dot{\Pi}(0) \Pi(t) \rangle_g], \quad (2.94)$$

which highlights the pump-on response is the correlation between the ground-state polarizability velocity $\dot{\Pi} = d\Pi/dt$ and the excited-state polarizability $\Pi(t)_e$. In other words, the solute excitation does not change the instantaneous value of polarizability velocity; what

[§]Throughout this thesis, Π stands for any element of the many-body polarizability (usually the off-diagonal elements when discussing the anisotropic four-wave-mixing response), and $\mathbf{\Pi}$ denotes the second-rank many-body polarizability tensor.

gets measured by the four-wave-mixing probe is the instantaneous polarizability velocity correlated with the time-delayed polarizability evolving on the final solute electronic state.

When the waiting time T is in an immediate range, the solute-pump/solvent-probe response function (Equation 2.87) cannot be simplified into some ordinary two-time or three-time correlation function as in ordinary four-wave-mixing response (Equation 2.52). The Poisson bracket in the solute-pump/solvent-probe response is part of the reason, since for functions with form $\langle A(0)\{B(t_1), C(t_2)\} \rangle$, there is no relation like $\langle \{A(0), B(t)\} \rangle = \beta \langle \dot{A}(0)B(t) \rangle$ that can transform the solute-pump/solvent-probe response function to some ordinary correlation functions. A similar situation happens in the fifth order Raman spectra¹⁹⁶⁻²¹⁷ where the initial excitation is a nonresonant light scattering event instead of a resonant solute-pump. The Poisson brackets exist in these 5th order experiments due to the fact that they are measuring the sensitivity of a four-wave-mixing light scattering to a initial perturbation, rather than measuring the light scattering itself. A Poisson bracket describes the sensitivity of a system's trajectories because it reports on how the value of some dynamical variable at time t is affected by variations in another dynamical variable at time 0.

In principle, one can resort to nested molecular dynamics to evaluate a Poisson bracket. For example, in our case, the Poisson brackets $\{\Pi(T), \Pi(T+t)\}$ can be expressed as follows, since the many-body polarizability depends only on the liquid configuration \mathbf{R} .

$$\{\Pi(T), \Pi(T+t)\} = \{\Pi[\mathbf{R}(T)], \Pi[\mathbf{R}(T+t)]\} = \sum_{i,k=1}^{3N} \left[\left(\frac{\partial \Pi}{\partial R_i} \right)_T \left(\frac{\partial \Pi}{\partial R_k} \right)_{T+t} \frac{\partial R_k(T+t)}{\partial P_i(T)} \right], \quad (2.95)$$

where the derivative $\partial R(T+t)/\partial P(T)$ can be numerically evaluated by performing a series of perturbed trajectories ($T \rightarrow T+t$) and averaging the changes in positions at time $T+t$ with respect to some initial momenta $P(T)$ that has a finite difference from that in the unperturbed trajectory. This numerical approach has been applied to calculate nonlinear spectroscopic responses in some well-behaved systems,^{196,197,234,235} but the

Poisson bracket is essentially fluctuating and practically difficult to compute, because of the intrinsically chaotic nature of classical many-body systems.^{236–238} The correlation function of a Poisson bracket with another fluctuation would be even more noisy.

An approach that one can take to avoid the issue of chaotic Poisson brackets is modeling the real experiment through carrying out (finite field) nonequilibrium simulations with explicit external perturbations.^{206,210,239} To increase the computational efficiency in evaluating 5th order Raman spectra, for instance, another approach has been proposed which combines equilibrium MD with nonequilibrium finite field trajectories.^{211,216,217} However, these approaches utilizing nonequilibrium trajectories abnegate the real power of linear response theory that enables one to predict a system's response based on equilibrium averages without actually perturbing the system. Besides computational advances in evaluating the Poisson bracket, analytical attempts using generalized-Langevin-equation language^{240,241} and the mode-coupling theory^{207,212,242–245} have been made. Moreover, quantum mechanics motivates valuable approximations into classical nonlinear spectroscopic responses.^{201–205} We will get back to the topic of evaluating Poisson brackets in chapter 4 where we will show a practical approach to calculate Poisson bracket taking advantage of the instantaneous-normal-mode approximation.

In this chapter, both traditional linear response theory and the linear response theory with Gaussian statistics are derived in a general way using classical statistical mechanics. The connection between the linear response theory and nonlinear spectroscopic responses has been made, and the solute-pump/solvent-probe response function is derived using the linear-response-theory formalism. Brief discussion about the difficulty in evaluating Poisson bracket is given. In the next chapter, we will focus on the long waiting time T case of the solute-pump/solvent-probe spectroscopy.

Chapter 3

Preferential Solvation Dynamics and Optical Kerr Effect Spectroscopy

3.1 Preferential Solvation Dynamics

The concept of solvation dynamics is introduced in chapter 1, a structural rearrangement process of solvent molecules to accommodate a change in the solute such as a charge redistribution triggered by a laser-induced electronic excitation. The driving force of the structural reorganization originates from the tendency of the solute–solvent composite system to lower its free energy. The questions relevant to the solvation process are: How fast is the solvation relaxation? What molecular features determine the relaxation rate? More interestingly, what is the molecular mechanism during the solvation process? For example, how would the presence of solvent alter the reaction pathway in chemical dynamics. How can one characterize the solvation dynamics theoretically and experimentally? One of the most representative approach to solvation dynamics is time-dependent fluorescence study on chromophore solutions.^{2,83,141} By watching characteristic emission fluorescence frequency of the excited chromophore solute, one can construct a solute–solvent interaction energy relaxation profile, which serves as the measure for the

progression of solvation.^{246,247} In dipolar solvents, the solvation relaxation has been found to be contributed mostly by reorientational motions of the solvent.⁸¹ The solvation profiles exhibit bimodal behavior — subpicosecond inertial motion of solvent and picosecond diffusive motion.⁸³ The ultrafast solvation time is mostly determined by the dynamics of the first solvation shell.^{81,248} The reason why only a local portion of molecules governs the solvation process is that the observable, potential energy of a single solute is only sensitive to the ambient solvent near the solute. Following an electronic excitation of the solute, such as creating or increasing the solute's dipole, a net number of solvent molecules translate into the first solvation shell leading to a more crowded arrangement (“electrostriction”).

However, in solvent mixtures, another translational relaxation pathway emerges as a result of the new choices of replacing one kind of the solvents with another in the first shell (“redistribution”). This redistribution process is the root of the preferential solvation.^{85–98} In preferential solvation, multiple solvents with different solvating abilities are mixed, for example, dipolar acetonitrile and nonpolar benzene⁸⁵ (Figure 1.7). An interesting phenomenon in preferential solvation is that the solvent mixture displays a much slower solvation than either pure solvent case, which is now believed to be a consequence of the slow redistribution process.⁸⁷ Moreover, the solvation rate depends on the solvent composition with observations such as a small percentage of the favored solvent exhibits the slowest solvation.^{85,87,220} Although the redistribution of different species of solvents is always present in liquid mixtures, a significant slowdown of the solvation is not guaranteed. In order to see a conspicuous preferential solvation, the dynamical properties of the solvents need to be different enough such that one solvent frustrates another solvent's relaxation thus impeding the overall solvation.^{90,92,95}

Solvent mixtures are often used in organic chemistry when a pure solvent cannot dissolve all the reactants. Table 3.1 shows some common solvents' average polarizabilities and dipoles. To date, solvation properties of many binary solvent mixtures have been investigated microscopically including dimethylsulfoxide (DMSO)/water,^{89,91,92,249–252} ben-

zene/acetonitrile (ACN),^{85,95} water/alcohol,^{89,253} alkane/alcohol,^{94,254} cyclohexane/benzene,¹⁶¹ tetrahydrofuran (THF)/water,²⁵⁵ THF/ACN, ethanol,²⁵⁶ *N,N*-dimethylformamide (DMF)/water, alcohol,²⁵⁷ DMSO/benzene,^{258,259} and CO₂/ACN, methanol, cyclohexane.^{260,261}

Solvent	Polarizability (\AA^3)	Dipole (D)
Water	1.47 ^a	1.88 ^c
Dimethylsulfoxide (DMSO)	7.97 ^b	3.96 ^d
<i>N,N</i> -Dimethylformamide (DMF)	7.81 ^d	3.82 ^d
Ethanol	5.11 ^c	1.44 ^c
Methanol	3.31 ^c	1.70 ^c
Acetonitrile (ACN)	4.51 ^c	3.91 ^c
Tetrahydrofuran (THF)	8.0 ^e	1.75 ^d
<i>p</i> -Dioxane	8.6 ^d	0
Acetone	6.33 ^d	2.88 ^d
Dichloromethane (DCM)	6.48 ^d	1.60 ^d
Chloroform	8.5 ^c	1.04 ^c
Cyclohexane	11.0 ^d	0
Hexane	11.9 ^d	0
Benzene	10.6 ^c	0

Table 3.1 Molecular polarizability and dipole of common solvents. (Conversion of polarizability unit, 1 a.u. = 0.148185 \AA^3 .) (a) W. F. Murphy, *J. Chem. Phys.* **67**, 5877 (1977); (b) K. J. Miller, *J. Am. Chem. Soc.* **112**, 8533 (1990); (c) C. G. Gray and K. E. Gubbins, *Theory of Molecular Fluids, Vol. 1: Fundamentals* (Oxford, New York, 1984); (d) W. M. Haynes, Ed., *CRC Handbook of Chemistry and Physics* (CRC, Boca Raton, 2013), 93rd ed.; (e) H. Reis, A. Grzybowski, and M. G. Papadopoulos, *J. Phys. Chem. A* **109**, 10106 (2005).

In this thesis, the idea of solute-pump/solvent-probe spectroscopy will be applied to a model problem showing preferential solvation. In the rest of this chapter, I will begin with introducing an atomic liquid model for molecular dynamics simulation and show the solvation responses with respect to different solvent compositions. Then the following section describes the solute-pump/solvent-probe spectra at the infinite waiting time limit for this preferential solvation problem (which gives the difference in optical Kerr effect spectra between equilibrated excited-state system and ground-state system). This result will enable us to distinguish how the ultrafast intermolecular dynamics varies with solute's electronic states. Molecular-level analysis of the spectra reveals local solvent dynamics.

3.2 Molecular Dynamics Simulation

The major reason for the slow preferential solvation is the solvent redistribution, which is mostly translational motions.^{85–88,93–95,254} It is not only straightforward but also wise to choose an atomic liquid model to simulate a preferential solvation process over some realistic molecular liquid models. It turns out that an atomic solute with mixture of two different atomic solvents is sufficient to reproduce the whole dynamical phenomenology of preferential solvation that we are interested in.

The atomic liquid model we are going to use was first proposed by Sakurai and Yoshimori.⁹⁷ It consists of a single atomic solute (u) dissolved in a mixture of strongly solvating (S) and weakly solvating (W) solvents. The solute could be in its ground electronic state (u-g) or its excited electronic state (u-e). All atoms have identical mass (m) and diameter (σ). The interaction between every pair of atoms are described by the Lennard–Jones (LJ) potentials,

$$u(r_{ab}) = 4\epsilon_{ab} \left[\left(\frac{\sigma}{r_{ab}} \right)^{12} - \left(\frac{\sigma}{r_{ab}} \right)^6 \right], \quad (a, b = \text{u-g, u-e, S, W}). \quad (3.1)$$

$$\epsilon_{ab} = \epsilon, \quad (\text{all interactions except those involving u-e})$$

$$\epsilon_{\text{u-e,S}} = 3\epsilon, \quad \epsilon_{\text{u-e,W}} = 1.5\epsilon.$$

The dynamics of the system with a ground-state solute is no different from that of a pure Lennard–Jones liquid, whereas when the solute is promoted to the excited state, the solute–solvent attraction increases and the S solvent has a deeper energy well depth than the W solvent. The physical timescale is defined by choosing argon LJ parameters $m = 39.948$ amu, $\sigma = 3.405 \text{ \AA}$, $\epsilon/k_B = 119.8$ K, and the corresponding time unit $\tau_{LJ} = \sqrt{m\sigma^2/\epsilon} = 2.16$ ps. Molecular dynamics simulations for the system are performed with thermal conditions density $\rho\sigma^3 = 0.8$ and temperature $k_B T/\epsilon = 1.00 \pm 0.03$.

In simulations with total atom number $N = 256$, there are one solute and 255 solvent

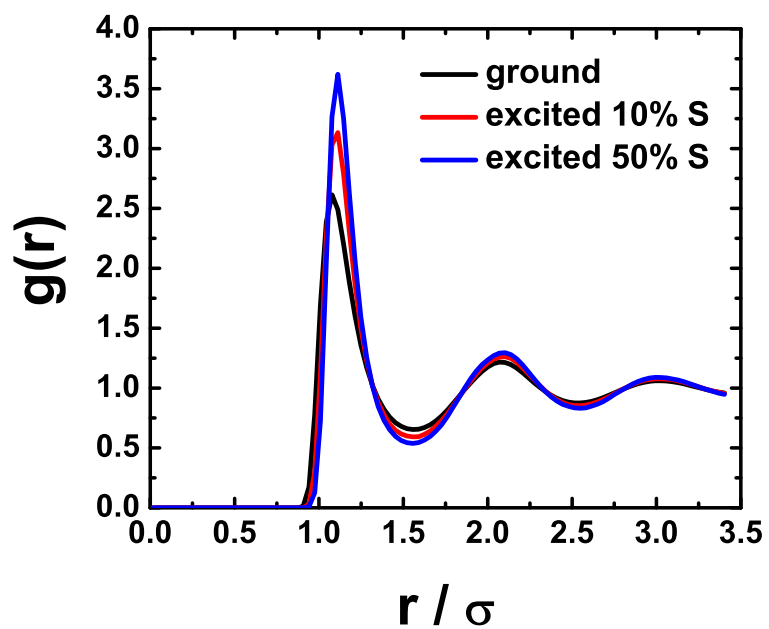


Figure 3.1 Solute–solvent radial distribution function in atomic liquid with ground-state solute, 10% S system with excited-state solute, and 50% S system with excited-state solute. Total number of atoms is 256 including one solute. Radial distribution functions are averaged over 10^6 liquid configurations.

atoms. In a 10% S system, there are 26 S solvent atoms and 229 W solvent atoms. Molecular dynamics is simulated with cubic periodic boundary conditions using the velocity Verlet propagation algorithm.⁵⁹ The time step δt is 0.0025 $\tau_{LJ} = 5.4$ fs, and ensemble averages are computed by sampling the liquid configurations every 10 time steps. Equilibration is achieved by performing standard procedure whose details are shown in Appendix D. Figure 3.1 shows the solute–solvent distribution function $g(r)$ for the ground-state system and excited-state systems with 10% S and 50% S. The radial distribution function is defined as $g(r) = n(r)/(\rho \cdot 4\pi r^2 dr)$, where $n(r)$ is the number of solvent atoms at a distance between r and $r + dr$ from the solute, and ρ is the average number density. Shown in Figure 3.1 are typical equilibrium liquid-state radial distributions. The location of first minimum of the solute–solvent radial distribution defines the boundary of the first solvation shell, $r_{1st \min} = 1.556 \sigma = 5.298 \text{ \AA}$. Similarly the second shell cutoff radius $r_{2nd \min} = 2.548\sigma = 8.676 \text{ \AA}$. It is worth noting that the minimum locations do not vary with the solute’s electronic state nor the solvent composition. Another check for the equilibrium in ground state is the velocity autocorrelation function (Figure 3.2), whose definition is as follows.

$$C_{\mathbf{v}\mathbf{v}}(t) = \frac{\langle \mathbf{v}(0) \cdot \mathbf{v}(t) \rangle}{\langle \mathbf{v}^2 \rangle}. \quad (3.2)$$

The negative velocity correlation in the region $0.3 < t < 0.7$ indicates that liquid atoms have more probability moving in the opposite directions to those they used to move along at a time t earlier. After 1.25 ps, atoms almost lose all the memory of their velocities at time 0 corresponding to $C_{\mathbf{v}\mathbf{v}} \rightarrow 0$.

The solute–solvent interaction energy is the excited-state/ground-state energy gap that can be expressed as follows

$$\Delta V = \sum_{v \in \text{S,W}} \left[u_{\text{u-e},v}(r_{uv}) - u_{\text{u-g},v}(r_{uv}) \right], \quad r_{uv} = |\mathbf{r}_u - \mathbf{r}_v|. \quad (3.3)$$

In our case, the normalized nonequilibrium solvation relaxation profile $S(t)$ and the nor-

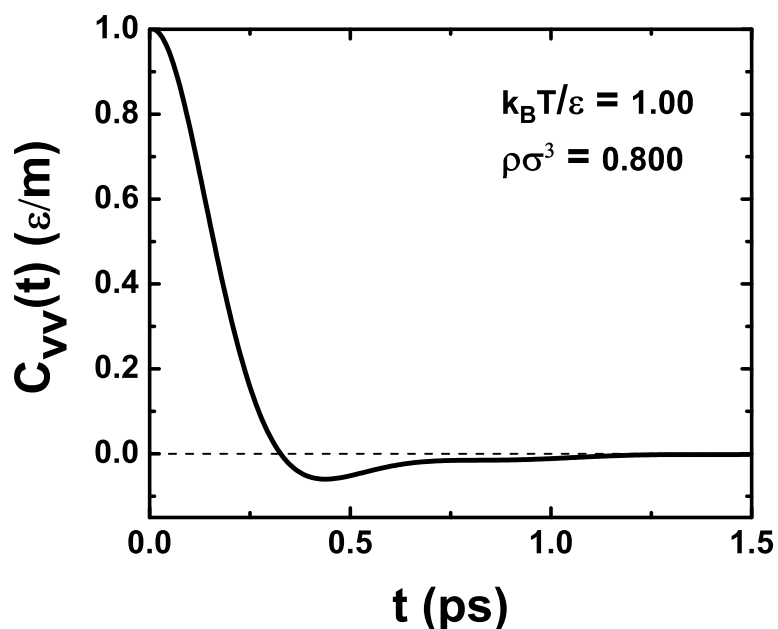


Figure 3.2 Normalized velocity autocorrelation function for Lennard–Jones liquid at density $\rho\sigma^3 = 0.8$ and temperature $k_B T/\varepsilon = 1.00$. Total number of atoms $N = 256$. Velocity correlation function is averaged over 2×10^6 liquid configurations.

normalized equilibrium correlation function $C(t)$ defined in chapter 1 can be written as

$$S(t) = \frac{\overline{\Delta V(t)} - \langle \Delta V \rangle}{\overline{\Delta V(0)} - \langle \Delta V \rangle}, \quad C(t) = \frac{\langle \delta \Delta V(0) \delta \Delta V(t) \rangle}{\langle \delta \Delta V(0)^2 \rangle}. \quad (3.4)$$

Figure 3.3 shows the simulated equilibrium $C(t)$ and the nonequilibrium $S(t)$ for this model in a range of solvent compositions including pure solvent cases. An evident solvent composition dependence is observed and the slowest relaxation takes place in the case most dilute in S, 10% S system, which is consistent with the experimental observations in Figure 1.7. Thus this atomic liquid mixture model imitates the phenomenology of preferential solvation successfully. The excellent agreement between $C(t)$ and $S(t)$ also validates the linear response theory in this model system. Moreover, the pure W solvent (0% S) and the pure S solvent (100% S) exhibit identical solvation responses for time longer than a picosecond.

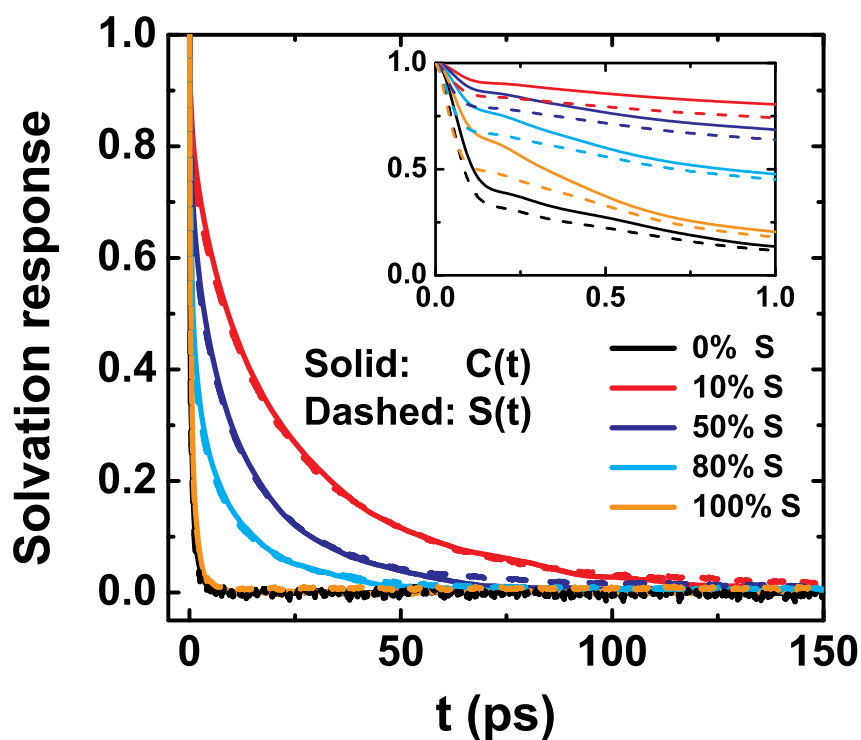


Figure 3.3 Solvation dynamics for the atomic liquid preferential solvation model in a range of solvent compositions. Shown here are both the equilibrium solvation correlation function $C(t)$ and the nonequilibrium solvation relaxation function $S(t)$, with the detailed view of subpicosecond relaxations in the inset. The $C(t)$ and $S(t)$ profiles are averaged over 5×10^6 and 10^5 liquid configurations respectively.

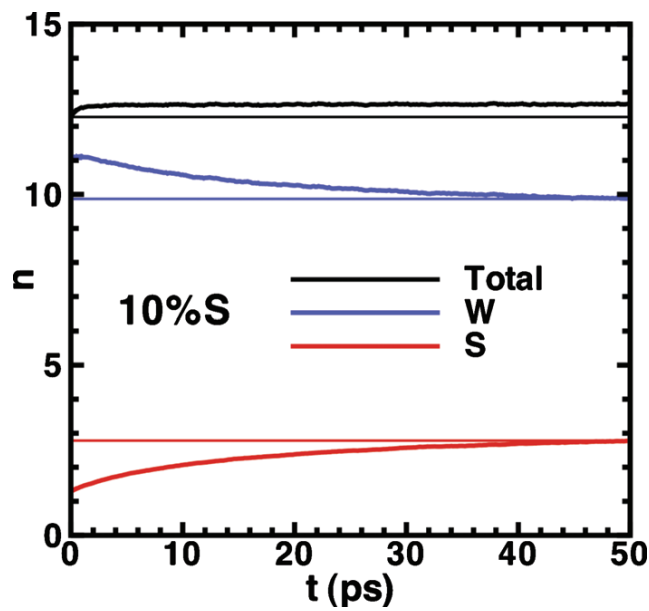


Figure 3.4 Time evolution of the first shell population in 10% S solvent mixture after solute excitation. The same atomic liquid model is used as described in the text. Total number of solvent in the first shell is the black curve, the number of S solvent in the first shell is the red curve and the number of the W solvent in the first shell is the blue curve. [From C. N. Nguyen, R. M. Stratt, *J. Chem. Phys.* **133**, 124503 (2010).]

The two stages of preferential solvation, electrostriction and solvent redistribution, can be identified in Figure 3.4 where the time evolution of the first shell population in 10% S mixture is plotted against the time after switching the solute’s electronic state. The $1/e$ time for the relaxation of the total number of solvents in the first solvation shell is less than 1 ps, corresponding to the solvent compression (“electrostriction”), while the $1/e$ time for S solvent population relaxation is 12 ps corresponding to the solvent exchanging process (“redistribution”). A recent geodesic (most efficient) pathway^{262–264} investigation to the same atomic liquid model performed by Nguyen and Stratt demonstrates that the slow solvent exchanging process exhibits rather a sequential mechanism than a concerted mechanism.⁸⁷ The number of S and W solvent population and their $1/e$ time constants are summarized in Table 3.2. Two systems are particularly interesting: the 10% S solvent mixture has the largest S solvent percentage change (1.3 S \rightarrow 3.0 S) and the 50% S solvent mixture has the largest S solvent number change (+3.2 S). Hence these two systems are

going to be investigated using the solute-pump/solvent-probe spectroscopy, and the long waiting time T limit spectra will be discussed in rest of this chapter.

	1st-shell eq. population			time scale		
	g	e	e-g	S	W	Tot
10% S	1.3 S + 11 W	3.0 S + 9.7 W	+1.7 S - 1.3 W	12	15	0.7
50% S	6.2 S + 6.1 W	9.4 S + 3.5 W	+3.2 S - 2.6 W	10	12.8	0.8
80% S	10 S + 2.4 W	12 S + 1.1 W	+2.0 S - 1.3 W	5.5	8.7	0.8

Table 3.2 Averaged first shell population and 1/e relaxation time (ps). S and W solvent populations on equilibrium ground state (g), equilibrium excited state (e) along with the difference between the two (e-g) are shown on the left side. The 1/e times for population relaxation of S, W and total solvent in the first shell are shown on the right side. [From C. N. Nguyen, Ph.D. thesis, Brown University (2011), chapter 2.]

3.3 Optical Kerr Effect (OKE) Spectroscopy

In chapter 2, the solute-pump/solvent-probe response function at the long waiting time T limit is proven to be the difference between the excited-state optical Kerr effect (OKE) response and the ground-state OKE response (Equation 2.92). As mentioned in chapter 1, OKE spectroscopy^{20, 142, 145–159} is a four-wave-mixing technique with a pump–probe laser configuration. Essentially, OKE spectroscopy is a kind of third-order time-domain nonresonant coherent Fourier transform Raman spectroscopy, and is an excellent tool for the interrogation of ultrafast dynamics in liquids. In this section, a more detailed description of the OKE experiment is given followed by our theoretical route.

3.3.1 OKE experiment

The experimental implementation of optical Kerr measurement is straightforward by using a pump–probe geometry of lasers. Figure 3.5 shows the pump–probe setup of the experiment. The simplest way to measure an OKE signal is called homodyne detection.¹⁴² The pump pulse polarized at 45° with respect to the vertical direction perturbs the sample and induces a transient birefringence. Then the probe pulse polarized vertically (0°)

arrives at the sample at a delayed time to read out the effect of the perturbation. After the sample, the probe pulse hits an analyzing polarizer (analyzer) before it gets detected. The analyzer is set to allow horizontally (90°) polarized light to pass, so if there were no nonlinear optical effect (for instance the index of refraction were still isotropic), the probe pulse would not be able to pass the analyzer and thus no signal could be detected. In fact, the transient birefringence created by the pump pulse provokes depolarization of the probe pulse, allowing a signal to leak through the analyzer. By scanning the delay time between the pump pulse and the probe pulse, time-dependent optical Kerr effect can be measured. This polarization spectroscopy configuration is sensitive to the depolarized response $R_{xzxz}^{(3)}(t)$ that is proportional to the difference between two elements of the third-order response, $R_{zzzz}^{(3)}(t) - R_{xxzz}^{(3)}(t)$.²⁶⁵ In an isotropic medium, this $R_{xzxz}^{(3)}(t)$ is known as the anisotropic response,

$$R_{aniso}(t) = \frac{1}{2} \left[R_{zzzz}^{(3)}(t) - R_{xxzz}^{(3)}(t) \right] = R_{xzxz}^{(3)}(t). \quad (3.5)$$

In the homodyne detection, the intensity of the signal is measured by the square-law photodiode detector, $I_{OKE}(t) \propto \left| R_{xzxz}^{(3)}(t) \right|^2$.

By setting the angle between the pump pulse polarizer and the probe pulse polarizer to the magic angle ($m = 54.7^\circ$ which is the root of the second order Legendre polynomial $P_2(\cos \theta) = 0$), one can measure the isotropic response¹⁵²

$$R_{iso}(t) = \frac{1}{3} \left[R_{zzzz}^{(3)}(t) + 2R_{xxzz}^{(3)}(t) \right] = R_{zzmm}^{(3)}(t). \quad (3.6)$$

Partitioning the many-body polarizability into the isotropic (scalar) and the anisotropic

(traceless) parts $\mathbf{\Pi} = \mathbf{\Pi}^{iso} + \mathbf{\Pi}^{aniso}$, the isotropic and anisotropic responses^{152, 266}

$$R_{aniso}(t) = -\frac{\beta}{15} \frac{d}{dt} \langle \mathbf{\Pi}^{aniso}(t) \mathbf{\Pi}^{aniso}(0) \rangle, \quad (3.7)$$

$$R_{iso}(t) = -\beta \frac{d}{dt} \langle \mathbf{\Pi}^{iso}(t) \mathbf{\Pi}^{iso}(0) \rangle. \quad (3.8)$$

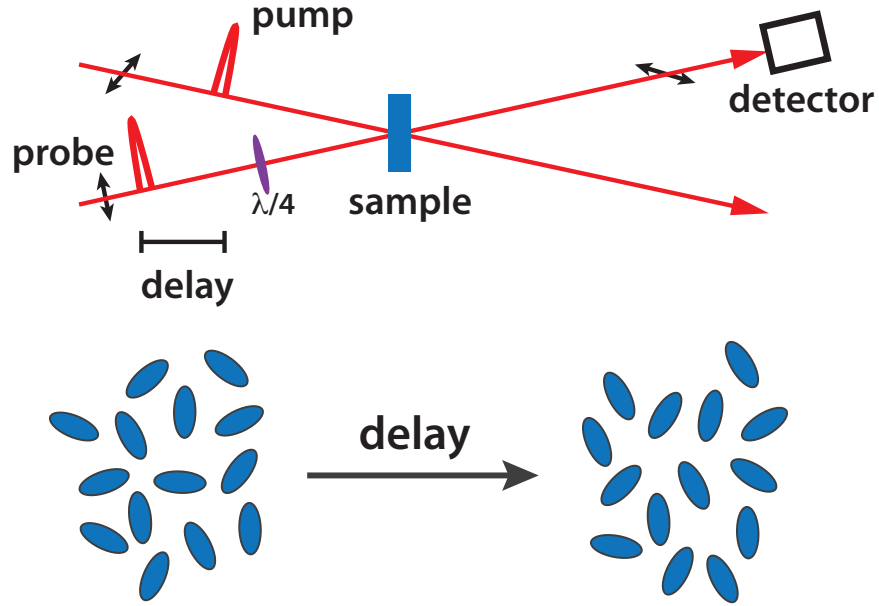


Figure 3.5 Schematic illustration of optical Kerr effect (OKE) spectroscopy. The upper panel shows the pump–probe polarization spectroscopy implementation of OKE experiment. The pump pulse has a polarization at 45° and the delayed probe pulse is polarized vertically. Before the detector, there is an analyzer polarizer that allows horizontally polarized light. In optical heterodyne detection (OHD), a quarter-wave plate ($\lambda/4$) is inserted after the polarizer in the probe beam. The bottom panel depicts a transient molecular structural change induced by the pump pulse — transient birefringence that is a result of a net alignment of the molecules along some specific direction defined by the pump pulse.

In isotropic media, there are 21 nonzero elements out of total $3^4 = 81$ elements of third-order response tensor $R_{\mu\nu\gamma\delta}^{(3)}$, but only 3 elements are independent $R_{zzzz} = R_{xzzx} + R_{xxzz} + R_{zxzx}$.¹³⁰ As in third-order Raman measurement, $R_{xzxz} = R_{xzzx}$,²⁶⁶ only two independent response functions are enough to completely describe the third-order nonlinear optical behavior. Conventionally one can choose independent pairs of responses to characterize an isotropic fluid, anisotropic/isotropic (R_{aniso} & R_{iso}) or polarized/depolarized (R_{zzzz} & R_{xzxz}).

The traditional OKE spectroscopy refers to the anisotropic or the depolarized spectra. The isotropic spectra can be measured through the spatial mask technique developed by Tokmakoff and co-workers.¹⁵² However, the signal-to-noise ratio in isotropic OKE response measurement is not as good as that in anisotropic studies. Recent development of OKE spectroscopy can be found in Hunt, Jaye and Meech.¹⁵⁴

Applying the rotational average, the response functions of third-order four-wave-mixing spectroscopy are given by²⁶⁷ (where pair product PP and trace Tr are defined in Equations 2.55, 2.56)

$$R_{aniso}(t) = R_{xzxz}^{(3)}(t) = -\beta \frac{d}{dt} \left\langle \frac{1}{10} \text{PP}(\Pi(t), \Pi(0)) - \frac{1}{30} \text{Tr}(\Pi(t)) \cdot \text{Tr}(\Pi(0)) \right\rangle, \quad (3.9)$$

$$R_{iso}(t) = R_{zzmm}^{(3)}(t) = -\beta \frac{d}{dt} \left\langle \frac{1}{9} \text{Tr}(\Pi(t)) \cdot \text{Tr}(\Pi(0)) \right\rangle, \quad (3.10)$$

$$R_{zzzz}^{(3)}(t) = -\beta \frac{d}{dt} \left\langle \frac{2}{15} \text{PP}(\Pi(t), \Pi(0)) + \frac{1}{15} \text{Tr}(\Pi(t)) \cdot \text{Tr}(\Pi(0)) \right\rangle. \quad (3.11)$$

Optical heterodyne detection (OHD)

Heterodyne detection overcomes the disadvantages in the homodyne detection including a generally weak OKE signal that is quadratic in the response function. In optical heterodyne detection (OHD),^{145, 147, 149, 150, 154} a large-amplitude phase-controlled electric field called a local oscillator (LO) is mixed with the signal field. So the total measured intensity has three terms,

$$I(t) \propto |\mathbf{E}_{LO} + \mathbf{E}_{OKE}(t)|^2 = I_{LO} + 2\text{Re}[\mathbf{E}_{LO}^* \mathbf{E}_{OKE}(t)] + I_{OKE}(t). \quad (3.12)$$

The first term I_{LO} is the largest, but does not depend on delay time t , thus this constant term can be filtered out by a lock-in detector. The second term is the heterodyne signal which is linear in the OKE signal and therefore linear in the response function $R_{xzxz}^{(3)}$. The last term is the weak homodyne signal that can be removed by taking the difference of two

heterodyne measurements with opposite-signed local oscillators.

The implementation of heterodyne detection is accomplished simply^{142, 154} by inserting a quarter-wave plate after the probe-pulse polarizer (Figure 3.5). The quarter-wave plate is aligned with one of its fast or slow axes along the polarization of the probe pulse. Then if one rotates the probe-pulse polarizer by a small angle like 1° , a 90° out-of-phase field with respect to the probe is generated and can pass through the analyzing polarizer, producing the local oscillator. What is measured by the detector is the intensity of the total electric field consisting the signal field and the local oscillator. If one rotates the probe-pulse polarizer by the same amount but in the opposite direction, the cross term (the heterodyne signal) changes its sign but the squared OKE intensity does not. So by taking the difference of the heterodyne detected signals with probe-pulse polarizer oriented at $\pm 1^\circ$, the OHD-OKE signal $S_{OKE}(t)$ can be obtained.

Since the laser pulses are not infinitely sharp, appreciable dynamics do occur on the time scale of the pulse duration. McMorro and Lotshaw^{145, 268} developed the Fourier-transform deconvolution technique that removes the effects of finite pulse duration from the OKE signal. Given that the local oscillator is out-of-phase with respect to the probe $\mathbf{E}_{LO} = i\epsilon\mathbf{E}_{pr}$ (ϵ is small), the OHD-OKE signal $S_{OKE}(t)$ can be shown to be the convolution of the OKE response function with the second order instrument correlation function²⁶⁹

$$S_{OKE}(t) \propto \int_{-\infty}^{\infty} dt' G^{(2)}(t') R_{xzxz}^{(3)}(t-t') = G^{(2)}(t) * R_{xzxz}^{(3)}(t), \quad (3.13)$$

where $*$ demotes a convolution, and the instrument response $G^{(2)}(t)$ is identical to the second-harmonic-generation intensity cross-correlation (convolution) between pump and probe pulses, $G^{(2)}(t) = I_{pump}(t) * I_{probe}(t)$. Using the property of convolutions $\mathcal{F}[G^{(2)}(t) * R_{xzxz}^{(3)}(t)] = \mathcal{F}[G^{(2)}(t)] \times \mathcal{F}[R_{xzxz}^{(3)}(t)]$, the Fourier transform of the third-order response $D(\omega)$ is simply

$$D(\omega) = \mathcal{F}[R_{xzxz}^{(3)}(t)] = \frac{\mathcal{F}[S_{OKE}(t)]}{\mathcal{F}[G^{(2)}(t)]}. \quad (3.14)$$

In fact, the total response function contains contributions from the electronic and nuclear polarization, where the electronic response is a delta function peaked at time zero, $b\delta(t)$, so its Fourier transform is a real constant. Therefore, the imaginary portion of $D(\omega)$ which is often called the spectral density (SD) is determined solely by nuclear response (dynamics). The time-domain nuclear response can be retrieved by performing inverse Fourier transform, $R^{nucl}(t) = \theta(t)\mathcal{F}^{-1}\text{Im}[D(\omega)]$.

$$SD(\omega) = \text{Im}[D(\omega)] = \int_0^\infty dt R_{xzxz}^{(3)}(t) \sin \omega t. \quad (3.15)$$

In most cases, we are interested in the ultrafast intermolecular dynamics, so we could remove the long-time orientational diffusion contribution from the spectral density $\text{Im}[D(\omega)]$ to obtain the reduced spectral density (RSD), $\text{Im}[D'(\omega)]$.^{142, 145, 154} The long-time diffusive contribution of the time-domain response (for example $t > 2-3$ ps) can be fitted by a sum of exponentials,

$$R_{fit}(t) = A_1 e^{-t/\tau_1} + A_2 e^{-t/\tau_2}, \quad (A_1, A_2 > 0). \quad (3.16)$$

After subtracted the diffusive portion, the response function is then Fourier transformed to calculate the RSD.

$$R_{diff}^{(3)}(t) \approx \left(1 - e^{-t/\tau_{rise}}\right) R_{fit}(t), \quad (3.17)$$

$$RSD(\omega) = \text{Im}[D'(\omega)] = \mathcal{F}[R_{xzxz}^{(3)}(t) - R_{diff}^{(3)}(t)] = \int_0^\infty dt R'(t) \sin \omega t. \quad (3.18)$$

In the diffusive portion of response function, the rise time τ_{rise} can be evaluated by $\tau_{rise} = (2\langle v \rangle)^{-1}$ with $\langle v \rangle = \langle \omega/2\pi \rangle = \int d\omega \frac{\omega}{2\pi} SD(\omega) / \int d\omega SD(\omega)$, giving a typical value of several hundred fs. Its precise value does not have a substantial effect on the shape of the RSD.¹⁵³

Experimental OKE spectra of 2,4,6-trifluoropyridine at 306 K are shown in Figure 3.6. The spectral density and the reduced spectral density are the upper and lower panels

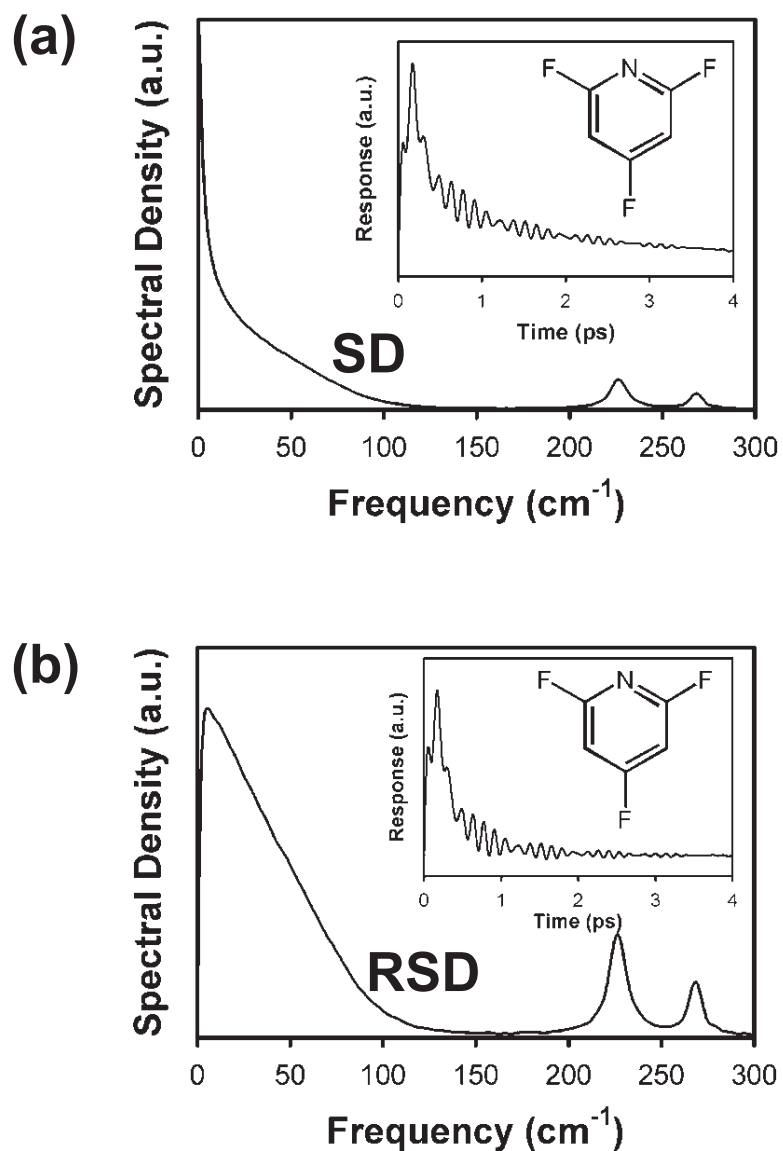


Figure 3.6 Optical Kerr effect spectra for 2,4,6-trifluoropyridine at 306 K. Upper panel (a) shows the spectral density (SD) and the lower panel (b) shows the reduced spectral density (RSD) (that is the spectral density removed the contribution from orientational diffusion). Insets in both panels are time-domain response functions which are the Fourier transform of the spectral density and the reduced spectral density, respectively. The peak near 230 and 270 cm^{-1} results from intramolecular vibrations. [From Q. Zhong, J. T. Fourkas, *J. Phys. Chem. B* **112**, 15529 (2008).]

respectively in which the low-frequency ($0 - 150 \text{ cm}^{-1}$) spectra arise from intermolecular motions and the two peaks with frequency higher than 200 cm^{-1} represent Raman-active intramolecular vibrations. Note that the RSD has less low-frequency diffusive contribution, as can be also seen in the time-domain response functions in the insets. The persistent oscillations in these responses result from the intramolecular vibrations.

3.3.2 Many-body polarizability (dipole-induced-dipole model)

Many-body polarizability is a central quantity in Raman spectroscopies with examples like OKE and transient grating spectroscopy. For a single molecule, the polarizability enters simply: the induced dipole moment is defined as $\boldsymbol{\mu}_{\text{ind}} = \boldsymbol{\alpha} \cdot \mathbf{E}$, where $\boldsymbol{\alpha}$ is the isolated molecular polarizability and \mathbf{E} is the applied electric field. The isolated molecular polarizability $\boldsymbol{\alpha}$ tensor has three principal axes components $\alpha_1, \alpha_2, \alpha_3$ and can be partitioned into the spherical isotropic part

$$\alpha = \frac{1}{3}(\alpha_1 + \alpha_2 + \alpha_3) = \frac{1}{3}\text{Tr}\boldsymbol{\alpha} \quad (3.19)$$

and the traceless anisotropic part $\boldsymbol{\gamma} = \boldsymbol{\alpha} - \alpha\mathbf{1}$. Note that the polarizability anisotropy is defined as²⁷⁰

$$\gamma^2 = \frac{1}{2}[(\alpha_1 - \alpha_2)^2 + (\alpha_2 - \alpha_3)^2 + (\alpha_3 - \alpha_1)^2]. \quad (3.20)$$

For instance, for a cylindrically symmetrical molecule (only one symmetric axis, e.g. linear or symmetric top molecule), $\alpha_1 = \alpha_2 = \alpha_{\perp}$, $\alpha_3 = \alpha_{\parallel}$. Thus, the isotropic polarizability $\alpha = \frac{1}{3}(\alpha_{\parallel} + 2\alpha_{\perp})$ and the anisotropy $\gamma = \alpha_{\parallel} - \alpha_{\perp}$. The isolated molecular polarizability tensor for a symmetrical top is given by

$$\boldsymbol{\alpha}_i = \left(\alpha - \frac{\gamma}{3}\right)\mathbf{1} + \gamma\hat{\Omega}_i\hat{\Omega}_i, \quad (3.21)$$

which is determined by its isotropic(α) and anisotropic(γ) polarizability and by orienta-

tional unit vector $\hat{\Omega}$ prescribing the principle axis of the molecule.²⁰

For isotropic atoms, the anisotropic part $\gamma = 0$ since there is no orientational degrees of freedom, therefore $\boldsymbol{\alpha} = \alpha \mathbf{1}$.

As for a group of N molecules, the many-body polarizability $\boldsymbol{\Pi}$ is not simply the sum of all the isolated molecular polarizabilities since the dipoles on other molecules can create an extra induced electric field. In the absence of an external electric field, the induced electric field at molecule i arises from the dipole moments of other molecules in the liquid,

$$\mathbf{E}_{\text{ind}}(\mathbf{r}_i) = \sum_{j \neq i}^N \mathbf{T}_{ij} \cdot \boldsymbol{\mu}_j, \quad (3.22)$$

where \mathbf{T}_{ij} is the dipole–dipole interaction tensor between molecules i and j

$$\mathbf{T}_{ij} \equiv \mathbf{T}(\mathbf{r}_{ij}) = \nabla \nabla \left(\frac{1}{r_{ij}} \right) = \frac{3\hat{\mathbf{r}}\hat{\mathbf{r}} - \mathbf{1}}{r^3} \quad (3.23)$$

$$= \frac{3}{r^5} \begin{pmatrix} x^2 - r^2/3 & xy & xz \\ yx & y^2 - r^2/3 & yz \\ zx & zy & z^2 - r^2/3 \end{pmatrix}.$$

$$\mathbf{r} = \mathbf{r}_{ij} = \mathbf{r}_i - \mathbf{r}_j = (x, y, z), \quad r = |\mathbf{r}|, \quad \hat{\mathbf{r}} = \mathbf{r}/r, \quad (3.24)$$

where $\mathbf{1}$ is the unit tensor. On applying an external electric field, the total induced dipole moment at molecule i is given by

$$\boldsymbol{\mu}_i = \boldsymbol{\alpha}_i \cdot \mathbf{E}_{\text{total}}(\mathbf{r}_i) = \boldsymbol{\alpha}_i \cdot \left[\mathbf{E}_{\text{ext}} + \sum_{j \neq i}^N \mathbf{T}_{ij} \cdot \boldsymbol{\mu}_j \right]. \quad (3.25)$$

This is the so-called dipole-induced-dipole (DID) model.²⁷¹ The effective molecular polarizability of a single molecule i , $\boldsymbol{\pi}_i$, ($i = 1, \dots, N$) is defined as follows

$$\boldsymbol{\mu}_i = \boldsymbol{\pi}_i \cdot \mathbf{E}_{\text{ext}}. \quad (3.26)$$

Substituting Equation 3.26 into Equation 3.25, then gives the expression for this effective polarizability *

$$\boldsymbol{\pi}_i = \boldsymbol{\alpha}_i \cdot \left[\mathbf{1} + \sum_{j \neq i}^N \mathbf{T}_{ij} \cdot \boldsymbol{\pi}_j \right]. \quad (3.28)$$

Finally the full many-body polarizability of the entire liquid is the sum of all the effective molecular polarizabilities

$$\boldsymbol{\Pi} = \sum_{i=1}^N \boldsymbol{\pi}_i. \quad (3.29)$$

Calculation of many-body polarizability

To calculate the effective molecular polarizability in Equation 3.28, there are multiple methods we can use corresponding to various orders in the DID approximation.

(1) First order DID approximation.

$$\boldsymbol{\pi}_i = \boldsymbol{\alpha}_i + \boldsymbol{\alpha}_i \cdot \sum_{j \neq i}^N \mathbf{T}_{ij} \cdot \boldsymbol{\alpha}_j. \quad (3.30)$$

(2) Second order DID approximation.

$$\boldsymbol{\pi}_i = \boldsymbol{\alpha}_i + \boldsymbol{\alpha}_i \cdot \sum_{j \neq i}^N \mathbf{T}_{ij} \cdot \boldsymbol{\alpha}_j + \boldsymbol{\alpha}_i \cdot \sum_{j \neq i}^N \mathbf{T}_{ij} \cdot \boldsymbol{\alpha}_j \cdot \sum_{k \neq j}^N \mathbf{T}_{jk} \cdot \boldsymbol{\alpha}_k. \quad (3.31)$$

(3) Infinite order DID approximation using iteration method.²⁷²

$$\boldsymbol{\pi}_i^{(n+1)} = \boldsymbol{\alpha}_i \cdot \left[\mathbf{1} + \sum_{j \neq i}^N \mathbf{T}_{ij} \cdot \boldsymbol{\pi}_j^{(n)} \right]. \quad (3.32)$$

The effective molecular polarizabilities are evaluated by solving the equation above iteratively. The initial guess of $\boldsymbol{\pi}_i$ is just the isolated molecular polarizabilities $\boldsymbol{\alpha}_i$. The

*The DID approximation can also be written as the following infinite series,

$$\boldsymbol{\pi}_i = \boldsymbol{\alpha}_i + \boldsymbol{\alpha}_i \cdot \sum_{j \neq i}^N \mathbf{T}_{ij} \cdot \boldsymbol{\alpha}_j + \boldsymbol{\alpha}_i \cdot \sum_{j \neq i}^N \mathbf{T}_{ij} \cdot \boldsymbol{\alpha}_j \cdot \sum_{k \neq j}^N \mathbf{T}_{jk} \cdot \boldsymbol{\alpha}_k + \dots \quad (3.27)$$

convergence condition is the sum of the absolute value of difference between every element in present and previous iteration steps less than $1 \times 10^{-6} \sigma^3$ or $3.95 \times 10^{-6} \text{\AA}^3$.

$$\sum_{\mu, \nu=x,y,z} \left| \Pi_{\mu\nu}^{(n+1)} - \Pi_{\mu\nu}^{(n)} \right| < 1 \times 10^{-6} \sigma^3. \quad (3.33)$$

(4) Infinite order DID approximation (Appelquist method)²⁷³ by inverting a large matrix.²⁷¹

Equation 3.25 may be rearranged to give the external electric field

$$\boldsymbol{\alpha}_i^{-1} \boldsymbol{\mu}_i - \sum_{j \neq i}^N \mathbf{T}_{ij} \cdot \boldsymbol{\mu}_j = \mathbf{E}_i. \quad (3.34)$$

This equation is a system of N 3×3 matrix equations

$$\begin{pmatrix} \boldsymbol{\alpha}_1^{-1} & -\mathbf{T}_{12} & \cdots & -\mathbf{T}_{1N} \\ -\mathbf{T}_{21} & \boldsymbol{\alpha}_2^{-1} & \cdots & \mathbf{T}_{2N} \\ \vdots & \vdots & \ddots & \vdots \\ -\mathbf{T}_{N1} & -\mathbf{T}_{N2} & \cdots & \boldsymbol{\alpha}_N^{-1} \end{pmatrix} \begin{pmatrix} \boldsymbol{\mu}_1 \\ \boldsymbol{\mu}_2 \\ \vdots \\ \boldsymbol{\mu}_N \end{pmatrix} = \begin{pmatrix} \mathbf{E}_1 \\ \mathbf{E}_2 \\ \vdots \\ \mathbf{E}_N \end{pmatrix}, \quad (3.35)$$

or briefly

$$\mathbf{B} \tilde{\boldsymbol{\mu}} = \tilde{\mathbf{E}}, \quad \implies \quad \tilde{\boldsymbol{\mu}} = \mathbf{B}^{-1} \tilde{\mathbf{E}} \equiv \mathbf{A} \tilde{\mathbf{E}}, \quad (3.36)$$

where $\tilde{\boldsymbol{\mu}}$ and $\tilde{\mathbf{E}}$ are $3N \times 1$ vectors, \mathbf{A} and \mathbf{B} are a pair of reciprocal $3N \times 3N$ matrices with 3×3 block matrix elements A_{ij} and $B_{ij} = \boldsymbol{\alpha}_i^{-1} \delta_{ij} - \mathbf{T}_{ij}(1 - \delta_{ij})$.

$$\mathbf{A}_{3(i-1)+\mu, 3(j-1)+\nu} = A_{ij}^{\mu\nu}, \quad (3.37)$$

$$\mathbf{B}_{3(i-1)+\mu, 3(j-1)+\nu} = B_{ij}^{\mu\nu}, \quad (3.38)$$

in which μ and ν denote Cartesian components.

The equivalent N matrix equations of Equation 3.36 are

$$\boldsymbol{\mu}_i = \sum_{j=1}^N A_{ij} \mathbf{E}_j = \left(\sum_{j=1}^N A_{ij} \right) \mathbf{E} \implies \boldsymbol{\pi}_i = \sum_{j=1}^N A_{ij}. \quad (3.39)$$

Assuming uniform field $\mathbf{E}_j = \mathbf{E}$, then the total dipole moment is

$$\boldsymbol{\mu} = \sum_i \boldsymbol{\mu}_i = \left(\sum_{i=1}^N \sum_{j=1}^N A_{ij} \right) \mathbf{E}. \quad (3.40)$$

Thus, the many-body polarizability is

$$\boldsymbol{\Pi} = \sum_{i=1}^N \boldsymbol{\pi}_i = \sum_{i=1}^N \sum_{j=1}^N A_{ij}. \quad (3.41)$$

Polarizability parameters for our model

In order to calculate the many-body polarizability for our atomic liquid mixture model, we have to assign the isolated polarizabilities for each species, i.e. the solute, strong-solvating S solvent, and weak-solvating W solvent. The commonly used coumarin solutes in solvation studies usually carry the largest polarizabilities in the solution; one such example is coumarin 153 (C153) whose structure is shown in Figure 1.6. The ground-state and excited-state isotropic polarizabilities of C153 are 23.4 \AA^3 and 35.7 \AA^3 respectively.²²² It is a common case that the S and W solvents have different polarizabilities, sometimes they are significantly distinct from one another. In widely-studied preferential solvation systems, for example the DMSO/water binary mixture,^{89,91,92,251} $\alpha_{\text{DMSO}} = 7.97 \text{ \AA}^3$ ²⁷⁴ and $\alpha_{\text{water}} = 1.47 \text{ \AA}^3$.²⁷⁵ In this particular case, the ratio of solvents' polarizabilities is about 5.

In light of the fact that the most obvious preferential solvation occurs when only a small fraction of S solvent is present, it is reasonable to study cases in which the polarizability of the S solvent is much larger than that of the W solvent, because it is easier to distinguish the polarizability change due to a few large-polarizability solvent immersed in a large number of small-polarizability solvent background than the case with a few small-polarizability

molecules against an abundant large-polarizability solvent background. Consequently, in order to get a maximized signal, we have chosen the solute and solvent polarizabilities for our atomic liquid model,

$$\alpha_u = 0.2 \sigma^3 = 7.90 \text{ \AA}^3, \quad (3.42)$$

$$\alpha_S = 0.101 \sigma^3 = 3.99 \text{ \AA}^3, \quad (3.43)$$

$$\alpha_W = 0.0186 \sigma^3 = 0.73 \text{ \AA}^3. \quad (3.44)$$

The polarizability of the S solvent has a factor of 5.5 difference with respect to the W solvent, the same ratio as DMSO/water. The largest polarizability of the solute is kept constant on resonant solute excitation and is twice as large as the strong-solvent value. The reason for choosing a constant solute polarizability is to avoid complicating the inceptive calculations of solute-pump/solvent-probe spectroscopy. Changing the polarizability of the solute is definitely worth consider in future studies.²²²

The reader may have noticed that the polarizabilities of solvents chosen is half the size of the experimental values of DMSO/water. The reason for this choice is to circumvent the so-called polarizability catastrophe which refers to the divergence of the many-body polarizability with infinite order DID approximation, when the distance between two interacting sites approaches $(4\alpha_i\alpha_j)^{1/6}$.²⁷⁶ This issue of polarizability divergence is solved by Thole through modifying the dipole–dipole tensor.^{277,278} When more complex polarizable systems are concerned, the Thole model is a good candidate.^{279–281}

With the polarizability parameters above, we tested the four evaluation methods in a 10% S solvent mixture plus an excited-state solute, with total number of particles $N = 256$. The following many-body polarizabilities (unit σ^3) are averaged over 200 liquid configurations. In the infinite-order iterative calculation, the numbers of iterations till convergence are typically 9 – 14 with absolute tolerance 10^{-5} . The zeroth order many-body polarizability is $\Pi^{0\text{th}} = (\sum_i \alpha_i) \cdot \mathbf{1} = 7.0854 \cdot \mathbf{1}$.

(1) First order DID:

$$\mathbf{\Pi}^{1st} = \begin{bmatrix} 7.073 \pm 0.033 & -0.005183 \pm 0.027377 & 0.02739 \pm 0.02424 \\ -0.005183 \pm 0.027377 & 7.088 \pm 0.029 & 0.01504 \pm 0.01641 \\ 0.02739 \pm 0.02424 & 0.01504 \pm 0.01641 & 7.096 \pm 0.037 \end{bmatrix}$$

(2) Second order DID:

$$\mathbf{\Pi}^{2nd} = \begin{bmatrix} 7.130 \pm 0.029 & -0.002191 \pm 0.029720 & 0.03451 \pm 0.02616 \\ -0.002191 \pm 0.029720 & 7.151 \pm 0.032 & 0.008034 \pm 0.020589 \\ 0.03451 \pm 0.02616 & 0.008034 \pm 0.020589 & 7.162 \pm 0.030 \end{bmatrix}$$

(3) Infinite order DID – iteration:

$$\mathbf{\Pi}^{inf} = \begin{bmatrix} 7.130 \pm 0.032 & -0.001822 \pm 0.032146 & 0.03753 \pm 0.02820 \\ -0.001822 \pm 0.032146 & 7.153 \pm 0.035 & 0.01003 \pm 0.02237 \\ 0.03753 \pm 0.02820 & 0.01003 \pm 0.02237 & 7.164 \pm 0.033 \end{bmatrix}$$

(4) Infinite order DID – matrix inversion:

$$\mathbf{\Pi}^{inf} = \begin{bmatrix} 7.130 \pm 0.032 & -0.001822 \pm 0.032146 & 0.03753 \pm 0.02820 \\ -0.001822 \pm 0.032146 & 7.153 \pm 0.035 & 0.01003 \pm 0.02237 \\ 0.03753 \pm 0.02820 & 0.01003 \pm 0.02237 & 7.164 \pm 0.033 \end{bmatrix}$$

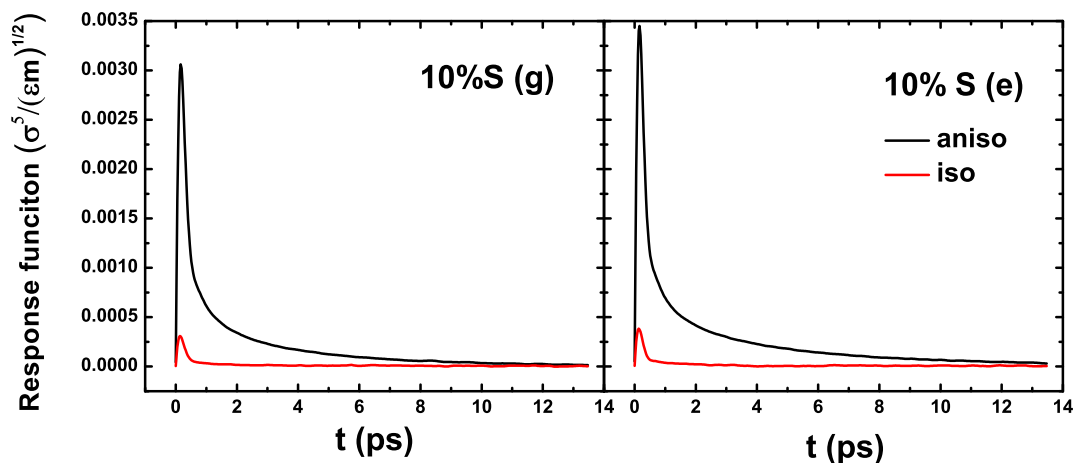
From above results, we can conclude that the first order DID is qualitatively correct compared with the infinite order DID, and the second order is quantitatively correct compared with the infinite order DID. Two infinite order DID methods give the same results. However, the iterative approach is less time-consuming compared with the matrix inversion approach. Furthermore, in the iterative approach, controllable maximum cycles of iteration make it easy to calculate arbitrary order DID approximated polarizabilities. We

will choose the first order DID approximation for computational efficiency and iterative infinite-order method for accuracy in evaluation of polarizabilities. It is worth noting that the fluctuations of the off-diagonal elements make a difference when we look at the difference in the OKE spectra with a ground- and excited-state solute, even though the DID approximated many-body polarizability has almost identical values as the zeroth-order many-body polarizability.

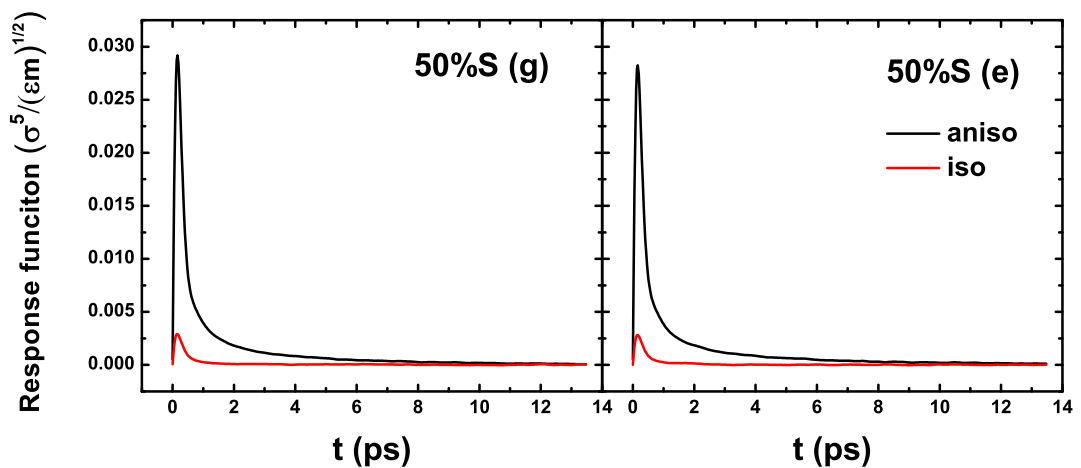
3.3.3 OKE spectra for our model

The time-domain OKE response functions for 10% S and 50% S systems (total number of atoms $N = 256$), each equilibrated in the presence of ground- and excited-state solute, are shown in Figure 3.7 and Figure 3.8. These typical response functions are computed using Equation 3.9 and 3.10 taking advantage of tensor invariants and the time derivatives are calculated by central-difference finite-difference methods. Figure 3.7 also includes the isotropic responses which are much weaker than the anisotropic responses making subsequent spectra analysis more difficult, thus we will focus on the anisotropic OKE spectra later in this thesis. For the same anisotropic OKE responses, Figure 3.7 is a linear plot and Figure 3.8 is a log plot. From both figures, we can observe that there is a sharp peak in the ultrafast region (1–2 ps) corresponding to the vibrational intermolecular dynamics and after 2–3 ps there is mostly long-time diffusion. Since we are mainly interested in the ultrafast dynamics in liquids, it is useful to remove the long-time diffusive portion of the response function and obtain the intermolecular vibrational and librational part of the response. By then performing Fourier transformation on the response without the diffusive portion, one obtains the reduced spectral density, the conventional OKE spectra.

The frequency-domain OKE spectra are shown in Figure 3.9. Both the full spectral density and the reduced spectral density are derived from the imaginary parts of corresponding time-domain responses. (Equation 3.15 and 3.18). The diffusive portion fitting results are shown in Table 3.3. (Table 3.4 is the first order equivalent fitting results.) The diffusion-



(a)



(b)

Figure 3.7 Anisotropic and isotropic OKE responses in 10% S and 50% S systems on equilibrated ground (g) and excited (e) states. Using exact infinite-order DID approximation for polarizability, the results are averaged over 10^7 configurations sampled every 5 time steps.

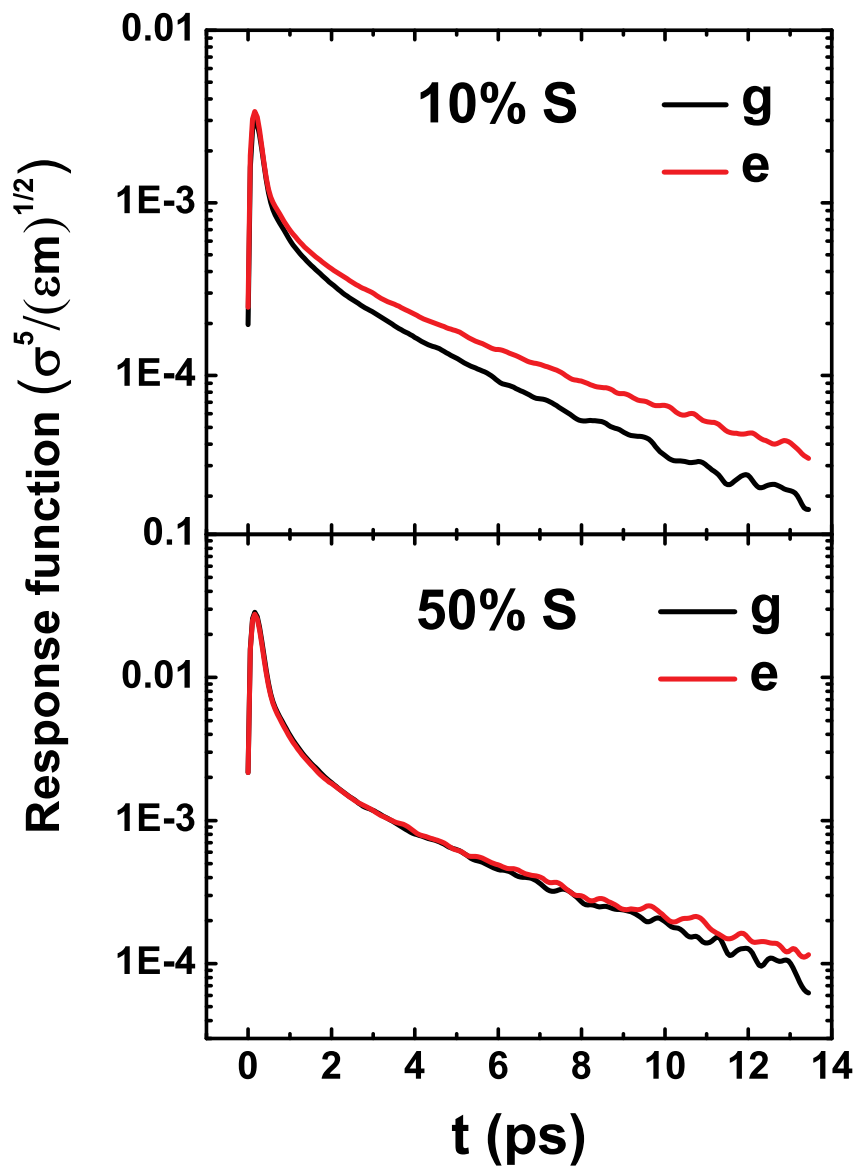


Figure 3.8 Time-domain OKE response functions for two different solvent mixtures, 10% S and 50% S systems in the equilibrated ground state (g) and excited state (e). Exact infinite-order DID approximation are used to calculate many-body polarizability, and the results are averaged over 10^7 configurations sampled every 5 time steps. Note there is a order of magnitude difference in scales between the panels.

removal procedure only alters the spectra in the low frequency region ($<30 \text{ cm}^{-1}$) and the important high-frequency spectra are not changed. The difference between the ground- and excited-state OKE responses is more distinguishable in the frequency domain than in the time domain. In spite of a large solvent background which is presumably not be affected by the solute excitation, the e–g differences are 5%–10% of the full excited- and ground-state spectra, an amount which is significant and reproducible. These substantial e–g differences suggest the capability of OKE spectra to single out the effect of the solute excitation on solvent dynamics. The most striking feature is that the e–g difference has opposite signs in 10% S and 50% S systems, an occurrence whose molecular origin will be discussed soon in the last section of this chapter.

	A_1	τ_1	A_2	τ_2	$\langle \nu \rangle$	τ_{rise}	adj. R^2
10% S (g)	5.7743E-4	1.1426	3.8276E-4	4.2377	35.424	0.4708	0.99939
10% S (e)	5.1617E-4	1.6498	3.6480E-4	5.7469	37.0284	0.4504	0.99969
50% S (g)	0.00207	1.6605	0.00151	4.6133	38.8421	0.4294	0.99696
50% S (e)	0.00266	2.2324	6.8201E-4	7.5971	39.2645	0.4248	0.99502

Table 3.3 Fitting results for the long-time diffusive portion of OKE response function in 10% S and 50% S mixtures on the equilibrium ground and excited state. The OKE response function is calculated by averaging 10^7 infinite order DID polarizabilities, sampled every 5 time steps. Fit starts from 2 ps for 10% S and from 3 ps for 50% S. As in Equation 3.16 and 3.17, A_1 and A_2 have unit $\sigma^5/(\epsilon m)^{1/2}$, τ_1 , τ_2 and τ_{rise} have unit ps, and average frequency $\langle \nu \rangle$ based on the spectral density has unit cm^{-1} . When fitting the time-domain response, the data points are $dt = 0.054$ ps apart and consequently in the frequency-domain the spectral points are $d\nu = 2.41294 \text{ cm}^{-1}$ apart. The rise time is defined as $\tau_{\text{rise}} = (2\langle \nu \rangle)^{-1}$. The adj. R^2 is the indicator of goodness of the fit.

We begin our analysis of the solute-pump/solvent-probe spectra of the preferential solvation model by comparing the reduced spectral densities of 10% S and 50% S with their e–g differences on the same scale as shown in Figure 3.10. Here the first order DID approximation is utilized to improve the computational efficiency which still is able to capture the general behavior of the non-diffusive OKE response. The most direct observation about Figure 3.10 is that the magnitude of OKE spectra for 50% S solvent mixture is much larger than the 10% S mixture with both ground- and excited-state solutes.

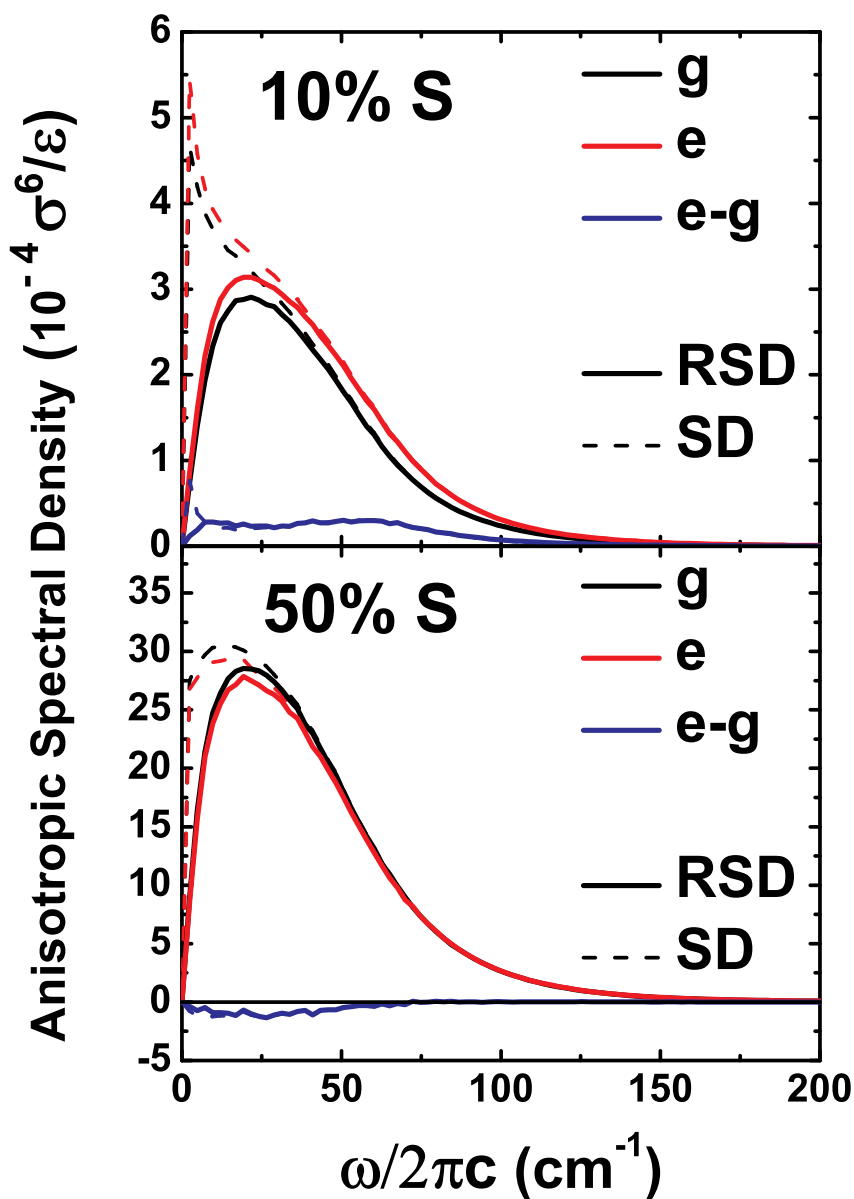


Figure 3.9 Frequency-domain OKE spectra for 10% S and 50% S systems (Fourier transformed from Figure 3.8). For each system, shown are the results with equilibrated ground-state (g) solute, excited-state (e) solute and the difference between the two (e-g). For each case, there are full spectral density (SD, dashed lines) and reduced spectral density (RSD, solid lines) with long-time diffusive behavior removed. Exact infinite-order DID approximation are used to calculate many-body polarizability, and the results are averaged over 10^7 configurations sampled every 5 time steps. Note that the scales in two panels are different.

	A_1	τ_1	A_2	τ_2	$\langle \nu \rangle$	τ_{rise}	adj. R^2
10% S (g)	3.8239E-4	2.1184	1.7869E-4	5.4728	31.8039	0.5244	0.99993
10% S (e)	3.8454E-4	2.0506	2.6838E-4	6.0915	32.6986	0.5101	0.99995
50% S (g)	0.00292	1.6523	0.00136	5.0666	34.4044	0.4848	0.99992
50% S (e)	0.0028	1.8203	0.00114	6.0463	34.6765	0.4810	0.99987

Table 3.4 Fitting results for the long-time diffusive portion of OKE response function in 10% S and 50% S mixtures on the equilibrium ground and excited state. The OKE response function is calculated by averaging 10^8 *first order* DID polarizabilities, sampled every 10 time steps. Fit starts from 3 ps for all cases. As in Equation 3.16 and 3.17, A_1 and A_2 have unit $\sigma^5/(\epsilon m)^{1/2}$, τ_1 , τ_2 and τ_{rise} have unit ps, and average frequency $\langle \nu \rangle$ based on the spectral density has unit cm^{-1} . When fitting the time-domain response, the data points are $dt = 0.054$ ps apart and consequently in the frequency-domain the spectral points are $d\nu = 2.41294 \text{ cm}^{-1}$ apart. The rise time is defined as $\tau_{\text{rise}} = (2\langle \nu \rangle)^{-1}$. The adj. R^2 is the indicator of goodness of the fit.

The areas under the 50% S RSD curves differ from the areas of 10% S RSDs by a factor of 10. Consequently the e–g difference of 50% S system is larger than that of 10% S system. But the magnitude difference of full OKE spectra has little dynamical importance since there are 5 times more of the spectroscopically visible S solvents in the 50% S case than in the 10% S case, which predominantly composed of an insipid background.

3.3.4 Difference spectra

The e–g difference, on the other hand, tells the dynamical change after the solute excitation. Figure 3.11 highlights these essential e–g differences in 10% S and 50% S mixtures. These are the primary results of this chapter: the long waiting time T limits of the solute-pump/solvent-probe spectra. The most astonishing trait of these difference spectra is that the signs of the spectra in the low-frequency region ($< 70 \text{ cm}^{-1}$) are reversed when switching the solvent mixture, yet the relative magnitudes of these difference spectra are also worth noting. The absolute area of the e–g difference in 50% S is only 3 times as large as that of 10% S although the ratio of full spectra area is about 10. So the fraction for the e–g difference is about 3 times higher in 10% S than in 50% S, implying that the solute excitation requires more dramatic structural rearrangement for each S solvent in the 10% S

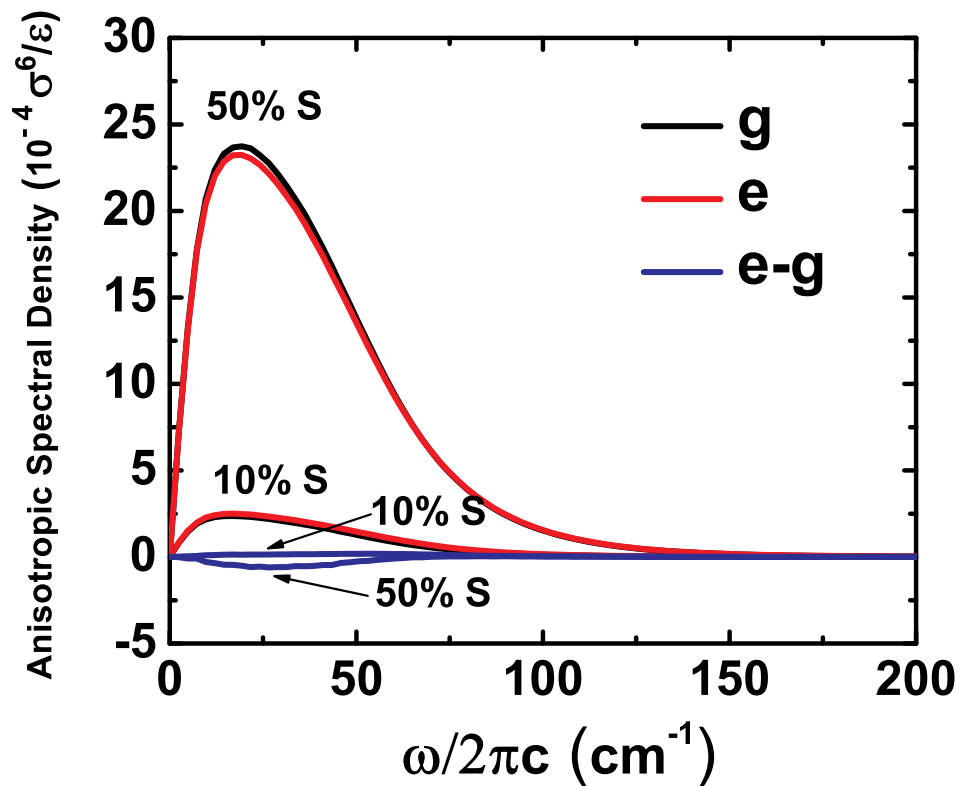


Figure 3.10 Comparison of the OKE reduced spectral densities for 10% S and 50% S solvent mixtures with ground-state solute (g), excited-state solute (e) and their difference spectrum (e-g). First-order DID approximation are used to calculate many-body polarizability, and the results are averaged over 10^8 liquid configurations. For each case, fitting parameters of the long-time diffusive portion are shown in Table 3.4.

case, which is also consistent with the previous solvation dynamics studies that show that the dilute S case is the slowest.^{85,87,93,98}

A second feature of the e–g difference is that 10% S has a flat shaped difference spectra with peak position around 60 cm^{-1} , and 50% S has a sharper peak with position around 25 cm^{-1} . The shapes of spectra indicate that in 10% S system, the intermolecular vibrational modes are excited more uniformly than those in 50% S system. Furthermore, above 75 cm^{-1} both systems have positive e–g differences, and the e–g difference of 10% S is even larger than that of 50% S. As high frequency is dominated by pair motions, does it mean 10% S gets more pair motions excited than 50% S? If so, what are these pairs?

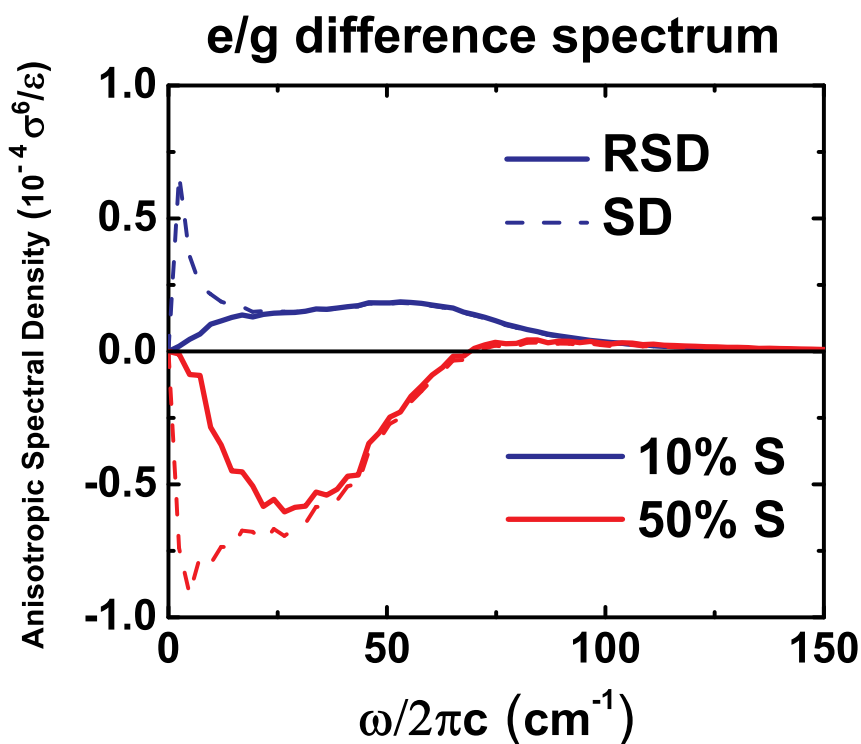
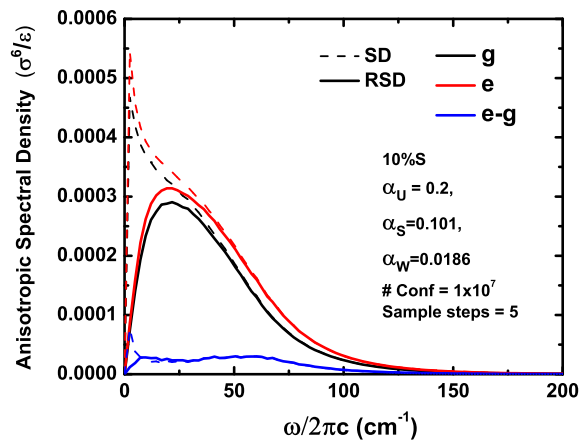
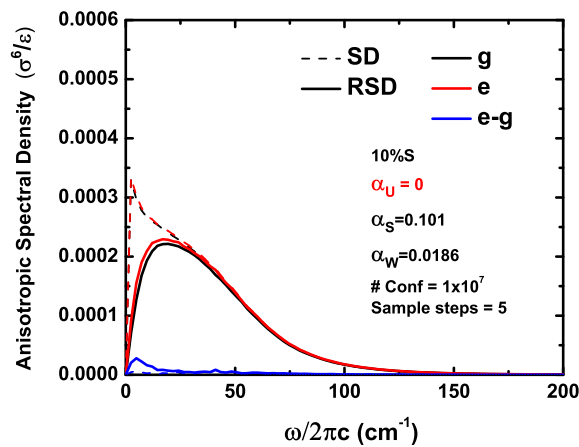


Figure 3.11 Comparison of the long waiting time limit anisotropic RP-PORS spectra for 10% S and 50% S solvent mixtures. The equilibrated excited-state-solute/ground-state-solute RP-PORS spectra correspond to the e–g differences in the OKE reduced spectral density (RSD, solid lines), and the e–g differences in full spectral density (SD, dashed lines) are also shown. First-order DID approximation are used to calculate many-body polarizability, and the results are averaged over 10^8 liquid configurations. The e–g differences in RSD plotted here are the same curves as in Figure 3.10.

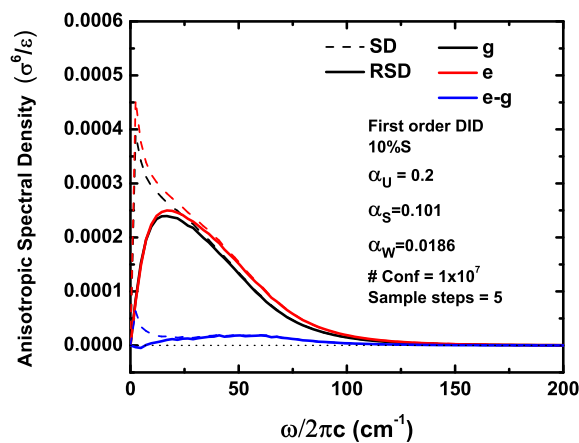
To understand this result, one can selectively turn on/off certain molecular effects



(a)

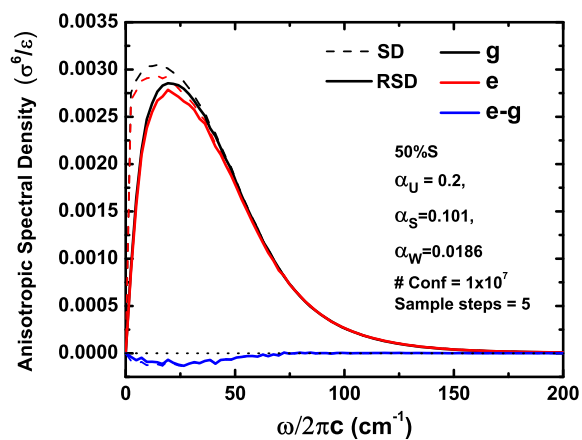


(b)

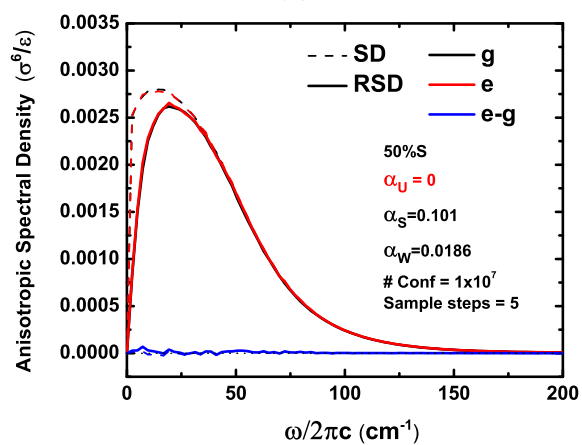


(c)

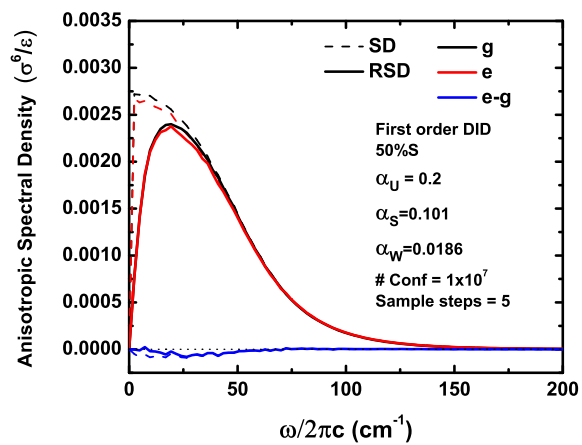
Figure 3.12 Comparison of OKE spectra in 10% S system, (a) infinite order DID approximation and full solute polarizability, (b) infinite order DID approximation with the solute's polarizability set to zero and (c) first order DID approximation with full solute polarizability. Number of configurations to average is 1×10^7 and configurations are sampled every 5 steps.



(a)



(b)



(c)

Figure 3.13 Comparison of OKE spectra in 50% S system, (a) infinite order DID approximation and full solute polarizability, (b) infinite order DID approximation with the solute's polarizability set to zero and (c) first order DID approximation with full solute polarizability. Number of configurations to average is 1×10^7 and configurations are sampled every 5 steps.

in order to isolate the roles of different contributions, in our case, to the many-body polarizability. First of all, one can compare the first order DID approximation with the exact infinite order results in order to see if higher order DID terms have a crucial influence on the difference spectra. Moreover, one can set the solute's polarizability as zero making the solute spectroscopically invisible so as to see if the solute-solvent terms are important to the e-g difference at all. Accordingly, Figure 3.12, 3.13 offer evidence of which contribution to the many-body polarizability is predominant in the OKE spectra. The effects are difficult to see on this scale, but Figure 3.14 is the summary of the above mentioned figures plotting only the e-g differences in all the cases. One can observe that the first order DID and the infinite order DID spectra are qualitatively equivalent except for the 10% S spectrum in the low-frequency region, although the higher order DID terms contribute almost a half of the result. Now we are convinced that the first order DID approximation warrants a qualitative prediction to the solute-pump/solvent-probe spectra. Moreover, when turning off the solute's polarizability $\alpha_u=0$, almost all the high-frequency portions get demolished. We thereby conclude that the physically most important polarizability terms detected by the spectra are those involving the solute/S-solvent pairs. From Equation 3.30, the dominant polarizability terms are

$$2\alpha_u\alpha_S \sum_{j \in S} \mathbf{T}(\mathbf{r}_{0j}), \quad \mathbf{r}_{0j} = \mathbf{r}(\text{solute}) - \mathbf{r}(\text{solvent-}j). \quad (3.45)$$

Then exactly which group of the S solvents is responsible for the measured difference? Is it a local portion of the solvent near the solute? To answer these questions, one can take advantage of the projection operator technique that will be discussed in the upcoming section.

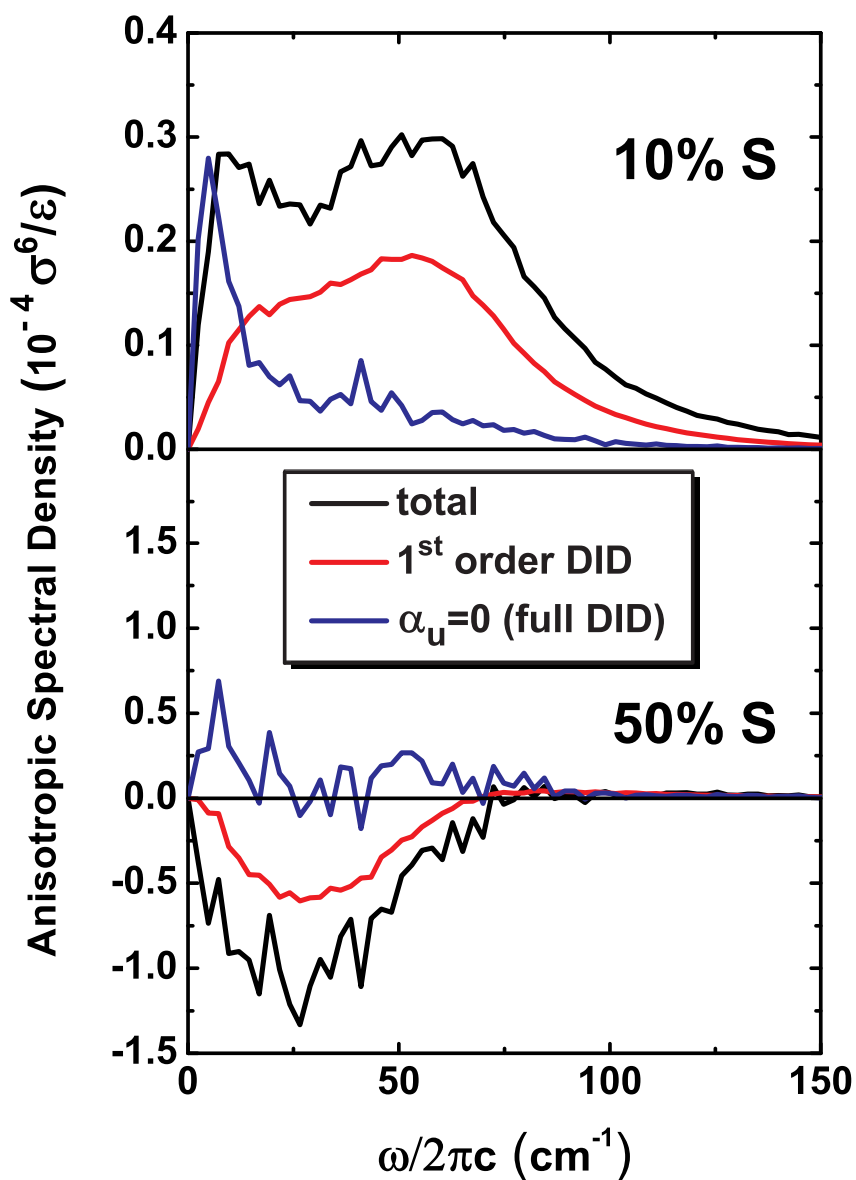


Figure 3.14 Comparison of different polarizability contributions to the long waiting limit anisotropic RP-PORS spectra for 10% S and 50% S solvent mixtures. “Total” uses the infinite order DID approximation for many-body polarizability; “1st order DID” curve neglects all higher order DID terms; and “ $\alpha_u=0$ ” uses the infinite order DID approximation but with a zero-polarizability solute. The results shown are reduced spectral density differences averaged over 10^7 , 10^8 , 10^7 liquid configurations respectively.

3.4 Projection Operator Analysis of Molecular Contributions

The projection operator discussed here, e.g. $\hat{\mathbf{P}}_X$, acts on a summation of the atom coordinates and results in a selected sum of certain degrees of freedom ($j \in X$). There must be a complementary projection operator $\hat{\mathbf{P}}_Y$ that has no common degree of freedom as in $\hat{\mathbf{P}}_X$. Moreover, projection operator is idempotent — it can be applied multiple times without changing the result of applying just once.

$$\hat{\mathbf{P}}_X \sum_{j=1}^N = \sum_{j \in X}, \quad \hat{\mathbf{P}}_Y \sum_{j=1}^N = \sum_{j \notin X} \quad (\text{definition}), \quad (3.46)$$

$$\hat{\mathbf{P}}_X + \hat{\mathbf{P}}_Y = \hat{\mathbf{1}} \quad (\text{complementariness}), \quad (3.47)$$

$$\hat{\mathbf{P}}_X \hat{\mathbf{P}}_Y = 0 \quad (\text{orthogonality}), \quad (3.48)$$

$$\hat{\mathbf{P}}_X^2 = \hat{\mathbf{P}}_X \quad (\text{idempotent}). \quad (3.49)$$

For a correlation function $C(t) = \langle A(0)B(t) \rangle$, if variables $A(t)$ and $B(t)$ contain a sum \sum_j , one can use projection operator to isolate certain types of contributions. For example, if projected into two sets X and Y, the choice of the partitioning sets could be based on regional separation like the first solvation shell vs. outer shells or based on different degrees of freedom like translational vs. rotational motions.

$$C(t) = \langle A(0)B(t) \rangle = \langle (\hat{\mathbf{P}}_X + \hat{\mathbf{P}}_Y)A(0) (\hat{\mathbf{P}}_X + \hat{\mathbf{P}}_Y)B(t) \rangle \quad (3.50)$$

$$\begin{aligned} &= \langle \hat{\mathbf{P}}_X A(0) \hat{\mathbf{P}}_X B(t) \rangle + \langle \hat{\mathbf{P}}_Y A(0) \hat{\mathbf{P}}_Y B(t) \rangle \\ &\quad + \langle \hat{\mathbf{P}}_X A(0) \hat{\mathbf{P}}_Y B(t) \rangle + \langle \hat{\mathbf{P}}_Y A(0) \hat{\mathbf{P}}_X B(t) \rangle \\ &= C_{XX}(t) + C_{YY}(t) + C_{XY,YX}(t). \end{aligned} \quad (3.51)$$

Partitioning into two complementary sets is the simplest case. One certainly can do more, such as partitioning the whole set into three subsets, X, Y, Z. Similarly, we have

$$\hat{\mathbf{I}} = \hat{\mathbf{P}}_X + \hat{\mathbf{P}}_Y + \hat{\mathbf{P}}_Z, \quad (3.52)$$

$$C(t) = \langle A(0)B(t) \rangle = \langle (\hat{\mathbf{P}}_X + \hat{\mathbf{P}}_Y + \hat{\mathbf{P}}_Z)A(0) (\hat{\mathbf{P}}_X + \hat{\mathbf{P}}_Y + \hat{\mathbf{P}}_Z)B(t) \rangle \quad (3.53)$$

$$\begin{aligned} &= \langle \hat{\mathbf{P}}_X A(0) \hat{\mathbf{P}}_X B(t) \rangle + \langle \hat{\mathbf{P}}_Y A(0) \hat{\mathbf{P}}_Y B(t) \rangle + \langle \hat{\mathbf{P}}_Z A(0) \hat{\mathbf{P}}_Z B(t) \rangle \\ &\quad + \langle \hat{\mathbf{P}}_X A(0) \hat{\mathbf{P}}_Y B(t) \rangle + \langle \hat{\mathbf{P}}_Y A(0) \hat{\mathbf{P}}_X B(t) \rangle \\ &\quad + \langle \hat{\mathbf{P}}_X A(0) \hat{\mathbf{P}}_Z B(t) \rangle + \langle \hat{\mathbf{P}}_Z A(0) \hat{\mathbf{P}}_X B(t) \rangle \\ &\quad + \langle \hat{\mathbf{P}}_Y A(0) \hat{\mathbf{P}}_Z B(t) \rangle + \langle \hat{\mathbf{P}}_Z A(0) \hat{\mathbf{P}}_Y B(t) \rangle \end{aligned} \quad (3.54)$$

$$= C_{XX}(t) + C_{YY}(t) + C_{ZZ}(t) + C_{XY,YX}(t) + C_{XZ,ZX}(t) + C_{YZ,ZY}(t). \quad (3.55)$$

The first three “self” terms are resulted from the same subset of degrees of freedom, and the last three terms are called cross terms.

Polarizability-velocity correlation function

A spectroscopic “velocity” autocorrelation function, $G(t)$ is defined as the autocorrelation function of time derivative of variable $A(t)$ (chapter 1) and it can be also partitioned into different contributions using projection operators.

$$G_{AA}(t) = \langle \dot{A}(0)\dot{A}(t) \rangle = \frac{d}{dt} \langle \dot{A}(0)A(t) \rangle = -\frac{d^2}{dt^2} \langle A(0)A(t) \rangle \quad (3.56)$$

$$\begin{aligned} &= \langle \dot{A}_X(0)\dot{A}_X(t) \rangle + \langle \dot{A}_Y(0)\dot{A}_Y(t) \rangle \\ &\quad + \langle \dot{A}_X(0)\dot{A}_Y(t) \rangle + \langle \dot{A}_Y(0)\dot{A}_X(t) \rangle \\ &= G_{XX}(t) + G_{YY}(t) + G_{XY,YX}(t), \end{aligned} \quad (3.57)$$

where

$$\dot{A}_X(t) = \hat{\mathbf{P}}_X \dot{A}(t) = \hat{\mathbf{P}}_X \sum_{j=1}^N \frac{\partial A(t)}{\partial \mathbf{r}_j} \cdot \frac{\partial \mathbf{r}_j}{\partial t} = \sum_{j \in X} \frac{\partial A(t)}{\partial \mathbf{r}_j} \cdot \mathbf{v}_j(t), \quad (3.58)$$

$$\dot{A}_Y(t) = \hat{\mathbf{P}}_Y \dot{A}(t) = \hat{\mathbf{P}}_Y \sum_{j=1}^N \frac{\partial A(t)}{\partial \mathbf{r}_j} \cdot \frac{\partial \mathbf{r}_j}{\partial t} = \sum_{j \notin X} \frac{\partial A(t)}{\partial \mathbf{r}_j} \cdot \mathbf{v}_j(t). \quad (3.59)$$

In OKE spectroscopy, the quantity $A(t)$ is the many-body polarizability $\mathbf{\Pi}(t)$, so the corresponding ‘‘velocity’’ autocorrelation function is $G(t) = \langle \dot{\mathbf{\Pi}}(0) \otimes \dot{\mathbf{\Pi}}(t) \rangle$, which is also called the polarizability-velocity correlation function. The time derivatives of many-body polarizability of certain sets of degrees of freedom X and Y are

$$\dot{\mathbf{\Pi}}_X(t) = \hat{\mathbf{P}}_X \dot{\mathbf{\Pi}}(t) = \sum_{j \in X} \nabla_j \mathbf{\Pi}(t) \cdot \mathbf{v}_j(t), \quad (3.60)$$

$$\dot{\mathbf{\Pi}}_Y(t) = \hat{\mathbf{P}}_Y \dot{\mathbf{\Pi}}(t) = \sum_{j \in Y} \nabla_j \mathbf{\Pi}(t) \cdot \mathbf{v}_j(t). \quad (3.61)$$

Appendix E shows the detailed derivation of the spatial derivative of many-body polarizability with respect to a particular molecule k 's coordinate, $\nabla_k \mathbf{\Pi}$.

$$\nabla_k \mathbf{\Pi} = \sum_i \nabla_k \boldsymbol{\pi}_i \quad \text{or} \quad \frac{\partial}{\partial r_{k\mu}} (\mathbf{\Pi})_{\alpha\beta} = \sum_i \frac{\partial}{\partial r_{k\mu}} (\boldsymbol{\pi}_i)_{\alpha\beta}. \quad (3.62)$$

The spatial derivative of the effective molecular polarizability of molecule i in component form is (Equation E.7)

$$\begin{aligned} \frac{\partial}{\partial r_{k\mu}} (\boldsymbol{\pi}_i)_{\alpha\beta} = & \alpha_i \cdot \sum_{j \neq i} \sum_{\gamma}^{x,y,z} \left[\frac{3 r_{ij}^2 (r_{ij\mu} \delta_{\alpha\gamma} + r_{ij\alpha} \delta_{\mu\gamma} + r_{ij\gamma} \delta_{\mu\alpha}) - 15 r_{ij\mu} r_{ij\alpha} r_{ij\gamma}}{r_{ij}^7} \right. \\ & \left. \cdot (\delta_{ki} - \delta_{kj}) \cdot (\boldsymbol{\pi}_j)_{\gamma\beta} + \frac{3 r_{ij\alpha} r_{ij\gamma} - r_{ij}^2 \delta_{\alpha\gamma}}{r_{ij}^5} \cdot \frac{\partial}{\partial r_{k\mu}} (\boldsymbol{\pi}_j)_{\gamma\beta} \right]. \end{aligned} \quad (3.63)$$

To select the local portion of the OKE spectra, one can partition contributions into (1) first shell and everything else or (2) first shell, second shell and everything else. We expect

that the innermost first-solvation shell would be the largest contribution to the change in many-body polarizability, thus the e–g difference spectra. For the polarizability-velocity correlation function $G(t)$, we have

(1) First choice of partition: X includes all particles in the first solvation shell, and Y is everything else.

$$G(t) = G_{XX}(t) + G_{YY}(t) + G_{XY,YX}(t) \quad (3.64)$$

$$\begin{aligned} &= \langle \dot{\mathbf{\Pi}}_X(0) \otimes \dot{\mathbf{\Pi}}_X(t) \rangle + \langle \dot{\mathbf{\Pi}}_Y(0) \otimes \dot{\mathbf{\Pi}}_Y(t) \rangle \\ &\quad + \langle \dot{\mathbf{\Pi}}_X(0) \otimes \dot{\mathbf{\Pi}}_Y(t) \rangle + \langle \dot{\mathbf{\Pi}}_Y(0) \otimes \dot{\mathbf{\Pi}}_X(t) \rangle, \end{aligned} \quad (3.65)$$

where the first/outer shell partition is based on the instantaneous ($t = 0$) liquid configuration — whether a given solvent is inside or outside the cutoff radius of the first shell that is the first minimum of the solute-solvent radial distribution function, 1.556σ (Figure 3.1). Figure 3.15 shows all components of the polarizability-velocity correlation $G(t)$ for partition of 1st shell and all else. The first order DID approximation is used to calculate the spatial derivatives of many-body polarizability. Comparing Figure 3.15(a) and Figure 3.15(b), we can observe that in 10% S the pure first-shell term (XX) changes relatively more dramatically when the solute gets excited, than the pure first-shell contribution does in 50% S. As for the pure outer shell component (YY), the absolute magnitude keeps almost the same when the solute gets excited for both systems and noticeably larger than the pure first-shell component. Consequently, we wonder if the second-shell term is the contribution to the pure outer shell component. This is the reason we test the second shell partition below. Figure 3.15(c) are the e–g differences in these projections. This result is of only qualitative significance. From this figure one can observe that the outer-shell component in 50% S has a large oscillation (which is not trustworthy) with amplitude about $1.0 \sigma^4/m$ which results from different oscillation frequencies of the excited- and ground-state $G_{YY}(t)$; all components in 10% S have a positive value in the first hundred femtoseconds. The cross

terms are negligible compared with “self” terms. It seems that the larger magnitude of 50% S projections does not guarantee the same effect on e–g differences.

(2) Second choice of partition: X=1st shell, Y=2nd shell and Z=else. The corresponding projected polarizability-velocity correlation function is

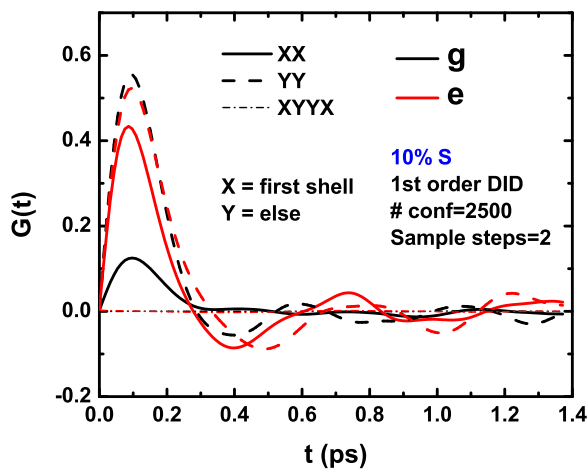
$$G(t) = G_{XX}(t) + G_{YY}(t) + G_{ZZ}(t) + G_{XY,YX}(t) + G_{XZ,ZX}(t) + G_{YZ,ZY}(t). \quad (3.66)$$

Figure 3.16 shows the projected components under the first-shell/second-shell/else partition for both systems, where 10% S has more obvious changes in all “self” terms before and after the solute’s excitation, whereas 50% S system exhibits no significant change. Figure 3.16(a) and 3.16(c) tells us that the first shell and second shell both have an increase in polarizability on solute excitation, consistent with the fact that more atoms come into these closest shells, and so the outer shells lose some polarizabilities. Figure 3.16(c) and 3.16(d) shows the e–g differences of $G(t)$, from which we can observe that all components in 10% S have comparable contributions and only the outer-shell contribution has a significant fluctuation in 50% S.

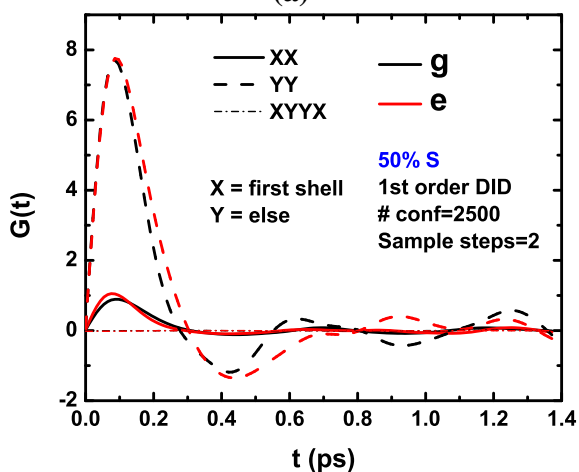
To summarize these two choices of projection partitioning, 10% S has more obvious changes in $G(t)$ in early times, and 50% S seems doesn’t change much except for the outer-shell term oscillating with a big amplitude all the time (questionably). These observations in time-domain polarizability-velocity correlation function cannot lead us to an answer to the question about the signs of e–g difference OKE spectra. Probably the frequency-domain projections can tell us more information.

Projection Analysis of the OKE Spectra

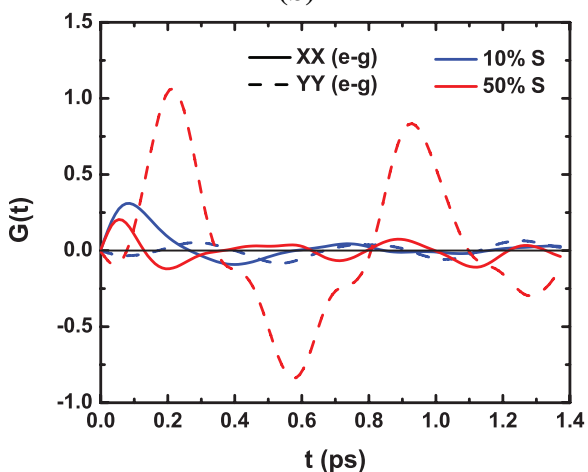
The relation between OKE response function and polarizability-velocity correlation function is as follows $R(t) = \langle \dot{\mathbf{\Pi}}(0) \otimes \mathbf{\Pi}(t) \rangle = \int G(t) dt$. But numerical integration has more instability than directly calculation of OKE response function using the following projec-



(a)



(b)



(c)

Figure 3.15 Polarizability-velocity correlation function $G(t)$ projected to first shell (X) and everything else (Y) contributions. Shown are the first-shell, outer-shells and cross components of $G(t)$ (unit σ^4/m). (a) 10% S solvent mixture, (b) 50% S solvent mixture, (c) e–g differences of both 10% S and 50% S mixtures. Results are computed by averaging 2500 liquid configurations.

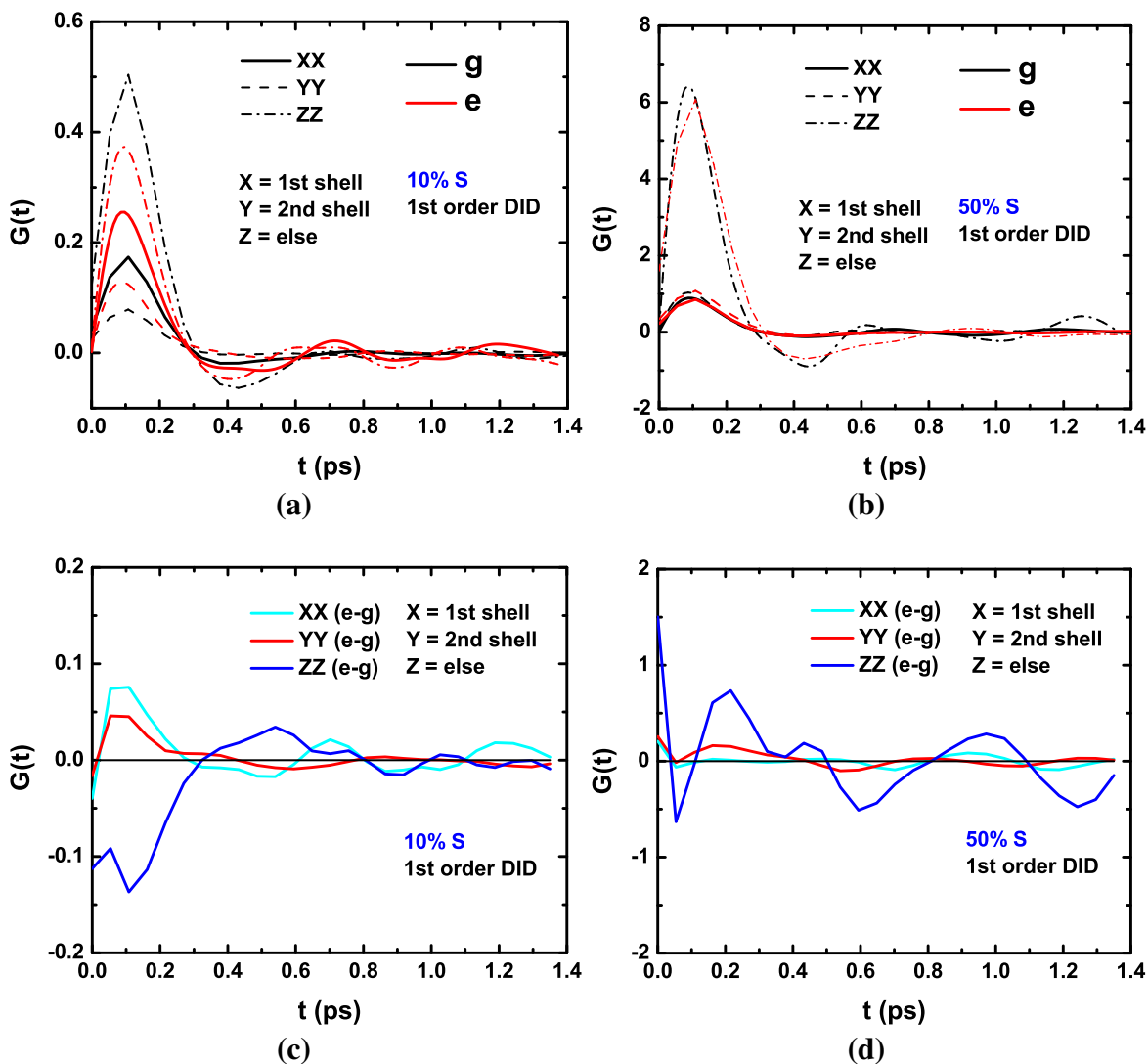


Figure 3.16 Polarizability-velocity correlation function $G(t)$ projected to first shell (X), second shell (Y) and else (Z) contributions. Shown are pure first-shell, second-shell and outer-shells components of $G(t)$ (unit σ^4/m). (a) 10% S solvent mixture, (b) 50% S solvent mixture, (c) e-g differences in 10% S solvent mixture and (d) e-g differences in 50% S solvent mixture. Results are computed by averaging 2500 liquid configurations.

tion method. We can apply projection operators on both a variable and its time derivative.

$$\dot{\mathbf{\Pi}}_X(t) = \hat{\mathbf{P}}_X \dot{\mathbf{\Pi}}(t) = \sum_{j \in X} \nabla_j \mathbf{\Pi}(t) \cdot \mathbf{v}_j(t), \quad (3.67)$$

$$\mathbf{\Pi}_X(t) = \hat{\mathbf{P}}_X \sum_{j=1}^N \boldsymbol{\pi}_j(t) = \sum_{j \in X} \boldsymbol{\pi}_j(t). \quad (3.68)$$

(1) Choosing partition X=1st shell and Y=else like in the previous section, we have

$$R(t) = R_{XX}(t) + R_{YY}(t) + R_{XY,YX}(t), \quad (3.69)$$

$$R_{XX}(t) = \langle \dot{\mathbf{\Pi}}_X(0) \otimes \mathbf{\Pi}_X(t) \rangle, \quad (3.70)$$

$$R_{YY}(t) = \langle \dot{\mathbf{\Pi}}_Y(0) \otimes \mathbf{\Pi}_Y(t) \rangle, \quad (3.71)$$

$$R_{XY,YX}(t) = \langle \dot{\mathbf{\Pi}}_X(0) \otimes \mathbf{\Pi}_Y(t) \rangle + \langle \dot{\mathbf{\Pi}}_Y(0) \otimes \mathbf{\Pi}_X(t) \rangle. \quad (3.72)$$

Figure 3.17 shows these time-domain OKE response functions with partitioning into the first shell and the outer shells. Performing a Fourier transformation on these responses, one gets the frequency-domain spectral densities which is plotted in Figure 3.18. From these frequency-domain spectra, the outer shells compose the largest contribution to the OKE spectral densities and the cross terms are negligible. The first-shell contributions are weighted differently in the two solvent mixtures: in 10% S, the first-shell contribution is modest, about a third of the largest outer-shells contribution; in 50% S, the first-shell contribution is comparable to the cross term which is less than 10% of the largest outer-shells contribution.

Key result here is that the change of first-shell contribution due to the $g \rightarrow e$ transition is noticeably larger than the other two contributions in 10% S mixture, whereas in 50% S mixture all three contributions contribute roughly the same amount in the frequency domain. The differences between the excited-state and ground-state spectral densities are shown in Figure 3.19. In both mixtures, the contributions of cross terms to the e–

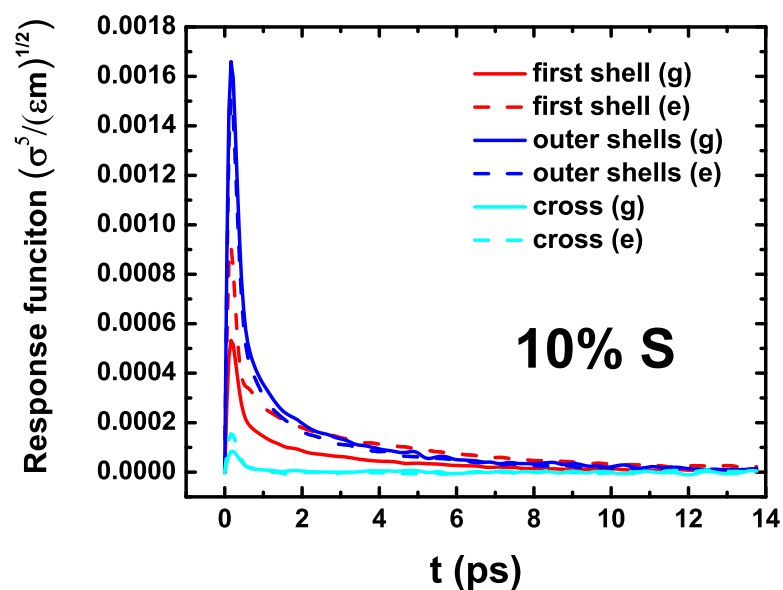
g difference are not negligible any more, and are likely to counteract the outer-shells contributions.

The frequency-domain results most relevant to ultrafast intermolecular dynamics though are the reduced spectral densities. Figure 3.20 shows the projection of OKE reduced spectral densities into the first shell and outer shells partition for 10% S and 50% S mixtures on equilibrated ground and excited states. Taking the e–g difference, we have the most important result of this section, Figure 3.21 presenting the projection of long waiting time limit solute-pump/solvent-probe spectra into first shell and outer shells. For the 10% S solvent mixture, the full e–g difference must be determined by the first shell contribution, at least for frequencies greater than 30 cm^{-1} , since the first-shell projection has the same positive sign as the full response (Figure 3.11). The outer-shells projection, on the other hand, is negative and is partially canceled by the cross term, which is easy to see in e–g differences of projected spectral densities in Figure 3.19. By contrast, for 50% S solvent mixture, the outer shells seem to be more important in that the outer shells have the largest contribution to the overall negative response ($30 \text{ cm}^{-1} - 70 \text{ cm}^{-1}$); the positive cross term partially cancels the first shell’s negative contribution.

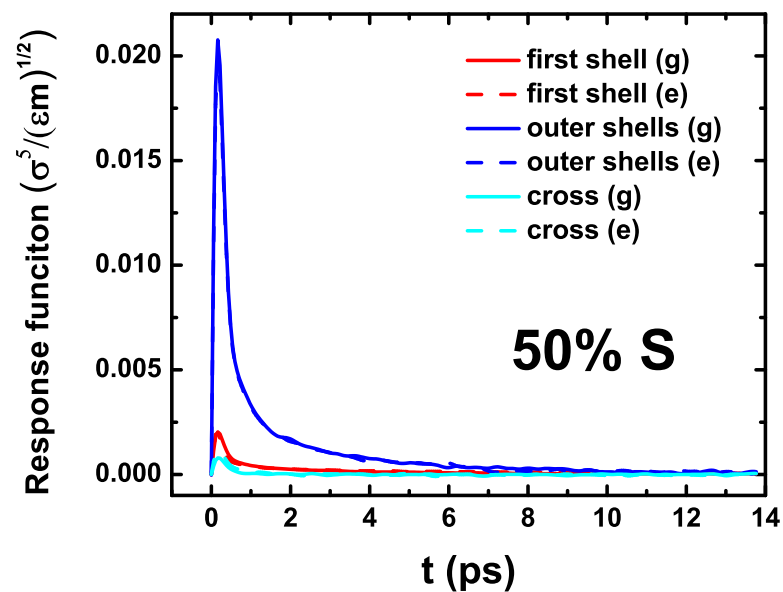
(2) Choosing partition X=1st shell, Y=2nd shell, Z=everything else, we have

$$R(t) = R_{XX}(t) + R_{YY}(t) + R_{ZZ}(t) + R_{XY,YX}(t) + R_{XZ,ZX}(t) + R_{YZ,ZY}(t). \quad (3.73)$$

Figure 3.22 shows the OKE spectral densities with partitioning into 1st shell, 2nd shell and else. One can observe that the “self” terms (R_{XX}, R_{YY}, R_{ZZ}) are less noisy than the cross terms ($R_{XY,YX}, R_{XZ,ZX}, R_{YZ,ZY}$) in both 10% S and 50% S solvent mixtures. Figure 3.23 shows the e–g difference spectra of these three “self” terms. These results are noisy due to much less averaging than the first-shell/outer-shells partitioning, but it is still useful in providing some qualitative hints. The first shell contribution reproduces the signs in Figure 3.21. The second shell contribution in 10% S is almost zero and in 50% S it has negative e–g

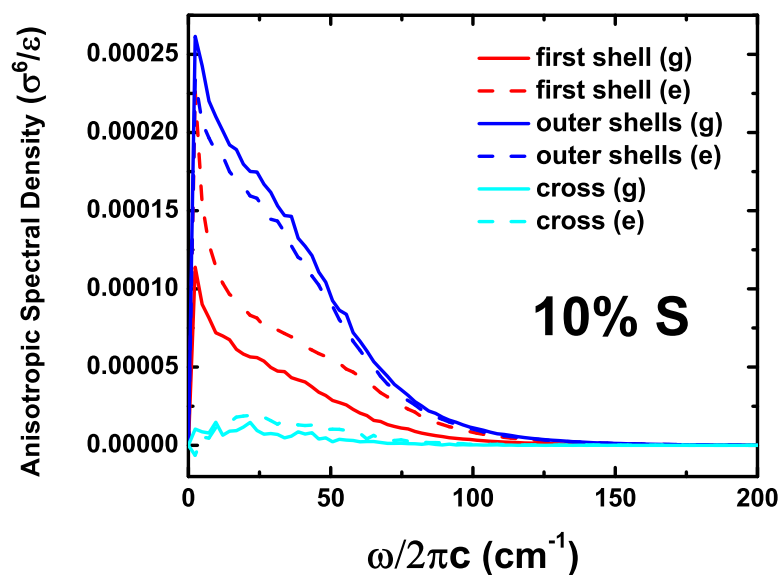


(a)

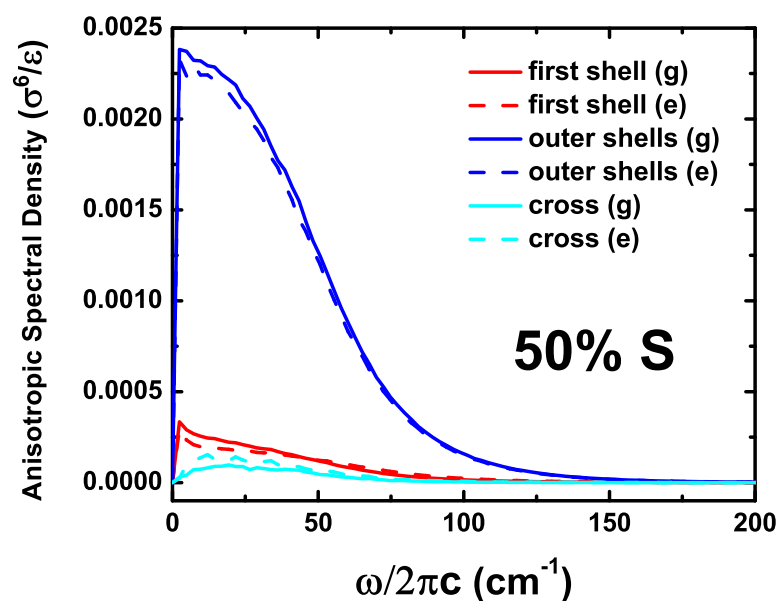


(b)

Figure 3.17 Projection of the OKE responses for 10% S and 50% S solvent mixtures into first-shell, outer-shells and cross contributions. The ground-state (g, solid lines) and excited-state (e, dashed lines) curves are computed with first-order DID polarizabilities and averaged over 5×10^5 and 2.5×10^6 liquid configurations for 10% S and 50% S solvent mixtures respectively.

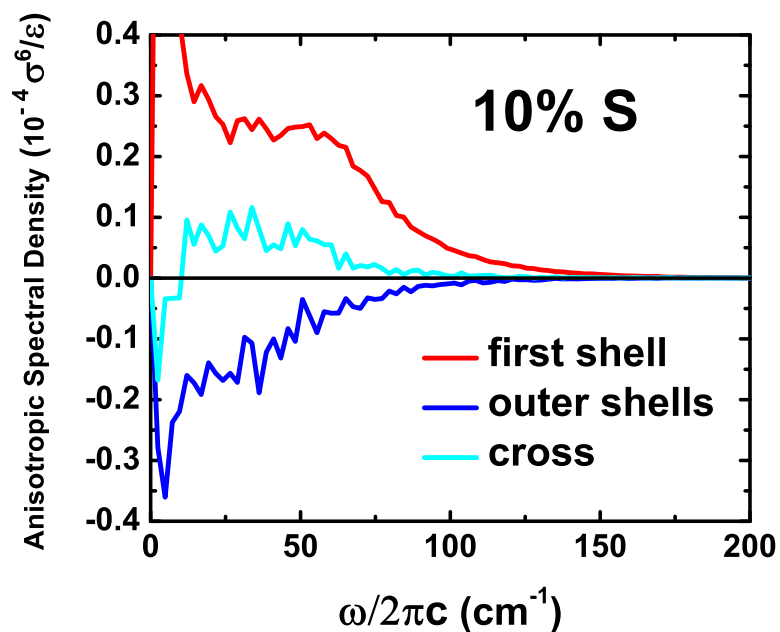


(a)

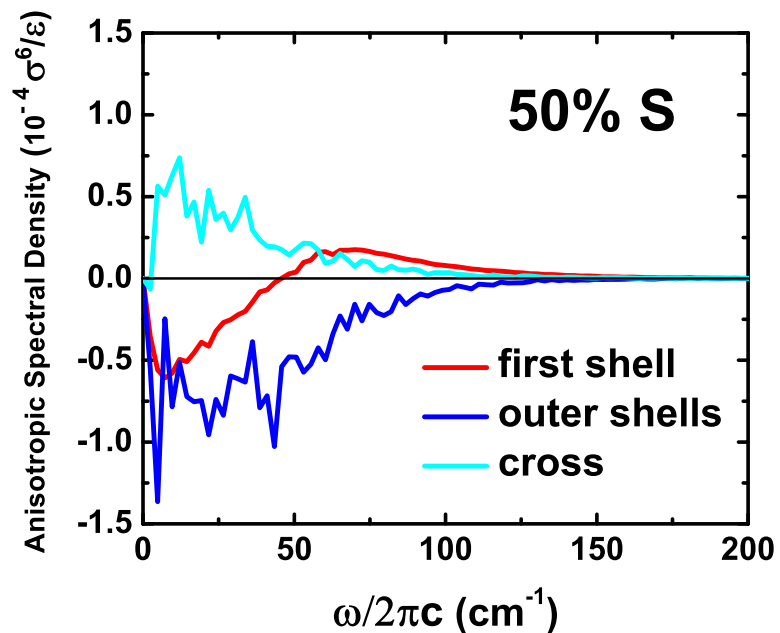


(b)

Figure 3.18 Projection of the OKE spectral densities for 10% S and 50% S solvent mixtures into first-shell, outer-shells and cross contributions. The ground-state (g, solid lines) and excited-state (e, dashed lines) spectral densities are computed with first-order DID polarizabilities and averaged over 5×10^5 and 2.5×10^6 liquid configurations for 10% S and 50% S solvent mixtures respectively.

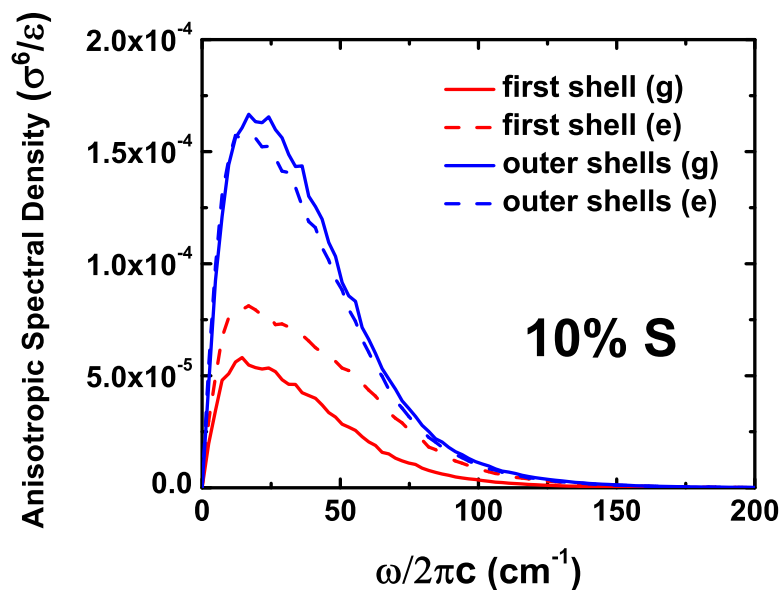


(a)

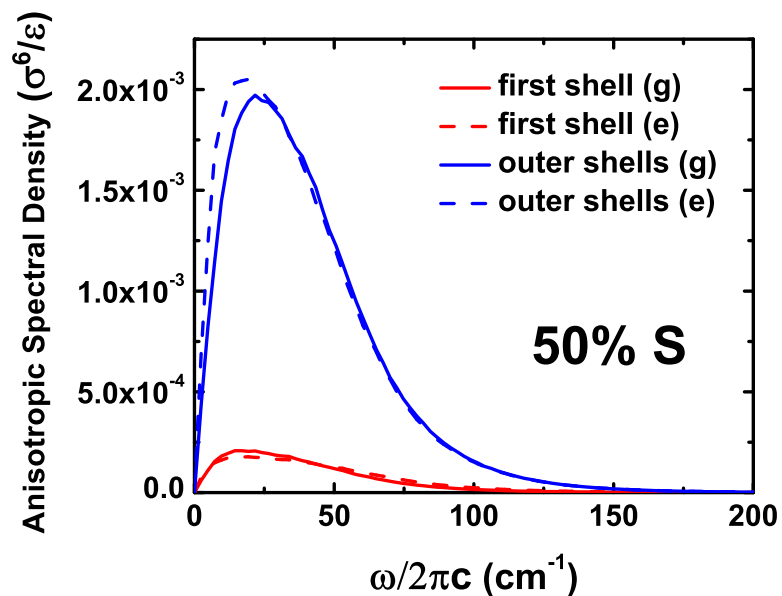


(b)

Figure 3.19 Projection of the e–g difference in spectral densities for 10% S and 50% S solvent mixtures into first-shell, outer-shells and cross contributions. The e–g differences are computed with first-order DID polarizabilities and averaged over 5×10^5 and 2.5×10^6 liquid configurations for 10% S and 50% S solvent mixtures respectively.



(a)



(b)

Figure 3.20 Projection of the OKE reduced spectral densities for 10% S and 50% S solvent mixtures into first-shell and outer-shells. The cross terms are not shown. The equilibrium ground (g) and excited (e) state OKE spectra are computed with first-order DID polarizabilities and averaged over 5×10^5 and 2.5×10^6 liquid configurations for 10% S and 50% S solvent mixtures respectively.

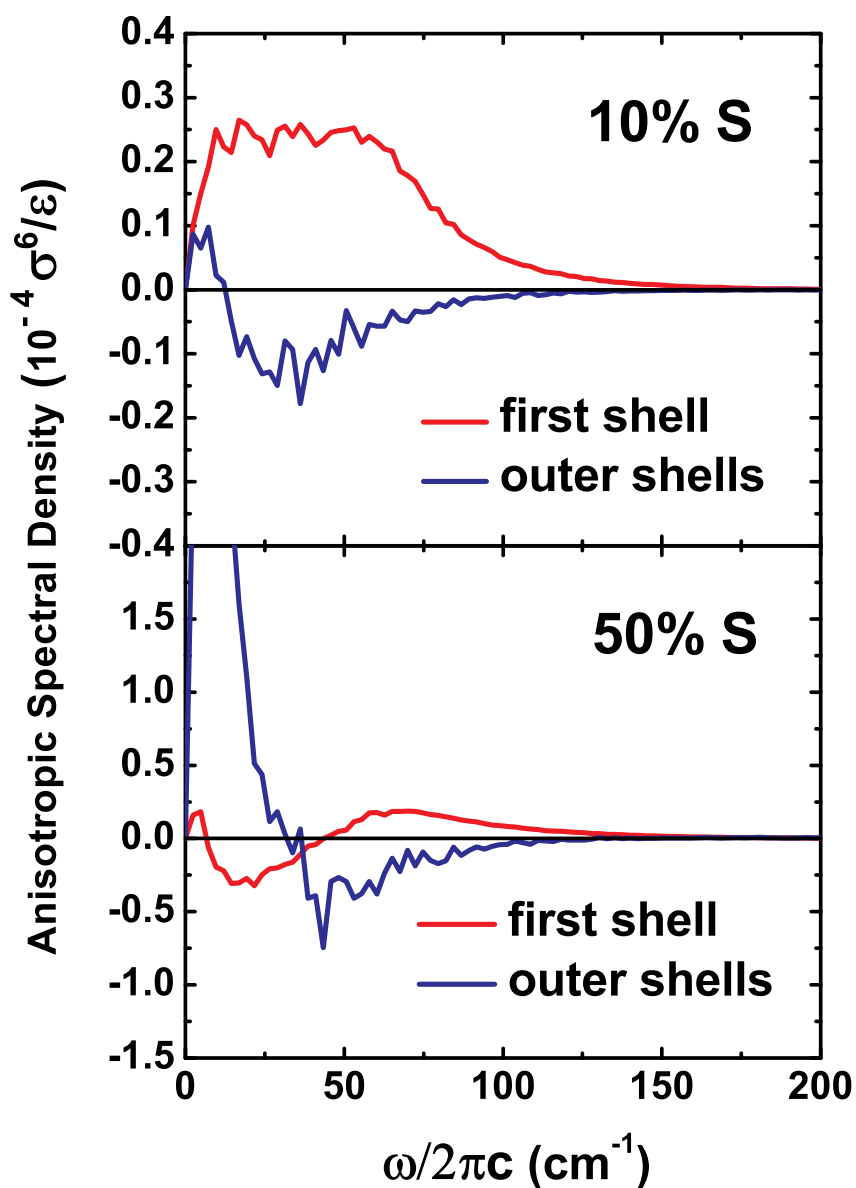


Figure 3.21 Projection of the long waiting time limit anisotropic solute-pump/solvent-probe spectra for 10% S and 50% S solvent mixtures into first-shell and outer-shells contributions. Cross terms are not shown. The long waiting time limit results are the e–g differences in the partitioned reduced spectral densities that are computed with first-order DID polarizabilities and averaged over 5×10^5 and 2.5×10^6 liquid configurations for 10% S and 50% S solvent mixtures, respectively.

difference below 25 cm^{-1} and positive e–g difference above 25 cm^{-1} , which is similar with the first shell behavior in Figure 3.21. Back to Figure 3.23, the outer-shells contribution (ZZ) to the e–g difference seems to have more negative data points than positive ones; these negative points serves as the major contribution for the negative total e–g difference spectra in frequency region $30 \text{ cm}^{-1} - 70 \text{ cm}^{-1}$. Thus, for 10% S mixture, the second shell contribution is almost zero and for 50% S mixture, the second shell resembles the first shell projection for frequency higher than 30 cm^{-1} and the outer shells determine the overall negative response for these high frequencies.

Finally after all the projection analysis we can conclude that in 10% S solvent mixture the first shell determines the total e–g difference, whereas in 50% S solvent mixture, all the solvation shells participate in determining the overall e–g difference.

Snapshot of the initial response

From previous analysis we know that the first order DID and solute(u)/S-solvent(v) interaction are important for the e–g difference. Thus, (uvuv) and (uvvv) terms defined below are the leading ingredients in the e–g difference spectrum.

$$(\boldsymbol{\alpha}_u \dot{\mathbf{T}}_{uj} \boldsymbol{\alpha}_j)_{t_1} \otimes (\boldsymbol{\alpha}_u \mathbf{T}_{uk} \boldsymbol{\alpha}_k)_{t_2}, j, k \in \text{S} \quad (\text{uvuv}) \text{ terms} \quad (3.74)$$

$$(\boldsymbol{\alpha}_u \dot{\mathbf{T}}_{uj} \boldsymbol{\alpha}_j)_{t_1} \otimes (\boldsymbol{\alpha}_k \mathbf{T}_{kl} \boldsymbol{\alpha}_l)_{t_2}, j, k, l \in \text{S} \quad (\text{uvvv}) \text{ terms} \quad (3.75)$$

We also know that in the 10% S the first shell is the most visible region in the difference spectra, but in 50% S system both the first shell and the outer shells have significant contributions to the overall e–g difference. We now step back and ask what are those most important terms contributing to the instantaneous value of response at time 0, $R(0)$,

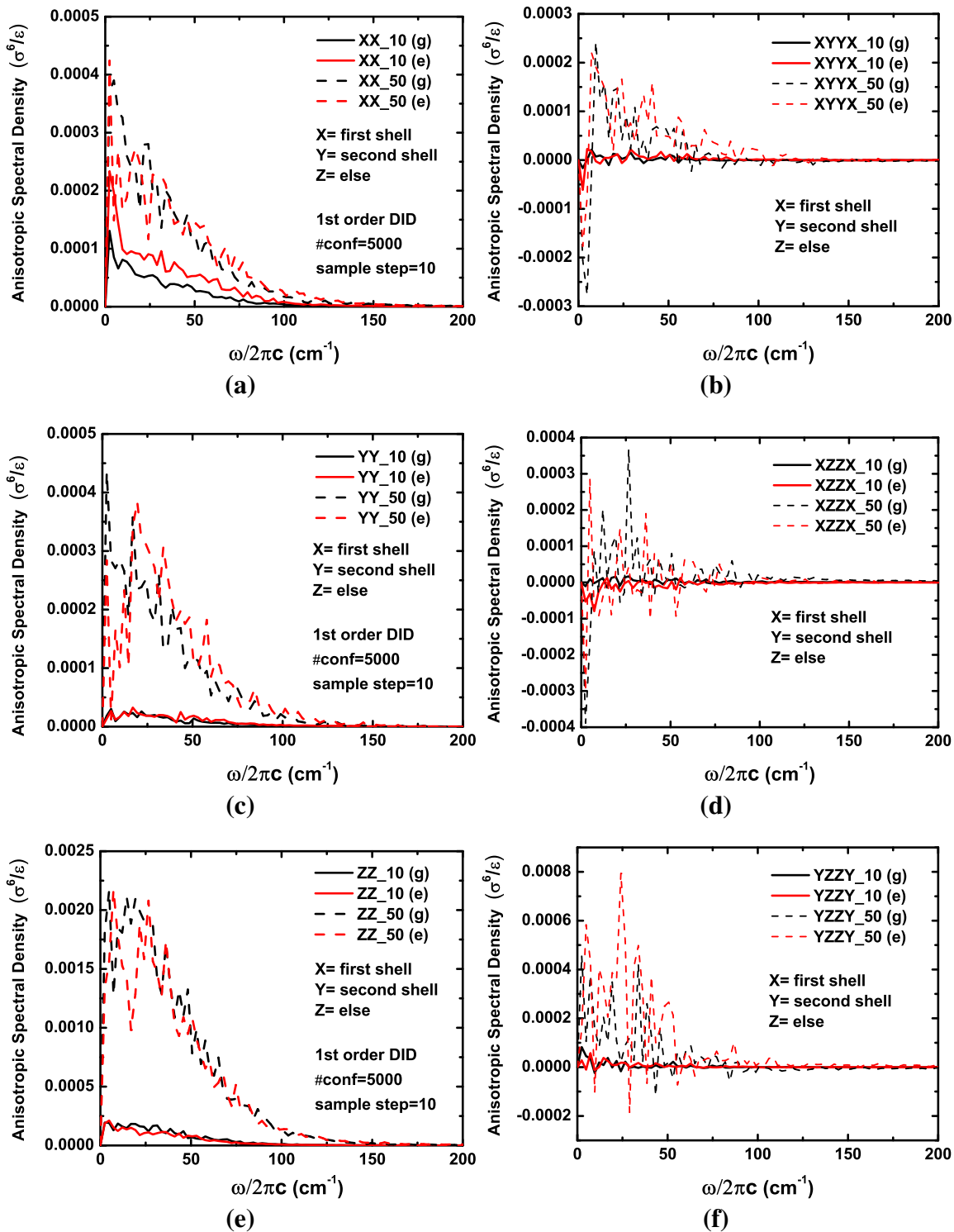


Figure 3.22 Projection of the OKE spectral densities for 10% S and 50% S solvent mixtures into first-shell (X), second-shell (Y) and outer-shells (Z) contributions. “Self” terms are shown on the left column and cross terms are shown on the right column. The spectral densities are computed with first-order DID polarizabilities and averaged over 5000 liquid configurations.

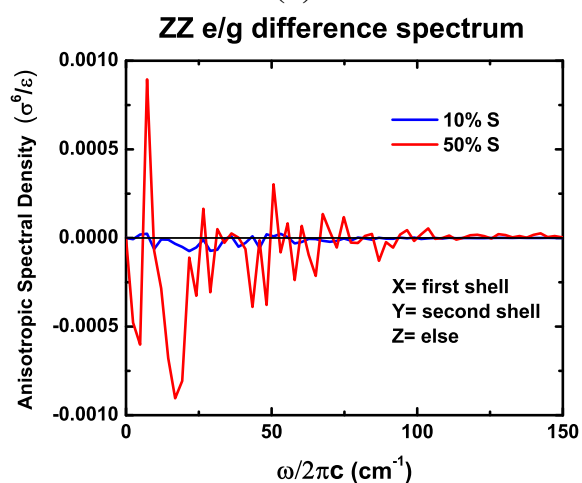
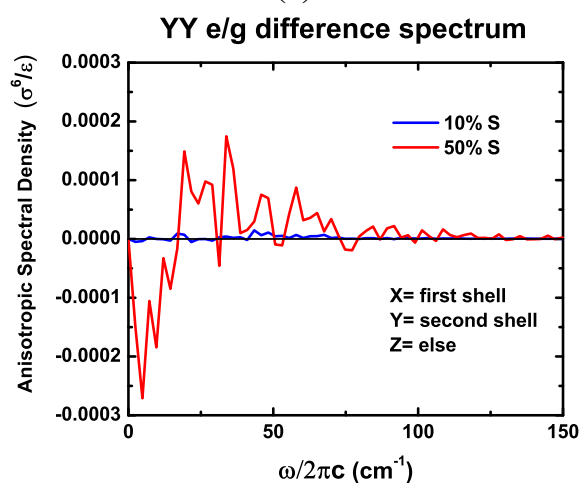
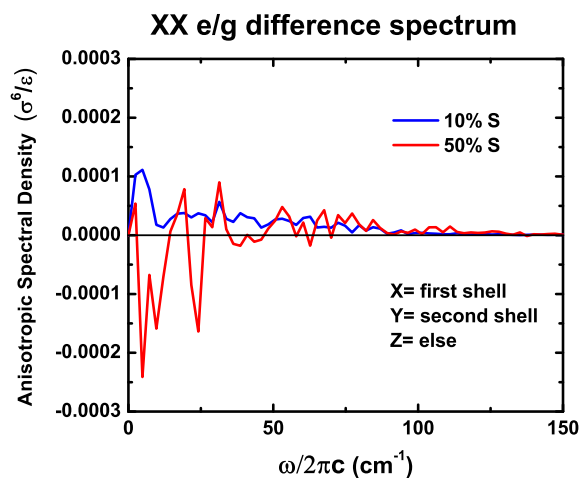


Figure 3.23 Projection of the e–g difference in spectral densities for 10% S and 50% S solvent mixtures into first-shell (a), second-shell (b) and outer-shells (c) contributions. The e–g differences are computed with first-order DID polarizabilities and averaged over 5000 liquid configurations.

for a single phase space point in the first shell to the first order DID.

$$R(0) = -\beta \frac{d}{dt} \mathbf{\Pi}(t) \otimes \mathbf{\Pi}(0) \Big|_{t=0} = -\beta \dot{\mathbf{\Pi}}(0) \otimes \mathbf{\Pi}(0) \quad (3.76)$$

$$= -\frac{\beta}{30} \left[3PP(\dot{\mathbf{\Pi}}(0), \mathbf{\Pi}(0)) - \text{Tr}(\dot{\mathbf{\Pi}}(0)) \cdot \text{Tr}(\mathbf{\Pi}(0)) \right]. \quad (3.77)$$

To the first order DID, the many-body polarizability and its time derivative are

$$\mathbf{\Pi}(t) = \sum_i \boldsymbol{\alpha}_i + \sum_{i \neq j} \boldsymbol{\alpha}_i \mathbf{T}_{ij} \boldsymbol{\alpha}_j, \quad (3.78)$$

$$\dot{\mathbf{\Pi}}(t) = \sum_{i \neq j} \boldsymbol{\alpha}_i \cdot \mathbf{T}_{ij} \boldsymbol{\alpha}_j. \quad (3.79)$$

So all the contributing terms to $k_B TR(0) = \dot{\mathbf{\Pi}}(0) \otimes \mathbf{\Pi}(0)$ are (u is the solute, v_i is solvent, and the sum of all particles in the first shell)

$$k_B TR(0) = \left(\boldsymbol{\alpha}_u \sum_{v_j} \dot{\mathbf{T}}_{uv_j} \boldsymbol{\alpha}_{v_j} + \sum_{v_i} \boldsymbol{\alpha}_{v_i} \sum_{v_j \neq v_i} \dot{\mathbf{T}}_{v_i v_j} \boldsymbol{\alpha}_{v_j} \right) \otimes \left(\sum_{v_i} \boldsymbol{\alpha}_{v_i} + \boldsymbol{\alpha}_u \sum_{v_k} \mathbf{T}_{uv_k} \boldsymbol{\alpha}_{v_k} + \sum_{v_k} \boldsymbol{\alpha}_{v_k} \sum_{v_l \neq v_k} \mathbf{T}_{v_k v_l} \boldsymbol{\alpha}_{v_l} \right) \quad (3.80)$$

$$\equiv \left(\sum_{v_j} \dot{\Pi}_{uv_j} + \sum_{v_i} \sum_{v_j \neq v_i} \dot{\Pi}_{v_i v_j} \right) \otimes \left(\sum_i \alpha_i + \sum_{v_k} \Pi_{uv_k} + \sum_{v_k} \sum_{v_l \neq v_k} \Pi_{v_k v_l} \right) \quad (3.81)$$

$$\begin{aligned} &= \sum_j \sum_k \Pi_{uvuv}(j; k) \\ &+ \sum_j \sum_k \sum_{l \neq k} \Pi_{uvvv}(j; k, l) \\ &+ \sum_i \sum_{j \neq i} \sum_k \Pi_{vvuv}(i, j; k) \\ &+ \sum_i \sum_{j \neq i} \sum_k \sum_{l \neq k} \Pi_{vvvv}(i, j; k, l), \end{aligned} \quad (3.82)$$

where $\dot{\Pi}_{ij} \otimes \sum_k \alpha_k \mathbf{1} = \alpha_i \alpha_j \sum_k \alpha_k \left[\frac{1}{10} \text{PP}(\dot{\mathbf{T}}, \mathbf{1}) - \frac{1}{30} \text{Tr}(\mathbf{T}) \text{Tr}(\dot{\mathbf{1}}) \right] = 0$ (see Equation 3.88). For instance, a typical number of particles in the first shell is 12, so (uvuv) has about 12^2 terms, (uvvv)/(vvuv) has 12^3 terms and (vvvv) has 12^4 terms. Listing all these terms in the indices order is tedious and pointless. Instead, sorting these terms based on their absolute value may give us some inspiration. So the largest 100 absolute values of each term tagged with their solvent indices for the four categories are sorted out. The largest 20 terms in each category for 10% S and 50% S on ground and excited states are listed in Appendix F. Table 3.5 is the summary of the dominant terms of each system.

	ground		excited	
10% S	$k_B TR(0) = -4 \times 10^{-3}$		$k_B TR(0) = -8.5 \times 10^{-4}$	
(uvuv)	$us_j us_j$	-9×10^{-4}	$us_j us_j$ & $us_k us_k$	-2×10^{-4}
(uvvv)	$us_j w_k s_j$	4×10^{-5}	$us_j w_k s_l$	-5×10^{-5}
(vvuv)	$s_j w_k us_j$	5×10^{-5}	$s_j w_k us_l$	-5×10^{-5}
(vvvv)	$s_j w_k s_j w_k$	-7×10^{-6}	$s_j w_k s_j s_l$	-1×10^{-5}
50% S	$k_B TR(0) = 2.6 \times 10^{-3}$		$k_B TR(0) = 2.8 \times 10^{-3}$	
(uvuv)	$us_j us_j$	-9×10^{-4}	$us_j us_j$	1.3×10^{-3}
	$us_k us_k$	6×10^{-4}		
(uvvv)	$us_j s_k s_l$	-5×10^{-4}	$us_j s_k s_l$	6×10^{-4}
(vvuv)	$s_j s_k us_j$	3×10^{-4}	$s_j s_k us_l$	3×10^{-4}
(vvvv)	$s_j s_k s_j s_k$	-2×10^{-4}	$s_j s_k s_j s_l$	-3×10^{-4}

Table 3.5 Summary of single snapshot analysis of $k_B TR(0)$ and its largest term(s) (unit in $\sigma^5 \cdot (\epsilon/m)^{1/2}$) of each category with “u” for the solute, “v” for a solvent. s and w stand for strong solvent and weak solvent with subscripts j, k, l to distinguish different solvent atoms. The same ground state equilibrium configuration is used in both 10% S and 50% S, and different excited equilibrium configurations are used in 10% S and 50% S. Details are included in Appendix F.

We can see that $k_B T \Delta R(0)$ of $g \rightarrow e$ transition are positive for both 10% S and 50% S, but the overall signs of $k_B TR(0)$ are negative for 10% S and positive for 50% S. The dominant term’s sign matches $k_B TR(0)$ ’s sign (a dominant term should be about a order of magnitude larger than the second largest contribution). More obviously in 10% S system, the leading contributions to $k_B TR(0)$ are solute/single-S-solvent terms ($us_j us_j$). First order

DID $us_j us_j$ term can be expressed analytically:

$$(\alpha_u \alpha_j \dot{\mathbf{T}}_{uj}) \otimes (\alpha_u \alpha_j \mathbf{T}_{uj}) = \alpha_u^2 \alpha_j^2 \left(\dot{\mathbf{T}}_{uj} \otimes \mathbf{T}_{uj} \right), \quad (j \in S). \quad (3.83)$$

Denoting the unit vector as $\hat{\mathbf{r}} = (e_x, e_y, e_z)$, we can express the dipole-dipole tensor as follows.

$$\begin{aligned} T_{\mu\nu}(t) &= \frac{\partial}{\partial r_\mu} \frac{\partial}{\partial r_\nu} \frac{1}{(x^2 + y^2 + z^2)^{1/2}} = \frac{3r_\mu r_\nu - r^2 \delta_{\mu\nu}}{r^5} \\ &= \frac{1}{r^3} (3e_\mu e_\nu - \delta_{\mu\nu}), \end{aligned} \quad (3.84)$$

where $\delta_{\mu\nu}$ is the Kronecker delta. The pair product and the trace of the dipole-dipole tensor are

$$\text{Tr}(\mathbf{T}(t)) = \sum_{\mu} T_{\mu\mu}(t) = \frac{1}{r^3} \sum_{\mu} (3e_\mu^2 - 1) = 0. \quad (3.85)$$

$$\begin{aligned} \text{PP}(\mathbf{T}(0), \mathbf{T}(0)) &= \sum_{\mu, \nu} T_{\mu\nu}(0) T_{\mu\nu}(0) = \frac{1}{r^6} \sum_{\mu, \nu} (9e_\mu e_\nu e_\mu e_\nu - 6e_\mu e_\nu \delta_{\mu\nu} + \delta_{\mu\nu}^2) \\ &= \frac{6}{r^6}. \end{aligned} \quad (3.86)$$

In addition, the time derivative of the dipole-dipole tensor is then

$$\dot{T}_{\mu\nu}(t) = \frac{d}{dt} \left(\frac{3r_\mu r_\nu - \delta_{\mu\nu}}{r^5} \right) = \frac{3}{r^5} (\dot{r}_\mu r_\nu + r_\mu \dot{r}_\nu) - \frac{15}{r^6} r_\mu r_\nu \dot{r} + \frac{3}{r^4} \delta_{\mu\nu} \dot{r}. \quad (3.87)$$

So the trace of the derivative of dipole-dipole tensor is

$$\text{Tr}(\dot{\mathbf{T}}) = \text{PP}(\dot{\mathbf{T}}, \mathbf{1}) = \sum_{\mu} \dot{T}_{\mu\mu} = \frac{\dot{r}}{r^4} (6 - 15 + 9) = 0. \quad (3.88)$$

The pair product of the derivative of dipole-dipole tensor is

$$\begin{aligned}
\text{PP}(\dot{\mathbf{T}}(0), \mathbf{T}(0)) &= \sum_{\mu, \nu} \left\{ \left[\frac{3}{r^5} (\dot{r}_\mu r_\nu + r_\mu \dot{r}_\nu) - \frac{15}{r^6} r_\mu r_\nu \dot{r} + \frac{3}{r^4} \delta_{\mu\nu} \dot{r} \right] \cdot \frac{3r_\mu r_\nu - r^2 \delta_{\mu\nu}}{r^5} \right\} \quad (3.89) \\
&= \sum_{\mu, \nu} \left\{ \frac{9}{r^{10}} (\dot{r}_\mu r_\mu r_\nu^2 + \dot{r}_\nu r_\nu r_\mu^2) - \frac{45}{r^{11}} r_\mu^2 r_\nu^2 \dot{r} + \frac{9}{r^9} r_\mu^2 \dot{r} \right. \\
&\quad \left. - \frac{3}{r^8} (2\dot{r}_\mu r_\mu) + \frac{15}{r^9} r_\mu^2 \dot{r} - \frac{3}{r^7} \delta_{\mu\nu}^2 \dot{r} \right\} \\
&= (2 \times 9 - 45 + 9 - 6 + 15 - 9) \frac{\dot{r}}{r^7} \\
&= -18 \frac{\dot{r}}{r^7}, \quad (3.90)
\end{aligned}$$

$$\text{where } \dot{r} = \frac{d}{dt} \sqrt{\sum_\gamma r_\gamma^2} = \frac{1}{2} \frac{1}{\sqrt{\sum_\gamma r_\gamma^2}} \cdot \sum_\gamma 2r_\gamma \dot{r}_\gamma = \frac{1}{r} \sum_\gamma r_\gamma \dot{r}_\gamma. \quad (3.91)$$

The instantaneous response function at time 0 is then

$$R(0) = -\frac{\beta}{10} \text{PP}(\dot{\mathbf{\Pi}}(0), \mathbf{\Pi}(0)) = \frac{9\beta}{5} \alpha_u^2 \alpha_S^2 \left(\frac{\dot{r}}{r^7} \right)_{r=\text{solute/S-solvent distance}} \quad (3.92)$$

The above equation can be rewritten in a more illuminating form.

$$R(0) = -\beta \frac{d}{dt} \left(\frac{3}{10} \alpha_u^2 \alpha_S^2 \frac{1}{r^6} \right). \quad (3.93)$$

This equation highlights the most important contributions to the magnitude of the initial response: $\alpha_u^2 \alpha_S^2$ reflects the importance of solute/single-S-solvent pairs, and fast decaying $1/r^6$ emphasizes the contribution from the innermost solvation shell.

3.5 Discussions

In this chapter, we have seen the long waiting time limit solute-pump/solvent-probe spectra for a preferential solvation model. In this limit, the solute-pump/solvent-probe spectra

is just the excited-state/ground-state OKE difference. The traditional OKE spectroscopy measures the entire liquid polarizability fluctuation, which cannot tell us about any local dynamical information. The OKE e–g difference spectra, on the other hand, emphasize the change of dynamics focusing on the nearby region around the solute. A striking feature of the e–g difference spectra is for 10% S system, the e/g difference is positive and flat; for 50% S system, the e–g difference is negative in low frequency region ($\omega/2\pi c < 75\text{cm}^{-1}$). Another interesting feature is above 75cm^{-1} , both systems have positive e–g difference, and 10% S is even larger than 50% S. To understand these, we turn off the solute’s polarizability (set as 0) and find that the e–g difference is almost zero; then we compare first order DID approximation with the exact infinite order DID approximation. The e–g difference remains even if the magnitude is smaller. So the e–g difference must primarily come from the solute–solvent interaction up to the first order DID.

Projection operators are used to selectively isolate the influence of certain physical degrees of freedom on a physical variable. The physical variable in our case is the many-body polarizability. Applying projection operator to correlation functions leads to different contributions made up with “self” terms and cross terms. The partition of degrees of freedom we choose here is (1) first shell and else, (2) first shell, second shell and else. The correlation functions we calculated are polarizability-velocity correlation function, $G(t)$ and the OKE response function, $R(t)$. It turns out that all components using both partitions of $G(t)$ or $R(t)$ of 10% S has a notable change after a transition from g to e. In frequency domain, projected e–g difference spectra show that first shell contribution qualitatively agrees with full e–g difference for 10% S solvent mixture. As for 50% S solvent mixture, the role of outer shells seems to be more substantial.

In order to have a closer look at the first shell polarizability interaction, we take a snapshot of first shell contributing terms to an instantaneous response $R(0)$ in the first order DID approximation. In the analyzed 10% S configuration, the dominant term in $k_B T R(0)$ determines magnitude of $k_B T R(0)$. The dominant term in 10% S system, if any, tends to be

a (us_jus_j) term, or instantaneous dipole-induced dipole interaction between the solute and the same strong solvent. The 50% S system is more likely to have multiple important terms or a dominant term involving the solute and two distinct solvents.

In brief, the solute/1st-shell-S-solvent term to the first order is essential to the OKE e–g difference spectra, especially for the 10% S mixture. The big question that still puzzles us is why the signs of e–g difference are different in 10% S and 50% mixtures.

To interpret the sign of e–g difference spectra in Figure 3.11, one have to reconsider exactly how many S solvents locate in the immediate vicinity of the solute in both solvent mixtures. According to the first shell solvent populations in 10% S and 50% S (Table 3.2), the average number of S solvent increases drastically from 1.3 S to 3.0 S in the 10% S mixture, and the average number of S solvent increases moderately from 6.2 S to 9.4 S in the 50% mixture. It is easy to understand that in 10% S, more than 100 percent rise in the population of bright S solvent leads to a gain in the spectra. In the 50% S, the number of S solvent only increases by 50%, not to mention that even on the ground state, the S solvent populates more than a half if the first shell. The relative population in the first shell is a key quantity. A typical total number in the first shell is 12–13 solvents, so for the 10% S mixture, the spectroscopic bright S solvent is a minority with the solute on whatever electronic state. But for 50% S mixture, the S solvent is about 3 times more population than the S solvent in the 10% S mixture, and is always a majority, which indicates that the first shell is crowded with spectroscopically bright atoms. Since we know the solute/S-solvent terms dominate the OKE response function, we have a general expression as follows

$$\begin{aligned} \langle \dot{\Pi}(0)\Pi(t) \rangle &= \left\langle \sum_{j,k} \dot{\pi}_j(0)\pi_k(t) \right\rangle \\ &\approx 4\alpha_u^2\alpha_S^2 \left\langle \sum_{j \in S} \dot{\mathbf{T}}(\mathbf{r}_{0j}(0)) \sum_{k \in S} \mathbf{T}(\mathbf{r}_{0k}(t)) \right\rangle. \end{aligned} \quad (3.94)$$

In the dilute S solvent case (10% S), the major contribution for the many-body polarizability

probably comes from two-body terms involving the solute and a single S solvent ($j = k$ terms); yet in a dense S solvent case (50% S), the major contribution for the response could come from three-body terms ($j \neq k$ terms).

A schematic illustration in Figure 3.24 helps us to think about the signs of the responses. It depicts typical arrangements of instantaneous dipoles in 10% S and 50% S mixtures. Although there is no permanent dipole in either the solute or the solvent in our model, instantaneous dipoles can exist in any atom. In the dilute S solvent case (10% S), the instantaneous dipole on an S solvent (μ_j) always tend to align with the instantaneous dipole on the solute (μ_0) in order to minimize the energy. By contrast, in the dense S solvent case (50% S), with a second S solvent, the minimum-energy arrangement can lead to instantaneous dipoles on two solvents pointing to opposite directions such that $\mu_j \cdot \mu_k < 0$. As a result of this partial cancellation, the many-body polarizability could become lower when the S solvent number increases in the 50% S case. Consequently, the e–g differences have opposite signs.

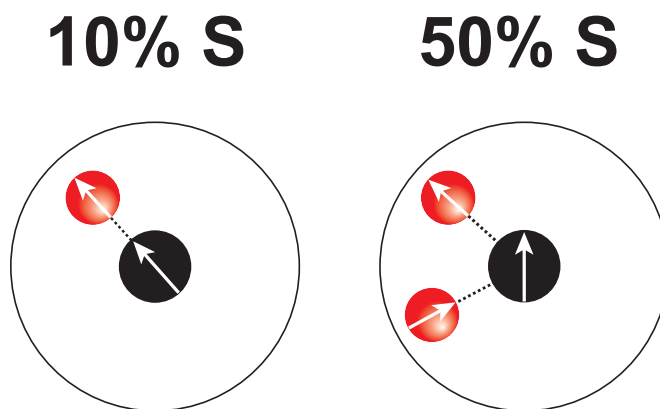


Figure 3.24 Illustration of how interaction-induced polarizabilities are affected by number of spectroscopic bright solvent, leading to sign changes in the solute-pump/solvent-probe spectra. When an instantaneous dipole is created in the solute (black circle), instantaneous dipoles induced in the most polarizable solvent (denotes as S, red circles) tend to have an arrangement that leads to a minimum energy. In the case of dilute S solvent (10% S), the dipole–dipole interaction results in aligned instantaneous dipoles on the solute and on the single S solvent, which results in a reinforced many-body polarizability. By contrast, in the case of dense S solvent (50% S), three-body solute-solvent-solvent triplets begin to be more important, inducing a diminished many-body polarizability since the unaligned instantaneous dipoles on solvents are partially canceled.

The following simple calculation is illustrative. As the average of the OKE response at time 0 vanishes, $\langle R(0) \rangle = 0$ since $\langle \dot{r} \rangle = 0$, we consider the integrated OKE correlation function $C(0)$ in the first order DID approximation. Again, the biggest contribution comes from the solute/S-solvent terms, so the integrated OKE correlation function is approximately

$$C(0) = \langle \Pi_{xz}(0) \Pi_{xz}(0) \rangle \approx 4\alpha_u^2 \alpha_S^2 \left\langle \sum_{j,k \in S} T_{xz}(\mathbf{r}_{0j}) T_{xz}(\mathbf{r}_{0k}) \right\rangle \quad (3.95)$$

$$= 36\alpha_u^2 \alpha_S^2 \left\langle \sum_{j,k \in S} \left(\frac{xz}{r^5} \right)_{\mathbf{r}_{0j}} \left(\frac{xz}{r^5} \right)_{\mathbf{r}_{0k}} \right\rangle \quad (3.96)$$

$$= \frac{36\alpha_u^2 \alpha_S^2}{r^6} \left\langle \sum_{j,k \in S} \overline{\hat{X}_{0j} \hat{Z}_{0j} \hat{X}_{0k} \hat{Z}_{0k}} \right\rangle. \quad (3.97)$$

In the 10% S case, consider only the solute and a single strong solvent j with distance r , we apply rotational averaging (using the notation defined in Appendix C) by integrating over all possible θ, ϕ for the solute–solvent displacement vector

$$\hat{\mathbf{r}}_{0j} = (\hat{X}_{0j}, \hat{Y}_{0j}, \hat{Z}_{0j})^T = (\sin \theta \cos \phi, \sin \theta \sin \phi, \cos \theta)^T. \quad (3.98)$$

The rotational average in this case is

$$\begin{aligned} \overline{(\hat{X}_{0j} \hat{Z}_{0j})^2} &= \overline{(\sin \theta \cos \phi \cdot \cos \theta)^2} \\ &= \frac{1}{4\pi} \int_0^{2\pi} d\phi \cdot \int_0^\pi d\theta \sin \theta (\sin \theta \cos \phi \cdot \cos \theta)^2 = \frac{1}{15}. \end{aligned} \quad (3.99)$$

Therefore,

$$C(0) = \frac{36\alpha_u^2 \alpha_S^2}{r^6} \left(\frac{1}{15} \right) > 0. \quad (3.100)$$

In the 50% S case, consider there is a solute-(solvent j)-(solvent k) equilateral triangle

in the first shell. We fix the angle between $\hat{\mathbf{r}}_{0j}$ and $\hat{\mathbf{r}}_{0k}$ as 60° and perform the rotational averaging. (Figure 3.25)

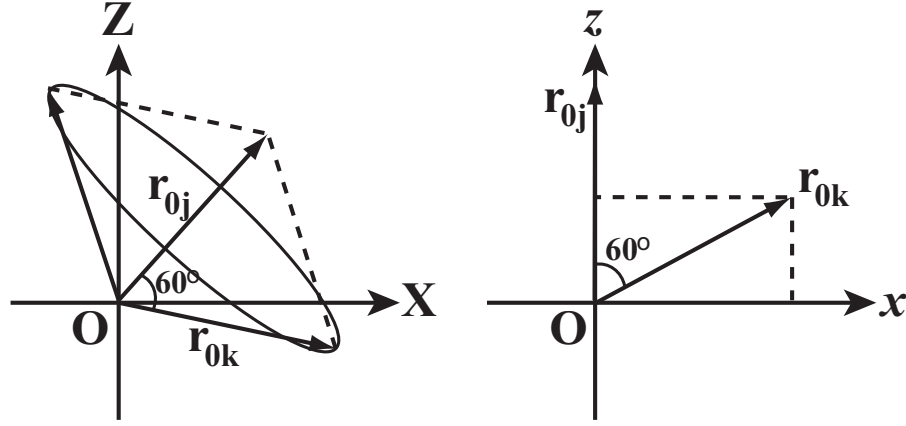


Figure 3.25 Rotational averaging of a solute-solvent-solvent equilateral triangle.

Still, $\hat{\mathbf{r}}_{0j}$ has two dimensional degrees of freedom, θ, ϕ . We can choose a fix point $\hat{\mathbf{r}}_{0k} = (\hat{x}_{0k}, \hat{y}_{0k}, \hat{z}_{0k})^T = (\sqrt{3}/2, 0, 1/2)^T$ that has a 60° angle with respect to z -axis in the molecule-frame xyz , then transform it into laboratory frame XYZ ,

$$\begin{pmatrix} \hat{X}_{0k} \\ \hat{Y}_{0k} \\ \hat{Z}_{0k} \end{pmatrix} = \begin{pmatrix} c\phi c\theta c\chi - s\phi s\chi & -c\phi c\theta s\chi - s\phi c\chi & c\phi s\theta \\ s\phi c\theta c\chi + c\phi s\chi & -s\phi c\theta s\chi + c\phi c\chi & s\phi s\theta \\ -s\theta c\chi & s\theta s\chi & c\theta \end{pmatrix} \begin{pmatrix} \hat{x}_{0k} \\ \hat{y}_{0k} \\ \hat{z}_{0k} \end{pmatrix}. \quad (3.101)$$

$\hat{\mathbf{r}}_{0k}$ has three degrees of freedom: θ, ϕ associated with solvent j and χ associated with the rotation along the $\hat{\mathbf{r}}_{0j}$ direction with a fixed 60° angle. The rotational average in this case

is

$$\begin{aligned} \overline{\hat{X}_{0j}\hat{Z}_{0j}\hat{X}_{0k}\hat{Z}_{0k}} &= \sin\theta \cos\phi \cdot \cos\theta \cdot \left[\frac{\sqrt{3}}{2}(\cos\phi \cos\theta \cos\chi - \sin\phi \sin\chi) \right. \\ &\quad \left. + \frac{1}{2} \cos\phi \sin\theta \right] \cdot \left[-\frac{\sqrt{3}}{2} \sin\theta \cos\chi + \frac{1}{2} \cos\theta \right] \\ &= -\frac{1}{120}. \end{aligned} \quad (3.102)$$

Therefore,

$$C(0) = \frac{36\alpha_u^2\alpha_S^2}{r^6} \left(-\frac{1}{120} \right) < 0. \quad (3.103)$$

Unlike the dilute 10% S system, in which the instantaneous dipole gets reinforced by just the solute/S-solvent pair, the instantaneous dipole in the more concentrated 50% S solution gets frustrated by the non-collinear solute/S-solvent/S-solvent arrangement within the first shell, resulting in a negative e-g difference distinct from that of the more dilute 10% S case. †

†Note: the polarization choice of YZYZ is equivalent to XZXZ by symmetry, checking $\overline{(\hat{Y}_{0j}\hat{Z}_{0j})^2} = 1/15$, and $\overline{\hat{Y}_{0j}\hat{Z}_{0j}\hat{Y}_{0k}\hat{Z}_{0k}} = -1/120$.

Chapter 4

Nonequilibrium Two-Dimensional Solute-Pump/Solvent-Probe Spectroscopy

4.1 Introduction

In the last chapter, we have seen the long waiting time limit ($T \rightarrow \infty$) of the solute-pump/solvent-probe spectra in our model atomic liquid mixtures; the response degenerates into the difference between the optical Kerr effect (OKE) spectra for a solution with an electronically excited solute and that with a ground-state solute. Even at this large T limit, the solute-pump/solvent-probe spectroscopy proves its capability at unveiling microscopic features of preferential solvation dynamics. The sign of the difference changes when the mole fraction of the solvent components is adjusted. Perhaps coincidentally, the sign change occurs in experimental long- T measurements as well, when different pure dipolar solvents are examined, displaying a sensitivity of the spectra to the specifics of the solvent.²²⁶ Figure 1.12 shows the first experimentally measured full two-dimensional (2D) solute-pump/solvent-probe spectra scanning both solvation time T and ultrafast dy-

namical time t , the resonant-pump polarizability response spectra (RP-PORS).²²⁷ This RP-PORS experiment is designed to detect the evolution of the solvent dynamics as structural relaxation proceeds during solvation. However, the 2D spectra still lack a molecular interpretation. Finding this interpretation is the primary aim of this chapter.

Most commonly used experimental avenues for probing solvation dynamics have been relying on the solute's energy gap as the indicator of the solvent's dynamics. For example, as discussed in chapter 1, traditional time-dependent fluorescence spectroscopy tells us about the relaxation of solvents around a newly excited dye solute by measuring the solute's red-shifting fluorescence emission frequency, which is equivalent to measuring the energy gap between the excited-state-solute and ground-state-solute potentials.^{2, 83, 246} Moreover, alternative photon-echo route into solvation dynamics such as 3-pulse photon echo peak shift (3PEPS) tracks the same solute-solvent interaction energy following an electronic excitation of the solute.^{141, 172, 176, 177, 282}

How much does the evolution of the energy gap disclose the full dynamics of solvent structural rearrangement? Since different solvent structures may share common solute-solvent interaction energies, the time scale for solvent structural relaxation may or may not be the same as that for the energetic relaxation. For example, consider the situation that the solute-solvent interaction energy is dominated by solvents in the first shell, yet the solvent molecules in the outer shells needed more time to reorganize even after the first-shell equilibrium solute-solvent organization is achieved. Any energy-gap spectroscopy would lead to a potential-energy relaxation that is faster than the actual full structural relaxation. On the contrary, if considerable rearrangement in the outer shells were needed before the first shell starts its own repositioning, the energetic spectroscopy would display a potential-energy relaxation that is slower than most of the structural relaxation.

The solute-pump/solvent-probe spectroscopy, on the other hand, grants a possibility of directly monitoring the solvent structure following a resonant solute excitation, and thus could serve as a 2D solvation spectroscopy. This spectroscopy is essentially a nonequi-

librium four-wave-mixing light scattering measurement. A resonant electronic excitation in the solute triggers the solvation, and the four-wave-mixing spectra are measured at a time T later. The nonresonant four-wave-mixing light scattering employs the many-body polarizability as the observable that is sensitive to the intermolecular distances between all the spectroscopically bright species, not just the solute-solvent distances, and thus may be more responsive to solvent structure than energy-gap spectroscopies.

As briefly mentioned in chapter 2, the practical difficulty of calculating the full solute-pump/solvent-probe spectra lies in the evaluation of the classical Poisson bracket. In the following sections of this chapter, a hybrid method using a combination of molecular dynamics and instantaneous-normal-mode theory to evaluate the 2D response will be described. The full 2D spectra for our previously studied preferential solvation model will be shown, as well as a molecular analysis on what information can be extracted from the them. Finally we offer some general discussions on the utility of the hybrid method to two-dimensional spectroscopic responses.

4.2 Instantaneous-Normal-Mode (INM) Theory

The idea behind instantaneous normal modes is stated in chapter 1. The INM theory works well in predicting short-time dynamics in liquids and also can provide a practical approach to evaluating the classical Poisson bracket,²⁰ which is a computational challenge in our calculation of the solute-pump/solvent-probe spectra. The independent harmonic nature of the INMs makes the Poisson bracket easy to evaluate. In the current section, we will familiarize ourselves with the notations and then discuss the connection of INM theory to the OKE spectra through the INM influence spectra. The INM predictions on OKE spectra for the previously studied preferential solvation model will be demonstrated to have a good agreement with the exact MD result.

4.2.1 Mass-weighted INM

The instantaneous-normal-mode theory treats the microscopic short-time liquid⁹ and cluster⁶ dynamics as a set of independent simple harmonic motions. For example, for an atomic liquid with N atoms, the classical Hamiltonian can be written as

$$H(\mathbf{R}, \dot{\mathbf{R}}) = \sum_{j=1}^N \frac{1}{2} m_j \dot{r}_j^2 + V(\mathbf{R}), \quad (4.1)$$

where \mathbf{R} is the complete set of $3N$ coordinates $\mathbf{R} = \{\mathbf{r}_1, \dots, \mathbf{r}_N\}$. The coordinate dimensionality is $5N$ (including $2N$ rotational coordinates) for rigid linear molecules¹⁶ or $6N$ (including $3N$ rotational coordinates) for rigid nonlinear molecules.^{20,283} In the mass-weighted approach of INM theory that provides a general description on systems with multiple atom types, we define the mass-weighted coordinates as

$$\mathbf{Z} = \{z_{j\mu}; j = 1, \dots, N; \mu = x, y, z\}, \quad z_{j\mu} = \sqrt{m_j} r_{j\mu}. \quad (4.2)$$

If denote diagonal mass matrix $\mathbf{M} = \text{diag}\{m_1, m_1, m_1, m_2, m_2, m_2, \dots, m_N, m_N, m_N\}$, in the case of pure atomic liquid, $\mathbf{M} = m\mathbf{1}$, with $\mathbf{1}$ the $3N \times 3N$ identity matrix and m the atom mass. Then the mass-weighted coordinates can be written as

$$\mathbf{Z} = \mathbf{M}^{1/2} \cdot \mathbf{R}. \quad (4.3)$$

Assuming that the time t is short enough, the Hamiltonian at time t can be expand about initial configuration \mathbf{R}_0 ,⁷

$$H \approx \frac{1}{2} \dot{\mathbf{Z}}_t \cdot \dot{\mathbf{Z}}_t + V(\mathbf{Z}_0) - \mathbf{F}(\mathbf{R}_0) \cdot (\mathbf{Z}_t - \mathbf{Z}_0) + \frac{1}{2} (\mathbf{Z}_t - \mathbf{Z}_0) \cdot \mathbf{D}(\mathbf{R}_0) \cdot (\mathbf{Z}_t - \mathbf{Z}_0), \quad (4.4)$$

where except for the first kinetic energy term, the right-hand side is the potential energy.

The instantaneous force vector is defined as

$$\mathbf{F}_{j\mu}(\mathbf{R}_0) = - \left. \frac{\partial V}{\partial z_{j\mu}} \right|_{\mathbf{R}_0} = - \frac{1}{\sqrt{m_j}} \left. \frac{\partial V}{\partial r_{j\mu}} \right|_{\mathbf{R}_0}, \quad (4.5)$$

and the dynamical (instantaneous Hessian) matrix is defined as

$$\mathbf{D}_{j\mu, kv}(\mathbf{R}_0) = \left. \frac{\partial^2 V}{\partial z_{j\mu} \partial z_{kv}} \right|_{\mathbf{R}_0} = \frac{1}{\sqrt{m_j m_k}} \left. \frac{\partial^2 V}{\partial r_{j\mu} \partial r_{kv}} \right|_{\mathbf{R}_0}. \quad (4.6)$$

If the orthogonal matrix $\mathbf{U}(\mathbf{R}_0)$ can diagonalize the real symmetric dynamical matrix,

$$\mathbf{UDU}^T = \begin{pmatrix} \omega_1^2 & & & \\ & \omega_2^2 & & \\ & & \ddots & \\ & & & \omega_{3N}^2 \end{pmatrix}, \quad (4.7)$$

where ω_α are frequencies of the α -th INM $q_\alpha(t; \mathbf{R}_0)$. The mutually independent INMs are the eigenvectors as follows

$$q_\alpha(t; \mathbf{R}_0) = [\mathbf{U}(\mathbf{R}_0) \cdot (\mathbf{Z}_t - \mathbf{Z}_0)]_\alpha, \quad (\alpha = 1, \dots, 3N), \quad (4.8)$$

whose conjugate momenta are

$$p_\alpha(t; \mathbf{R}_0) = [\mathbf{U}(\mathbf{R}_0) \cdot (\dot{\mathbf{Z}}_t - \dot{\mathbf{Z}}_0)]_\alpha, \quad (\alpha = 1, \dots, 3N). \quad (4.9)$$

The INMs compose the optimum basis for describing the short-time dynamics, and the

transformation matrix to the Cartesian coordinate is

$$\mathbf{U}_{\alpha,j\mu}(\mathbf{R}_0) = \frac{\partial q_\alpha}{\partial z_{j\mu}} = \frac{1}{\sqrt{m_j}} \frac{\partial q_\alpha}{\partial r_{j\mu}}, \quad (4.10)$$

$$\mathbf{U}_{kv,\beta}^T(\mathbf{R}_0) = \frac{\partial z_{kv}}{\partial q_\beta} = \sqrt{m_k} \frac{\partial r_{kv}}{\partial q_\beta}. \quad (4.11)$$

The instantaneous forces associated with each mode α are

$$f_\alpha = [\mathbf{U}(\mathbf{R}_0) \cdot \mathbf{F}(\mathbf{R}_0)]_\alpha. \quad (4.12)$$

Now the potential energy can be written in the INM basis as

$$V(\mathbf{R}_t) \approx V(\mathbf{R}_0) + \sum_{\alpha=1}^{3N} \left[-f_\alpha q_\alpha(t) + \frac{1}{2} \omega_\alpha^2 q_\alpha^2(t) \right], \quad (4.13)$$

$$\text{where } q_\alpha(t) = \frac{f_\alpha}{\omega_\alpha^2} (1 - \cos \omega_\alpha t) + \frac{v_\alpha(0)}{\omega_\alpha} \sin \omega_\alpha t, \quad (4.14)$$

$$v_\alpha(t) = \dot{q}_\alpha(t) = v_\alpha(0) \cos \omega_\alpha t + \frac{f_\alpha}{\omega_\alpha} \sin \omega_\alpha t. \quad (4.15)$$

So we have the dynamics of a liquid that is governed by INMs at short times,

$$r_{j\mu}(t) = r_{j\mu}(0) + \frac{1}{\sqrt{m_j}} \sum_{\alpha} \mathbf{U}_{j\mu,\alpha}^T q_\alpha(t). \quad (4.16)$$

In other words, one would only need to know the probability distribution of the set of f_α , ω_α , and $v_\alpha(0)$ so as to know the complete dynamics of a liquid in a short time scale.

The instantaneous normal mode spectrum is the density of states of a liquid (or the phonon spectrum), i.e. the distribution of instantaneous normal mode frequencies averaged over liquid configurations,

$$D(\omega) = \left\langle \frac{1}{3N} \sum_{\alpha=1}^{3N} \delta(\omega - \omega_\alpha) \right\rangle. \quad (4.17)$$

The density of states is normalized such that the integral

$$\int d\omega D(\omega) = 1, \quad (4.18)$$

and for us the unit of $D(\omega)$ is $1/[\omega] = 1/\text{cm}^{-1} = \text{cm}$.

4.2.2 INM density of states in liquid argon

In chapter 1, the INM spectrum of liquid argon is shown (Figure 1.1). Here we show some related details starting from looking closer at the structure of the dynamical matrix \mathbf{D} . If our system has N atoms with identical mass m , interactions between which are described by pair potential $u(r)$, then the 3×3 dynamical matrix for a pair of atoms i and j is defined as $\mathbf{D}_{\mu,\nu}(i,j) = \mathbf{D}_{i\mu,j\nu}$, and in tensor form,⁵

$$\mathbf{D}(i,j) = \frac{1}{m} \nabla_i \nabla_j V(\mathbf{R}(0)) = \frac{1}{m} \cdot \begin{cases} \sum_{k \neq i} \mathbf{t}(\mathbf{r}_{ik}), & i = j \\ -\mathbf{t}(\mathbf{r}_{ij}), & i \neq j \end{cases}, \quad (4.19)$$

$$\mathbf{t}(\mathbf{r}) = [u'(r)/r] \mathbf{1} + [u''(r) - u'(r)/r] \hat{\mathbf{r}} \hat{\mathbf{r}}. \quad (4.20)$$

In practice, liquid argon is modeled by molecular dynamics simulation in which there are 256 argon atoms under thermal conditions of temperature $k_B T / \varepsilon = 1.00$ and density $\rho \sigma^3 = 0.80$. The potential energy is the sum of pair potentials between each pair of atoms, and the pair potential used here is the Lennard-Jones potential,

$$V(\mathbf{R}) = \sum_{i < j} u(r_{ij}) = \sum_{i < j} 4\varepsilon_{ij} \left[(\sigma/r_{ij})^{12} - (\sigma/r_{ij})^6 \right]. \quad (4.21)$$

The dynamical matrix is then

$$\begin{aligned}
[\mathbf{D}(t)]_{i\mu, j\nu} &= \frac{1}{m} \frac{\partial^2 V(t)}{\partial r_{i\mu}(t) \partial r_{j\nu}(t)} & (4.22) \\
&= \delta_{ij} \frac{1}{m} \sum_{k \neq i} 4\varepsilon_{ik} \left[\left(168 \cdot \frac{\sigma^{12}}{r_{ik}^{16}} - 48 \cdot \frac{\sigma^6}{r_{ik}^{10}} \right) (r_{i\mu} - r_{k\mu})(r_{i\nu} - r_{k\nu}) \right. \\
&\quad \left. + \left(-12 \cdot \frac{\sigma^{12}}{r_{ik}^{14}} + 6 \cdot \frac{\sigma^6}{r_{ik}^8} \right) \delta_{\mu\nu} \right] \\
&\quad - (1 - \delta_{ij}) \frac{1}{m} 4\varepsilon_{ij} \left[\left(168 \cdot \frac{\sigma^{12}}{r_{ij}^{16}} - 48 \cdot \frac{\sigma^6}{r_{ij}^{10}} \right) (r_{i\mu} - r_{j\mu})(r_{i\nu} - r_{j\nu}) \right. \\
&\quad \left. + \left(-12 \cdot \frac{\sigma^{12}}{r_{ij}^{14}} + 6 \cdot \frac{\sigma^6}{r_{ij}^8} \right) \delta_{\mu\nu} \right]. & (4.23)
\end{aligned}$$

Periodic boundary condition and minimum image convention are utilized in calculating forces and dynamical matrices.²⁸⁴

There are two fundamentally equivalent ways to calculate the INM spectrum; the first one is to bin the INM frequencies into a histogram (the discrete method to evaluate the average of a delta function) and the other way is applying the same approach to the dynamical matrix eigenvalues and then convert the distribution of eigenvalues into that of frequencies. We denote the eigenvalues of dynamical matrix as $\lambda_\alpha = \omega_\alpha^2$. From the normalization condition of the distribution of eigenvalues, we can derive the relation between the frequency distribution and the eigenvalue distribution:

$$\begin{aligned}
1 &= \int d\lambda \rho(\lambda) \\
&= \int d\omega 2\omega \cdot \rho(\lambda = \omega^2) \\
&= \int d\omega D(\omega), \\
\therefore D(\omega) &= 2\omega \cdot \rho(\lambda = \omega^2). & (4.24)
\end{aligned}$$

The INM spectrum using the frequency histogram (200 bins) is shown in Figure 4.1, the comparison with zero frequency removed INM spectrum is shown in Figure 4.2 and the distribution of eigenvalues is shown in Figure 4.3. The comparison of frequency-binning and eigenvalue-binning is shown in Figure 4.4.

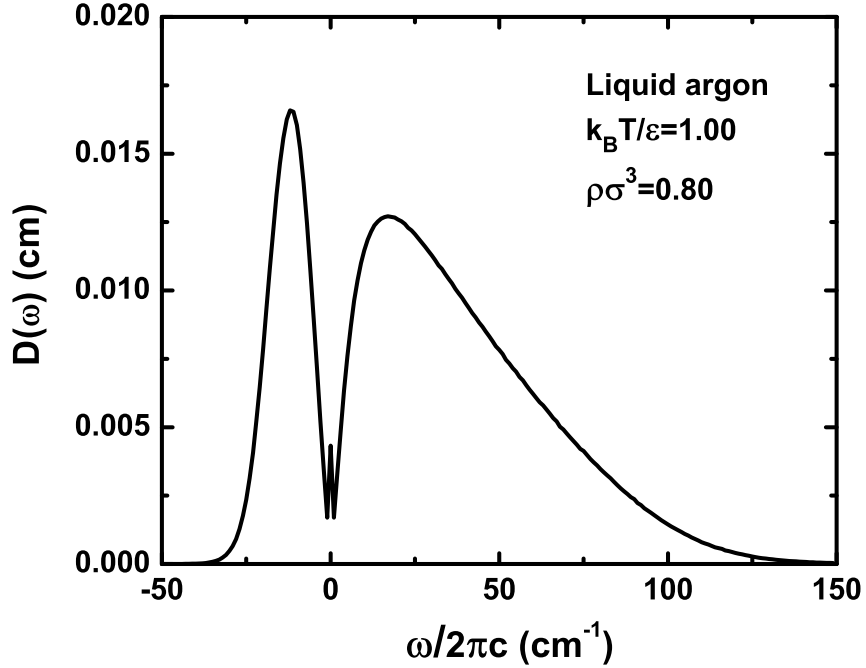


Figure 4.1 Instantaneous-normal-mode spectrum (density of states) of liquid Ar at temperature $k_B T/\epsilon = 1.00$ and density $\rho\sigma^3 = 0.80$ averaged 20,000 configurations. The imaginary frequencies are plotted on the negative frequency axis. Note that there is a small peak at zero frequency, corresponding to the three translational modes.

Notice that in simulation, the LJ reduced unit is used with the argon reference temperature $\epsilon/k_B=119.8$ K, length $\sigma=3.405$ Å and mass $m_{Ar}=40.0$ amu.²⁸⁴ Any quantity using the reduced unit is indicated by a star superscript.

$$m^* = m/m_{Ar} = 1, \quad (4.25)$$

$$\omega^* = \omega\tau_{LJ}, \quad (4.26)$$

$$\lambda^* = \frac{\omega^{*2}}{1/\tau_{LJ}^2} = \frac{\lambda}{\epsilon/(m_{Ar}\sigma^2)}. \quad (4.27)$$

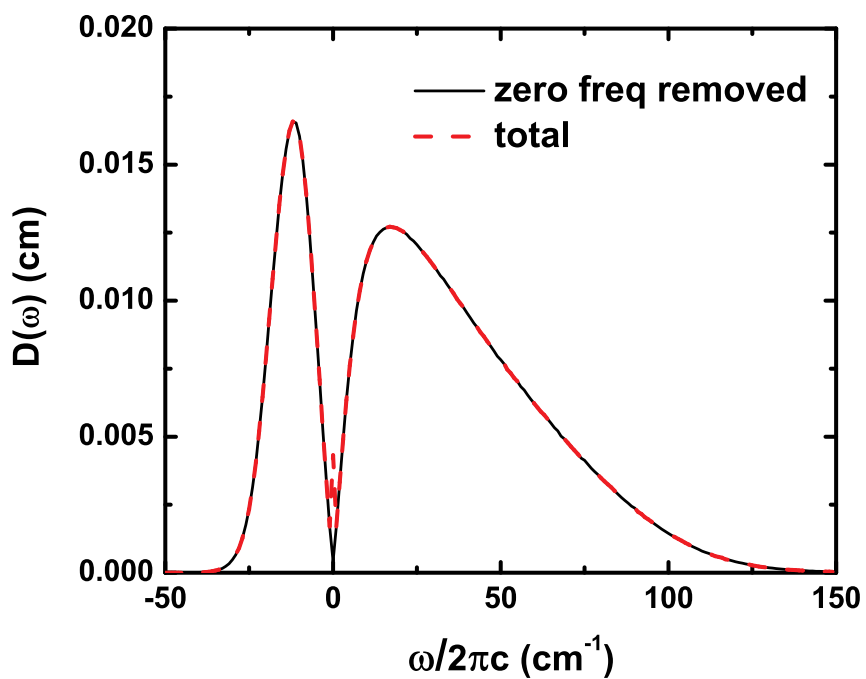


Figure 4.2 Instantaneous-normal-mode spectrum (density of states) of liquid Ar with (black, solid) and without zero frequencies removed (red, dashed). The simulation is performed at temperature $k_B T / \varepsilon = 1.00$ and density $\rho \sigma^3 = 0.80$ and 20,000 configurations are averaged. The imaginary frequencies are plotted on the negative frequency axis. When the three zero-frequency translational modes are not counted in histogram, the small peak at zero frequency vanishes leading to a continuous smooth INM spectrum.

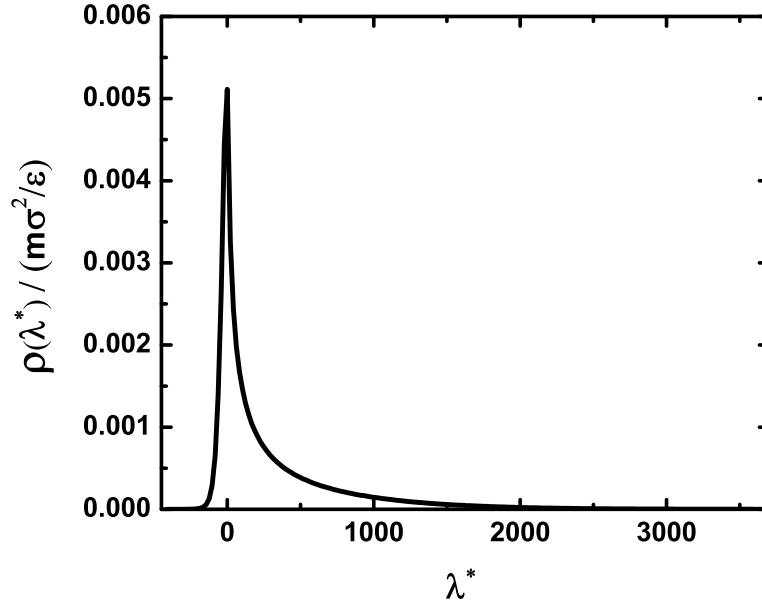


Figure 4.3 Distribution of eigenvalues of the dynamical matrix for liquid Ar at temperature $k_B T / \epsilon = 1.00$ and density $\rho \sigma^3 = 0.80$ averaged 20,000 configurations. Eigenvalue is in Lennard-Jones reduced units.

Finally we usually convert frequency unit to wavenumbers (cm^{-1}) as is commonly done in spectroscopies and the conversion rule is as follows

$$\tilde{\nu}(\text{cm}^{-1}) = \frac{\omega}{2\pi c} = \frac{\omega^*}{2\pi c \tau_{LJ}} = \omega^* \cdot \frac{3.33565 \times 10^{-11} (\text{cm}^{-1}/\text{Hz})}{2\pi \cdot 2.1560 \times 10^{-12} (\text{s})} = \omega^* \times 2.4578 (\text{cm}^{-1}). \quad (4.28)$$

Check simulations

The matrix diagonalization is performed by a Fortran library LAPACK.²⁸⁵ To make sure the simulation is correct and the INM indexing is right, one has to check some properties of the INMs. Those checks are listed below.

- (1) The sum of elements of any row or column of the dynamical matrix is zero. $\sum_k \mathbf{D}(j, k) = \sum_k \mathbf{D}(k, j) = \mathbf{0}$. I checked sum of one row is zero ($< 10^{-13}$).
- (2) Three zero eigenvalues corresponding to three zero-frequency translational modes.

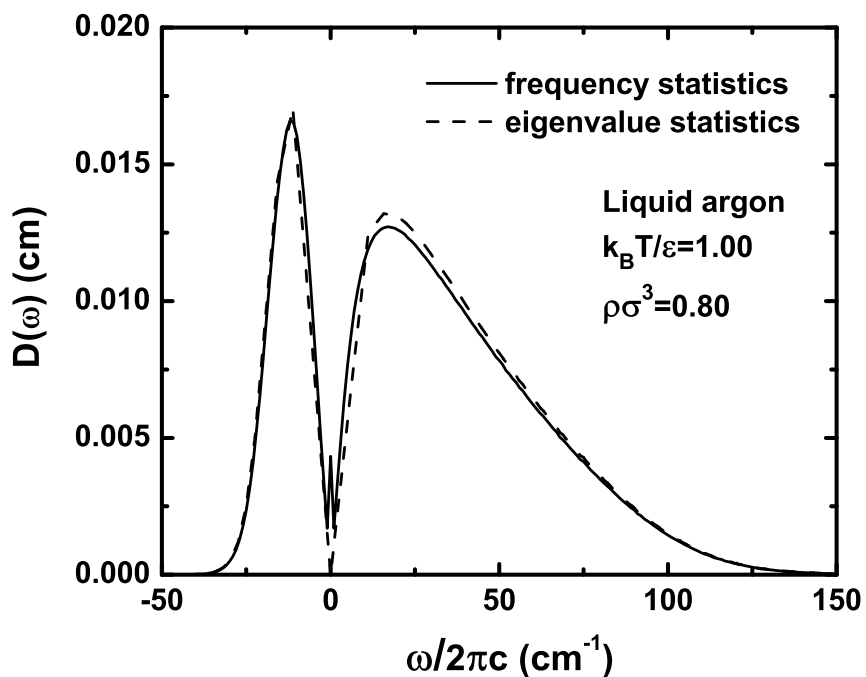


Figure 4.4 Comparison of the instantaneous-normal-mode spectra of liquid Ar using frequency histogram and eigenvalue histogram, at temperature $k_B T/\epsilon = 1.00$ and density $\rho\sigma^3 = 0.80$ averaged 20,000 configurations. Both spectra are conceptually equivalent. Although eigenvalue approach gives a zero density of states at zero frequency, it has less data points at the low frequency region than the high frequency region, not like the frequency histogram approach that bins the frequency evenly.

Checked one configuration and the 9 eigenvalues around zero are as follows

-0.804426857204
-0.363150031495
-0.0872967319105
-1.993958527e-16
1.14488423151e-13
1.38218188184e-13
0.0440473625128
0.349046510601
0.493732811159

(3) The averaged sum of diagonal elements of the dynamical matrix is equal to the averaged sum of all eigenvalues of the dynamical matrix. The simulation gives two identical sums (normalized, divided by $3N$), 279.505020419 ($\epsilon/m\sigma^2$).

(4) Einstein frequency, ω_E .

The square of Einstein frequency is equal to the average of the diagonal element of dynamical matrix.⁶

$$\omega_E^2 = \left\langle \frac{1}{3N} \sum_{j\mu} \mathbf{D}_{j\mu, j\mu} \right\rangle = \left\langle \frac{1}{3Nm} \sum_{j=1}^N \nabla_j^2 u(r_{jk}) \right\rangle = \frac{1}{3m} \rho \int d\mathbf{r} g(r) \nabla^2 u(r). \quad (4.29)$$

From the result of check (3), we know that average of the diagonal element is 279.505 $\epsilon/m\sigma^2$. And we can use the formula at the last of the above equation where $g(r)$ is the radial distribution function and also shown in Figure 3.1. In evaluating $g(r)$, 700 bins are used and I assume $g(r)$ is 1 for r is larger than the half of the simulation box. Then, we can calculate the integral as follows

$$\omega_E^2 = \frac{1}{3m} \rho 4\pi \int_0^\infty dr \cdot r^2 g(r) \nabla^2 u(r) = 270.740 (\epsilon/m\sigma^2). \quad (4.30)$$

These results are of about 3% difference, and can be considered the same. One could

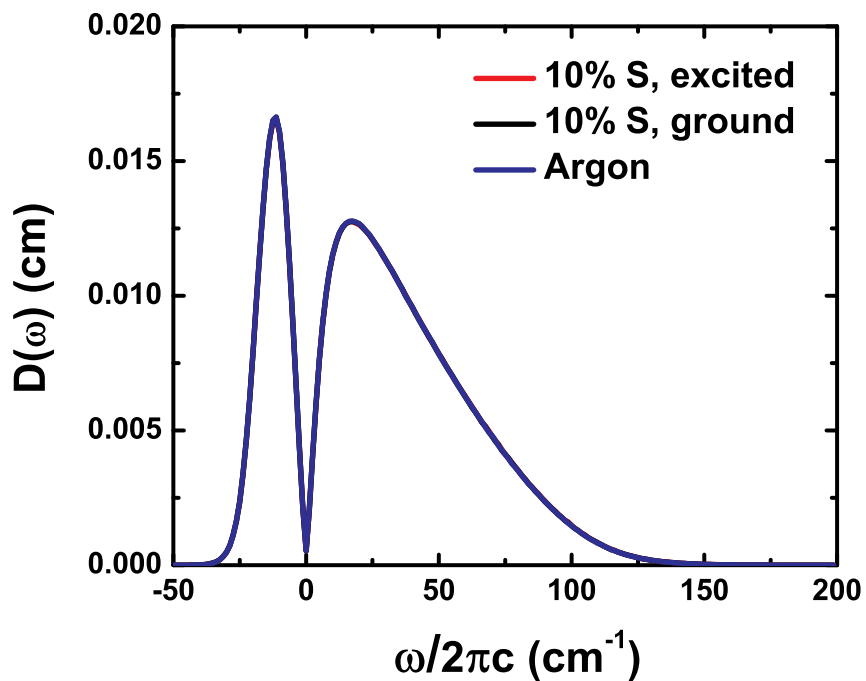
increase the number of bins for $g(r)$ and average more configurations to have a better sampling around 0.9–1.3 σ region where the integrand has a significant value. Another origin of error comes from the assumption for $g(r)=1$ for large r values.

(5) Check the order of eigenvectors by performing matrix multiplication of $\mathbf{UDU}^T (= \mathbf{\Lambda})$. The first 3×3 submatrix of \mathbf{UDU}^T is

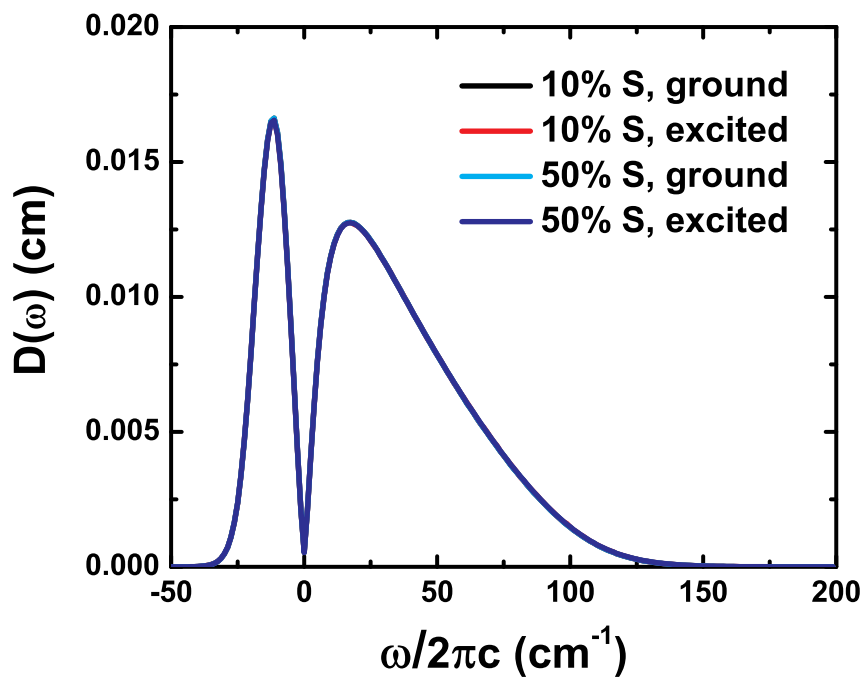
$$\begin{array}{ccc} -125.052838464 & -1.01167119861\text{e-}13 & 8.58009376167\text{e-}14 \\ -6.5685077413\text{e-}14 & -116.405159786 & 3.22481841578\text{e-}14 \\ 8.81489552982\text{e-}14 & 2.72363749121\text{e-}14 & -113.388715178 \end{array}$$

where the diagonal elements are the first three eigenvalues (first three diagonal elements of $\mathbf{\Lambda}$).

Figure 4.5 summarizes the density of states for liquid argon and atomic solvent mixtures (10% S and 50% S) and under thermodynamic condition of temperature $k_B T / \epsilon = 1.00$ and density $\rho \sigma^3 = 0.80$. They have the identical density of states distributions. The real part is dominant in area (real:imaginary=2.9:1) but the imaginary part has higher peak height. Part of the reason of there are imaginary modes in an atomic liquid is that the translational motion has a diffusive portion that could contribute to the imaginary modes and in our atomic liquid model there is no orientational motion (especially librations) that usually has a relatively large contribution to real-frequency INMs. The imaginary frequencies correspond to the unstable INMs meaning the negative curvature of the potential energy surface⁵ (curvature is proportional to the square of the frequency) such that the motion will not possess any oscillatory character. We will focus on stable real modes when discuss the influence spectrum later in this chapter. The non-diffusive part of the imaginary modes is not completely known and how imaginary modes contribute to a spectral observable is still an open question. But we are sure that some local negative curvature do contribute to a well-defined global oscillation as illustrated by the Morse oscillator with a energy higher than the energy at the curvature turning point x_0 at which $u''(x_0) = 0$.



(a)



(b)

Figure 4.5 Instantaneous-normal-mode spectra (density of states) of (a) liquid argon, 10% S on the ground and the excited state, and (b) 10% S vs 50% S on the ground and the excited state. The molecular dynamics simulations are performed at temperature $k_B T / \varepsilon = 1.00$ and density $\rho \sigma^3 = 0.80$ and averaged 20,000 configurations (sampling 1 configuration every 10 time steps, and time step is $\delta t = 0.0025 \tau_{LJ}$). The imaginary frequencies are plotted on the negative frequency axis. All density of states curves overlap on this scale.

4.2.3 INM influence spectrum

The INM influence spectrum^{17,18} connects the INMs with the correlation function of the physical quantity we are interested in. For any dynamical variable A (or called generalized force), the Taylor expansion at some initial configuration in powers of the INMs is

$$A(t) = A(0) + \sum_{\alpha=1}^{3N} \left(\frac{\partial A}{\partial q_{\alpha}} \right)_{t=0} q_{\alpha}(t) + \frac{1}{2} \sum_{\alpha,\beta} \left(\frac{\partial^2 A}{\partial q_{\alpha} \partial q_{\beta}} \right)_{t=0} q_{\alpha}(t) q_{\beta}(t) + \dots \quad (4.31)$$

In the linear INM theory,⁸¹ neglecting terms after the first order in q , we have the time derivative of A as follows

$$\dot{A}(t) = \sum_{j\mu} \left(\frac{\partial A}{\partial r_{j\mu}} \right)_{t=0} \frac{dv_{j\mu}}{dt} = \sum_{\alpha} \left(\frac{\partial A}{\partial q_{\alpha}} \right)_{t=0} \dot{q}_{\alpha}(t) = \sum_{\alpha} c_{\alpha} \dot{q}_{\alpha}(t), \quad (4.32)$$

where the coupling coefficient is

$$c_{\alpha} = \left(\frac{\partial A}{\partial q_{\alpha}} \right)_{t=0} = \sum_{j\mu} \frac{\partial A}{\partial r_{j\mu}} \cdot \frac{\partial r_{j\mu}}{\partial q_{\alpha}} \Big|_{t=0}. \quad (4.33)$$

The generalized force velocity autocorrelation function^{17,81} is then

$$\begin{aligned} G_{AA}(t) &= \langle \dot{A}(t) \dot{A}(0) \rangle = \left\langle \sum_{\alpha,\beta} c_{\alpha} \dot{q}_{\alpha}(0) c_{\beta} \dot{q}_{\beta}(t) \right\rangle = \left\langle \sum_{\alpha} c_{\alpha}^2 \dot{q}_{\alpha}(0) \dot{q}_{\alpha}(t) \right\rangle \\ &= k_B T \left\langle \sum_{\alpha} c_{\alpha}^2 \cos \omega_{\alpha} t \right\rangle = k_B T \int d\omega \cos \omega t \left\langle \sum_{\alpha} c_{\alpha}^2 \delta(\omega - \omega_{\alpha}) \right\rangle \\ &= k_B T \int d\omega \cos \omega t \rho_A(\omega). \end{aligned} \quad (4.34)$$

As any autocorrelation function is even, the cosine transformation is equivalent to the Fourier transformation, i.e. $G_{AA}(t) = k_B T \int d\omega e^{i\omega t} \rho_A(\omega)$. According to Wiener-Khintchine theorem,¹² $\rho_A(\omega)$ is the spectral density (or power spectrum) of $\dot{A}(t)$.[†] Now

[†]The property of delta function $\int dx f(x) \delta(x-a) = f(a)$ has been used in above derivation as well as the change of order of integration with respect to ω and the phase space $\langle \cdot \rangle$ and the equipartition theorem¹⁸

we define the *influence spectrum* $\rho_A(\omega)$,

$$\rho_A(\omega) = \left\langle \sum_{\alpha} c_{\alpha}^2 \delta(\omega - \omega_{\alpha}) \right\rangle, \quad (4.35)$$

which is a weighted INM density of states, and the weighting factor is square of the derivative of the generalized force with respect to the INM (the coupling coefficient c_{α}).

There are two normalization methods for the influence spectrum. (1) the area of the influence spectrum is normalized to the sum of c_{α}^2 with all frequencies; (2) the area of the influence spectrum for real frequencies is normalized to the sum of c_{α}^2 with only real frequencies.

$$(1) \quad \int_{\text{all}} d\omega \rho_A(\omega) = \left\langle \sum_{\text{all } \omega_{\alpha}} c_{\alpha}^2 \right\rangle, \quad (4.36)$$

$$(2) \quad \int_{\text{real}} d\omega \rho_A(\omega) = \left\langle \sum_{\text{real } \omega_{\alpha}} c_{\alpha}^2 \right\rangle. \quad (4.37)$$

The above formulas are these two methods correspondingly and we use the all-frequency normalization only when the comparison of real and imaginary of the influence spectra is needed (Figure 4.6) and we use the real-frequency normalization for OKE related spectra (Figure 4.7, 4.9) and our solute-pump/solvent-probe spectra. It is worth noting that both methods give almost the same normalization factors, whose relative difference is only about 2×10^{-5} .

The generalized force autocorrelation function $C_{AA}(t)$ can be calculated from the velocity autocorrelation function $G_{AA}(t)$ defined by Equation 4.34,²⁸⁶ using the following

$$\langle \dot{q}_{\alpha} \dot{q}_{\beta} \rangle = k_B T \delta_{\alpha\beta}.$$

relation.

$$C_{AA}(t) = \frac{\langle \delta A(t) \delta A(0) \rangle}{\langle \delta A(0) \delta A(0) \rangle}, \quad (4.38)$$

$$\frac{d^2 C_{AA}(t)}{dt^2} = -\frac{G_{AA}(t)}{\langle \delta A(0) \delta A(0) \rangle}, \quad (4.39)$$

$$C_{AA}(t) = 1 - \frac{k_B T}{\langle (\delta A)^2 \rangle} \int d\omega \rho_A(\omega) (1 - \cos \omega t) / \omega^2. \quad (4.40)$$

4.2.4 INM approach to OKE spectra

The OKE response function is the time correlation function of the many-body polarizability,

$$\begin{aligned} R_{xzxz}(t) &= \langle \{ \Pi_{xz}(0), \Pi_{xz}(t) \} \rangle = \beta \langle \dot{\Pi}_{xz}(0) \Pi_{xz}(t) \rangle, \\ \frac{d}{dt} R_{xzxz}(t) &= \beta \langle \dot{\Pi}_{xz}(0) \dot{\Pi}_{xz}(t) \rangle = \int_0^\infty d\omega \rho_{xzxz}(\omega) \cos \omega t, \end{aligned} \quad (4.41)$$

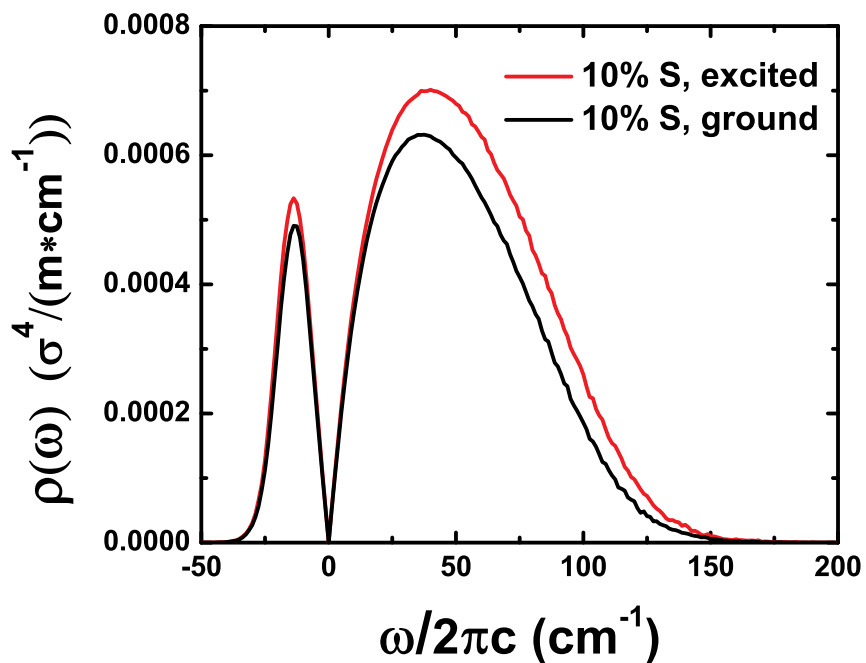
by analogy to Equation 4.34. So in OKE spectroscopy, the dynamical variable A is Π_{xz} and the polarizability influence spectrum can be expressed as

$$\rho_{xzxz}(\omega) = \langle (\Pi_{xz,\alpha})^2 \delta(\omega - \omega_\alpha) \rangle, \quad \text{where } \Pi_{xz,\alpha} \equiv \frac{\partial \Pi_{xz}}{\partial q_\alpha}. \quad (4.42)$$

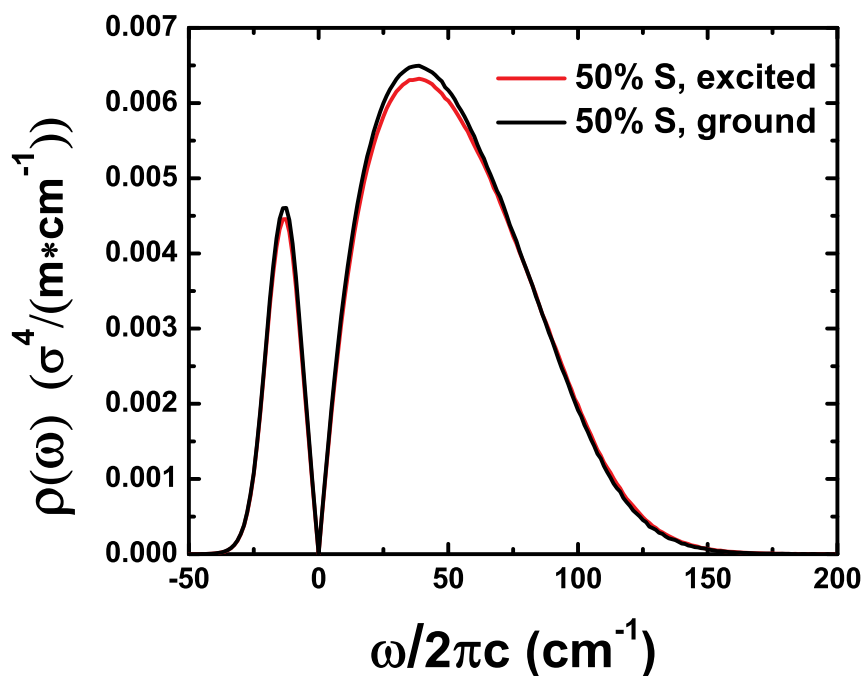
In practice, the rotational invariance in isotropic system is applied, $\langle A_{\mu\nu} B_{\mu\nu} \rangle_{\text{rot}} = \frac{1}{10} \text{PP}(A, B) - \frac{1}{30} \text{Tr}(A) \text{Tr}(B)$, thus we have

$$\left\langle \left(\frac{\partial \Pi_{xz}}{\partial q_\alpha} \right)^2 \right\rangle_{\text{rot}} = \frac{1}{10} \text{PP} \left(\frac{\partial \Pi}{\partial q_\alpha}, \frac{\partial \Pi}{\partial q_\alpha} \right) - \frac{1}{30} \text{Tr} \left(\frac{\partial \Pi}{\partial q_\alpha} \right)^2. \quad (4.43)$$

Figure 4.6 shows the polarizability influence spectra for 10% S and 50% S systems. Atomic polarizabilities are chosen as in the previous chapter, $\alpha_U = 0.2\sigma^3$, $\alpha_S = 0.101\sigma^3$, and $\alpha_W = 0.0186\sigma^3$. The first order DID approximated many-body polarizabilities are



(a)



(b)

Figure 4.6 Instantaneous-normal-mode polarizability influence spectra of (a) 10% S and (b) 50% S on the ground state (black curve) and on the excited state (red curve) at temperature $k_B T / \epsilon = 1.00$ and density $\rho \sigma^3 = 0.80$ and averaged 100,000 configurations (sampling 1 configuration every 10 time steps, and time step is $\delta t = 0.0025 \tau_{LJ}$). The imaginary frequencies are plotted on the negative frequency axis. Normalization of the area of the influence spectrum $\rho(\omega)$ of all frequencies to the sum of c_α^2 with all frequencies is utilized.

used. From this figure, we observe that the shape of influence spectra are similar and the magnitude of excited state is higher than ground state for 10% S and the magnitude of excited state is lower than ground state for 50% S which is consistent with our previous MD results in chapter 3. However, the polarizability influence spectrum is not the OKE spectrum itself. The INM prediction for the OKE spectrum is called the *OKE influence spectrum* that is shown in the following equation. Note that the OKE influence spectrum is called the “modified” influence spectrum in literature.²⁰

$$\text{Im}[R_{xzxz}(\omega)] = \int_0^\infty dt R_{xzxz}(t) \sin \omega t = \frac{\pi \rho_{xzxz}(\omega)}{2 \omega}. \quad (4.44)$$

To derive the above relation, we start by express the Poisson bracket in the INM basis.

$$\{\Pi_{xz}(0), \Pi_{xz}(t)\} = \sum_{j\mu} \frac{\partial \Pi_{xz}(0)}{\partial r_{j\mu}(0)} \cdot \frac{\partial \Pi_{xz}(t)}{\partial p_{j\mu}(0)} \quad (4.45)$$

$$= \sum_{j\mu} \sum_{\alpha, \beta} \frac{\partial \Pi_{xz}}{\partial q_\alpha} \Big|_0 \frac{\partial q_\alpha(0)}{\partial r_{j\mu}(0)} \cdot \frac{\partial \Pi_{xz}}{\partial q_\beta} \Big|_t \frac{\partial q_\beta(t)}{\partial p_{j\mu}(0)} \quad (4.46)$$

$$= \sum_{\alpha, \beta} \frac{\partial \Pi_{xz}}{\partial q_\alpha} \Big|_0 \{q_\alpha(0), q_\beta(t)\} \frac{\partial \Pi_{xz}}{\partial q_\beta} \Big|_t. \quad (4.47)$$

The INM fundamental Poisson bracket¹⁹⁸ below can be derived from Equation 4.14 and 4.15,

$$\begin{aligned} \chi_{\alpha, \beta}(t_1, t_2) &\equiv \{q_\alpha(t_1), q_\beta(t_2)\} = \sum_{j\mu} \frac{\partial q_\alpha(t_1)}{\partial r_{j\mu}(t_1)} \frac{\partial q_\beta(t_2)}{\partial p_{j\mu}(t_1)} \\ &= \frac{\sin \omega_\alpha(t_2 - t_1)}{\omega_\alpha} \delta_{\alpha\beta} = \chi_\alpha(t_2 - t_1) \delta_{\alpha\beta}, \end{aligned} \quad (4.48)$$

$$\text{where } \chi_\alpha(t) = \int_0^t d\tau C_{vv}^\alpha(\tau) = \frac{\sin \omega_\alpha t}{\omega_\alpha}, \quad (4.49)$$

$$C_{vv}^\alpha(\tau) = \frac{\langle v_\alpha(0) v_\alpha(\tau) \rangle}{\langle v_\alpha^2 \rangle} = \cos \omega_\alpha \tau. \quad (4.50)$$

We then have the OKE response function in INM basis:

$$R(t) = \langle \{ \Pi_{xz}(0), \Pi_{xz}(t) \} \rangle = \left\langle \frac{\partial \Pi_{xz}}{\partial q_\alpha} \Big|_0 \{ q_\alpha(0), q_\beta(t) \} \frac{\partial \Pi_{xz}}{\partial q_\beta} \Big|_t \right\rangle, \quad (4.51)$$

In the linear INM theory, we assume the coupling coefficient is constant in such a short time,

$$\frac{\partial \Pi_{xz}}{\partial q_\alpha} \Big|_t \approx \frac{\partial \Pi_{xz}}{\partial q_\alpha} \Big|_0 = \Pi_{xz,\alpha}. \quad (4.52)$$

So the OKE response function becomes

$$R_{\text{INM}}(t) = \left\langle \sum_{\alpha} (\Pi_{xz,\alpha})^2 \chi_{\alpha}(t) \right\rangle. \quad (4.53)$$

The OKE spectral density is the imaginary part of the Fourier transform (sine transform) of the response function,

$$\begin{aligned} \text{Im}[R_{\text{INM}}(\omega)] &= \int_0^{\infty} dt R(t) \sin \omega t \\ &= \int_0^{\infty} dt \left\langle \sum_{\alpha} (\Pi_{xz,\alpha})^2 \chi_{\alpha}(t) \right\rangle \sin \omega t \\ &= \left\langle \sum_{\alpha} (\Pi_{xz,\alpha})^2 \int_0^{\infty} dt \frac{\sin \omega_{\alpha} t}{\omega_{\alpha}} \sin \omega t \right\rangle. \end{aligned}$$

Using following identity

$$\int_0^{\infty} \sin \omega t \sin \omega' t dt = \frac{\pi}{2} [\delta(\omega - \omega') - \delta(\omega + \omega')]. \quad (4.54)$$

To prove above relation, one needs to use the following property of delta function

$$\delta(\omega) = \frac{1}{2\pi} \int_{-\infty}^{\infty} dt \cos \omega t = \frac{1}{2\pi} \int_{-\infty}^{\infty} dt e^{\pm i\omega t}. \quad (4.55)$$

Thus, the OKE spectrum using INM approximation is given by

$$\text{Im}[R_{\text{INM}}(\omega)] = \frac{\pi}{2} \left\langle \sum_{\alpha} (\Pi_{xz,\alpha})^2 \frac{1}{\omega_{\alpha}} [\delta(\omega - \omega_{\alpha}) - \delta(\omega + \omega_{\alpha})] \right\rangle \quad (4.56)$$

$$= \frac{\pi}{2} \frac{\rho_{xzxz}(\omega)}{\omega}. \quad (4.57)$$

Check simulations

The sum of the squares of spatial derivative of the polarizability are equivalent using either the INM q_{α} basis or Cartesian coordinates $r_{j\mu}$ basis as a result of the transformation matrix being unitary:

$$\sum_{\alpha} \left(\frac{\partial \Pi_{xz}}{q_{\alpha}} \right)^2 = \sum_{j\mu} \left(\frac{\partial \Pi_{xz}}{r_{j\mu}} \right)^2. \quad (4.58)$$

For one configuration of 10%S system, the sum is 0.056834 using both methods, and the sum is 0.049215 if only real modes are included in the INM-basis method which is about 13% less than the full INM result.

OKE spectra: comparison between INM and MD methods

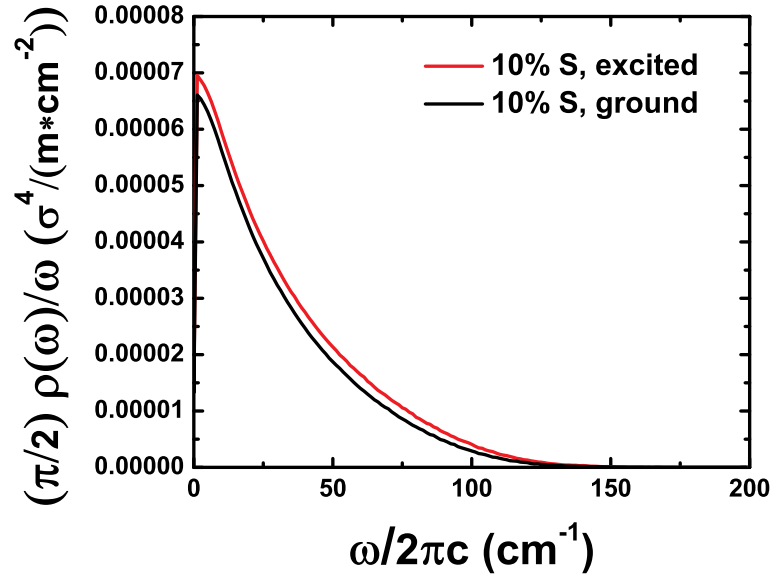
Figure 4.7 shows the OKE influence spectra for 10% S and 50% S systems and the relative peak heights of the excited vs. ground is in the same order with the polarizability influence that is also consistent with previous results. Comparing with the molecular-dynamics results for the OKE spectra (Figure 4.8), the INM approximation works well for frequency larger than 25 cm^{-1} in 10% S system with ground- and excited-state solute. But what we are most interested in is the difference of excited-state and ground-state OKE influence spectra, so we show the comparisons with the previous molecular-dynamics OKE spectra in Figure 4.9 and 4.10. [‡]

Figure 4.9 and 4.10 are the major findings of this section. They indicate a good

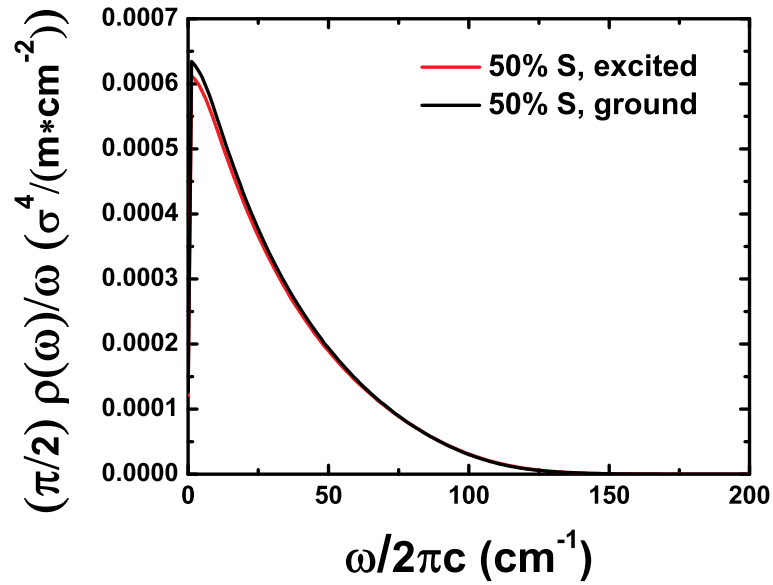
[‡]The OKE influence spectrum $\frac{\pi}{2} \frac{\rho(\omega)}{\omega}$ has a unit of $\sigma^4 / (\text{m} * \text{cm}^{-2})$ which can be transformed to the LJ reduced unit σ^6 / ϵ by multiplying 2.4578^2 since $1 \tau_{LJ}^{-1} = 2.4578 \text{ cm}^{-1}$ and $\tau_{LJ} = \sqrt{m \sigma^2 / \epsilon}$.

agreement between INM and MD methods for predicting OKE e-g difference spectra in the high-frequency region. First of all, the signs of e-g difference for both 10% S and 50% S in Figure 4.9 are the same as the MD results. Furthermore, the magnitudes of the difference spectra using the INM approach is quite similar with that of the exact MD results. Figure 4.10 compares full OKE spectra with e-g difference calculated with INM and exact MD methods as well as corresponding results of spectra densities. Highlighted is the region where the INM prediction works well in 10% S system — for frequencies above 25 cm^{-1} . The top panel compares the INM prediction to the OKE spectra for the 10% S with an excited-state solute with the exact MD results (showing both reduced spectral densities and spectral densities). The overall OKE spectra shapes are in a quantitative agreement, where the spectral densities agree better with the INM predictions than the reduced spectral densities. The bottom panel shows the solute-pump/solvent-probe spectrum at the large T limit, which reflects the fact that the INM theory can capture the distinction between the excited- and ground-state dynamics, although INM prediction for the difference spectrum is less quantitative than for the full OKE spectra. In short, the INM theory can provide us a qualitative and quasi-quantitative estimate of the OKE spectra for the most interesting high frequencies (larger than 25 cm^{-1}) and it will be demonstrated to be expandable to the nonequilibrium 2D solute-pump/solvent-probe spectra with finite waiting time T .

Figure 4.11 provides comparisons between INM predictions of e-g difference using different system sizes and different averaging with MD results. One can observe that the system size has some influence on the overall magnitude of the e-g difference spectra: the larger system, the larger the e-g difference, because the first-order DID approximated polarizability increases with system size. But the system-size dependence is not pronounced. One also can observe that more averaging gives a bit lower e-g difference. However, all mentioned variations will not affect the qualitative accuracy of the INM approximation.

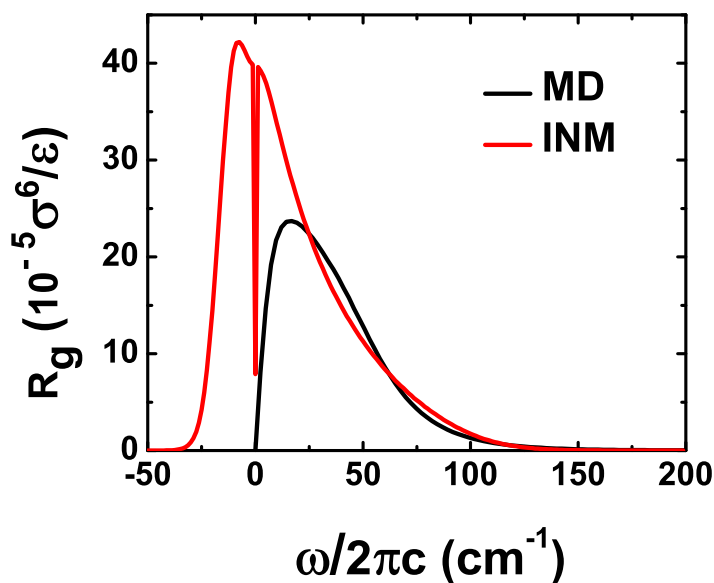


(a)

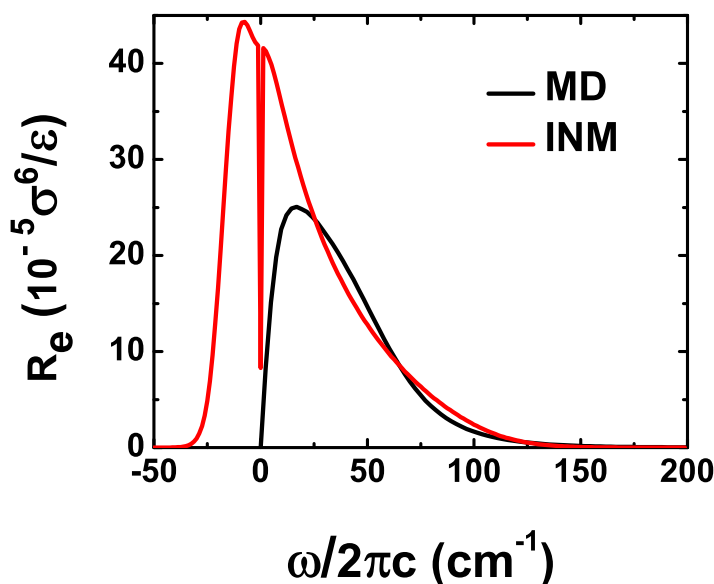


(b)

Figure 4.7 Instantaneous-normal-mode OKE influence spectra of (a) 10% S and (b) 50% S on the ground state (black curve) and on the excited state (red curve) at temperature $k_B T/\epsilon = 1.00$ and density $\rho\sigma^3 = 0.80$ and averaged 100,000 configurations (sampling 1 configuration every 10 time steps, and time step is $\delta t = 0.0025\tau_{LJ}$). Normalization of the area of the influence spectrum $\rho(\omega)$ of real frequencies to the sum of c_α^2 with real frequencies is utilized.

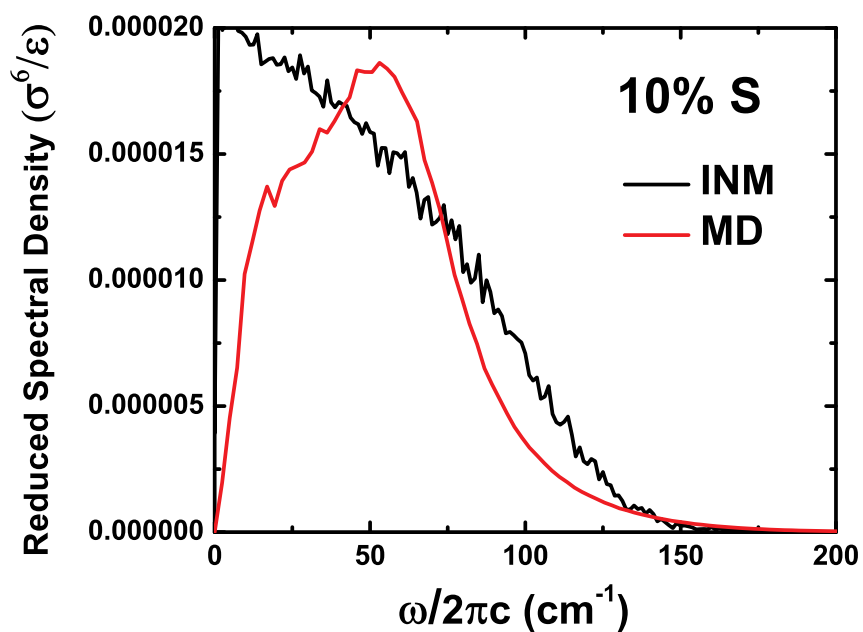


(a)

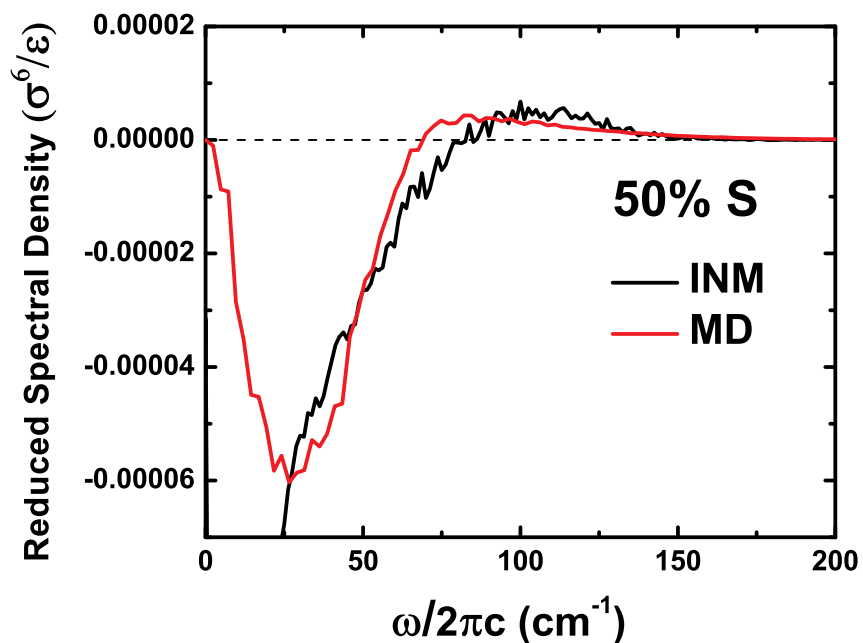


(b)

Figure 4.8 Comparison of instantaneous-normal-mode (INM) and exact molecular-dynamics (MD) predictions of optical Kerr effect spectra for the 10% S solvent mixture (255 solvents in total) with an atomic solute. The upper panel is the OKE spectrum of the system with a ground-state solute and the lower panel is the OKE spectrum with an excited-state solute. The imaginary INM frequencies are plotted on the negative frequency axis. Molecular dynamics results are reduced spectral densities (solid black curves) that are retrieved from Figure 3.10, calculated by averaging over 10^8 liquid configurations, and the INM results are calculated by averaging over 1.6×10^6 liquid configurations. The first order DID approximation is utilized in evaluating the many-body polarizability.



(a)



(b)

Figure 4.9 Comparison of e-g difference of the OKE spectra using instantaneous-normal-mode approximation (black) and exact molecular dynamics results (red) for (a) 10% S and (b) 50% S at temperature $k_B T/\epsilon = 1.00$ and density $\rho\sigma^3 = 0.80$. Molecular dynamics results are reduced spectral densities that are retrieved from Figure 3.10, calculated by averaging over 10^8 liquid configurations, and the INM results are calculated by averaging over 10^5 configurations. The first order DID approximation is utilized in evaluating the many-body polarizability.

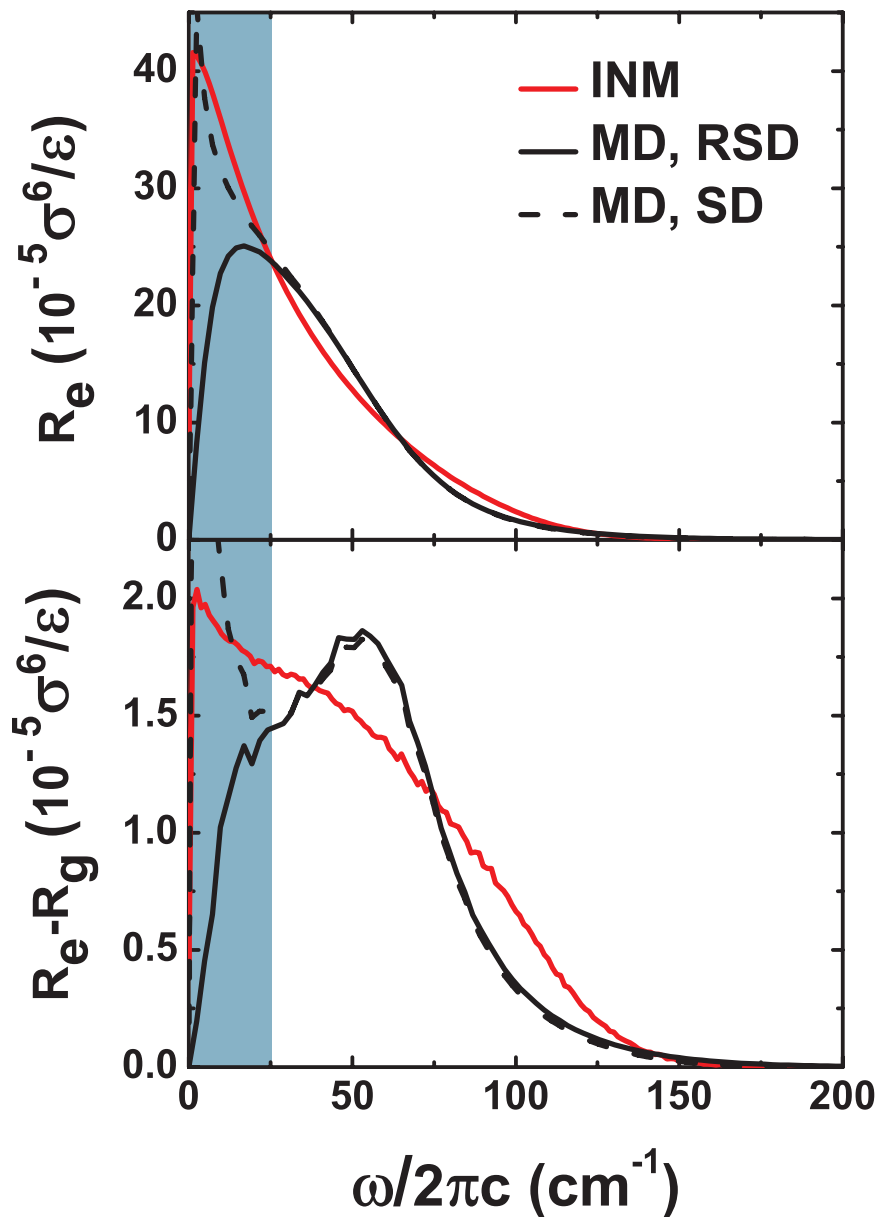


Figure 4.10 Comparison of instantaneous-normal-mode (INM) and exact molecular-dynamics (MD) predictions of optical Kerr effect spectra for the 10% S solvent mixture (255 solvents in total) with an atomic solute. The upper panel is the OKE spectrum of the system with an excited-state solute and the lower panel is the difference spectrum between the excited- and ground-state-solute OKE spectra. Molecular dynamics results including reduced spectral densities (RSD, solid black curves) that are retrieved from Figure 3.10 and spectral densities (SD, dashed black curves) are calculated by averaging over 10^8 liquid configurations, and the INM results are calculated by averaging over 1.6×10^6 liquid configurations. The first order DID approximation is utilized in evaluating many-body polarizability. The shaded region for frequency less than 25 cm^{-1} indicates that the INM methods are not suitable for this domain.

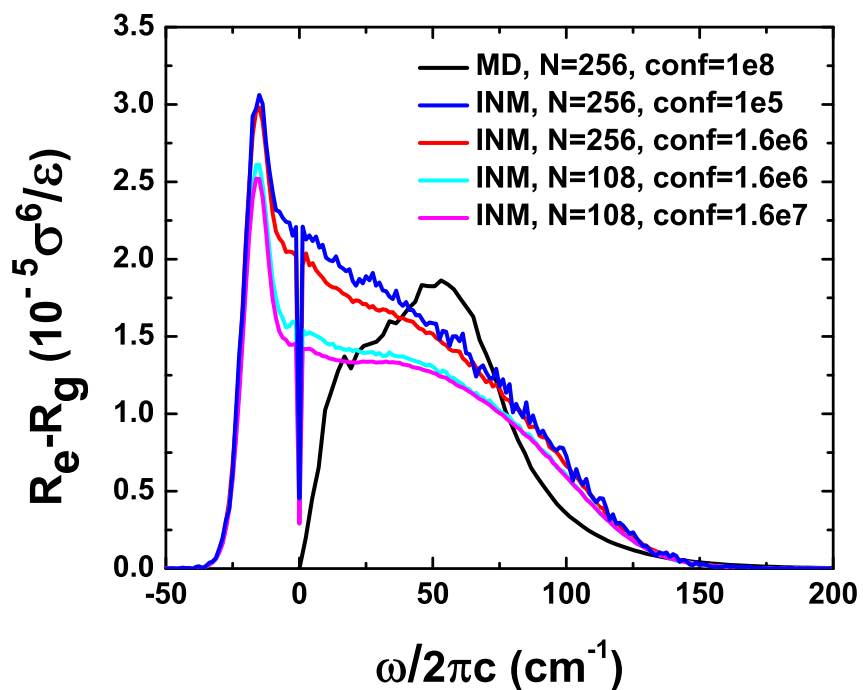


Figure 4.11 Comparison of instantaneous-normal-mode (INM) and exact molecular-dynamics (MD) predictions of e-g difference of optical Kerr effect spectra for the 10% S solvent mixture with an atomic solute. System sizes ($N=108, 256$) and numbers of configurations for averaging are indicated in the legend. The imaginary INM frequencies are plotted on the negative frequency axis. The first order DID approximation is utilized in evaluating the many-body polarizability.

4.2.5 INM solvation influence spectrum

In studying the solvation dynamics, the physical variable A is the solute-solvent interaction energy gap $\Delta V = V_e - V_g$ and the *solvation influence spectrum* is defined as²⁸⁶

$$\rho_{solv}(\omega) = \left\langle \left(\frac{\partial \Delta V}{\partial q_\alpha} \right)^2 \delta(\omega - \omega_\alpha) \right\rangle. \quad (4.59)$$

In a Lennard-Jones system, the coupling coefficients are

$$\frac{\partial \Delta V}{\partial q_\alpha} = \sum_{j\mu} \frac{\partial \Delta V}{\partial r_{j\mu}} \frac{\partial r_{j\mu}}{\partial q_\alpha}, \quad (4.60)$$

$$\frac{\partial \Delta V}{\partial r_{i\mu}} = \begin{cases} \sum_{j \neq 0} 4\Delta\varepsilon(j) \left[-12 \frac{\sigma^{12}}{r_{0j}^{14}} + 6 \frac{\sigma^6}{r_{0j}^8} \right] (r_{0\mu} - r_{j\mu}), & (i = 0) \\ -4\Delta\varepsilon(i) \left[-12 \frac{\sigma^{12}}{r_{0i}^{14}} + 6 \frac{\sigma^6}{r_{0i}^8} \right] (r_{0\mu} - r_{i\mu}), & (i \neq 0) \end{cases} \quad (4.61)$$

$$\text{where } \Delta\varepsilon(j) = \varepsilon_{\text{solute-solvent}(j)}^e - \varepsilon_{\text{solute-solvent}(j)}^g. \quad (4.62)$$

Figure 4.12 shows how different the influence could be when different physical variable A is used in the coupling factor. Here the polarizability influence and the solvation influence are compared and clearly the solvation influence spectrum has more high frequency contribution and much smaller imaginary frequency contribution than the polarizability influence spectrum.

4.3 Evaluation of Solute-Pump/Solvent-Probe Response

Although in the large T limit, the response function of a solute-pump/solvent-probe spectroscopy can be easily calculated by taking the difference of ordinary four-wave-mixing responses (such as optical Kerr effect spectra) on two equilibrated states,

$$\Delta R(0, T, T+t)|_{T \rightarrow \infty} = \beta \left[\langle \dot{\Pi}_{xz}(0) \Pi_{xz}(t) \rangle_e - \langle \dot{\Pi}_{xz}(0) \Pi_{xz}(t) \rangle_g \right], \quad (4.63)$$

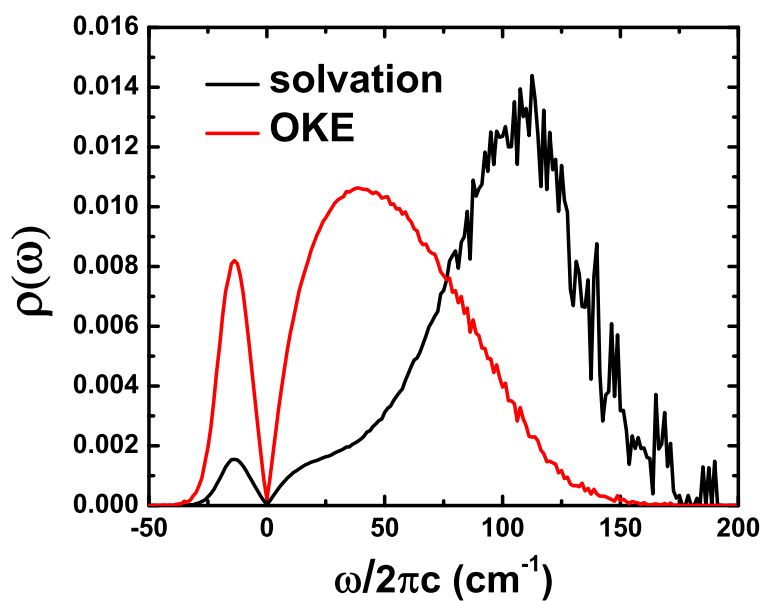


Figure 4.12 Instantaneous-normal-mode polarizability influence spectrum (OKE, red curve) vs. solvation influence spectrum (solvation, black curve) of 10% S solvent mixture with an excited-state solute at thermal condition of temperature $k_B T / \epsilon = 1.00$ and density $\rho \sigma^3 = 0.80$. Both the polarizability influence spectrum and the solvation influence spectrum are calculated by averaging 20,000 configurations. The imaginary frequencies are plotted on the negative frequency axis. The total areas of both influence spectra are normalized to 1.

for finite T , the solute-pump/solvent-probe response function is given by Equation 2.90 which we restate here as follows.

$$\Delta R(0, T, T+t) = \frac{\left\langle e^{\beta \delta \Delta V(0)} \{ \Pi_{xz}(T), \Pi_{xz}(T+t) \} \right\rangle_e}{\left\langle e^{\beta \delta \Delta V(0)} \right\rangle_e} - \beta \left\langle \dot{\Pi}_{xz}(0) \Pi_{xz}(t) \right\rangle_g. \quad (4.64)$$

As mentioned earlier, a practical problem in evaluating the response is the Poisson bracket, which is a measurement of the interference of two classical trajectories starting their evolution from initial conditions with a small difference.²⁸⁷ The difficulty for calculating the Poisson bracket is that for each time a new configuration generated, the whole trajectory of the Poisson bracket has to be updated, which is governed by a different equation of motion than the Newton's law in molecular dynamics simulation.¹⁹⁷ Another concern is the chaotic nature of classical dynamics gives rise to the divergence issue of the stability matrix for some systems²³⁶ (the 2nd order stability matrix is the fundamental Poisson bracket),²³⁷ and the ensemble averaging can tame the divergence only for a very short time scale.^{197,234} The instantaneous-normal-mode theory, on the other hand, provides an analytical approach to evaluate classical Poisson bracket. The INM treatment to the OKE spectra has been discussed in the previous section. In this section, we will focus on the solute-pump/solvent-probe spectra starting with a hybrid approach incorporating the INM approximation and molecular dynamics followed by another analytical attempt. For completeness, the direct numerical approach to evaluate Poisson bracket will be included at the end of this section.

4.3.1 Hybrid INM/MD method

There are two time scales associated with the 2D solute-pump/solvent-probe spectra, the solvation time T and the ultrafast dynamical time t . In most of the situations in solvation, these two time scales tend to be widely separated. The solvation time T needs to be long enough to distinguish an overall liquid geometrical reorganization, whereas the t time only

needs to be long enough to reflect the intermolecular vibrations. The ultrafast time scale measured by optical Kerr effect spectra lies in sub-picosecond regime corresponding to vibrational frequencies larger than 30 cm^{-1} .

The INM theory gives a reasonably reliable prediction to the ultrafast dynamics corresponding to any such high-frequency intermolecular motions.^{20,177} We also demonstrated the applicability of INM theory to our preferential solvation model in the previous section. Here we present a hybrid approach, in which the ultrafast dynamics is treated with INM approximation but the long-time solvation is still simulated with the exact molecular dynamics. Like the INM treatment to OKE spectra, the $\{\Pi_{xz}(T), \Pi_{xz}(T+t)\}$ Poisson bracket in the solute-pump/solvent-probe response (Equation 4.64) can be evaluated analytically using dynamical information at time T from the primary molecular dynamical trajectory. We perform the INM analysis on each instantaneous configuration \mathbf{R}_T , obtaining the INM $q_\alpha(t; \mathbf{R}_T)$, ($\alpha = 1, \dots, 3N$). Equation 2.95 can be evaluated in that INM basis,

$$\{\Pi_{xz}(T), \Pi_{xz}(T+t)\} = \sum_{\alpha, \beta=1}^{3N} \left[\Pi_{xz, \alpha}(T) \Pi_{xz, \beta}(T+t) \frac{\partial q_\beta(t; \mathbf{R}_T)}{\partial p_\alpha(0; \mathbf{R}_T)} \right] \quad (4.65)$$

$$\approx \sum_{\alpha, \beta=1}^{3N} \left[\Pi_{xz, \alpha}(T) \Pi_{xz, \beta}(T) \frac{\partial q_\beta(t; \mathbf{R}_T)}{\partial p_\alpha(0; \mathbf{R}_T)} \right], \quad (4.66)$$

where the sensitivity of the polarizability with respect to the INM α is

$$\Pi_{xz, \alpha}(T) \equiv \left. \frac{\partial \Pi_{xz}}{\partial q_\alpha} \right|_T = \frac{1}{\sqrt{m}} \sum_{i=1}^{3N} \left. \frac{\partial \Pi_{xz}}{\partial r_i} \right|_T \cdot \mathbf{U}_{i, \alpha}^T(\mathbf{R}_T). \quad (4.67)$$

Taking advantage of the facts that the INM modes are mutually orthogonal and each mode α has a harmonic frequency $\omega_\alpha(\mathbf{R}_T)$, we have the INM fundamental Poisson bracket

$$\frac{\partial q_\beta(t; \mathbf{R}_T)}{\partial p_\alpha(0; \mathbf{R}_T)} = \delta_{\alpha\beta} \frac{\sin[\omega_\alpha(\mathbf{R}_T)t]}{\omega_\alpha(\mathbf{R}_T)}. \quad (4.68)$$

In Equation 4.66, the observable is linearized. This approximation (which is an example of

the linear INM theory we referred to earlier) will be discussed in more detail in section 4.7. The Poisson bracket we need is then simply

$$\{\Pi_{xz}(T), \Pi_{xz}(T+t)\} = \sum_{\alpha=1}^{3N} \Pi_{xz,\alpha}^2(T) \frac{\sin[\omega_{\alpha}(T)t]}{\omega_{\alpha}(T)}, \quad (4.69)$$

where for convenience, $\omega_{\alpha}(T) \equiv \omega_{\alpha}(\mathbf{R}_T)$.¹⁹⁸

As a result, one avoids calculating any secondary ($T \rightarrow T+t$) trajectories altogether. The response function that is a three-time ensemble average $\Delta R(0, T, T+t)$ now can be evaluated based on two-time dynamical information (at time 0 and time T). Substituting this result in Equation 4.64, we have the time-domain solute-pump/solvent-probe response function

$$\Delta R(0, T, T+t) = \frac{\left\langle e^{\beta\Delta V(0)} \sum_{\alpha=1}^{3N} \Pi_{xz,\alpha}^2(T) \frac{\sin \omega_{\alpha}(T)t}{\omega_{\alpha}(T)} \right\rangle_e}{\left\langle e^{\beta\Delta V(0)} \right\rangle_e} - \beta \left\langle \dot{\Pi}_{xz}(0) \Pi_{xz}(t) \right\rangle_g. \quad (4.70)$$

Taking imaginary part of the Fourier transform of the response with respect to the ultrafast time scale t ,

$$\Delta R(\omega, T) = \int_0^{\infty} dt \sin \omega t \Delta R(0, T, T+t), \quad (4.71)$$

we have the solute-pump/solvent-probe spectra

$$\Delta R(\omega, T) = \frac{\pi}{2\omega} \frac{\left\langle e^{\beta\Delta V(0)} \sum_{\alpha=1}^{3N} \Pi_{xz,\alpha}^2(T) \delta(\omega - \omega_{\alpha}(T)) \right\rangle_e}{\left\langle e^{\beta\Delta V(0)} \right\rangle_e} - \frac{\pi}{2\omega} \left\langle \sum_{\alpha=1}^{3N} \Pi_{xz,\alpha}^2 \delta(\omega - \omega_{\alpha}) \right\rangle_g \quad (4.72)$$

This equation is the most important result of this chapter. The total solute-pump/solvent-probe spectrum consists of a T -dependent part and a T -independent part. The T -dependent part (the first term in above equation) is the nonequilibrium four-wave-mixing spectrum explicitly dependent on the time delay between the solute excitation and the solvent-probe

light scattering. The T -independent part (the last term in above equation) is the OKE spectra of solution with a ground-state solute. We can check the long T limit behavior of the nonequilibrium part: when $T \rightarrow \infty$, the exponential $e^{\beta\Delta V(0)}$ gets uncorrelated with the Poisson bracket, giving rise to an ordinary OKE spectra for the solution with an excited-state solute. This long T limit agrees with our exact expression without INM approximation in Equation 2.92. Before showing the calculated 2D spectra, let us see another analytical attempt to evaluate the Poisson bracket.

4.3.2 SHO-like approximation

From the previous discussions, the central question in calculating solute-pump/solvent-probe spectra is how to evaluate the correlation function of the following form,

$$R(0, t_1, t_2) = \langle A(0) \{B(t_1), C(t_2)\} \rangle. \quad (4.73)$$

Although the dynamical variable A corresponding to the fluctuation of potential energy gap $\delta\Delta V$ in Equation 4.64, is only dependent on liquid configuration, for generality, we still treat this variable as a function of coordinates $\mathbf{R} = \{r_{j\mu}\}$ and momenta $\mathbf{P} = \{p_{j\mu}\}$, where the label j is the individual atom, and $\mu = x, y, z$ is every degree of freedom of an individual atom.

$$A = A(\mathbf{R}, \mathbf{P}), \quad A(t) = A(\mathbf{R}(t), \mathbf{P}(t)). \quad (4.74)$$

Since polarizability is a function of positions, we assume B and C are functions of coordinates \mathbf{R} alone,

$$B = B(\mathbf{R}), \quad C = C(\mathbf{R}). \quad (4.75)$$

The Poisson bracket of B and C is then

$$\{B(t_1), C(t_2)\} = \frac{\partial B(\mathbf{R}(t_1))}{\partial \mathbf{R}(t_1)} \cdot \frac{\partial C(\mathbf{R}(t_2))}{\partial \mathbf{P}(t_1)} - \frac{\partial C(\mathbf{R}(t_2))}{\partial \mathbf{R}(t_1)} \cdot \frac{\partial B(\mathbf{R}(t_1))}{\partial \mathbf{P}(t_1)} \quad (4.76)$$

$$\left(\text{since } \frac{\partial B(\mathbf{R}(t_1))}{\partial \mathbf{P}(t_1)} = 0 \right)$$

$$= \sum_{j\mu, kv} \frac{\partial B}{\partial r_{j\mu}} \Big|_{t_1} \cdot \frac{\partial C}{\partial r_{kv}} \Big|_{t_2} \left(\frac{\partial r_{kv}(t_2)}{\partial p_{j\mu}(t_1)} \right) \quad (4.77)$$

$$= \nabla B(t_1) \cdot \boldsymbol{\chi}(t_1, t_2) \cdot \nabla C(t_2), \quad (4.78)$$

where the fundamental Poisson bracket is defined as

$$\boldsymbol{\chi}_{j\mu, kv}(t_1, t_2) = \{r_{j\mu}(t_1), r_{kv}(t_2)\} = \frac{\partial r_{kv}(t_2)}{\partial p_{j\mu}(t_1)}, \quad (4.79)$$

denoting $\nabla \equiv \frac{\partial}{\partial \mathbf{R}}$.

So the exact T -dependent response function can be rewritten as follows

$$R(0, T, T+t) = \frac{\left\langle e^{\beta \Delta V(0)} \nabla \Pi(T) \cdot \boldsymbol{\chi}(T, T+t) \cdot \nabla \Pi(T+t) \right\rangle_e}{\left\langle e^{\beta \Delta V} \right\rangle_e} \quad (4.80)$$

$$= \frac{\left\langle e^{\beta \Delta V(0)} \sum_{j\mu, kv} \frac{\partial \Pi_{xz}}{\partial r_{j\mu}} \Big|_T \boldsymbol{\chi}_{j\mu, kv}(T, T+t) \frac{\partial \Pi_{xz}}{\partial r_{kv}} \Big|_{T+t} \right\rangle_e}{\left\langle e^{\beta \Delta V} \right\rangle_e}. \quad (4.81)$$

For a 1-dimensional simple harmonic oscillator (SHO), the time evolution of its position is $x(t) = x_0 \cos \omega t + \frac{p_0}{m\omega} \sin \omega t$, thus the fundamental Poisson bracket is a function of $(t_2 - t_1)$ and independent of phase space point $x(t_1)$ or $p(t_1)$.

$$\boldsymbol{\chi}(t_1, t_2) = \frac{\partial x(t_2)}{\partial p(t_1)} = \frac{\sin \omega(t_2 - t_1)}{m\omega}. \quad (4.82)$$

The SHO-like approximation to the fundamental Poisson bracket is the following:

replacing the fundamental Poisson bracket by its ensemble average and assuming it is diagonal.

$$\chi_{j\mu,k\nu}(t_1, t_2) \approx \delta_{j\mu,k\nu} \langle \{r_{j\mu}(t_1), r_{k\nu}(t_2)\} \rangle \quad (4.83)$$

$$= \delta_{j\mu,k\nu} \langle \{r_{j\mu}(0), r_{j\mu}(\tau)\} \rangle \quad (\tau = t_2 - t_1)$$

$$= \delta_{j\mu,k\nu} \left\langle \frac{\partial r_{j\mu}(\tau)}{\partial p_{j\mu}(0)} \right\rangle$$

$$= \delta_{j\mu,k\nu} \frac{1}{Q} \int dr_{j\mu}(0) \int dp_{j\mu}(0) e^{-\beta \left(\frac{p_{j\mu}^2(0)}{2m} + V \right)} \frac{\partial r_{j\mu}(\tau)}{\partial p_{j\mu}(0)}$$

$$= \delta_{j\mu,k\nu} \frac{1}{Q} \int dr_{j\mu}(0) e^{-\beta H} r_{j\mu}(\tau) \Big|_{p_{j\mu}(0)=-\infty}^{p_{j\mu}(0)=+\infty}$$

$$- \delta_{j\mu,k\nu} \frac{1}{Q} \int dp_{j\mu}(0) \int dr_{j\mu}(0) r_{j\mu}(\tau) \left(-\frac{\beta}{2m} \cdot 2p_{j\mu}(0) \right) e^{-\beta \left(\frac{p_{j\mu}^2(0)}{2m} + V \right)}$$

$$= \delta_{j\mu,k\nu} \frac{1}{Q} \frac{\beta}{m} \int dp_{j\mu}(0) \int dr_{j\mu}(0) r_{j\mu}(\tau) p_{j\mu}(0) e^{-\beta H}$$

$$= \delta_{j\mu,k\nu} \beta \langle v_{j\mu}(0) r_{j\mu}(\tau) \rangle \quad (4.84)$$

$$= \delta_{j\mu,k\nu} \frac{1}{m} \int_0^\tau C_{vv}(t) dt. \quad (4.85)$$

where the normalized velocity autocorrelation functions in one-dimensional and $3N$ -dimensional cases are respectively

$$C_{vv}(t) = \frac{\langle v_{j\mu}(0) v_{j\mu}(t) \rangle}{\langle v_{j\mu}^2(0) \rangle}, \quad \langle v_{j\mu}^2 \rangle = k_B T / m \quad (4.86)$$

$$C_{\mathbf{v}\mathbf{v}}(t) = \frac{\langle \mathbf{v}(0) \cdot \mathbf{v}(t) \rangle}{\langle \mathbf{v}^2(0) \rangle}, \quad \langle \mathbf{v}^2 \rangle = 3N k_B T / m \quad (4.87)$$

For 1d-SHO, $C_{vv}(t) = \cos \omega t$ and $\chi(\tau) = \frac{1}{m} \int_0^\tau C_{vv}(t) dt = \frac{\sin \omega \tau}{m \omega}$.

Thus, we get the SHO-like approximated evaluation of the solute-pump/solvent-probe

response function,

$$R(0, t_1, t_2) \approx \left(\frac{1}{m} \int_0^{t_2-t_1} C_{\mathbf{v}\mathbf{v}}(t) dt \right) \langle A(0) \nabla B(t_1) \cdot \nabla C(t_2) \rangle / \langle A \rangle, \quad (4.88)$$

where $A = e^{\beta\Delta V}$, $B = C = \Pi_{xz}$ as in Equation 4.81.

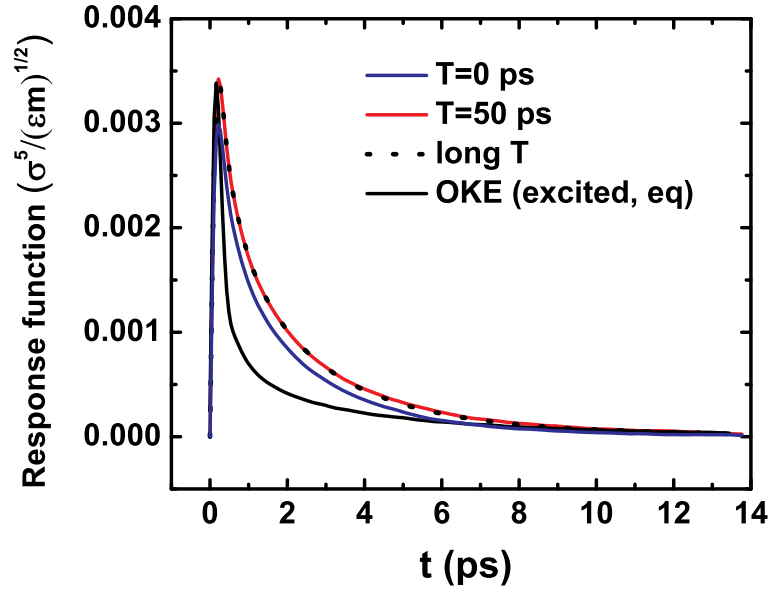
Check properties:

(1) when $t_1 = t_2$, the response should vanish, and I checked for the SHO-like approximation $R(0, t_1, t_1) = 0$.

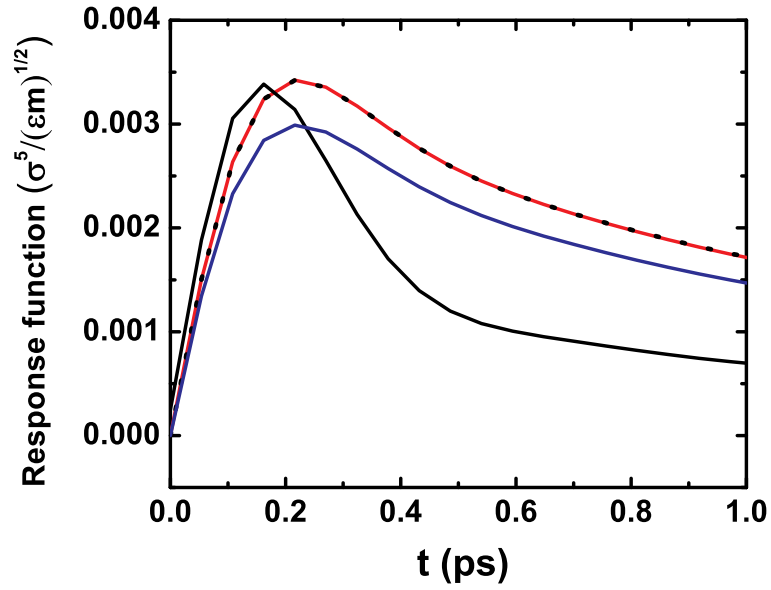
(2) if $B = C$, switching t_1 and t_2 should result in a sign change of the response, and I checked $R(0, t_1, t_2) = -R(0, t_2, t_1)$, since $\int_0^{-\tau} C_{\mathbf{v}\mathbf{v}}(t) dt = -\int_0^{\tau} C_{\mathbf{v}\mathbf{v}}(-t') dt' = -\int_0^{\tau} C_{\mathbf{v}\mathbf{v}}(t') dt'$.

(3) checked that the response function is exact for 1d-SHO.

Figure 4.13 shows the comparison of the SHO-like approximation with the exact equilibrium OKE response. At long waiting time T , the response function should converge to the excited-state equilibrium OKE response function. We observe that $T = 50$ ps and “long T ” curves overlap with each other, suggesting that 50 ps is long enough for the system to get almost relaxed. Also, we can observe that the large T results including both $T = 50$ ps and “long T ” responses are a little higher in magnitude than short T result ($T = 0$ ps). This observation is in agreement with the fact that in 10% S system, the excited-state OKE response is higher than the ground-state OKE response. For a short T , the geometric structure of system has not changed significantly thus should be close to the equilibrium ground state geometry. Figure 4.13 (b) shows the SHO-like approximation works well in the long T limit for very short time ($t < 0.2$ ps) comparing $T = 50$ ps and “long T ” results with exact result. But in the longer dynamical time t , SHO-like approach could not give a good estimate of the response (Figure 4.13(a)). Figure 4.14 shows that the magnitude of the infinite order $T = 0$ ps response is larger than that of the first order $T = 0$ ps response. However, the infinite order DID approximation and the first order DID approximation are qualitatively equivalent.



(a)



(b)

Figure 4.13 Comparison of response functions using SHO-like approximation at $T = 0$ ps, $T = 50$ ps, long T (uncorrelated with $\exp(\beta\Delta V)$) with the equilibrium excited state OKE response function. Equation 4.88 is used to calculate finite T responses, i.e. $T = 0$ ps, 50 ps. For the long T response, $R = ((1/m) \int_0^t C_{\mathbf{v}\mathbf{v}}(t) dt) \langle \nabla \Pi(0) \cdot \nabla \Pi(t) \rangle_e$. The equilibrium OKE response is evaluated using $R(t) = -\beta (d/dt) \langle \Pi(0) \Pi(t) \rangle_e$. All curves in this figure are calculated using the first order DID approximation. Upper panel (a) shows longer time scale and lower panel (b) shows only the first picosecond.

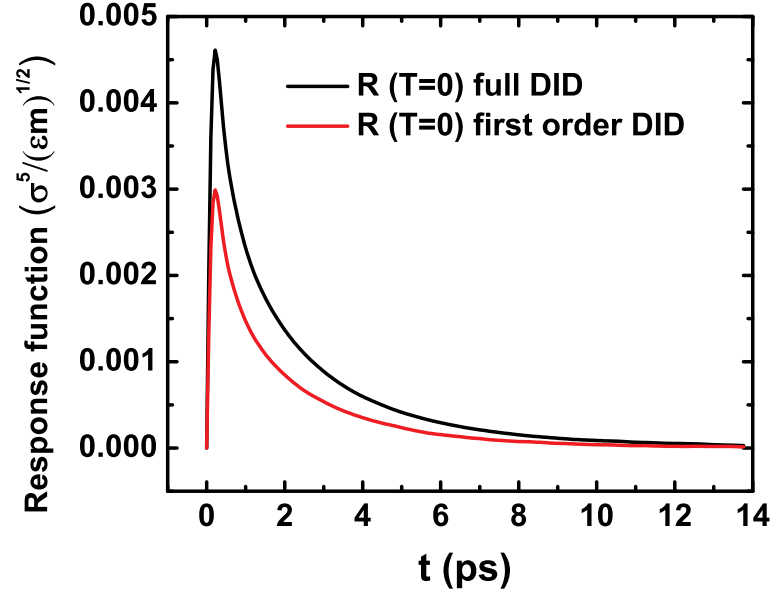


Figure 4.14 Comparison of full DID and first order DID response functions using SHO-like approximation at $T = 0$ ps.

So SHO-like approximation is not good enough to study picosecond dynamics in liquids. The difference between SHO-like approximation and the INM approximation is the basis. In INM treatment, the INM basis is mutually orthogonal, whereas in the SHO-like treatment, the Cartesian basis is usually not orthogonal thus bringing in some error.

4.3.3 Non-INM numerical evaluation

Although direct evaluation of the fundamental Poisson bracket is computing-challenging, it is possible to do so.¹⁹⁷ The fundamental Poisson bracket has its own equation of motion.

Define $3N \times 3N$ Jacobian matrix $\mathbf{J}^{RP}(t) = \boldsymbol{\chi}^T(0, t)$,

$$\boldsymbol{\chi}_{j\mu, kv}(t_1, t_2) = \frac{\partial r_{kv}(t_2)}{\partial p_{j\mu}(t_1)}, \quad (4.89)$$

$$[\mathbf{J}^{RP}(t)]_{j\mu, kv} = \frac{\partial r_{j\mu}(t)}{\partial p_{kv}(0)}. \quad (4.90)$$

Take partial derivative with respect to $p_{kv}(0)$ on the Newton's equation, we have

$$\frac{\partial}{\partial p_{kv}(0)} \left(\ddot{r}_{j\mu}(t) \right) = \frac{\partial}{\partial p_{kv}(0)} \left(-\frac{1}{m} \frac{\partial V}{\partial r_{j\mu}} \Big|_{\mathbf{R}(t)} \right) \quad (4.91)$$

$$\begin{aligned} \Rightarrow [\mathbf{J}^{RP}(t)]_{j\mu, kv} &= \frac{\partial \ddot{r}_{j\mu}(t)}{\partial p_{kv}(0)} = -\frac{1}{m} \sum_{l\xi} \frac{\partial^2 V}{\partial r_{j\mu}(t) \partial r_{l\xi}(t)} \cdot \frac{\partial r_{l\xi}(t)}{\partial p_{kv}(0)} \\ &= -\sum_{l\xi} [\mathbf{D}(t)]_{j\mu, l\xi} [\mathbf{J}^{RP}(t)]_{l\xi, kv}. \end{aligned} \quad (4.92)$$

The equation of motion for the fundamental Poisson bracket is thus

$$\dot{\mathbf{J}}^{RP}(t) = -\mathbf{D}(t)\mathbf{J}^{RP}(t), \quad (4.93)$$

and the initial condition is

$$\mathbf{J}^{RP}(0) = \mathbf{0}, \quad \dot{\mathbf{J}}^{RP}(0) = \frac{1}{m}\mathbf{1}. \quad (4.94)$$

One can solve the equation of motion for the fundamental Poisson bracket using a standard MD numerical integrator to propagate Newton's equation, such as the Verlet algorithm:

$$\mathbf{J}^{RP}(t + \delta t) = 2\mathbf{J}^{RP}(t) - \mathbf{J}^{RP}(t - \delta t) - (\delta t)^2 \mathbf{D}(t) \mathbf{J}^{RP}(t), \quad (4.95)$$

$$\mathbf{J}^{RP}(0) = \mathbf{0}, \quad \dot{\mathbf{J}}^{RP}(-\delta t) = -\frac{1}{m}(\delta t)\mathbf{1}. \quad (4.96)$$

Or the velocity Verlet algorithm:

$$\mathbf{J}^{RP}(t + \delta t) = \mathbf{J}^{RP}(t) + \delta t \dot{\mathbf{J}}^{RP}(t) + \frac{1}{2}(\delta t)^2 [-\mathbf{D}(t)\mathbf{J}^{RP}(t)], \quad (4.97)$$

$$\dot{\mathbf{J}}^{RP}(t + \delta t) = \dot{\mathbf{J}}^{RP}(t) + \frac{1}{2}\delta t [-\mathbf{D}(t)\dot{\mathbf{J}}^{RP}(t) - \mathbf{D}(t + \delta t)\dot{\mathbf{J}}^{RP}(t + \delta t)]. \quad (4.98)$$

$$\mathbf{J}^{RP}(0) = \mathbf{0}, \quad \dot{\mathbf{J}}^{RP}(0) = \frac{1}{m}\mathbf{1}. \quad (4.99)$$

I tested this numerical approach for our preferential solvation model and got noise. In this thesis, we are not going to pursue this numerical approach any further.

4.4 Short-time Expansion of Solute-Pump/Solvent-Probe Response

To test if our hybrid INM/MD method should give us a correct short time behavior, we can perform a Taylor expansion of the response about instantaneous configuration $\mathbf{R}(T)$. The two-dimensional solute-pump/solvent-probe response has the form²²⁰

$$R(0, T, T+t) = \langle A(0) \{B(T), C(T+t)\} \rangle, \quad (4.100)$$

where A, B, C are functions of configuration \mathbf{R} only,

$$A(t) = A(\mathbf{R}(t)) = e^{\beta \delta \Delta V(t)} / \left\langle e^{\beta \delta \Delta V(0)} \right\rangle_e, \quad (4.101)$$

$$B(t) = B(\mathbf{R}(t)) = \Pi_{xz}(t), \quad (4.102)$$

$$C(t) = C(\mathbf{R}(t)) = \Pi_{xz}(t). \quad (4.103)$$

The purpose of this section is to show that the short time t expansion of the solute-pump/solvent-probe response is the same as that obtained using the INM approximation and SHO-like approximation. The response function using the INM approximation is

$$R(0, T, T+t) = \left\langle A(0) \sum_{\alpha} \frac{\sin \omega_{\alpha} t}{m \omega_{\alpha}} \frac{\partial B}{\partial q_{\alpha}} \Big|_T \frac{\partial C}{\partial q_{\alpha}} \Big|_{T+t} \right\rangle. \quad (4.104)$$

and the response function using the SHO-like approximation is

$$R(0, T, T+t) = \frac{1}{m} \int_0^t C_{\mathbf{v}\mathbf{v}}(\tau) d\tau \langle A(0) \nabla_{\mathbf{R}} B(T) \cdot \nabla_{\mathbf{R}} C(T+t) \rangle. \quad (4.105)$$

4.4.1 Exact expansion

The central part of the response function is the Poisson bracket $\{B(T), C(T+t)\}$. Before showing the expansion of exact response function, we shall expand the configuration about $\mathbf{R}(T)$,

$$\mathbf{R}(T+t) = \mathbf{R}(T) + t\dot{\mathbf{R}}(T) + \frac{t^2}{2!}\ddot{\mathbf{R}}(T) + \frac{t^3}{3!}\dddot{\mathbf{R}}(T) + \dots, \quad (4.106)$$

denoting $\nabla \equiv \nabla_{\mathbf{R}} = \frac{\partial}{\partial \mathbf{R}}$, $\nabla_{\mathbf{P}} = \frac{\partial}{\partial \mathbf{P}}$.

$$\dot{\mathbf{R}}(T) = \frac{\mathbf{P}(T)}{m}, \quad (4.107)$$

$$\ddot{\mathbf{R}}(T) = \frac{\mathbf{F}(T)}{m}, \quad (4.108)$$

$$\dddot{\mathbf{R}}(T) = \frac{\partial}{\partial \mathbf{R}} \left(-\frac{\nabla V}{m} \right) \cdot \frac{d\mathbf{R}}{dt} \Big|_{\mathbf{R}(T)} = -\nabla \nabla V(T) \cdot \frac{\mathbf{P}(T)}{m^2}. \quad (4.109)$$

So,

$$\mathbf{R}(T+t) = \mathbf{R}(T) + \frac{t}{m}\mathbf{P}(T) + \frac{t^2}{2m}\mathbf{F}(T) - \frac{t^3}{3!m^2}\nabla \nabla V \cdot \mathbf{P}(T) + \dots. \quad (4.110)$$

Then one can expand the Poisson bracket $\{B(T), C(T+t)\}$ about $\mathbf{R}(T)$,

$$\begin{aligned} \{B(\mathbf{R}(T)), C(\mathbf{R}(T+t))\} &= \nabla_{\mathbf{R}} B|_{\mathbf{R}(T)} \cdot \nabla_{\mathbf{P}} C|_{\mathbf{R}(T+t)} \\ &= \nabla_{\mathbf{R}} B|_{\mathbf{R}(T)} \cdot \left[\nabla_{\mathbf{R}} C|_{\mathbf{R}(T+t)} \cdot \frac{\partial \mathbf{R}(T+t)}{\partial \mathbf{P}(T)} \right], \end{aligned} \quad (4.111)$$

$$\begin{aligned} \nabla_{\mathbf{R}} C|_{\mathbf{R}(T+t)} &= \nabla_{\mathbf{R}} C|_{\mathbf{R}(T)} + \nabla_{\mathbf{R}} \nabla_{\mathbf{R}} C|_{\mathbf{R}(T)} \cdot (\mathbf{R}(T+t) - \mathbf{R}(T)) \\ &\quad + \frac{1}{2} \nabla_{\mathbf{R}} \nabla_{\mathbf{R}} \nabla_{\mathbf{R}} C|_{\mathbf{R}(T)} : (\mathbf{R}(T+t) - \mathbf{R}(T))^2 + \dots. \end{aligned} \quad (4.112)$$

Substitute the expansion of $\mathbf{R}(T+t)$ and the following fundamental Poisson bracket into

the above equation,

$$\frac{\partial \mathbf{R}(T+t)}{\partial \mathbf{P}(T)} = \{\mathbf{R}(T), \mathbf{R}(T+t)\} = \frac{t}{m} \mathbf{1} - \frac{t^3}{3!m^2} \nabla \nabla V(T) + \dots \quad (4.113)$$

Finally, we get the exact short-time expansion of the Poisson bracket,

$$\begin{aligned} \{B(T), C(T+t)\} &= \frac{t}{m} [\nabla B \cdot \nabla C]_T \\ &+ \frac{t^2}{m^2} [\nabla B \cdot \nabla \nabla C \cdot \mathbf{P}]_T \\ &- \frac{1}{3!} \frac{t^3}{m^2} [\nabla B \cdot \nabla \nabla V \cdot \nabla C]_T \\ &+ \frac{1}{2} \frac{t^3}{m^2} [\nabla B \cdot \nabla \nabla C \cdot \mathbf{F}]_T \\ &+ \frac{1}{2} \frac{t^3}{m^3} [\nabla B \cdot \nabla \nabla \nabla C : \mathbf{PP}]_T + O(t^4), \end{aligned} \quad (4.114)$$

and the exact short-time expansion of the solute-pump/solvent-probe response,

$$\begin{aligned} \langle A(0) \{B(T), C(T+t)\} \rangle &= \frac{t}{m} \langle A(0) \nabla B(T) \cdot \nabla C(T) \rangle \\ &+ \frac{t^2}{m^2} \langle A(0) \nabla B(T) \cdot \nabla \nabla C(T) \cdot \mathbf{P}(T) \rangle \\ &- \frac{1}{3!} \frac{t^3}{m^2} \langle A(0) \nabla B(T) \cdot \nabla \nabla V(T) \cdot \nabla C(T) \rangle \\ &+ \frac{1}{2} \frac{t^3}{m^2} \langle A(0) \nabla B(T) \cdot \nabla \nabla C(T) \cdot \mathbf{F}(T) \rangle \\ &+ \frac{1}{2} \frac{t^3}{m^3} \langle A(0) \nabla B(T) \cdot \nabla \nabla \nabla C(T) : \mathbf{P}(T) \mathbf{P}(T) \rangle + O(t^4). \end{aligned} \quad (4.115)$$

4.4.2 INM approximation

By means of diagonalizing the dynamical matrix $\mathbf{D} = \nabla_{\mathbf{R}} \nabla_{\mathbf{R}} V|_{\mathbf{R}(0)}$, (in this section, we use the non-mass-weighted INM, the same as in chapter 1).

$$\mathbf{\Lambda} = \mathbf{U} \mathbf{D} \mathbf{U}^T = \text{diag}\{m\omega_{\alpha}^2\}, \quad (4.116)$$

$$\mathbf{U}_{\alpha, j\mu} = \left. \frac{\partial q_{\alpha}}{\partial r_{j\mu}} \right|_{\mathbf{R}(0)}, \quad (4.117)$$

$$\mathbf{U}_{j\mu, \alpha}^T = \left. \frac{\partial r_{j\mu}}{\partial q_{\alpha}} \right|_{\mathbf{R}(0)}, \quad (4.118)$$

one obtains the independent harmonic INMs ($\alpha = 1, \dots, 3N$)

$$\mathbf{q} = \mathbf{U}(\mathbf{R}(0)) \cdot [\mathbf{R}(t) - \mathbf{R}(0)], \quad (4.119)$$

$$q_{\alpha}(t) = \frac{f_{\alpha}}{m\omega_{\alpha}^2} (1 - \cos \omega_{\alpha} t) + \frac{v_{\alpha}(0)}{\omega_{\alpha}} \sin \omega_{\alpha} t \quad (4.120)$$

$$= v_{\alpha}(0)t + \frac{f_{\alpha}}{2m} t^2 + \dots, \quad (4.121)$$

$$p_{\alpha}(t) = m\dot{q}_{\alpha}(t) = m v_{\alpha}(t). \quad (4.122)$$

Now we can expand the Poisson bracket in the INM basis,

$$\begin{aligned} \{B(\mathbf{R}(t_1)), C(\mathbf{R}(t_2))\} &= \sum_{j\mu} \frac{\partial B(\mathbf{R}(t_1))}{\partial r_{j\mu}(t_1)} \frac{\partial C(\mathbf{R}(t_2))}{\partial p_{j\mu}(t_1)} \\ &= \sum_{j\mu} \sum_{kv} \left. \frac{\partial B(\mathbf{R})}{\partial r_{j\mu}} \right|_{t_1} \left. \frac{\partial C(\mathbf{R})}{\partial r_{kv}} \right|_{t_2} \frac{\partial r_{kv}(t_2)}{\partial p_{j\mu}(t_1)}, \end{aligned}$$

where the fundamental Poisson bracket is

$$\begin{aligned}
\frac{\partial r_{kv}(t_2)}{\partial p_{j\mu}(t_1)} &= \sum_{\alpha,\beta} \frac{\partial r_{kv}(t_2)}{\partial q_\alpha(t_2)} \cdot \frac{\partial q_\alpha(t_2)}{\partial p_\beta(t_1)} \cdot \frac{\partial p_\beta(t_1)}{\partial p_{j\mu}(t_1)} \\
&= \sum_{\alpha,\beta} \mathbf{U}_{kv,\alpha}^T(t_2) \cdot \frac{\partial q_\alpha(t_2)}{\partial p_\beta(t_1)} \cdot \frac{\partial r_{j\mu}(t_1)}{\partial q_\beta(t_1)} \\
&= \sum_{\alpha,\beta} \mathbf{U}_{kv,\alpha}^T(t_2) \cdot \frac{\partial q_\alpha(t_2)}{\partial p_\beta(t_1)} \cdot \mathbf{U}_{j\mu,\beta}^T(t_1) \\
&= \sum_{\alpha,\beta} \mathbf{U}_{kv,\alpha}^T(t_2) \cdot \frac{\sin \omega_\alpha(t_2 - t_1)}{m\omega_\alpha} \delta_{\alpha\beta} \cdot \mathbf{U}_{j\mu,\beta}^T(t_1) \\
&= \sum_{\alpha} \mathbf{U}_{kv,\alpha}^T(t_2) \cdot \frac{\sin \omega_\alpha(t_2 - t_1)}{m\omega_\alpha} \cdot \mathbf{U}_{j\mu,\alpha}^T(t_1). \tag{4.123}
\end{aligned}$$

In above derivation, the second equal sign used the “direct conditions” of the canonical transformation²⁸⁸ $(r_{j\mu}, p_{j\mu}) \rightarrow (q_\alpha, p_\alpha)$,

$$\frac{\partial p_\alpha}{\partial p_{j\mu}} = \frac{\partial r_{j\mu}}{\partial q_\alpha}, \quad \frac{\partial p_\alpha}{\partial r_{j\mu}} = -\frac{\partial p_{j\mu}}{\partial q_\alpha}, \tag{4.124}$$

$$\frac{\partial p_{j\mu}}{\partial p_\alpha} = \frac{\partial q_\alpha}{\partial r_{j\mu}}, \quad \frac{\partial r_{j\mu}}{\partial p_\alpha} = -\frac{\partial q_\alpha}{\partial p_{j\mu}}. \tag{4.125}$$

and the fourth equal sign $\frac{\partial q_\alpha(t_2)}{\partial p_\alpha(t_1)} = \frac{\sin \omega_\alpha(t_2 - t_1)}{m\omega_\alpha}$ is a consequence of $q_\alpha(t) = \frac{f_\alpha}{m\omega_\alpha^2} (1 - \cos \omega_\alpha t) + \frac{p_\alpha(0)}{m\omega_\alpha} \sin \omega_\alpha t$.

Then the derivative with respect to the INM is

$$\left. \frac{\partial B}{\partial q_\alpha} \right|_{t_1} = \sum_{j\mu} \left. \frac{\partial B(\mathbf{R})}{\partial r_{j\mu}} \right|_{t_1} \mathbf{U}_{j\mu,\alpha}^T(t_1), \tag{4.126}$$

$$\left. \frac{\partial C}{\partial q_\alpha} \right|_{t_2} = \sum_{kv} \left. \frac{\partial C(\mathbf{R})}{\partial r_{kv}} \right|_{t_2} \mathbf{U}_{kv,\alpha}^T(t_2). \tag{4.127}$$

The INM fundamental Poisson bracket is

$$\begin{aligned}\chi_{\alpha,\beta}(t_1, t_2) &\equiv \{q_\alpha(t_1), q_\beta(t_2)\} = \frac{\partial q_\alpha(t_2)}{\partial p_\beta(t_1)} = \frac{\sin \omega_\alpha(t_2 - t_1)}{m\omega_\alpha} \delta_{\alpha\beta} \\ &= \chi_\alpha(t_2 - t_1) \delta_{\alpha\beta},\end{aligned}\quad (4.128)$$

$$\chi_\alpha(t) = \frac{\sin \omega_\alpha t}{m\omega_\alpha} = \frac{t}{m} - \frac{1}{3!} \omega_\alpha^2 \frac{t^3}{m} + \dots \quad (4.129)$$

With a full INM treatment without assuming the observable only depends linearly on the coordinates, the Poisson bracket can be expanded into

$$\{B(T), C(T+t)\} = \sum_{\alpha,\beta} \left. \frac{\partial B}{\partial q_\alpha} \right|_T \{q_\alpha(T), q_\beta(T+t)\} \left. \frac{\partial C}{\partial q_\beta} \right|_{T+t} \quad (4.130)$$

$$= \sum_{\alpha} \left. \frac{\partial B}{\partial q_\alpha} \right|_T \frac{\sin \omega_\alpha t}{m\omega_\alpha} \left. \frac{\partial C}{\partial q_\alpha} \right|_{T+t}. \quad (4.131)$$

Within a linear INM theory (which assumes the observables only depend linearly on the INM coordinates), we find (using Equation 4.129) with notation $\nabla_{\mathbf{q}} = \frac{\partial}{\partial \mathbf{q}}$,

$$\begin{aligned}\sum_{\alpha} \left. \frac{\partial B}{\partial q_\alpha} \right|_T \frac{\sin \omega_\alpha t}{m\omega_\alpha} \left. \frac{\partial C}{\partial q_\alpha} \right|_{T+t} &= \frac{t}{m} \sum_{\alpha} \left. \frac{\partial B}{\partial q_\alpha} \right|_T \left. \frac{\partial C}{\partial q_\alpha} \right|_T \\ &\quad - \frac{1}{3!} \frac{t^3}{m^2} \sum_{\alpha} \left. \frac{\partial B}{\partial q_\alpha} \right|_T m\omega_\alpha^2 \left. \frac{\partial C}{\partial q_\alpha} \right|_T + \dots\end{aligned}\quad (4.132)$$

$$= \frac{t}{m} [\nabla_{\mathbf{q}} B \cdot \nabla_{\mathbf{q}} C]_T - \frac{1}{3!} \frac{t^3}{m^2} [\nabla_{\mathbf{q}} B \cdot \mathbf{\Lambda} \cdot \nabla_{\mathbf{q}} C]_T + \dots \quad (4.133)$$

For the full INM theory, the nonlinear INM terms result from the following higher-order terms

$$\left. \frac{\partial C}{\partial q_\alpha} \right|_{T+t} - \left. \frac{\partial C}{\partial q_\alpha} \right|_T = \sum_{\beta} \left. \frac{\partial^2 C}{\partial q_\alpha \partial q_\beta} \right|_T q_\beta(t) + \frac{1}{2!} \sum_{\beta,\gamma} \left. \frac{\partial^3 C}{\partial q_\alpha \partial q_\beta \partial q_\gamma} \right|_T q_\beta(t) q_\gamma(t) + \dots, \quad (4.134)$$

thus the higher-order terms contributing to the Poisson bracket are (using Equation 4.121)

$$\begin{aligned}
& \sum_{\alpha} \frac{\partial B}{\partial q_{\alpha}} \Big|_T \frac{\sin \omega_{\alpha} t}{m \omega_{\alpha}} \left[\frac{\partial C}{\partial q_{\alpha}} \Big|_{T+t} - \frac{\partial C}{\partial q_{\alpha}} \Big|_T \right] \\
&= \frac{t^2}{m} \sum_{\alpha, \beta} \frac{\partial B}{\partial q_{\alpha}} \Big|_T \frac{\partial^2 C}{\partial q_{\alpha} \partial q_{\beta}} \Big|_T v_{\beta}(T) \\
&\quad + \frac{t^3}{2m} \sum_{\alpha, \beta, \gamma} \frac{\partial B}{\partial q_{\alpha}} \Big|_T \frac{\partial^3 C}{\partial q_{\alpha} \partial q_{\beta} \partial q_{\gamma}} \Big|_T v_{\beta}(T) v_{\gamma}(T) \\
&\quad + \frac{t^3}{2m^2} \sum_{\alpha, \beta} \frac{\partial B}{\partial q_{\alpha}} \Big|_T \frac{\partial^2 C}{\partial q_{\alpha} \partial q_{\beta}} \Big|_T f_{\beta}(T) + O(t^4) \tag{4.135}
\end{aligned}$$

$$\begin{aligned}
&= \frac{t^2}{m} [\nabla_{\mathbf{q}} B \cdot \nabla_{\mathbf{q}} \nabla_{\mathbf{q}} C \cdot \mathbf{v}]_T + \frac{t^3}{2m} [\nabla_{\mathbf{q}} B \cdot (\nabla_{\mathbf{q}} \nabla_{\mathbf{q}} \nabla_{\mathbf{q}} C : \mathbf{v}\mathbf{v})]_T \\
&\quad + \frac{t^3}{2m^2} [\nabla_{\mathbf{q}} B \cdot \nabla_{\mathbf{q}} \nabla_{\mathbf{q}} C \cdot \mathbf{f}]_T + O(t^4). \tag{4.136}
\end{aligned}$$

So the full INM approximation to the Poisson bracket exactly matches the exact answer, Equation 4.114, through $O(t^4)$. To prove this statement, we simply use the invariance of these tensor products of gradients to a basis switch, for example, $\nabla_{\mathbf{q}} B \cdot \mathbf{\Lambda} \cdot \nabla_{\mathbf{q}} C = \nabla B \cdot \nabla \nabla V \cdot \nabla C$. However, the linear INM approximation omits terms involving multiple gradients of observables, such as the second, the fourth and the fifth terms on the right-hand side of the following expansion.

$$\begin{aligned}
\{B(T), C(T+t)\} &= \frac{t}{m} [\nabla_{\mathbf{q}} B \cdot \nabla_{\mathbf{q}} C]_T \\
&\quad + \frac{t^2}{m} [\nabla_{\mathbf{q}} B \cdot \nabla_{\mathbf{q}} \nabla_{\mathbf{q}} C \cdot \mathbf{v}]_T \\
&\quad - \frac{1}{3!} \frac{t^3}{m^2} [\nabla_{\mathbf{q}} B \cdot \mathbf{\Lambda} \cdot \nabla_{\mathbf{q}} C]_T \\
&\quad + \frac{t^3}{2m^2} [\nabla_{\mathbf{q}} B \cdot \nabla_{\mathbf{q}} \nabla_{\mathbf{q}} C \cdot \mathbf{f}]_T \\
&\quad + \frac{t^3}{2m} [\nabla_{\mathbf{q}} B \cdot (\nabla_{\mathbf{q}} \nabla_{\mathbf{q}} \nabla_{\mathbf{q}} C : \mathbf{v}\mathbf{v})]_T + O(t^4). \tag{4.137}
\end{aligned}$$

4.4.3 SHO-like approximation

The velocity autocorrelation function has a short-time expansion²⁸⁹

$$C_{\mathbf{v}\mathbf{v}}(t) = \frac{\langle \mathbf{v}(0) \cdot \mathbf{v}(t) \rangle}{\langle \mathbf{v}^2(0) \rangle} = 1 - \frac{t^2}{2} \frac{\langle \dot{\mathbf{v}}^2(0) \rangle}{\langle \mathbf{v}^2(0) \rangle} + \dots \quad (4.138)$$

$$\text{So, } \int_0^t d\tau C_{\mathbf{v}\mathbf{v}}(\tau) = t - \frac{t^3}{6} \frac{\langle \mathbf{F}^2(0) \rangle}{3Nmk_B T} + \dots \quad (4.139)$$

Insert the expansion of $\nabla C(T+t)$ (Equation 4.112) into the response

$$\begin{aligned} R(0, T, T+t) &= \frac{1}{m} \left[t - \frac{t^3}{6} \frac{\langle \mathbf{F}^2(0) \rangle}{3Nmk_B T} + \dots \right] \langle A(0) \nabla B(T) \cdot \nabla C(T+t) \rangle \quad (4.140) \\ &= \frac{t}{m} \langle A(0) \nabla B(T) \cdot \nabla C(T) \rangle \\ &\quad + \frac{t^2}{m^2} \langle A(0) \nabla B(T) \cdot \nabla \nabla C(T) \cdot \mathbf{P}(T) \rangle \\ &\quad - \frac{1}{3!} \frac{t^3}{m^2} \langle A(0) \nabla B(T) \cdot \nabla C(T) \rangle \cdot \frac{\langle \mathbf{F}^2(0) \rangle}{3Nk_B T} \\ &\quad + \frac{1}{2} \frac{t^3}{m^2} \langle A(0) \nabla B(T) \cdot \nabla \nabla C(T) \cdot \mathbf{F}(T) \rangle \\ &\quad + \frac{1}{2} \frac{t^3}{m^3} \langle A(0) \nabla B(T) \cdot \nabla \nabla \nabla C(T) : \mathbf{P}(T) \mathbf{P}(T) \rangle + O(t^4). \quad (4.141) \end{aligned}$$

Only the third term in the above equation appears different from the exact expansion $-\frac{1}{3!} \frac{t^3}{m^2} \langle A(0) \nabla B(T) \cdot \nabla \nabla V(T) \cdot \nabla C(T) \rangle$. Although they look similar considering the following relation

$$\langle \nabla \nabla V \rangle = \frac{1}{Q} \int d\mathbf{R} e^{-\beta V} \nabla \nabla V = -\frac{1}{Q} \int d\mathbf{R} \left(-\beta e^{-\beta V} \nabla V \right) \nabla V = \beta \langle \mathbf{F} \mathbf{F} \rangle, \quad (4.142)$$

they are fundamentally different because the ensemble average of a product is not equal to a product of ensemble averages. This term probably introduces a relatively large error. Thus the SHO-like approximation only gives the short-time expansion exact through $O(t^3)$.

4.5 2D Solute-Pump/Solvent-Probe Spectra for Our Model

In the previous section, it was demonstrated that the hybrid INM/MD method is able to handle the ultrafast dynamics in our model at the long waiting time limit ($T \rightarrow \infty$) and for finite waiting times, it was shown that the short-time expansion for the nonequilibrium solute-pump/solvent-probe response is exact through $O(t^4)$ (at least within a full nonlinear INM treatment). In this section, we are going to compute the full 2D solute-pump/solvent-probe spectra for our preferential solvation model. In order to have a good averaging, the simulated molecular system is chosen to be a single solute and 107 solvent atoms. For computational efficiency, the calculations are limited to first-order DID approximated polarizabilities. Figure 4.15 and Figure 4.16 display the full two-dimensional solute-pump/solvent-probe spectra for our 10% S and 50% S preferential solvation model calculated using the hybrid INM/MD method. For each waiting time T , the ultrafast intermolecular vibrational dynamics is evaluated in the basis of the INMs at that time, with the imaginary frequencies plotted on the negative frequency axis. However, from previous INM analysis of OKE spectra at the large waiting time limit, we know that the INM method is likely to overestimate the response for frequencies $\omega < 25 \text{ cm}^{-1}$, so the trustworthy region of the INM predictions to the 2D spectra is likely to be frequencies higher than 25 cm^{-1} . For the 10% S solvent mixture, we can clearly see the progression of the ultrafast vibrational spectra with increasing waiting time T . By contrast, for the 50% S solvent mixture, the progression of the ultrafast vibrational spectra is not so easy to observe.

We can find some answer to why it is hard to observe the progression of the ultrafast vibrational spectra in 50% S mixture from Figure 4.17, which reveals the error bars for finite- T spectra for both 10% S and 50% S solvent mixtures and their comparison with the e-g differences. The statistical error at a certain frequency and time delay T is calculated in the following way. For every single configuration, we treat the response function in each histogram bin with associated range of frequency as a data point, and the sample size is

the number of configurations, N_{conf} . The statistical errors for response functions $R(\omega, T)$, $R_g(\omega)$ and $\Delta R(\omega, T) = R(\omega, T) - R_g(\omega)$ are defined as $\sigma_R(\omega, T)$, $\sigma_g(\omega)$ and $\sigma_{\Delta R}(\omega, T)$, respectively. The error bars plotted in Figure 4.17 are $\pm\sigma_{\Delta R}(\omega, T)$ for fixed waiting time T .

$$\begin{aligned}\sigma_R(\omega, T) &= \frac{1}{\sqrt{N_{\text{conf}} - 1}} \sqrt{\langle [\delta R(\omega, T)]^2 \rangle} \\ &\approx \frac{1}{\sqrt{N_{\text{conf}}}} \sqrt{\langle R^2(\omega, T) \rangle - \langle R(\omega, T) \rangle^2},\end{aligned}\quad (4.143)$$

$$\text{and } \sigma_g(\omega) = \frac{1}{\sqrt{N_{\text{conf}}}} \sqrt{\langle R_g^2(\omega) \rangle - \langle R_g(\omega) \rangle^2},\quad (4.144)$$

$$\text{so } \sigma_{\Delta R}(\omega, T) = \sqrt{\sigma_R^2(\omega, T) + \sigma_g^2(\omega)}.\quad (4.145)$$

Accordingly an increase in the number of configurations leads to a smaller error.

In the 10% S case, the e-g difference has very small statistical errors across the whole range of frequencies, whereas the $T=15$ ps spectrum has somewhat bigger error bars but still quite narrow. In the 10% S system there is a clean separation between the finite- T result and the e-g difference due to relatively small fluctuations. On the contrary, the 50% S system has much larger relative fluctuations in the finite- T spectra than the 10% S system, to the point that the 50% S error bars are greater than the difference between the finite- T result and the e-g difference (even though the spectra of the 50% S system are computed by averaging over four times more number of liquid configurations as in the 10% S system). The reason for higher signal-to-noise level in 10% S than in 50% S is unclear, except for the fact that 10% S has a larger relative change in strong solvent population than 50% S. Based on this observation, the solute-pump/solvent-probe spectroscopy may not be keen on picking up the puny change of dynamics in the 50% S system, thus this system may not be a good candidate to test our newly developed theory for the 2D spectra. We will focus on the 10% S system in the rest of the chapter.

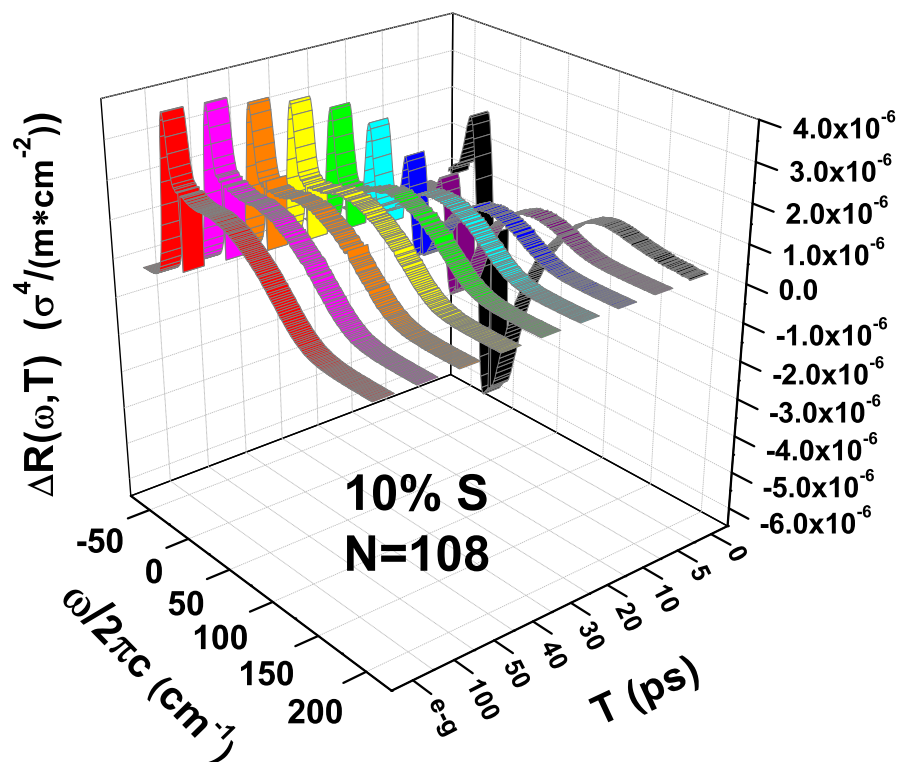


Figure 4.15 Two-dimensional solute-pump/solvent-probe spectra for our preferential solvation system 10% S solvent mixtures. The 2D spectra were calculated by hybrid INM/MD methods, and the simulated system contains a single solute and 107 solvent atoms. The frequency ω corresponds to the ultrafast intermolecular vibrational dynamics (t) and the imaginary INM frequencies are plotted on the negative frequency axis. The spectra show how the ultrafast dynamics evolves with the waiting time T after the solute excitation. The large T limit (e-g) is the difference between excited- and ground-state INM OKE influence spectra. The results are averaged over 1.6×10^7 liquid configurations using first-order many-body polarizabilities.

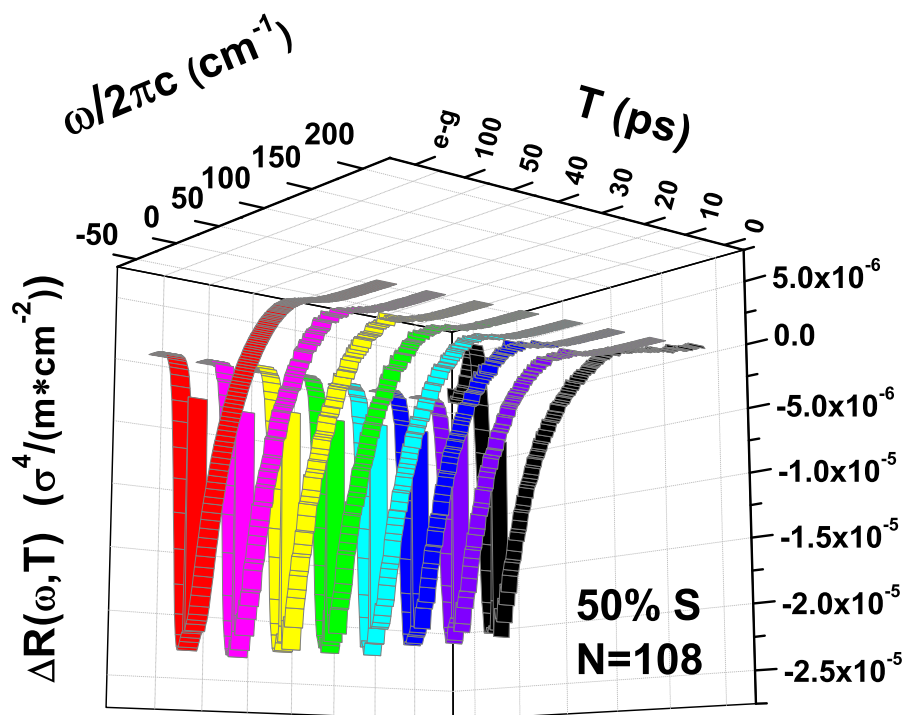
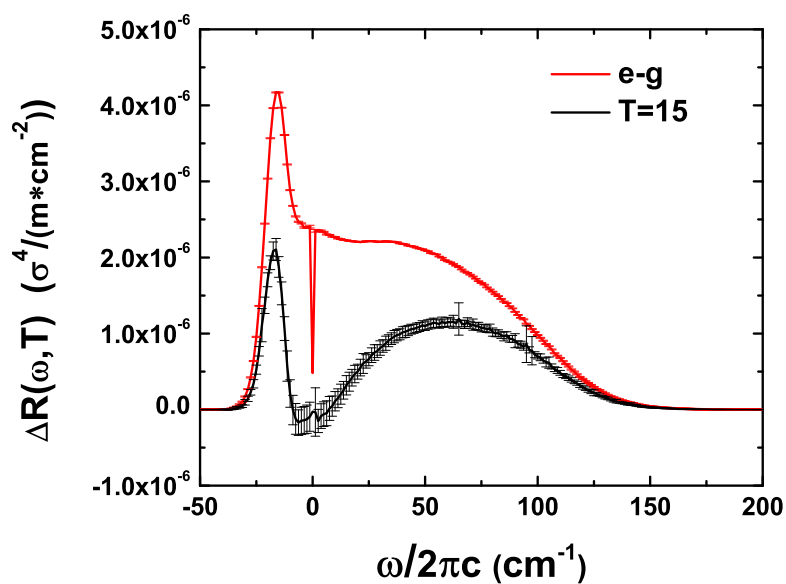
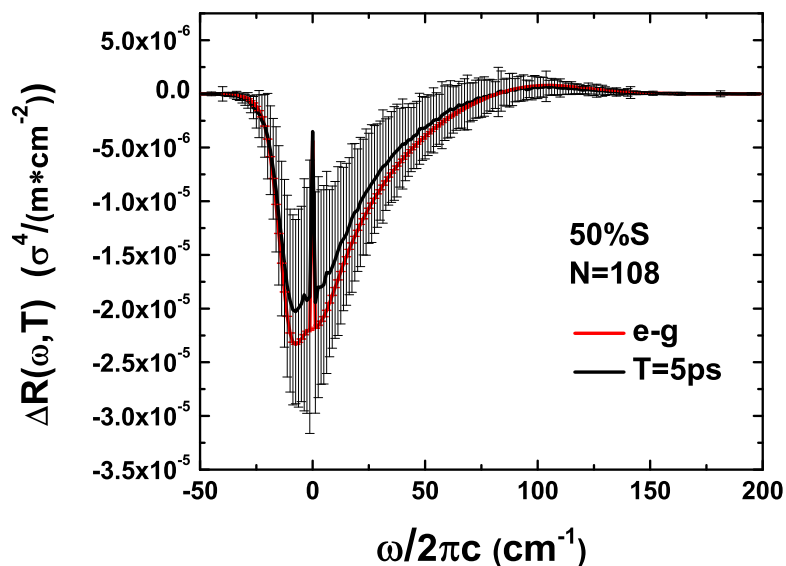


Figure 4.16 Two-dimensional solute-pump/solvent-probe spectra for our preferential solvation system 50% S solvent mixtures. The 2D spectra were calculated by hybrid INM/MD methods, and the simulated system contains a single solute and 107 solvent atoms. The frequency ω corresponds to the ultrafast intermolecular vibrational dynamics and the imaginary INM frequencies are plotted on the negative frequency axis. The spectra show how the ultrafast dynamics evolves with the waiting time T after the solute excitation. The large T limit (e-g) is the difference between excited- and ground-state INM OKE influence spectra. The results are averaged over 1.6×10^7 liquid configurations using first-order many-body polarizabilities.



(a)



(b)

Figure 4.17 Comparison of the fluctuations of solute-pump/solvent-probe responses at a finite waiting time T with that of the equilibrium e-g difference in INM OKE influence spectra for our preferential solvation system including a single solute and 107 solvent atoms. (a) 10% S solvent mixture, $T=15$ ps and e-g difference; (b) 50% S solvent mixture, $T=5$ ps and e-g difference. The results for 10% S and 50% S mixtures are calculated by averaging 1.6×10^7 and 8×10^7 liquid configurations, respectively, using first-order many-body polarizabilities. Note the two panels are different in scale.

4.6 Structural Information in Preferential Solvation

4.6.1 First-shell population dynamics

The most important result of this chapter, Figure 4.18, depicts the real-frequency 2D solute-pump/solvent-probe spectra for the 10% S solvent mixture. (Note that the direction of the waiting time T axis is opposite of that in Figure 4.15.) The T -dependent ultrafast vibrational spectra evidently converge to the equilibrium e–g difference in the optical Kerr spectra within 50–100 ps. The time scale for this convergence is broadly consistent with the time scale for the solvation correlation function of the same 10% S solvent mixture ($C(t)$ in Figure 3.3). However, to describe the relaxation observed by the 2D solute-pump/solvent-probe spectra quantitatively, one can define a normalized relaxation profile for the spectra at any chosen vibrational frequency ω :

$$S(T; \omega) = \frac{\Delta R(\omega; T) - \Delta R(\omega; T = \infty)}{\Delta R(\omega; T = 0) - \Delta R(\omega; T = \infty)}. \quad (4.146)$$

This profile $S(T; \omega)$ reflects the relaxation of the ultrafast dynamics that the spectroscopy is most sensitive to, at any given frequency. In Figure 4.19, the spectroscopic relaxation profiles $S(T)$ at fixed frequencies 50 cm^{-1} and 75 cm^{-1} are compared with the solute-solvent interaction energy relaxation $C_{\Delta V}(t)$, the first-shell population relaxation correlation function $C_{n_S}(t)$ and their cross correlation $C_{\Delta V, n_S}(t)$. These correlation functions are defined as follows.

$$C_{\Delta V}(t) = \frac{\langle \delta \Delta V(0) \delta \Delta V(t) \rangle_e}{\langle (\delta \Delta V)^2 \rangle_e}, \quad (4.147)$$

$$C_{n_S}(t) = \frac{\langle \delta n_S(0) \delta n_S(t) \rangle_e}{\langle (\delta n_S)^2 \rangle_e}, \quad (4.148)$$

$$C_{\Delta V, n_S}(t) = \frac{\langle \delta \Delta V(0) \delta n_S(t) \rangle_e}{\langle (\delta \Delta V)(\delta n_S) \rangle_e}, \quad (4.149)$$

where n_S is the number of S solvents in the first solvation shell of the solute and its fluctuation is defined as $\delta n_S \equiv n_S - \langle n_S \rangle_e$. Thus, correlation function $C_{n_S}(t)$ is a direct measure of the solvent structural relaxation.

Figure 4.19 displays a remarkable agreement between this structural correlation function and the spectroscopic relaxation profiles $S(T)$. The spectroscopic relaxation profiles at two frequencies (50 cm^{-1} and 75 cm^{-1}) are virtually identical. In addition, the mixed energy/structure cross correlation function $C_{\Delta V, n_S}(t)$ agrees quantitatively with the spectroscopic profiles. However, the spectroscopic profiles are noticeably faster than the standard potential-energy solvation relaxation $C_{\Delta V}(t)$. In other words, the solute-pump/solvent-probe spectra seems to be able to single out the explicitly structural dynamics featured by the first-shell population relaxation rather than the energetic dynamics described by the potential-energy solvation relaxation. Therefore, the two-dimensional spectra offers a new molecular perspective on solvation dynamics by reporting on direct structural dynamics of the solvent. This structural dynamics has a different relaxation rate from the energetic dynamics measured by traditional time-dependent fluorescence.

The error bars of the spectroscopic profiles $S(T)$ are essential — they are small enough to separate spectroscopic profiles from the potential-energy solvation relaxation. The determination of the error bars of $S(T)$ follows those formulas below. For any variable $X = u/v$, the standard deviation of X satisfies

$$\begin{aligned} \sigma_X^2 &= \sigma_u^2 \left(\frac{\partial X}{\partial u} \right)_{\bar{u}}^2 + \sigma_v^2 \left(\frac{\partial X}{\partial v} \right)_{\bar{v}}^2 = \frac{\sigma_u^2}{\bar{v}^2} + \frac{\sigma_v^2 \bar{u}^2}{\bar{v}^4} \\ \Rightarrow \left(\frac{\sigma_X}{\bar{u}/\bar{v}} \right)^2 &= \left(\frac{\sigma_u}{\bar{u}} \right)^2 + \left(\frac{\sigma_v}{\bar{v}} \right)^2. \end{aligned} \quad (4.150)$$

Applying the above relation, we have the errors for $S(T)$,

$$S(T; \omega) = \frac{R(\omega; T) - R_e(\omega)}{R(\omega; T=0) - R_e(\omega)} \quad (4.151)$$

$$\left(\frac{\sigma_{S(T; \omega)}}{S(T; \omega)} \right)^2 = \left(\frac{\sigma_{R(\omega, T) - R_e(\omega)}}{R(\omega, T) - R_e(\omega)} \right)^2 + \left(\frac{\sigma_{R(\omega, 0) - R_e(\omega)}}{R(\omega, 0) - R_e(\omega)} \right)^2, \quad (4.152)$$

where

$$\sigma_{R(\omega, T) - R_e(\omega)}^2 = \sigma_R^2(\omega, T) + \sigma_e^2(\omega), \quad (4.153)$$

$$\sigma_e^2(\omega) = \frac{1}{N_{\text{conf}}} [\langle R_e^2(\omega) \rangle - \langle R_e(\omega) \rangle^2]. \quad (4.154)$$

The error bars plotted in Figure 4.19 are $\pm \sigma_{S(T; \omega)}$.

Figure 4.20 presents the evolution of strong solvent population distributions in the first shell and second shell for our preferential solvation systems 10% S and 50% S. The first-shell population varies more dramatically than the second-shell population in both systems and exhibits no significant visible change after $T=60$ ps in 10% S and after $T=40$ ps in 50% S. Figure 4.21 compares the structural correlation with the energetic correlation along with their cross correlation in the 50% S system. The difference between the first-shell population relaxation and the solute-solvent energy correlation in the 50% S system is not as discernible as that in the 10% S system. The indistinguishable structural dynamics and energetic dynamics in the 50% S solvent mixture also make it difficult to tell what microscopic information the 2D spectra pick up.

It is important to note that the 2D nonequilibrium spectra are more sensitive to structural changes in some systems than in others. Besides noting that the 10% S has a better signal than 50% S system, one can switch the polarizabilities of S and W solvents (with $\alpha_S = 0.73 \text{ \AA}^3$ and $\alpha_W = 3.99 \text{ \AA}^3$) in the same preferential solvation system with 10% S solvent. The resulting 2D spectra are plotted in Figure 4.22 and look very different from the normal polarizability case plotted in Figure 4.18. Although the Hamiltonians, initial conditions and

hence the dynamics of the two 10% S systems are absolutely identical, now the primary structural change during the preferential solvation involves approximately a 130% increase in the spectroscopically dark S solvents in the first shell and only 12% decrease in the abundant spectroscopically bright background W solvents. It is not surprising to see almost no progression of the 2D spectra after the first 2 ps in Figure 4.22.

So why could this spectroscopy serve as a good structural probe and why is the spectrum closely connected to the first-shell population dynamics? According to our previous $T \rightarrow \infty$ analysis, the solvation shells beyond the first also contribute significantly to the difference spectrum. The key to answer these questions is related to *how* the solvation shell populations change. We will explore another piece of structural information in our preferential solvation model, the distributions of strong-solvent/solute/strong-solvent bond angles, in the following section.

4.6.2 Bond-angle distribution

For the sake of understanding the solute-pump/solvent-probe spectroscopy, we look at the T -dependent bond-angle distribution of solvent pairs with respect to the solute, which reflects the solvent orientational dynamics within the region close to the solute. Considering a solvent mixture with strong and weak kinds of solvent, we focus on strong solvent and denote θ as the bond angle between different solute-strong-solvent pairs in a given shell (or pair of shells), see Figure 4.23. We define the distribution of $\cos \theta$ as follows.

$$\rho(\cos \theta)_T = \frac{1}{\#\text{SSpairs}} \sum_{j < k} \delta [\cos \theta - \hat{\Omega}_j(T) \cdot \hat{\Omega}_k(T)], \quad (4.155)$$

where $\hat{\Omega}_j(T)$ is the unit vector with the direction from the solute to the solvent j at time T and the summation runs over all the strong solvent pairs in selected region such as the first shell and the second shell. To evaluate the $\cos \theta(T)$, one can take advantage of

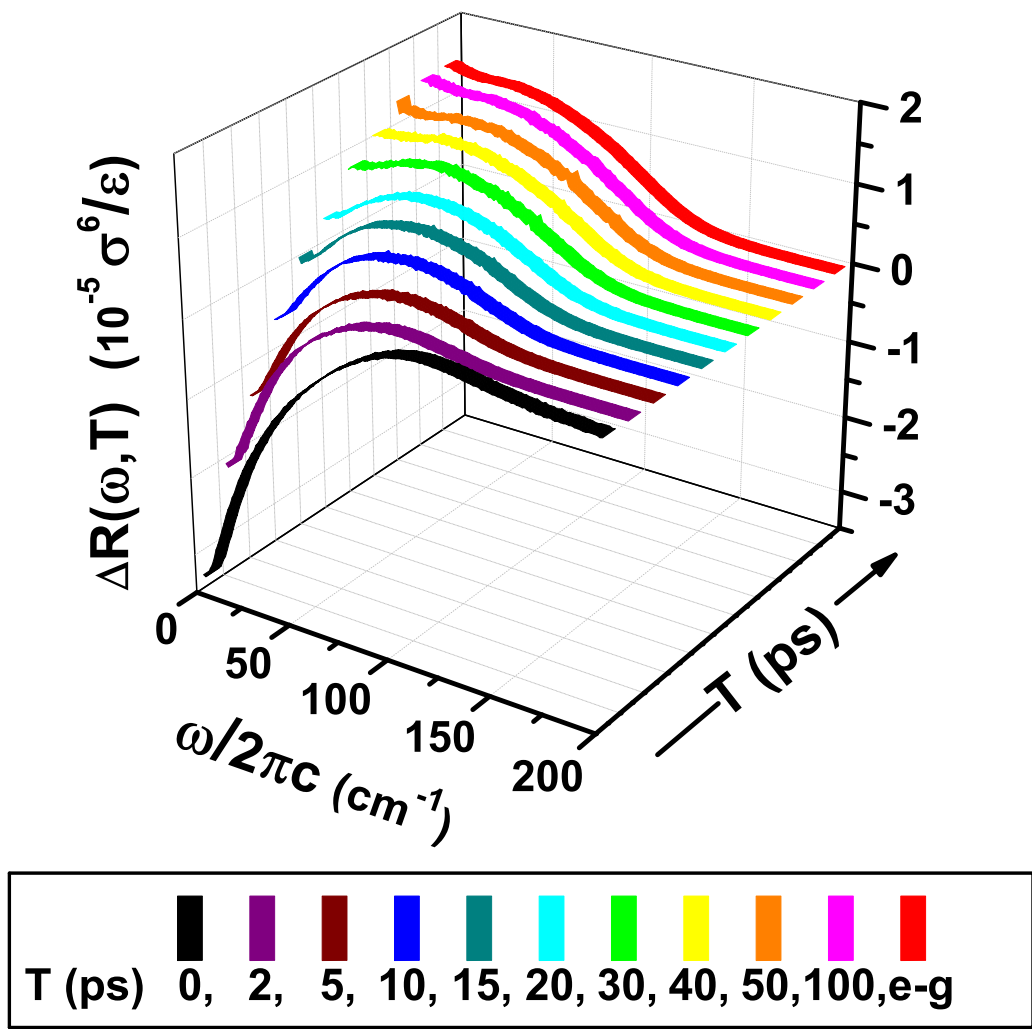


Figure 4.18 The principal result of this chapter: two-dimensional solute-pump/solvent-probe spectra for our 10% S preferential solvation system (a single solute atom and 107 solvent atoms). The spectra are calculated using hybrid INM/MD methods and averaging over 1.6×10^7 liquid configurations with first-order approximated many-body polarizabilities. The larger T limit (e-g) is the difference in INM optical Kerr influence spectra for solutions with excited- and ground-state solute. The 2D spectra show how the solution's intermolecular vibrational spectrum (as a function of ω) evolves with increasing delay time T after the solute excitation.

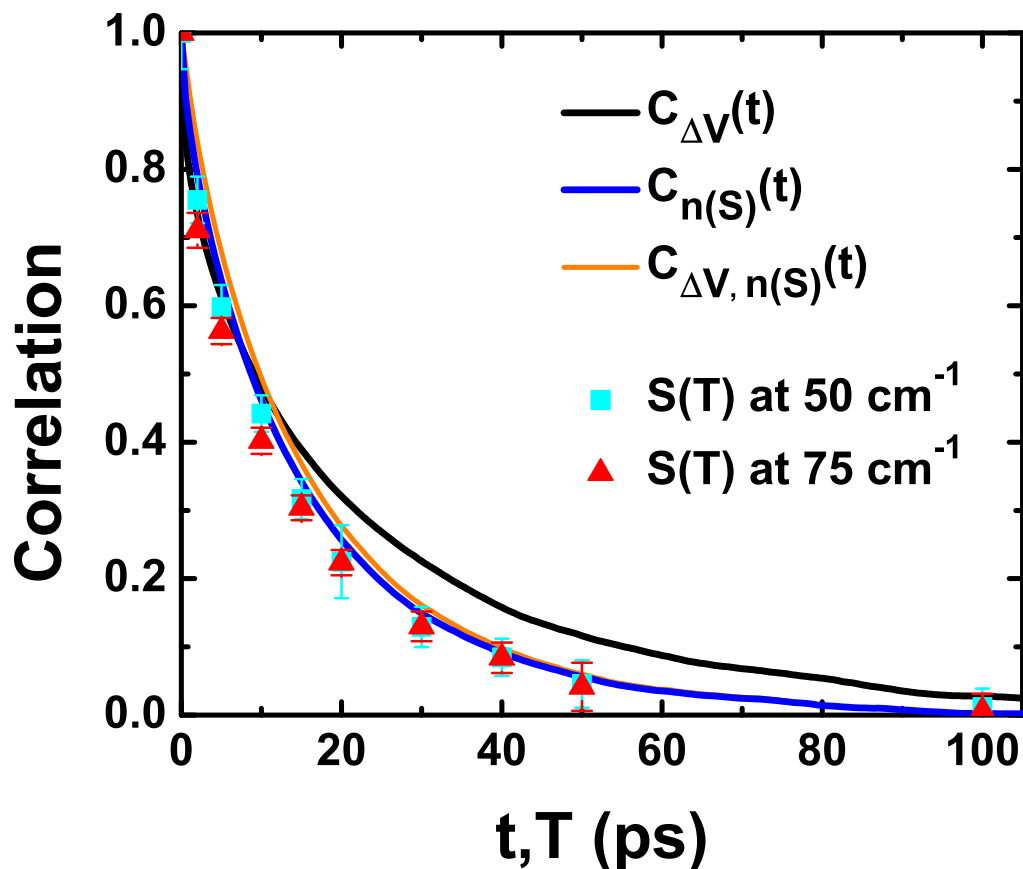


Figure 4.19 Most revealing analysis of this chapter: comparison of the relaxation profile observed by solute-pump/solvent-probe spectra with structure- and potential-energy-sensitive equilibrium solvation correlation functions for our 10% S preferential solvation system. The normalized relaxation profile $S(T)$ of the 2D spectra (Figure 4.18) is calculated by tracking the spectroscopic response functions $\Delta R(\omega, T)$ as a function of solvation time T for some fixed intermolecular vibrational frequencies ω . The chosen frequencies are $\omega/(2\pi c) = 50$ and 75 cm^{-1} shown here as triangles and squares, respectively. The potential-energy-sensitive measure of solvation (black line) is the standard solvation correlation function $C_{\Delta V}(t)$. The structure-sensitive measure of solvation (blue line) is the normalized correlation function for the number of strong solvent in the first solvation shell, $C_{n(S)}(t)$. The cross correlation (orange line) between the fluctuations of potential-energy gap and the number of strong solvent in the first shell $C_{\Delta V, n(S)}(t)$ is also included. Both the structure-sensitive and the cross correlation functions were computed by averaging over 9.2×10^5 liquid configurations in a solution with a single solute and 107 solvents.

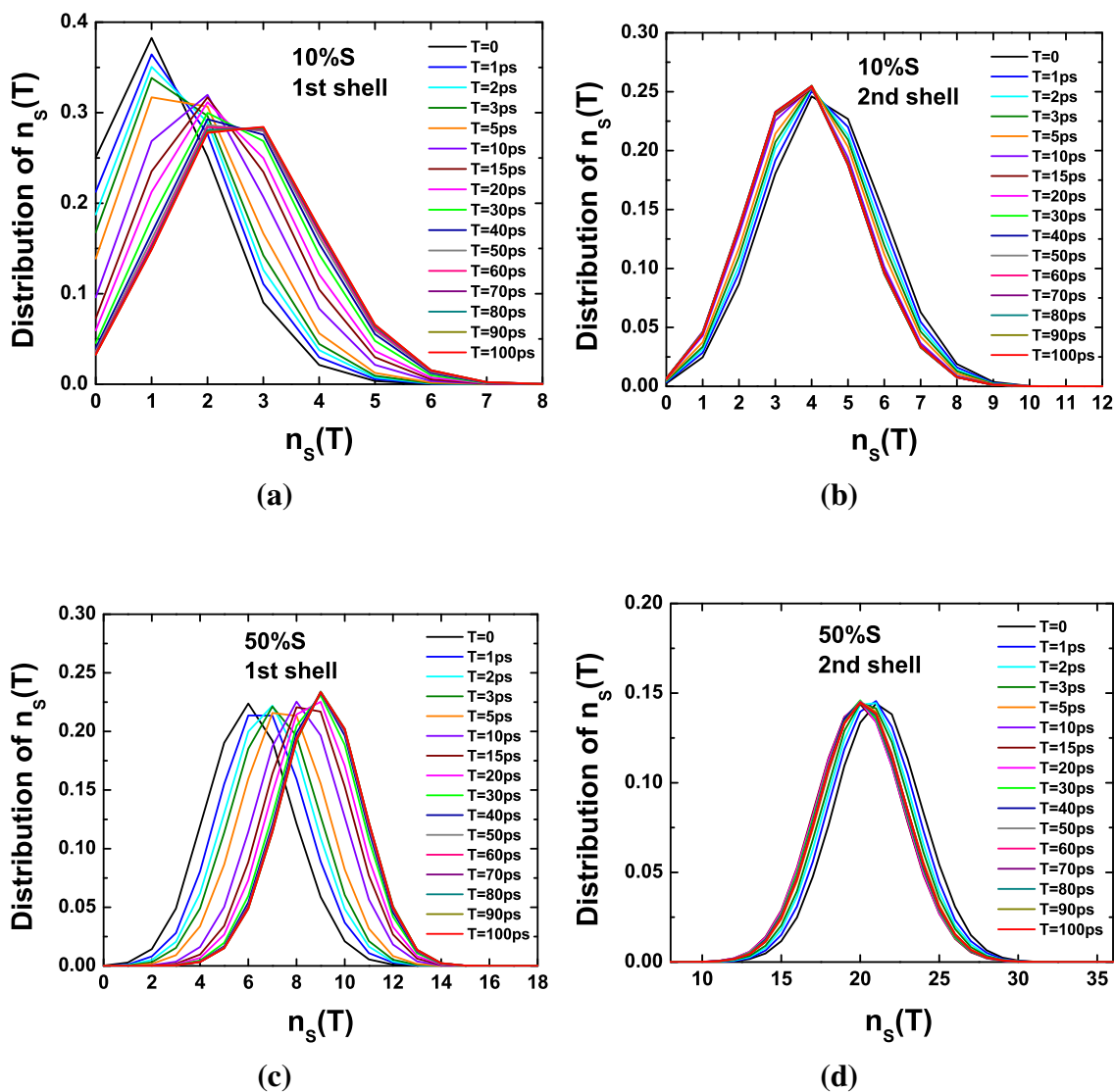


Figure 4.20 Evolution of strong solvent population distributions in the first solvation shell and in the second solvation shell for both 10% S solvent mixture and 50% S solvent mixture following the resonant solute excitation. The normalized population distribution functions are averaged over 5×10^5 nonequilibrium trajectories.

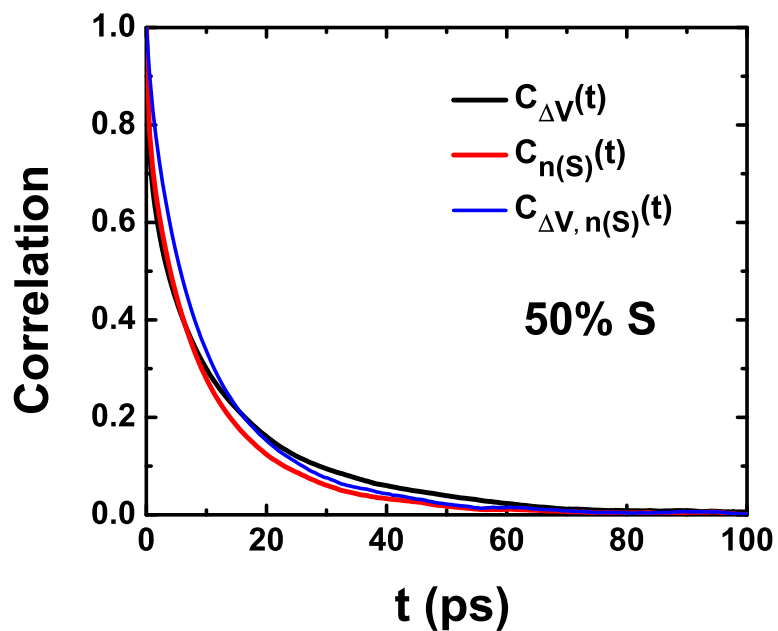


Figure 4.21 Comparison of the structure- and potential-energy-sensitive equilibrium solvation correlation functions for our 50% S preferential solvation system. The potential energy-sensitive measure of solvation (black line) is the standard solvation correlation function $C_{\Delta V}(t)$. The structure-sensitive measure of solvation (red line) is the normalized correlation function for the number of strong solvent in the first solvation shell, $C_{n(S)}(t)$. The cross correlation (blue line) between the potential-energy gap and the number of strong solvent in the first shell $C_{\Delta V, n(S)}(t)$ is also included. Both the structure-sensitive and the cross correlation functions were computed by averaging over 9.2×10^5 liquid configurations in a solution with a single solute and 107 solvents.

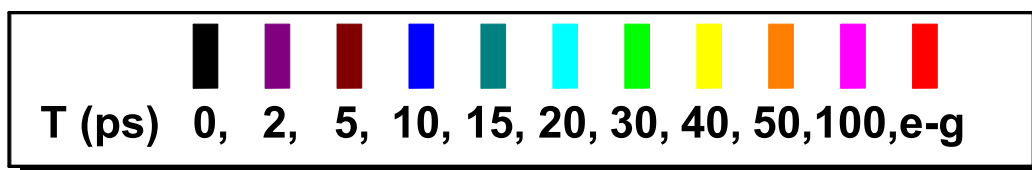
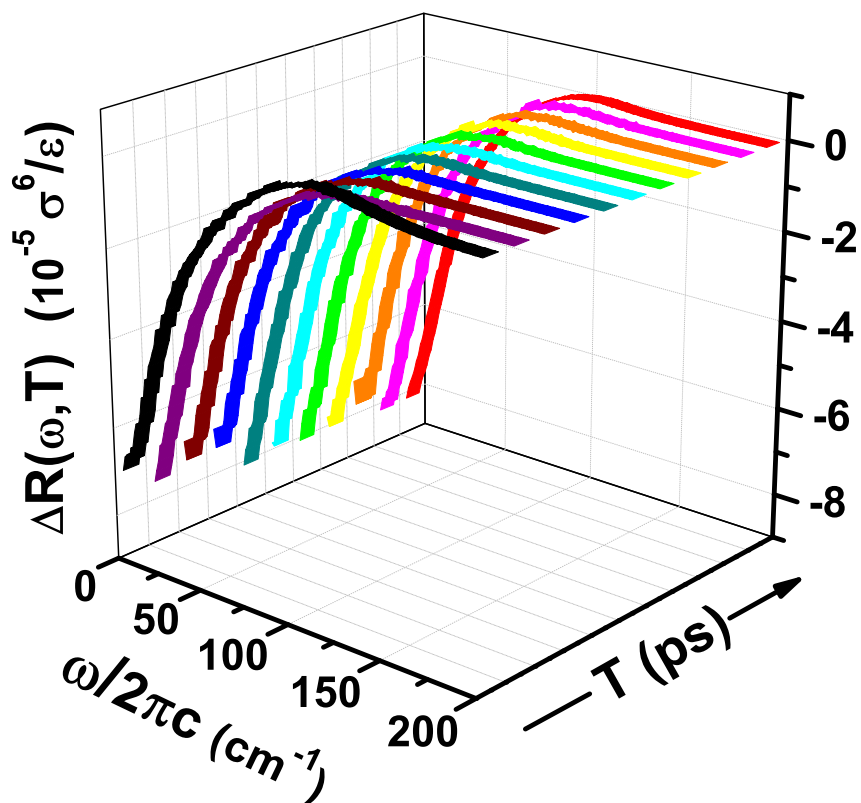


Figure 4.22 Two-dimensional solute-pump/solvent-probe spectra for our *polarizability-switched* 10% S preferential solvation system (a single solute atom and 107 solvent atoms). The spectra are calculated using hybrid INM/MD methods and averaging over 1.6×10^7 liquid configurations with first-order approximated many-body polarizabilities. The long T limit result (e-g) is the difference in INM OKE influence spectra for solutions with excited- and ground-state solute. The 2D spectra show how the solution's intermolecular vibrational spectrum (as a function of ω) evolves with increasing delay time T after the solute excitation.

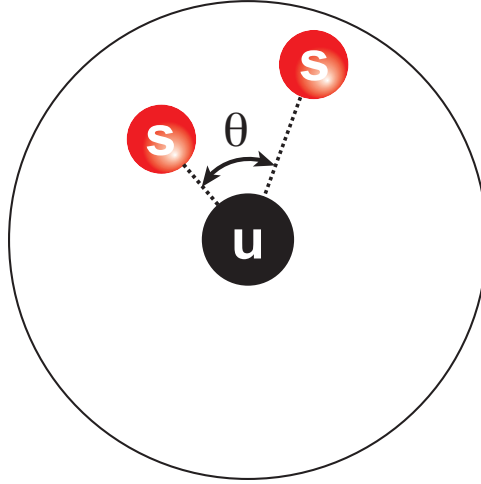


Figure 4.23 Illustration of the bond angle between strong solvent pair and the solute.

nonequilibrium simulations and average over different nonequilibrium trajectories whose initial configurations are samples from equilibrium ground state. For each configuration at time T , we first count the number of strong solvent pairs, i.e. $\#SSpairs$, in selected region such as the first shell and the second shell, then bin the dot product of orientation vectors with weight $1/\#SSpairs$. Once the histogram of $\cos \theta$ is obtained, one normalizes the histogram to get the angular distribution such that

$$\int_{-1}^1 d(\cos \theta) \rho(\cos \theta)_T = 1, \quad \forall T. \quad (4.156)$$

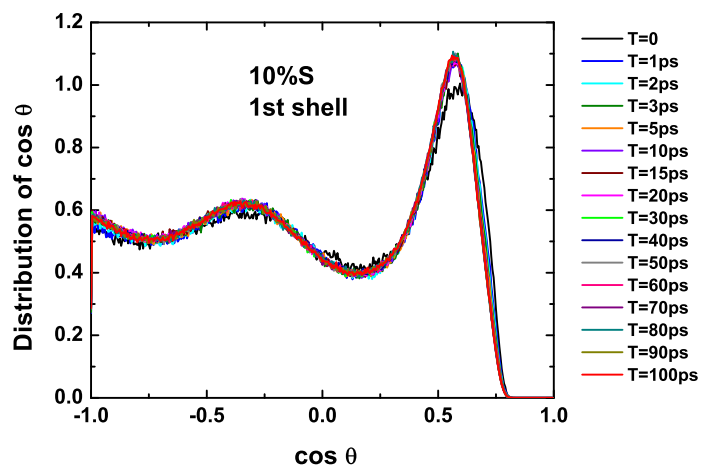
Figure 4.24 and Figure 4.25 show the T -dependent bond-angle distribution for 10%S and 50% systems ($N=108$) respectively. In the first shell bond-angle distributions, the highest peak is located at $\cos \theta=0.58$ which corresponds to an angle of 54.5° . This shape is similar with the literature.^{290,291} In the joint first-and-second-shell distributions, the highest peak at $\cos \theta=0.88$ decreases while the second highest peak ($\cos \theta=0.55$) grows. This corresponds to the small angle 30° population gets lower and the middle angle 57° population getting higher, because the strong solvent is more attracted to the excited solute and when the strong solvent gets close or even nearly close-packed around the solute, the small angle are rarer.

In both systems, the bond-angle distribution in the first shell arrives at equilibrium very quickly — in less than 2 ps. But the bond-angle distribution in the joint first and second shells has much longer time scale, which is closer to the $1/e$ solvation time scales in each system than the distribution in the first shell. For example, we observe that in 10% S system, the highest peak of the distribution in the first and second shells converges about 30 ps (see the inset in Figure 4.24 (c)). From T -dependent peaks of bond-angle distribution, we can determine a relaxation profile for this orientational dynamics and the profile can be used to compare with the time scales in the 2D spectra and other structural time scales. The definition of the bond-angle relaxation is

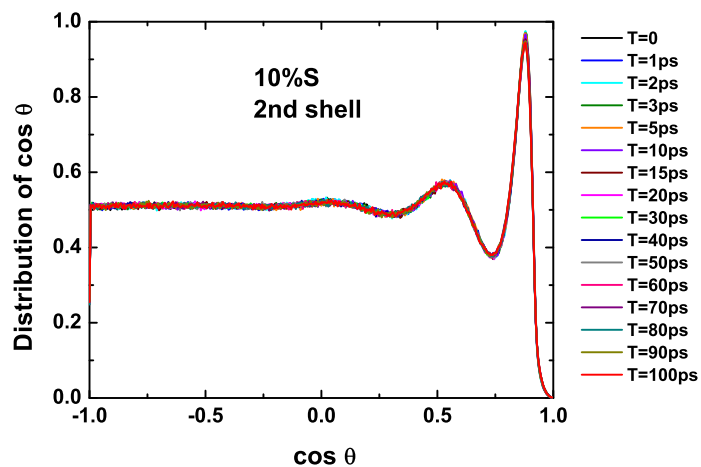
$$S_{\theta}(T) = \frac{\int_{\text{peak}} \rho(\cos \theta)_T d \cos \theta - \int_{\text{peak}} \rho(\cos \theta)_{T=\infty} d \cos \theta}{\int_{\text{peak}} \rho(\cos \theta)_0 d \cos \theta - \int_{\text{peak}} \rho(\cos \theta)_{T=\infty} d \cos \theta}, \quad (4.157)$$

where the integral are calculated over a peak region. Figure 4.26 shows the comparison between the bond-angle relaxation, the first-shell population relaxation and the potential energy gap correlation function. We can observe that the smaller angle (around 30°) relaxes faster than the first shell population whereas the larger angle (around 60°) relaxes slower than the first shell population. The distinction between bond-angle distributions of strong solvent in the first shell and the first+second shells in Figure 4.24 suggests that the overall solvation dynamics is not restricted to the first shell, and the second shell takes a very important part. But from the pure second-shell bond-angle distribution for the 10% S (Figure 4.24 (b)), there is no visible change in the whole range of waiting time T . This observation suggests that the slow changing bond angles seems to be those involving one strong solvent in the first shell and the other in the second shell.

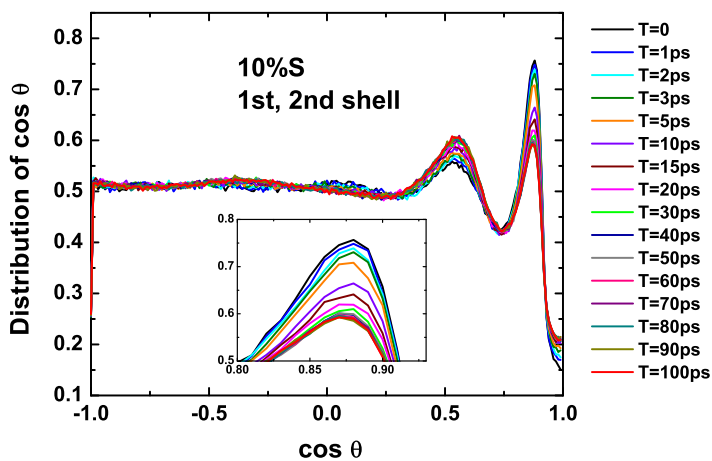
How do we interpret the bond-angle distribution in liquid, and how do we assign those peaks? Consider the equivalent bond-angle distribution one would get if the solution were ordered in a close-packed lattice structure.



(a)

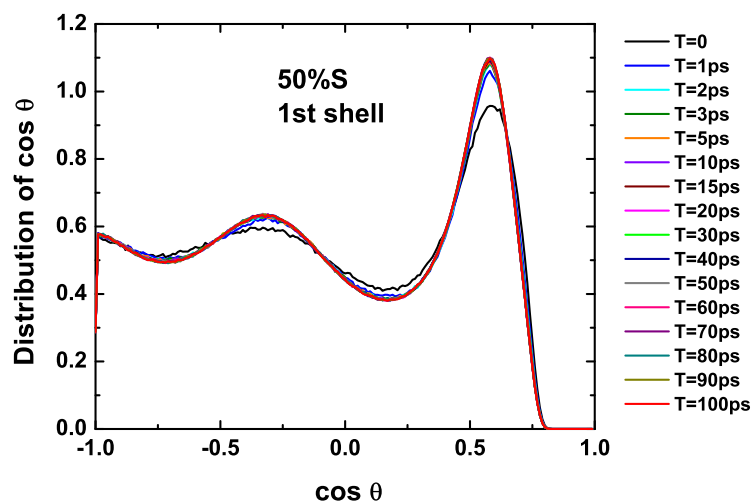


(b)

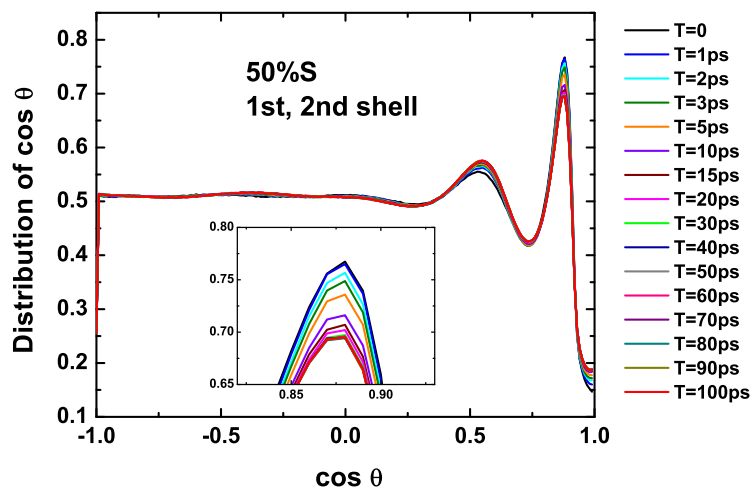


(c)

Figure 4.24 T -dependent angular distributions of strong solvent (a) in the first shell, (b) in the second shell and (c) in the first and second shells of 10% S solvent mixture including a single solute and 107 solvents. The results are averaged over 2×10^6 nonequilibrium trajectories. Inset in (c) shows the behavior of the largest peak in more detail.



(a)



(b)

Figure 4.25 T -dependent angular distributions of strong solvent (a) in the first shell and (b) in the first and second shell of 50% S solvent mixture including a single solute and 107 solvents. The results are averaged over 5×10^5 nonequilibrium trajectories. Inset in (b) shows the behavior of the largest peak in more detail.

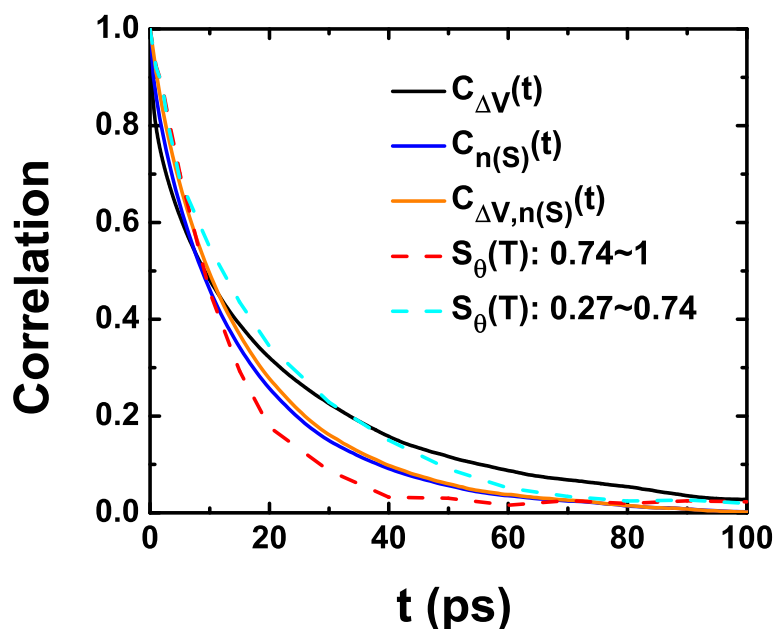


Figure 4.26 Comparison of first-shell population relaxation, solvation energy relaxation and the bond-angle relaxations in the 10% S system. The bond-angle relaxation profile is the normalized peak area in the indicated range of cosine of bond angle.

Bond-angle distribution in close-packed structures

To help us understanding the bond-angle distributions in liquids, we calculate the same distribution for close-packed lattices like face-centered cubic (*fcc*) and hexagonal close packing (*hcp*). The definition of the first shell bond-angle distribution is similar to that in liquids. First we select out the 12 closest atoms with respect to a center atom, then enumerate every possible pairs within in the closest shell. Following the same histogram procedure, one gets a discrete probabilities for each bin.

$$P(\cos \theta) = \frac{1}{\#SSpairs} \sum_{j < l} \delta_{\cos \theta, \hat{\Omega}_j \cdot \hat{\Omega}_l}, \quad (4.158)$$

where the sum of j and l is confined in the first shell, the 12 closest atoms. The normalization condition is that the sum of all probabilities of these countable limited

number of values of $\cos \theta$ is unity,

$$\sum_{\cos \theta} P(\cos \theta) = 1.$$

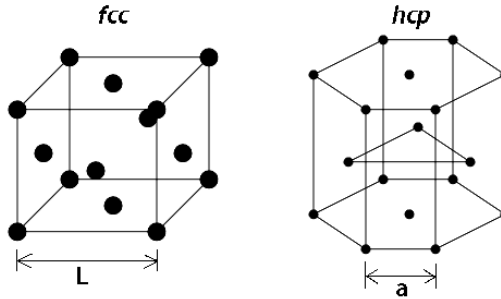


Figure 4.27 Illustration of the *fcc* and *hcp* close packing.

To compare with the liquid bond-angle distribution, we assume the close-packed lattice structure has the liquid's density. The cutoff radii of the first and second shells in the close-packed structures can be calculated from their counterparts in the liquid. For example, in a pure Lennard-Jones liquid with density $\rho\sigma^3=0.8$, the first minimum of the radial distribution function $g(r)$ is at 1.55607σ and the second minimum is at 2.54786σ . Using the same density but *fcc* geometry, the cubic cell length is $L = 1.70998 \sigma$ (Figure 4.27) and so the distance between the nearest pair of particles is $\sqrt{2}L/2 = 1.70998 \times \sqrt{2}/2 \sigma = 1.20914 \sigma$. So in a close packing configuration, if we set the distance between two nearest particles as $a = 1.20914 \sigma$, then the cutoff radius of the first shell is $1.28688 a$ and that of the second shell is $2.10717 a$. These definitions tell us that in the *fcc* configuration, the number of second shell sites is 42 and the *hcp* structure has 44 second shell sites. (In isotropic liquid, the first shell has 12 atoms and the second shell has 42 atoms on average.)

Figure 4.28 and Figure 4.29 show the bond-angle distributions for *fcc* and *hcp* close-packing structures in the first shell, second shell, and in the first and second shells combined. The first shell bond-angle distribution of *fcc* is identical to literature.²⁹² From these figures, we can observe that *fcc* has fewer angles than *hcp* and the reason is *fcc* has an “ABCABC...” layer arrangement that has more centers of inversion than *hcp*'s

“ABAB...” structure, so *fcc* has a symmetrical distribution of bond angles about the right angle, whereas the *hcp* is asymmetrical about the right angle. In the first shell results, the dominant angles are 60° and 120° corresponding to $\cos \theta = \pm 0.5$. For the combined first and second shells results, the dominant angle is 90° and there are some more angles emerging in the whole region.

If only a portion of sites are the kind of atom we are interested in (like the spectroscopically bright S solvent in our model), we need to average over choices of number of this kind by weight. Let p be the percentage of strong atom in the first shell (or the first and second shells) with total n atoms, then binomial expansion of $[p + (1 - p)]^n$ is

$$[p + (1 - p)]^n = \sum_{k=0}^n p^k (1 - p)^{n-k} \binom{n}{k} = 1. \quad (4.159)$$

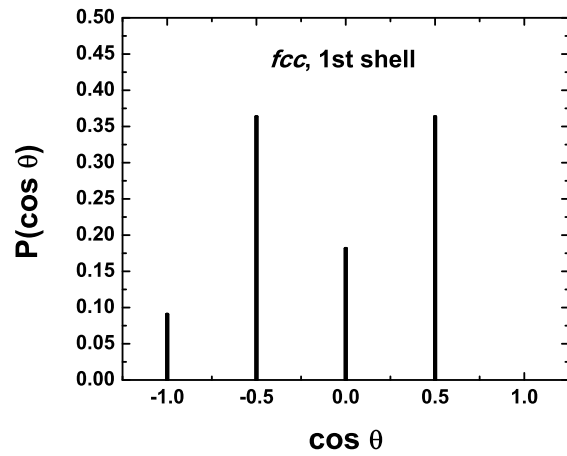
So the weight for k strong particle in the collection of n sites is

$$w(k) = p^k (1 - p)^{n-k} \binom{n}{k}, \quad (0 \leq k \leq n). \quad (4.160)$$

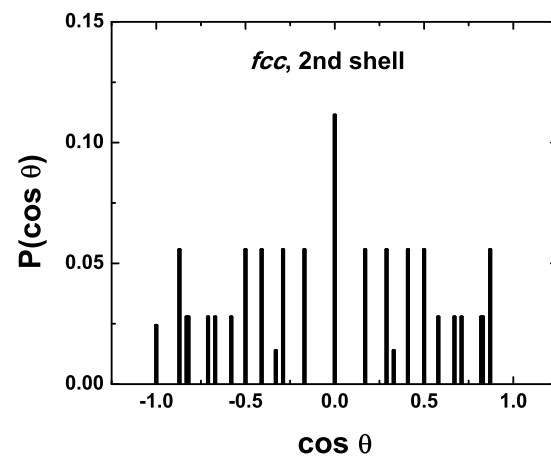
Thus the expectation value of the number of strong particles given p and total number of sites n is

$$\begin{aligned} \langle k \rangle &= \sum_{k=0}^n p^k (1 - p)^{n-k} \binom{n}{k} \cdot k & (4.161) \\ &= \sum_{k=1}^n p^k (1 - p)^{n-k} \frac{n!}{(k-1)!(n-k)!} \\ &= \sum_{m=0}^{n-1} p \cdot \left[p^m (1 - p)^{n-1-m} \frac{(n-1)!}{m!(n-1-m)!} \right] \cdot n \\ &= p \cdot n, & (4.162) \end{aligned}$$

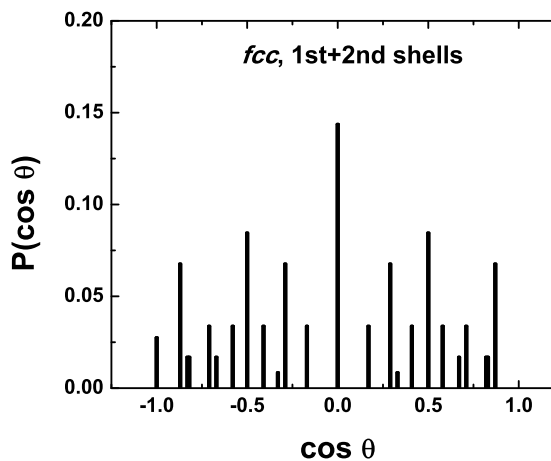
as expected.



(a)

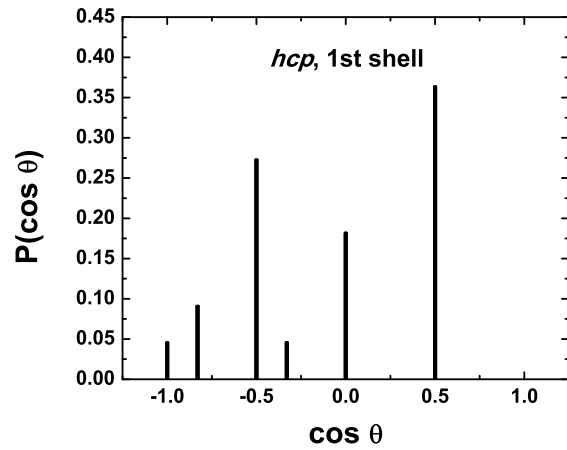


(b)

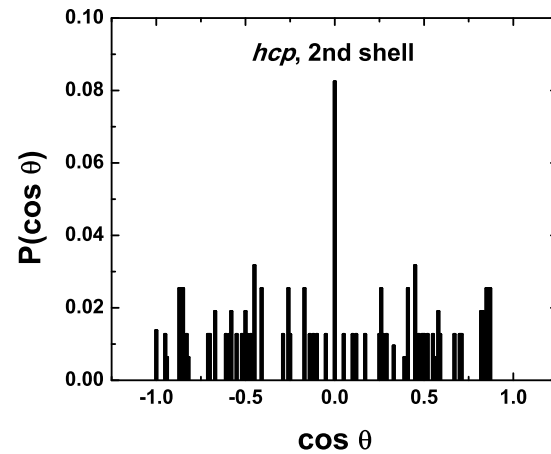


(c)

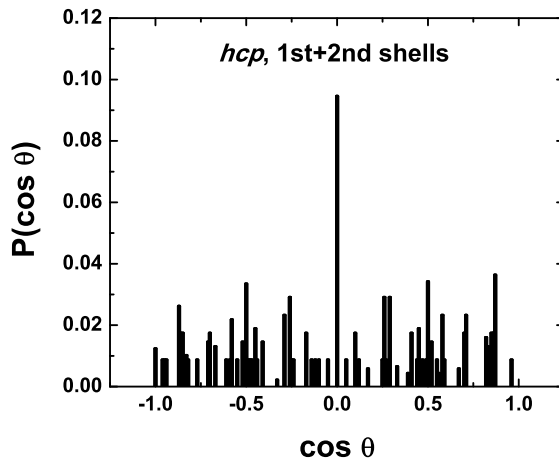
Figure 4.28 Angular distributions for liquid-equivalent *fcc* lattices for atoms (a) in the first shell, (b) in the second shell and (c) in the first and second shells taken together.



(a)



(b)



(c)

Figure 4.29 Angular distributions for liquid-equivalent *hcp* lattices for atoms (a) in the first shell, (b) in the second shell and (c) in the first and second shells taken together.

The bond-angle distribution for one kind of particle in n sites is

$$P(\cos \theta) = \sum_{k=0}^n w(k) \cdot P(\cos \theta, k), \quad (4.163)$$

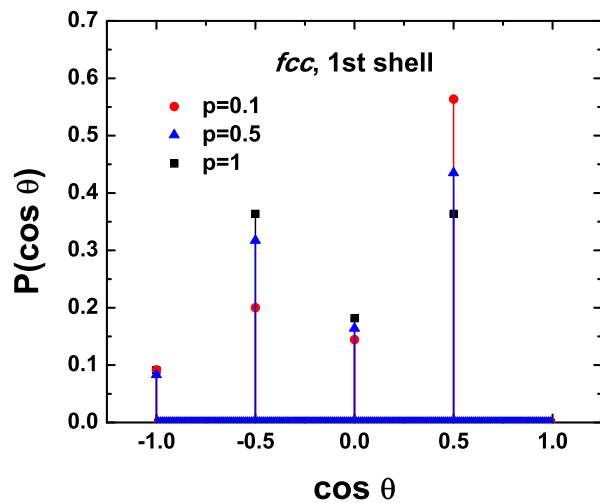
$$P(\cos \theta, k) = \frac{1}{\binom{n}{k} - \binom{n}{0} - \binom{n}{1}} \sum_{i=1}^{\binom{n}{k} - \binom{n}{0} - \binom{n}{1}} \left(\frac{1}{\#SSpairs} \sum_{\substack{j < l \\ j, k \in S}} \delta_{\cos \theta, \hat{\Omega}_j \cdot \hat{\Omega}_l} \right), \quad (4.164)$$

where $P(\cos \theta, k)$ is normalized probability of having the \cos (bond angle between strong particles) = $\cos \theta$ when there are k strong particles in the chosen area, and $P(\cos \theta)$ is the total normalized probability of having \cos (bond angle between strong particles) = $\cos \theta$, which is weighted average over every possible number of strong particles in the chosen area.

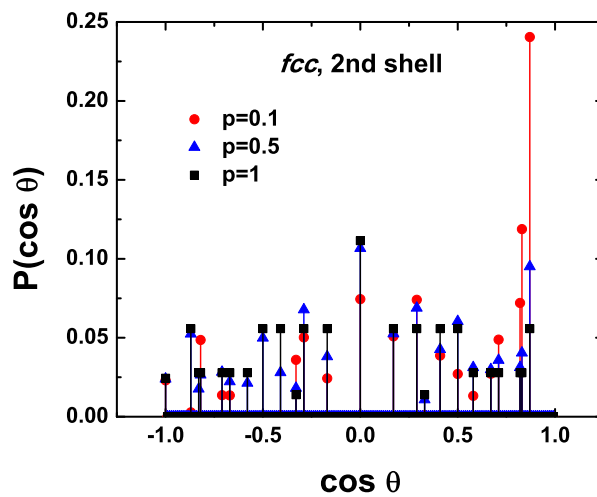
Applying these formulas, we calculate the bond-angle distributions in *fcc* and *hcp* in the first shell, in the second shell, and in the first and second shells with strong atom percentages $p = 0.1$ and $p = 0.5$. The results of mixture and pure systems are summarized in Figure 4.30 and Figure 4.31. The mixtures differ from pure system only by magnitudes of probabilities, so there are no angles different than those in the pure case. More specifically, one can observe that the smaller the percentages of strong particles, the more the population of the small angles between them.

Comparison of liquid and close-packed structure

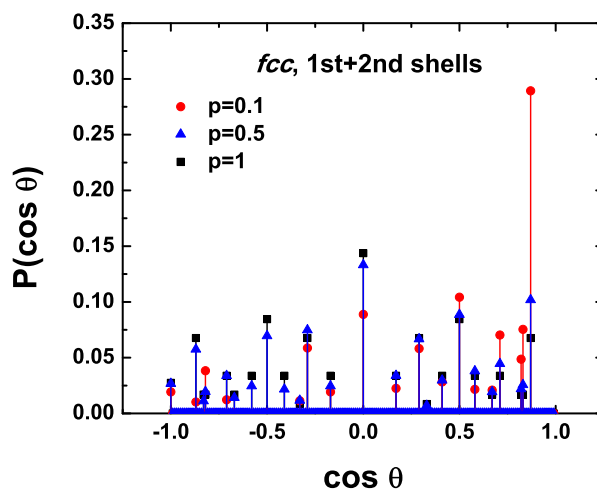
We compare bond-angle distributions of liquid and close-packed lattices in Figures 4.32 to 4.35. The overall shape for the first shell distributions in liquid and lattice look similar if one imagines that the liquid's distribution gets broadened around each isolated lattice peak. Figure 4.34 indicates that the parentage of the angles near 55° in the liquid's first shell probably corresponds to the 60° lattice angles ($\cos \theta \approx 0.5$). The high probability finding the smallest angle about 30° ($\cos \theta = 0.87$) in close-packed structures supports our observation in the liquid case. Since the liquid-state second-shell distribution exhibits no



(a)

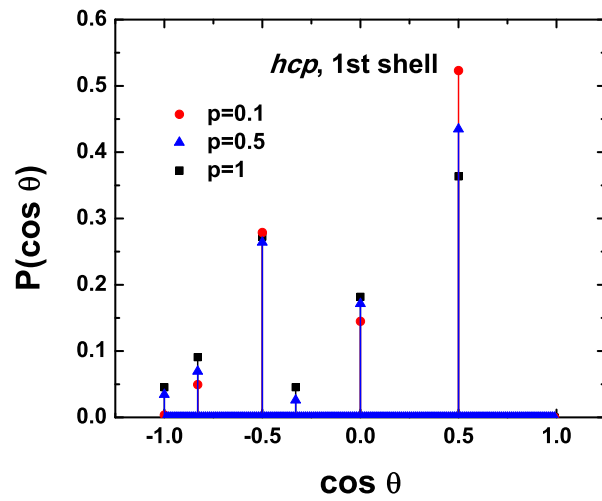


(b)

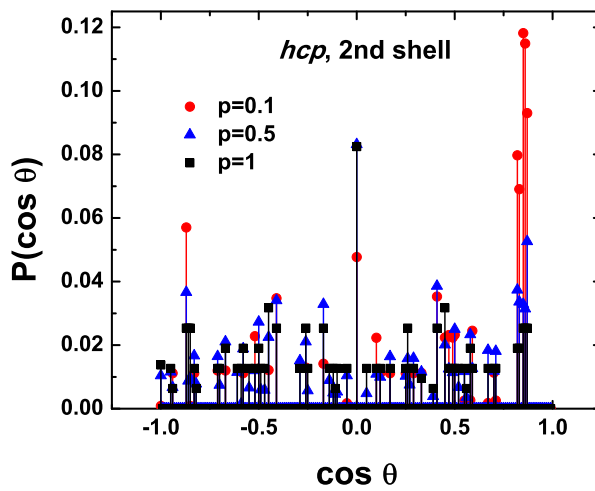


(c)

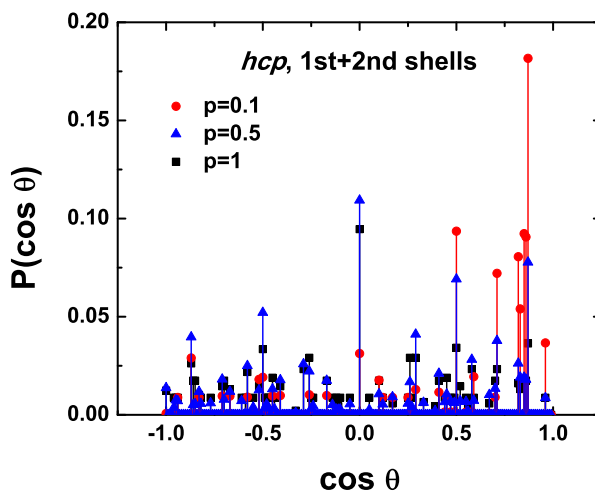
Figure 4.30 Angular distributions for liquid-equivalent *fcc* lattices for atoms (a) in the first shell, (b) in the second shell and (c) in the first and second shells with varying bright solvent percentages $p = 0.1, 0.5$ and 1 .



(a)



(b)



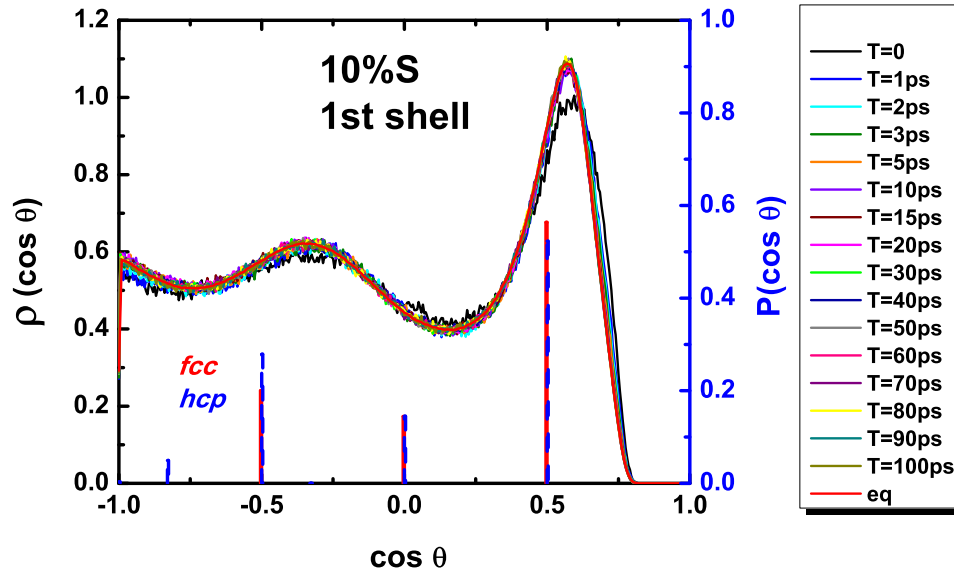
(c)

Figure 4.31 Angular distributions for liquid-equivalent *hcp* lattices for atoms (a) in the first shell, (b) in the second shell and (c) in the first and second shells with varying bright solvent percentages $p = 0.1, 0.5$ and 1 .

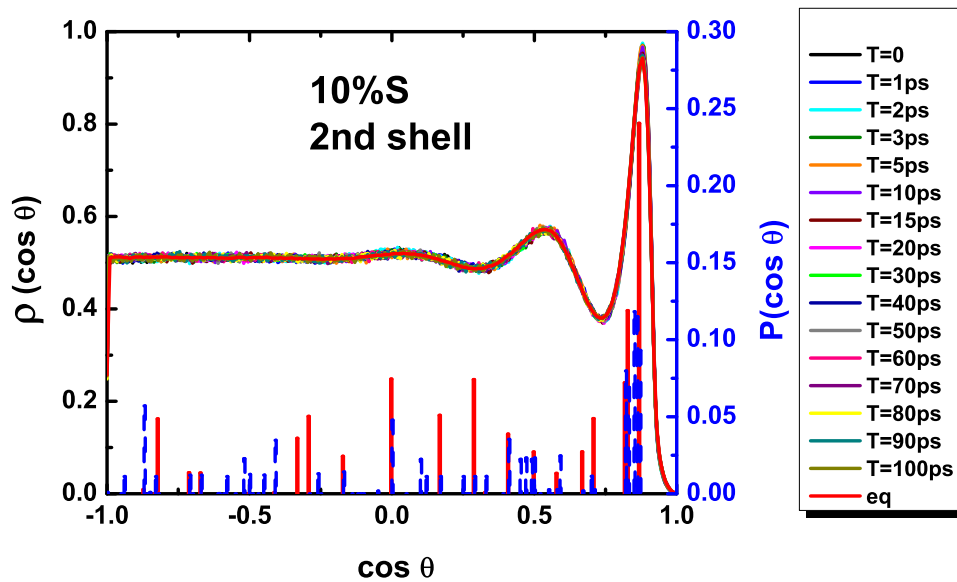
noticeable change with T , the assignment of the evolution in 30° angles in the joint first-second shell distribution must be to first-shell/second-shell solvent pairs.

Table 4.1 shows that the composition of first-shell/first-shell, first-shell/second-shell and second-shell/second-shell pair contributions to the two typical peak positions at $\cos \theta = 0.5$ and 0.87 in *fcc* and *hcp* close-packing structures. For instance, in a 10% S system, the angle 60° has its main contribution from the first-shell/first-shell pairs in both *fcc* and *hcp* configurations. So in 10% S system, the second highest peak in liquid bond-angle distribution could be assigned to mainly the first-shell/first-shell pairs. For the smaller angle of 30° , the first-shell/second-shell pair contributes a little more than second-shell/second-shell pair in an *hcp* lattice and the two kinds of pairs share more-or-less comparable weights in *fcc*. In fact, in all the systems studied, the small angle (30°) results from comparable contributions of first-shell/second-shell and second-shell/second-shell pairs. Thus we can say that the highest peak corresponding to the smallest liquid bond-angle is due to roughly equal contributions from first-shell/second-shell and second-shell/second-shell pairs.

Figure 4.36 depicts a typical structural change of the solvent after the solute excitation suggested by these data. The evolution of the combined first and second shell angular distribution is more essential than that of either shell alone. The slowness of replacing the W solvents by S solvents in the first shell is because the same replacement has to take place in the second and further shells beforehand.⁸⁷ Thus the fact that solute-pump/solvent-probe spectroscopy is not limited to the first solvation shell may be an important feature of its structure sensitivity.



(a)



(b)

Figure 4.32 Comparison of T -dependent angular distributions in 10% S solvent mixture (left axis) and angular distributions of liquid-equivalent fcc and hcp lattices (right axis) (a) in the first shell and (b) in the second shell. Nonequilibrium results are averaged over 2×10^6 trajectories in 10% S system with a single solute and 107 solvents; equilibrium distribution (“eq”) is averaged over 5×10^7 configurations.

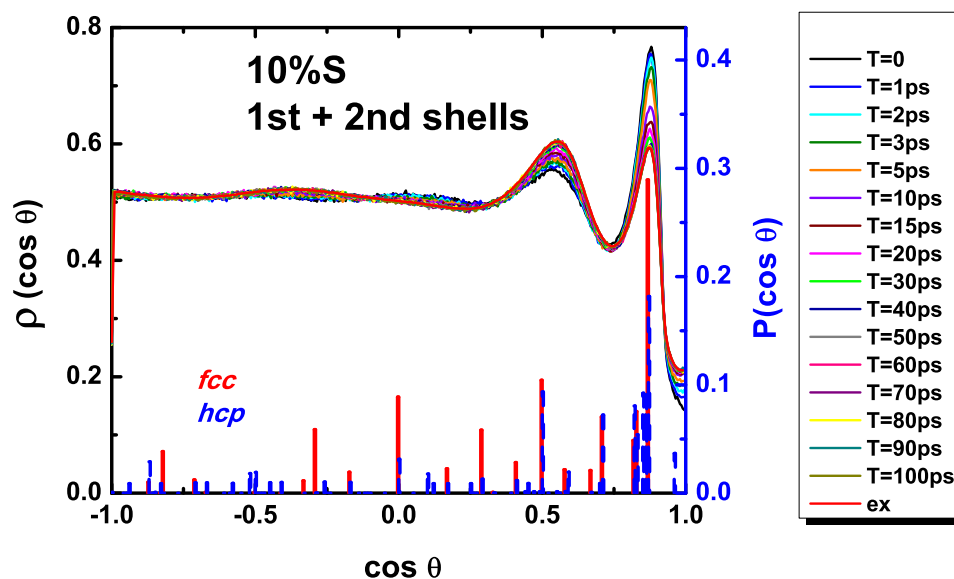


Figure 4.33 Comparison of T -dependent angular distributions in 10% S solvent mixture (left axis) and angular distributions of liquid-equivalent fcc and hcp lattices (right axis) in the first and second shells. Nonequilibrium results are averaged over 2×10^6 trajectories in 10% S system with a single solute and 107 solvents; equilibrium distribution (“ex”) is averaged over 5×10^7 configurations.

	first/first	first/second	second/second
$fcc, \cos \theta=0.5$			
$p = 0.1$	0.50	0.28	0.22
$p = 0.5$	0.16	0.39	0.45
$p = 1$	0.20	0.40	0.40
$fcc, \cos \theta=0.87$			
$p = 0.1$	0	0.45	0.55
$p = 0.5$	0	0.41	0.59
$p = 1$	0	0.50	0.50
$hcp, \cos \theta=0.5$			
$p = 0.1$	0.73	0.08	0.19
$p = 0.5$	0.41	0.38	0.20
$p = 1$	0.40	0.40	0.20
$hcp, \cos \theta=0.87$			
$p = 0.1$	0	0.59	0.41
$p = 0.5$	0	0.61	0.39
$p = 1$	0	0.60	0.40

Table 4.1 Compositions of first-shell/first-shell, first-shell/second-shell and second-shell/second-shell contributions to fcc and hcp lattice bond-angles $\cos \theta=0.5$ and 0.87 with strong solvent percentage $p = 0.1, 0.5$ and 1 .

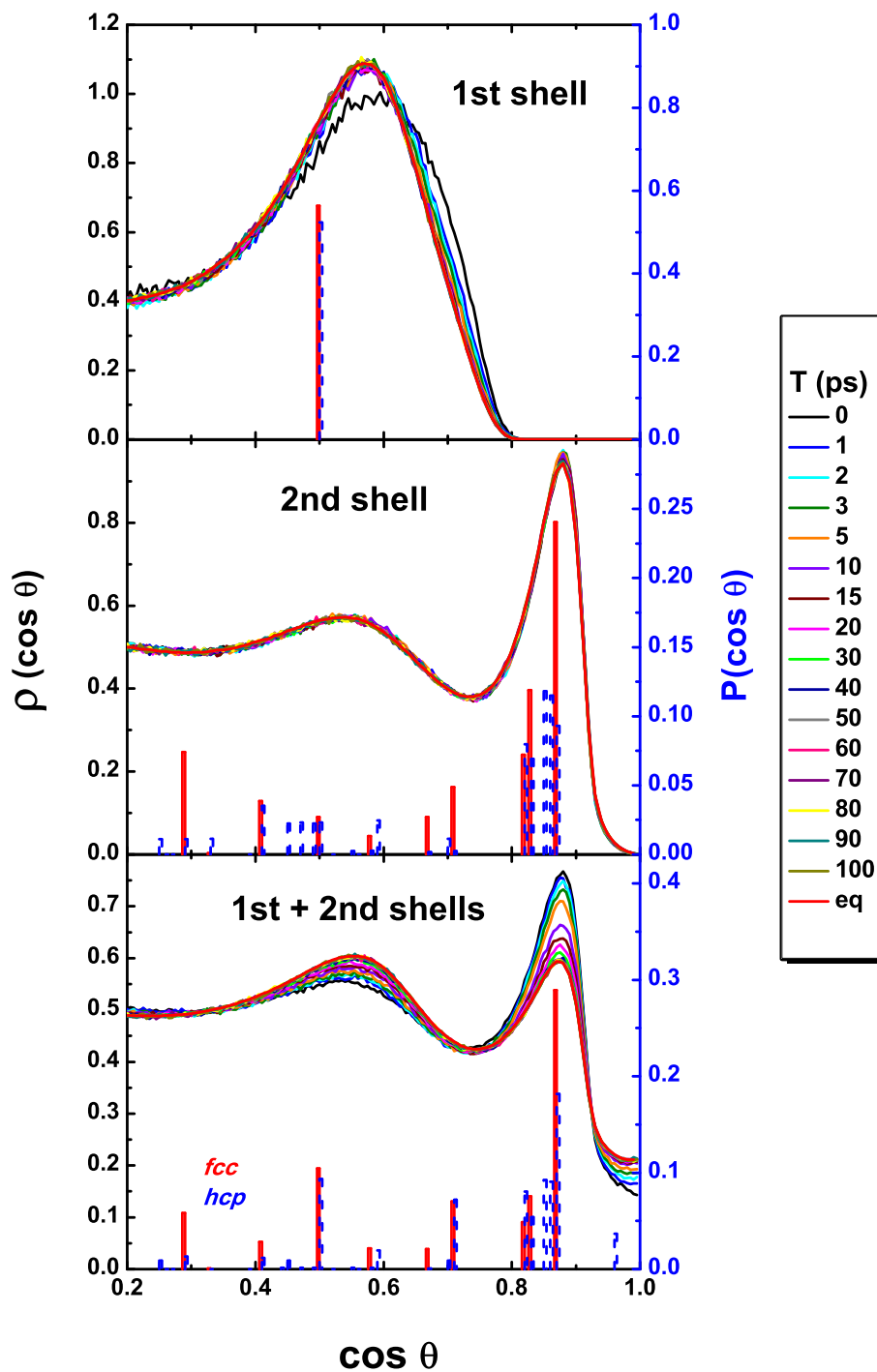


Figure 4.34 Enlarged view of comparison of T -dependent angular distributions in 10% S solvent mixture (left axis) and angular distributions of liquid-equivalent *fcc* and *hcp* lattices (right axis, blue) in the first shell (upper panel), in the second shell (middle panel) and in the first and second shells (bottom panel). Nonequilibrium results are averaged over 2×10^6 trajectories in 10%S system with a single solute and 107 solvents; the equilibrium distribution (“eq”) is averaged over 5×10^7 configurations.

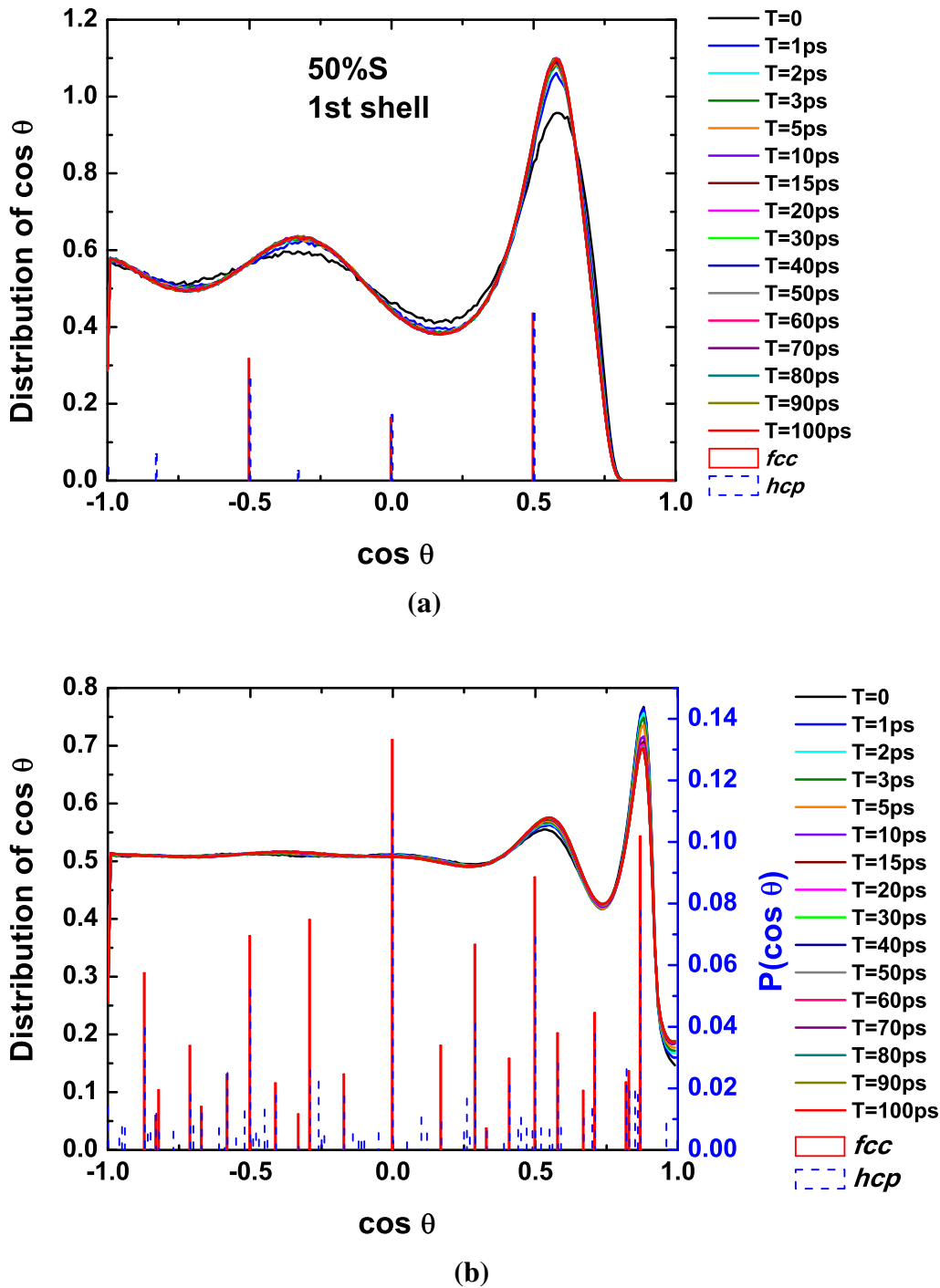


Figure 4.35 Comparison of T -dependent angular distributions in 50% S mixture (left axis) and angular distribution of liquid-equivalent *fcc* and *hcp* lattices (a) in the first shell, (b) in the first and second shells (right axis). Averaged over 5×10^5 trajectories in 50% S system ($N=108$).

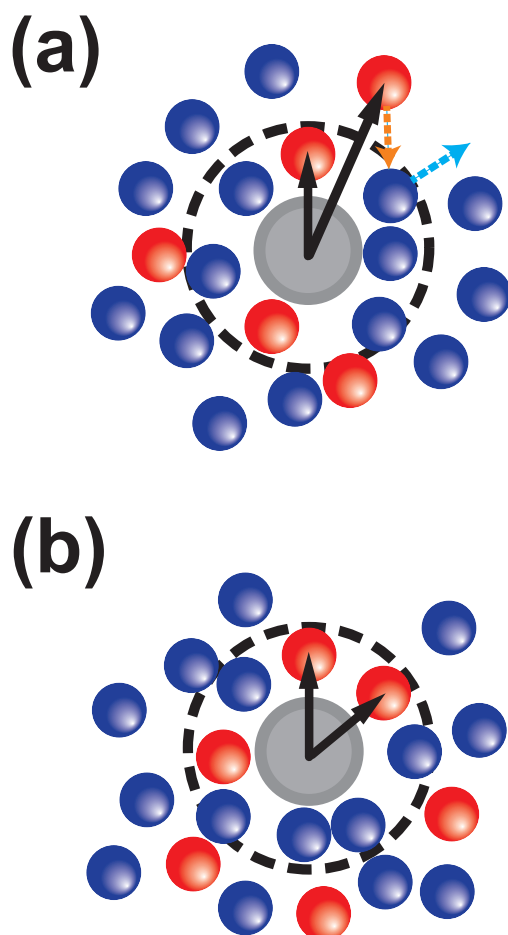


Figure 4.36 Schematic illustration of the solvent structural change induced by the solute excitation in a preferential solvation system. (a) Before the solute (gray circle) is excited, a typical ground-state equilibrium configuration including strong (red) and weak (blue) solvent atoms is portrayed. The boundary of the first solvation shell is indicated as the dashed circle. The most common acute S-solvent/solute/S-solvent angle θ in the first shell is about 60° , whereas a significant angle of 30° (black arrows) emerges when considering both first and second shells. After the solute excitation, extra strong solvents are attracted into the first shell expelling weak solvents (dashed arrows). (b) After relaxing for waiting time T , a net result of solvent rearrangement is an increase in the number of 60° angles (black arrows) and a decrease in the number of 30° angles in the combined first and second shells.

4.7 Discussions on Analytical Approximations for 2D Spectroscopic Responses

In this section, we are going to discuss the INM treatment of a general 2D spectroscopic response and compare the INM approximation with a literature method. Our purpose here is to see if the INM treatment could give us an accurate prediction of the response in a simple analytical model.

A general form of a classical two-dimensional spectroscopic response function is an ensemble average of two nested Poisson brackets involving dynamical variables at three different times $(0, t_1, t_2)$.

$$R(0, t_1, t_2) = \langle \{ \delta A(0), \{ \delta B(t_1), \delta C(t_2) \} \} \rangle = \langle \{ A(0), \{ B(t_1), C(t_2) \} \} \rangle. \quad (4.165)$$

For example in fifth-order Raman spectra, A , B and C all equal to many-body polarizabilities.¹⁹⁷ Since the outermost Poisson bracket inside an ensemble can be reduced (Appendix A), we have an equivalent expression for this response function

$$R(0, t_1, t_2) = \beta \langle \dot{A}(0) \{ B(t_1), C(t_2) \} \rangle. \quad (4.166)$$

In our solute-pump/solvent-probe spectroscopy, if linearize Equation 4.64 with respect to the energy gap, we have the solute-pump/solvent-probe response function

$$\begin{aligned} \Delta R(0, T, T+t) = & -\beta \frac{d}{dt} [\langle \Pi_{xz}(0) \Pi_{xz}(t) \rangle_e - \langle \Pi_{xz}(0) \Pi_{xz}(t) \rangle_g] \\ & - \beta \langle \delta \Delta V(0) \{ \Pi_{xz}(T), \Pi_{xz}(T+t) \} \rangle_e. \end{aligned} \quad (4.167)$$

The first two terms depend only on the ultrafast time interval t , which is the equilibrium e-g difference in OKE spectra. The last term is the linearized T -dependent response that correlates the time-zero solute-energy-gap fluctuation with the subsequent four-wave-

mixing light scattering. So the spectroscopy discussed in this thesis also fits into Equation 4.166, if we make the three dynamical variables $\dot{A} = \Delta V$, $B = C = \Pi_{xz}$.

An important test of an analytical approximation such as INM theory²¹³ for the 2D spectroscopic response functions is to look at its harmonic behavior: by evaluating the response function for a simple harmonic oscillator. Suppose we just consider a one-dimensional harmonic oscillator with frequency ω , and choose all the variables A , B and C as the fluctuation of the potential energy of the oscillator $\delta V(t)$,

$$\delta V(t) = \frac{1}{2}m\omega^2 x^2(t) - \frac{1}{2}k_B T. \quad (4.168)$$

Although the observables are nonlinear in coordinate $x(t)$ and a persistent non-decaying oscillation that may bring some difficulty for analytical theories, the harmonic limit is still straightforward to evaluate. The coordinate of a harmonic oscillator at any time t_j can be expressed in terms of a phase space point (x_k, p_k) , its coordinate and momentum at another time t_k ,

$$x_j = x_k \cos \omega(t_j - t_k) + \frac{p_k}{m\omega} \sin \omega(t_j - t_k), \quad (4.169)$$

where the subscripts j and k stand for time t_j and t_k , respectively. The potential energy at time t_2 can be expressed in terms of the phase space point at time t_1 .

$$V(t_2) = \frac{1}{2}m\omega^2 \left[x_1^2 \cos^2 \omega(t_2 - t_1) + \frac{2x_1 p_1}{m\omega} \sin \omega(t_2 - t_1) \cos \omega(t_2 - t_1) + \frac{p_1^2}{m^2 \omega^2} \sin^2 \omega(t_2 - t_1) \right]. \quad (4.170)$$

Substituting this harmonic model into Equation 4.166, we have

$$\begin{aligned} R(0, t_1, t_2) &= \beta \left\langle \dot{V}(0) \frac{\partial V(t_1)}{\partial x_1} \frac{\partial V(t_2)}{\partial p_1} \right\rangle \\ &= \beta \left\langle \dot{V}(0) \frac{\partial V(t_1)}{\partial x_1} \frac{\partial V(t_2)}{\partial x_2} \frac{\partial x_2}{\partial p_1} \right\rangle \\ &= \beta \left\langle (\omega^2 x_0 p_0) (m\omega^2 x_1) (m\omega^2 x_2) \frac{\partial x_2}{\partial p_1} \right\rangle. \end{aligned} \quad (4.171)$$

The exact result can be derived by substitute Equation 4.169 into the above expression, thus

$$\begin{aligned}
R(0, t_1, t_2) &= \beta m \omega^5 \sin \omega(t_2 - t_1) \langle x_0 p_0 x_1 x_2 \rangle \\
&= \beta m \omega^5 \sin \omega(t_2 - t_1) \left\langle x_0^2 p_0^2 \frac{1}{m \omega} (\cos \omega t_1 \sin \omega t_2 + \sin \omega t_1 \cos \omega t_2) \right\rangle \\
&= \omega^2 (k_B T) \sin \omega(t_2 - t_1) \sin \omega(t_2 + t_1), \tag{4.172}
\end{aligned}$$

where the ensemble average $\langle x_0^2 p_0^2 \rangle = (k_B T / \omega)^2$ is utilized. [§]

The full INM treatment of the response follows the same derivation and gives the same results as in the exact result, since the INM dynamics are harmonic. However, in the linear INM treatment (Equation 4.66), the sensitivity of observables with respect to INM coordinates are assumed to be constant during the ultrafast time scale. The linear INM approximated response function is

$$R_{\text{Linear INM}} \approx \beta \left\langle \dot{V}(0) \left(\frac{\partial V(t_1)}{\partial x_1} \right)^2 \frac{\partial x_2}{\partial p_1} \right\rangle \tag{4.173}$$

$$= \beta \left\langle (\omega^2 x_0 p_0) (m \omega^2 x_1)^2 \frac{\partial x_2}{\partial p_1} \right\rangle \tag{4.174}$$

$$= \omega^2 (k_B T) \sin \omega(t_2 - t_1) \sin 2\omega t_1. \tag{4.175}$$

Another approximation for evaluating the two-dimensional classical spectroscopic response function is developed by DeVane, Ridley, Space and Keyes (DRSK).^{201–205} Their treatment starts with quantum mechanical analogue of Equation 4.165 replacing classical dynamical variables and Poisson brackets with quantum mechanical operators and commutators. For harmonic systems, the classical limit of the response function is demonstrated to be closely related to the real part of the quantum time correlation functions. In their

[§]For harmonic oscillator, $\langle x_0^2 \rangle = \frac{k_B T}{m \omega^2}$, $\langle x_0^4 \rangle = 3 \left(\frac{k_B T}{m \omega^2} \right)^2$, $\langle x_0^6 \rangle = 15 \left(\frac{k_B T}{m \omega^2} \right)^3$, $\langle p_0^2 \rangle = m k_B T$, $\langle p_0^4 \rangle = 3(m k_B T)^2$ and $\langle p_0^6 \rangle = 15(m k_B T)^3$.

approximation, setting A , B and C all equal to $\delta V(t)$, the classical limit of the two-dimensional spectroscopy response can be expressed as the classical average^{201,204}

$$R_{DRSK}(0, T, T+t) = -\frac{1}{2}\beta^2 \left(\frac{\partial^2}{\partial T^2} - 2\frac{\partial^2}{\partial T \partial t} \right) \langle \delta V(0) \delta V(T) \delta V(T+t) \rangle \quad (4.176)$$

$$= \beta^2 \left[\langle \delta \dot{V}(0) \delta \dot{V}(T) \delta V(T+t) \rangle + \frac{1}{2} \langle \delta \ddot{V}(0) \delta V(T) \delta V(T+t) \rangle \right]. \quad (4.177)$$

Applying the harmonic potential (Equation 4.170) to the above DRSK approximation, we have the response function as follows.

$$R_{DRSK}(0, t_1, t_2) = \omega^2 (k_B T) \sin \omega(t_2 - t_1) \sin \omega(t_2 + t_1), \quad (4.178)$$

which is the exact result for the one-dimensional harmonic oscillator.

It is important to notice that both linear INM approximation and the DRSK approximation to the two-dimensional spectroscopic response function keep symmetrical properties. For example, when $t_1 = t_2$, the response $R = 0$ since $\{B(t_1), C(t_1)\} = 0$. Time reversal symmetry is conserved as in $R(0, -t_1, -t_2) = R(0, t_1, t_2)$. On switching $t = t_2 - t_1$ to $-t$ the response function changes sign; this antisymmetric property is required by the Poisson bracket property $\{B, C\} = -\{C, B\}$.

Comparing Equations 4.172, 4.175 and 4.178, the DRSK theory seems to be better than the linear INM approach in this simple harmonic oscillator model. The linear INM approach in Equation 4.66 assumes the observable in linear in the INM displacement, whereas the DRSK theory does not. The DRSK theory may be better at reporting on anharmonic dynamics in liquids when two time scales t_1 and t_2 are short, as shown by numerical simulations of 5th order Raman spectra that vanish for linear observables in pure harmonic systems.

The solute-pump/solvent-probe spectroscopy, on the other hand, has a rather separated

time scales, with the $T = t_1$ solvation time often much larger than the $t = t_2 - t_1$ intermolecular dynamical time scale. In this case, the time-dependent part of the response function in Equation 4.175, $\sin \omega t \sin 2\omega T$, is the same as that in the exact result in Equation 4.172. Thus, the linear INM idea handles the fast dynamics modulated by the slow dynamics well. Moreover, it is exactly the point of our 2D spectroscopy serving as a solvation spectroscopy when the T dynamics reflects overall solvent structural evolution. So treating the T dynamics most faithfully, our hybrid linear-INM/MD method is probably more suitable at representing nonequilibrium solvation dynamics.

Chapter 5

Concluding Remarks

The point of the thesis is to show that we can understand the solute-pump/solvent-probe spectra from a fully molecular perspective. It was demonstrated that one can formulate a solute-pump/solvent-probe experiment using classical statistical mechanics. We derived a linear response theory for this spectroscopy with the response function turning out to be a three-time correlation between the solute–solvent interaction energy and the many-body polarizabilities. By combining resonant potential-energy-gap spectroscopy with nonresonant four-wave-mixing light scattering measurement, our two-dimensional spectra enable us to track how the intermolecular dynamics of a liquid evolves along the solvation progression. The two time scales observed by the 2D spectra are the ultrafast intermolecular vibrational time t and the solvation evolution time T . Traditional spectroscopic methods can monitor only one of the two time scales, with examples like time-dependent fluorescence spectroscopy measuring the T time scale by watching the red shifting of the solute’s potential-energy gap, and the optical Kerr effect spectroscopy measuring the t time scale by watching the fluctuation of the many-body polarizability of the entire liquid. The solute-pump/solvent-probe spectroscopy provides an alternative measure of solvation, reporting structural dynamics of a local portion of solvent instead of the energetic dynamics that can be measured by time-dependent fluorescence.

In the limit of a long waiting time T , the solute-pump/solvent-probe experiment measures just the difference between ultrafast liquid dynamics in solutions with a ground-state solute and that with an excited-state solute. Even in this long T limit, the fluctuations of the many-body polarizability display the sensitivity to capture a net local change in solvent structure. In the model we studied here, a mixture of atomic liquids with an atomic solute exhibits preferential solvation phenomenon, a solvent-concentration-dependent slowdown of the excited-solute solvation process caused by the time required to exchange solvents. The polarizability fluctuations in this system directly reflect the liquid structure because fluctuating interatomic distances and local compositions affect the polarizability through the interaction-induced contribution. We were able to identify which solvents and which terms in the polarizability are essential in our simulated spectra.

Although some of the microscopic assignments of the solute-pump/solvent-probe spectra at the long waiting time limit are specific to our atomic preferential solvation model, some conclusions seem potentially more general. One such example is that the experiment has a natural focus on the change of liquid dynamics in a local region near the solute. The reasons behind the localized focus include not only a limited range of influence for the ground/excited-state solute excitation, but also the most visible polarizability fluctuations involve the solute itself. Another interesting phenomenon that stands out in the frequency domain is that the signs of the spectra change in different solvents. In our atomic liquid mixture model, the sign variability originates from the effects of different induced-dipole arrangements contributing to the interaction-induced polarizability in solvents with different concentrations of the spectroscopically bright species. However, the same sign changes show up in experimental measurements with neat molecular solvents.²²⁶

Unlike atoms, molecules can possess permanent polarizability anisotropies, so the re-orientational motions of molecules affect the many-body polarizability and thus have their own direct contributions to the spectroscopy.²⁹³ It is possible to interpret the sign changes between the experimental RP-PORS measurements in neat acetonitrile and chloroform in

terms of their different reorientational responses to the solute excitation. Acetonitrile is a prolate molecule whose dipole is parallel to the axis of symmetry. The almost linear-shaped acetonitrile molecule could easily pack into the first solvation shell keeping their dipole parallel to the dipole of the ground-state C153 solute.^{294,295} Upon the electronic excitation of the solute, the dipole of the solute increases resulting in a stronger electrostatic interaction that probably alter the librational motions of the solvent but is unlikely bring about large-amplitude reorientation redistribution within the first shell. By contrast, chloroform is an oblate molecule whose small dipole is perpendicular to the Cl-Cl-Cl molecular plane. The disk-like chloroform might prefer to pack more efficiently with its flat molecular plane against the ground-state solute and hence its dipole is perpendicular to that of the ground-state solute. However, after excitation the solute has a substantial increase in dipole, which could motivate large-amplitude solvent rotations sacrificing packing efficiency. The presence of large-amplitude solvent rotations gives rise to a negative RP-PORS response.

The molecular nature of the solute may yet have another consequence in the RP-PORS measurement. The polarized resonant solute pump will automatically selectively excite those solutes whose transition dipoles are orientated along the polarization of the exciting electric field, effectively creating a local reference direction for the surrounding solvents.²²⁶ Although the standard third-order transient-grating four-wave-mixing configuration grants the flexibility of measuring both isotropic and anisotropic signals with the following polarization choices^{226,227} (whereas the OKE configuration can only measure the transient birefringence or the anisotropic signal²²²)

$$\text{isotropic} = \frac{1}{3}(zzzz + 2xxzz), \quad (5.1)$$

$$\text{anisotropic} = \frac{1}{2}(zzzz - xxzz), \quad (5.2)$$

these two signals may no longer be orthogonal because of the special direction created by the solute pump, for example, a z -polarized exciting field. Perhaps, the third-

order simplification of the polarization combinations is not enough to describe a fifth-order solute-pump/solvent-probe spectroscopy. The experimental results display virtually identical isotropic and anisotropic RP-PORS spectra for acetonitrile,²²⁶ in contrast with strong anisotropic signals of normal four-wave mixing.^{152,159} The resemblance between isotropic and anisotropic RP-PORS responses possibly in turn suggest the effect of the local reference direction provided by the resonant pump is not trivial and thus may not be able to provide genuine isotropic/anisotropic dynamical distinctions. Different experimental polarization conditions need to be treated carefully in order to obtain accurate microscopic lessons.

The other experimental implementation of solute-pump/solvent-probe spectroscopy developed by Blank and co-workers is termed as the Resonant Pump Third Order Raman Spectroscopy (RaPTORS).²²⁸⁻²³¹ RaPTORS utilizes the same pulse sequence and measures the same solvent dynamics as in RP-PORS, but the principle difference between the two is the local oscillator. In RaPTORS, the local oscillator is the time-dependent solvent scattering field, hence dispersive and absorptive parts of the signal cannot be separately measured. By contrast, in RP-PORS, the local oscillator is time-independent and the phase of the local oscillator with respect to the signal can be controlled making it possible to separately measure both the dispersive and absorptive parts of the signal.²²⁶

The really promising aspects of the solute-pump/solvent-probe spectra are provided by the full 2D spectra that reveal how the solvent dynamics evolves as a function of the waiting time T or at different epochs in the evolution of liquid geometry. We have demonstrated that our solute-pump/solvent-probe spectroscopy is able to arrive at an alternative solvation coordinate that is essentially different from the solute-solvent interaction energetic measure of solvation. This alternative measure of solvation process, however, does not guarantee to describe the complete structural evolution of a solvent, but it does broaden our horizon on the solvent structural dynamics during the solvation. The fluctuations of many-body polarizability seem to be an especially appropriate choice for the alternative coordinate. As

stated earlier, the many-body polarizability is sensitive to interatomic distances, a complete knowledge of which is equivalent to the liquid structure.

It is not necessarily always the case that the progression of polarizability spectroscopy would follow more closely to the solvent structural evolution than the traditional time-dependent fluorescence. The surprising result in our preferential solvation case shows that the evolution of the polarizability spectra can be explicitly assigned to structural rearrangement. The reason why we can make this assignment is the significant separation of time scales between the ultrafast intermolecular vibration time t and the solvation evolution time T ; this separation of time scales also makes it technically feasible to perform the calculation. Therefore we can treat the ultrafast dynamics on the t axis as depending adiabatically on the position on the solvation time T axis. This feature allows us to evaluate the response function with an unconventional hybrid formalism where the high-frequency dynamics (t) is estimated with the instantaneous-normal-mode analysis on liquid configurations sampled from exact molecular dynamics simulation of the long-time behavior (T).

Unlike two-dimensional spectroscopic approaches such as the 3-pulse photon echo peak shift (3PEPS),^{172,176,177,282} in which the solute-solvent interaction energy serves as observables in both T and t time scales, the solute-pump/solvent-probe spectra measure the T and t dynamics with qualitatively different observables — solute's energy gap and fluctuation of polarizability. This different-in-character feature of spectroscopic observables makes the spectra potentially revealing and guarantees the mathematical separation of time scales to some extent. More importantly, the combination of energy-gap and polarizability observables seems to automatically lead to a division of probes specifically sensitive to energetic dynamics and specifically sensitive to structural dynamics. The energy-gap relaxation is evidently distinct from the structural evolution of the surrounding solvent at least in our atomic preferential solvation system, and our observables seem remarkably able to grasp this contrast.

Finding the solute-solvent interaction energy relaxing more slowly than the structural dynamics in our studied atomic preferential solvation system is somewhat surprising. A hypothesis for energetic dynamics being slower than structural dynamics is proposed in the beginning of chapter 4, emphasizing a plausible circumstance when an enormous amount of energy-neutral rearrangement in single solvation shell is needed before the shell-to-shell solvent transfers. The evolutions of bond-angle distributions we examined for our atomic liquid mixture model are excellent examples of structural arrangements that will not directly lead to a change in potential energy. Our calculation shows that there is no picosecond-scale single-solvation-shell angle changes, although the joint first/second-shell angles relax more slowly than single-shell angles and reaches the solvation time scale. The solute-solvent interaction energy, however, is a sensitive probe of the solute-solvent distances especially for those spectroscopically bright solvents in the crowded first solvation shell. Thus, it could take more time to achieve the optimized “non-structural” first-shell distances than to accomplish a single solvent entering the somewhat artificially defined first-solvation-shell region.

The solute-pump/solvent-probe spectroscopy seems to have its own selection rules. Our calculations with reversed polarizabilities of solvents indicate that the ability to unveil a part of the structural evolution of the liquid could be impeded in some liquid systems. In our atomic preferential solvation model, we chose solvents with significantly different polarizabilities in order to get a prominent signal. Furthermore, the dynamics in system with strongly solvating solvent with larger polarizability is easily picked up by the 2D spectra, but not vice versa. So when we delve into liquids with molecular solvents, the very question of how well the structural and energetic relaxations separate is still open. For dipolar solute dissolved in polar solvents, both the solute-solvent interaction energetic dynamics²⁸¹ and the many-body polarizability dynamics⁸¹ are governed by the first-solvation-shell reorientational motions. One hence might not expect an essential difference in time scales of these two dynamics.¹⁴⁶ But somewhat surprising experimental evidence of RP-PORS

measurement in a neat acetonitrile solvent²²⁷ indicates that the T and t dynamics have noticeably different time scales. As shown in Figure 1.12, the solvation relaxation occurs on a picosecond scale that is even more persistent than the slowest characteristic time, about 600 fs, of the time-dependent fluorescence relaxation of acetonitrile;⁸³ whereas the ultrafast dynamical time scale agrees with the 75 fs ($1/e$) dephasing time of acetonitrile intermolecular vibrations corresponding to the approximately 100 cm^{-1} bandwidth (FWHM) of its INM solvation spectrum.⁸¹

5.1 Future Studies

As a theorist, I do encourage experimentalists to carry out solute-pump/solvent-probe measurements on solutions with solvent mixtures. The enormous number of extra relaxation pathways within such mixtures could exhibit some spectroscopic signatures that are directly associated with solvent structural dynamics more easily than pure solvents. Similarly as in the atomic liquid case, one should choose molecular solvent mixture deliberately in order to see a significant change in the 2D spectra. Among those solvent mixtures mentioned before in preferential solvation studies, a few of them are suitable for future studies. Our guideline here is to choose solvent pairs with rather distinctive molecular properties, such as polarizability and dipole. As we imitated in our atomic liquid model, DMSO/water^{89,91,92} mixture has a large molecular polarizability ratio that is about 5 and reasonably large molecular dipole ratio that is about 2 (Table 3.1). This considerable difference in molecular properties suggests that DMSO/water is an excellent choice. Another favorable choice is the DMF/water mixture,²⁵⁷ although this solvent combination has been studied less than DMSO/water. The mixture of benzene/acetonitrile^{85,95} is a typical solvent mixture containing non-polar and polar solvents, yet the polar acetonitrile has a smaller polarizability. Even if benzene would solvate aromatic solutes better than non-aromatic solutes, acetonitrile would still be the strong solvent when dissolving both kinds of solutes because

of the large dipole. So the solute-pump/solvent-probe spectroscopy could not be sensitive to the structural dynamics of this solvent mixture. By contrast, solvent mixtures such as water/alcohol⁸⁹ and THF/water²⁵⁵ have comparable dipoles, which probably cannot lead to a significant change from ground-state dynamics to excited-state dynamics, thus may be hardly captured by the spectroscopy.

Since the target region that solute-pump/solvent-probe spectra focus on is the local area near the solute, the resulting 2D spectra are usually solute-specific. The coumarin dyes are widely used in resonant spectroscopic studies, for example, coumarin 153 (C153) solute is investigated with the RP-PORS in a neat solvent of acetonitrile.²²⁷ On the theoretical side, preferential solvation dynamics with both molecular (coumarin) and ionic solute have been simulated in the DMSO/water mixture.^{89,91,92} The charge redistribution in C153 is not enough to invoke any nonlinear solvation response, but maybe not large enough to bring us a significant change in the 2D spectra. By contrast, an atomic solute undergoing neutral to cation or anion excitation induces a dramatic charge redistribution, which may lead to an dramatic change in our 2D spectra. Study shows that a cation solute prefers DMSO and an anion solute prefers water in DMSO/water binary mixture, and their solvation relaxations have a noticeably distinctive time scales.⁸⁹ Perhaps, a solute-pump/solvent-probe study on ionic solute in DMSO/water mixture could provide interesting dynamical information.

The formalism developed in this thesis is a pure classical treatment to the solute-pump/solvent-probe spectroscopy and thus cannot provide any quantum dynamical information, such as quantum coherence. Quantum coherence in liquids usually decays much faster than solvation dynamics — the decay of which is called quantum decoherence²⁹⁶ — thanks to the frequent system–bath interactions.^{297–301} For most room-temperature simple liquids, quantum coherence is not significant in their nuclear dynamical timescale so a classical treatment should be accurate enough. However, when the quantum effects become significant, the language of density matrix and quantum Liouville pathways introduced in chapter 1 is useful to fully describe the nonlinear optical processes. When the studied

system's electronic states are resonant with the incoming lasers and the system–bath interaction is weak, electronic coherence (superposition of two distinctive electronic states) could persist in, for example, the electronically excited Fenna-Matthews-Olson (FMO) bacteriochlorophyll complex, which has been primarily studied with two-dimensional electronic spectroscopy to elucidate the mechanism of energy transfer in photosynthesis.^{302–305} In addition, long-lived vibrational coherences (superposition of two distinctive vibrational states) in high-pressure gases,^{306,307} liquids³⁰⁸ and solids^{309,310} have also been revealed by nonlinear spectroscopical techniques.

Practical theoretical treatments to quantum effects in condensed-phase dynamics includes semiclassical^{311,312} and mixed quantum-classical methods.^{313–315} For example, anions in polar solvents such as excited aqueous halide could lead to a quasi-bound charge-transfer-to-solvent (CTTS) state,^{316–320} which then ejects a solvated electron within a few hundred femtoseconds, leaving a neutral halogen atom behind.³²⁰ The atomic anion solute lacking internal degrees of freedom makes it easy to examine the CTTS-induced electron ejection, which is governed by the structure and motions of the nearest solvation shells. Such electron-transfer reactions in solutions have to be extensively studied with mixed quantum-classical approaches.^{318,319,321}

For the current treatment of the 2D solute-pump/solvent-probe spectra, however, there are still some features whose molecular interpretations are not perfect clear. For instance, the first experimental measurement of C153 in acetonitrile (Figure 1.12) shows that the high-frequency intermolecular vibrational motions relax faster than the low-frequency motions. By contrast, our calculations indicate that the relaxation profiles for different intermolecular vibrational frequencies exhibit no difference. Neither observations can be understood with the uniformly damped multimode oscillator model that is widely used in literature.^{227,322–325} The oscillator's Q value is proportional to their oscillating frequency. Consequently, high-frequency motion usually has a high Q, which corresponds to an underdamped oscillation, thus decays slowly. On the contrary, low-frequency motion

usually has a low Q , which corresponds to an overdamped oscillation, and thus decays quickly. Perhaps, one could test other frequencies like 100 cm^{-1} for the theoretical results, but the experimental result possibly suggests the necessity of a more delicate explanation than the oversimplified damped oscillator. The friction felt by molecules in liquids is not a constant after all, and the Q of damped oscillator is inversely proportional to the friction.^{19,326} Further detailed analysis is needed for the molecular assignment to the above mentioned difference in high-frequency/low-frequency decaying rates.

Besides, we have been confining ourselves to a linear INM treatment of the ultrafast dynamics. As we briefly discussed in chapter 4, the full nonlinear INM treatment should be able to provide more accurate predictions to the short-time dynamics in normal liquids. A detailed investigation focusing on the comparison between linear and full INM treatment to the solute-pump/solvent-probe spectra has a potential to elucidate how well the INM theory can tell us about spectroscopic measurements.

This thesis reports the first fully microscopic theoretical investigation on solute-pump/solvent-probe spectroscopy, and it suggests great prospects for other nonlinear spectroscopies. With the help of the hybrid MD/INM method, spectroscopies combining a resonant excitation and a nonresonant liquid-structure measurement could be treated similarly. I can imagine that this hybrid approach would be of utility dealing with high-dimensional spectroscopies like an as-yet unimplemented three-dimensional spectroscopy where molecular relaxation is initiated by a resonant excitation and its structure is measured by a subsequent fifth-order Raman process.

Appendix A

Poisson Bracket

In classical mechanics, Poisson bracket is defined as

$$\{f, g\} \equiv \sum_{i=1}^N \left(\frac{\partial f}{\partial q_i} \frac{\partial g}{\partial p_i} - \frac{\partial f}{\partial p_i} \frac{\partial g}{\partial q_i} \right) = \left(\frac{\partial f}{\partial \mathbf{q}} \cdot \frac{\partial g}{\partial \mathbf{p}} - \frac{\partial f}{\partial \mathbf{p}} \cdot \frac{\partial g}{\partial \mathbf{q}} \right), \quad (\text{A.1})$$

where f and g could be any dynamical variable, and in a $2N$ -dimensional phase space, the N -dimensional \mathbf{q} is the position coordinate, and \mathbf{p} is the conjugate momentum.

(1) Canonical invariance of Poisson bracket

If canonical transformation is made upon $(\mathbf{q}, \mathbf{p}) \rightarrow (\mathbf{Q}, \mathbf{P})$, for instance, these two sets of canonical coordinates are of time t difference, with dynamics on Hamiltonian H , $\mathbf{Q} = \mathbf{Q}(\mathbf{q}, \mathbf{p}; t)$ and $\mathbf{P} = \mathbf{P}(\mathbf{q}, \mathbf{p}; t)$, the Poisson brackets with respect to both sets of canonical coordinates are equal.

$$\begin{aligned} \{f, g\}_{\mathbf{q}, \mathbf{p}} &= \left| \begin{array}{cc} \frac{\partial f}{\partial \mathbf{q}} & \frac{\partial g}{\partial \mathbf{q}} \\ \frac{\partial f}{\partial \mathbf{p}} & \frac{\partial g}{\partial \mathbf{p}} \end{array} \right| = \frac{\partial(f, g)}{\partial(\mathbf{q}, \mathbf{p})} \\ &= \frac{\partial(f, g)}{\partial(\mathbf{Q}, \mathbf{P})} \cdot \frac{\partial(\mathbf{Q}, \mathbf{P})}{\partial(\mathbf{q}, \mathbf{p})} = \frac{\partial(f, g)}{\partial(\mathbf{Q}, \mathbf{P})} \\ &= \{f, g\}_{\mathbf{Q}, \mathbf{P}}. \end{aligned} \quad (\text{A.2})$$

$$\text{Jacobian } \frac{\partial(\mathbf{Q}, \mathbf{P})}{\partial(\mathbf{q}, \mathbf{p})} = 1 \Leftrightarrow (\mathbf{q}, \mathbf{p}) \rightarrow (\mathbf{Q}, \mathbf{P}) \text{ is canonical transformation.}^{327} \quad (\text{A.3})$$

(2) Cyclic invariance of Poisson bracket

Like the trace of the product of an operator and quantum commutator has cyclic invariance (for square matrices $\text{Tr}(AB) = \text{Tr}(BA)$),

$$\begin{aligned} \text{Tr}(\hat{C}[\hat{B}, \hat{A}]) &= \text{Tr}(\hat{C}\hat{B}\hat{A} - \hat{C}\hat{A}\hat{B}) \\ &= \text{Tr}(\hat{A}\hat{C}\hat{B} - \hat{A}\hat{B}\hat{C}) = \text{Tr}(\hat{A}[\hat{C}, \hat{B}]) \\ &= \text{Tr}(\hat{B}\hat{A}\hat{C} - \hat{B}\hat{C}\hat{A}) = \text{Tr}(\hat{A}[\hat{C}, \hat{B}]). \end{aligned} \quad (\text{A.4})$$

the classical Poisson bracket has the same property. Note $\text{Tr} \equiv \int d\mathbf{X} = \int dpdq$.

$$\begin{aligned} \text{Tr}(C\{B, A\}) &= \int d\mathbf{X} \sum_i \left(C \frac{\partial B}{\partial q_i} \frac{\partial A}{\partial p_i} - C \frac{\partial B}{\partial p_i} \frac{\partial A}{\partial q_i} \right) \\ &= -\sum_i \int d\mathbf{X} \left(A \frac{\partial}{\partial p_i} \left(C \frac{\partial B}{\partial q_i} \right) \right) + \sum_i \int d\mathbf{X} \left(A \frac{\partial}{\partial q_i} \left(C \frac{\partial B}{\partial p_i} \right) \right) \\ &= -\sum_i \int d\mathbf{X} \left(AC \frac{\partial^2 B}{\partial p_i \partial q_i} - AC \frac{\partial^2 B}{\partial q_i \partial p_i} \right) \\ &\quad + \sum_i \int d\mathbf{X} \left(A \frac{\partial C}{\partial q_i} \frac{\partial B}{\partial p_i} - A \frac{\partial B}{\partial q_i} \frac{\partial C}{\partial p_i} \right) \\ &= \text{Tr}(A\{C, B\}) \end{aligned} \quad (\text{A.5})$$

$$= \text{Tr}(B\{A, C\}). \quad (\text{A.6})$$

(3) Ensemble average of Poisson bracket

$$\langle \{F(\mathbf{X}_0), G(\mathbf{X}_1)\} \rangle = \beta \langle \dot{F}(\mathbf{X}_0) G(\mathbf{X}_1) \rangle, \quad (\beta = 1/k_B T). \quad (\text{A.7})$$

The following is the proof of this relation:

$$\begin{aligned} & \langle \{F(\mathbf{X}_0), G(\mathbf{X}_1)\} \rangle \\ &= \frac{\int d\mathbf{X}_0 e^{-\beta H(\mathbf{X}_0)} \{F(\mathbf{X}_0), G(\mathbf{X}_1)\}}{\int d\mathbf{X}_0 e^{-\beta H(\mathbf{X}_0)}} \\ &= \frac{1}{Q} \int d\mathbf{X}_0 e^{-\beta H(\mathbf{X}_0)} \left(\frac{\partial F(\mathbf{X}_0)}{\partial \mathbf{q}_0} \frac{\partial G(\mathbf{X}_1)}{\partial \mathbf{p}_0} - \frac{\partial G(\mathbf{X}_1)}{\partial \mathbf{q}_0} \frac{\partial F(\mathbf{X}_0)}{\partial \mathbf{p}_0} \right) \\ &= \frac{1}{Q} \left[\int d\mathbf{q}_0 e^{-\beta H(\mathbf{X}_0)} \frac{\partial F(\mathbf{X}_0)}{\partial \mathbf{q}_0} G(\mathbf{X}_1) \Big|_{\mathbf{p}_0=-\infty}^{\mathbf{p}_0=+\infty} - \int d\mathbf{p}_0 \int d\mathbf{q}_0 G(\mathbf{X}_1) \frac{\partial}{\partial \mathbf{p}_0} \left(e^{-\beta H(\mathbf{X}_0)} \frac{\partial F(\mathbf{X}_0)}{\partial \mathbf{q}_0} \right) \right] \\ &\quad - \frac{1}{Q} \left[\int d\mathbf{p}_0 e^{-\beta H(\mathbf{X}_0)} \frac{\partial F(\mathbf{X}_0)}{\partial \mathbf{p}_0} G(\mathbf{X}_1) \Big|_{\mathbf{q}_0=-\infty}^{\mathbf{q}_0=+\infty} - \int d\mathbf{q}_0 \int d\mathbf{p}_0 G(\mathbf{X}_1) \frac{\partial}{\partial \mathbf{q}_0} \left(e^{-\beta H(\mathbf{X}_0)} \frac{\partial F(\mathbf{X}_0)}{\partial \mathbf{p}_0} \right) \right] \\ &\quad \left(\text{surface terms vanish: } e^{-\beta H(\mathbf{X}_0)} = 0 \text{ at } q_0 = \pm\infty \text{ or } p_0 = \pm\infty \right) \\ &= \frac{1}{Q} \left[- \int d\mathbf{X}_0 G(\mathbf{X}_1) \left(\frac{\partial e^{-\beta H(\mathbf{X}_0)}}{\partial \mathbf{p}_0} \frac{\partial F(\mathbf{X}_0)}{\partial \mathbf{q}_0} + e^{-\beta H(\mathbf{X}_0)} \frac{\partial^2 F(\mathbf{X}_0)}{\partial \mathbf{q}_0 \partial \mathbf{p}_0} \right) \right] \\ &\quad + \frac{1}{Q} \left[\int d\mathbf{X}_0 G(\mathbf{X}_1) \left(\frac{\partial e^{-\beta H(\mathbf{X}_0)}}{\partial \mathbf{q}_0} \frac{\partial F(\mathbf{X}_0)}{\partial \mathbf{p}_0} + e^{-\beta H(\mathbf{X}_0)} \frac{\partial^2 F(\mathbf{X}_0)}{\partial \mathbf{p}_0 \partial \mathbf{q}_0} \right) \right] \\ &= \beta \frac{1}{Q} \int d\mathbf{X}_0 e^{-\beta H(\mathbf{X}_0)} G(\mathbf{X}_1) \left(\frac{\partial H(\mathbf{X}_0)}{\partial \mathbf{p}_0} \frac{\partial F(\mathbf{X}_0)}{\partial \mathbf{q}_0} - \frac{\partial H(\mathbf{X}_0)}{\partial \mathbf{q}_0} \frac{\partial F(\mathbf{X}_0)}{\partial \mathbf{p}_0} \right) \\ &= \beta \frac{1}{Q} \int d\mathbf{X}_0 e^{-\beta H(\mathbf{X}_0)} G(\mathbf{X}_1) \left(\dot{\mathbf{q}}_0 \frac{\partial F(\mathbf{X}_0)}{\partial \mathbf{q}_0} + \dot{\mathbf{p}}_0 \frac{\partial F(\mathbf{X}_0)}{\partial \mathbf{p}_0} \right) \\ &= \beta \frac{1}{Q} \int d\mathbf{X}_0 e^{-\beta H(\mathbf{X}_0)} \dot{F}(\mathbf{X}_0) G(\mathbf{X}_1) \\ &= \beta \langle \dot{F}(\mathbf{X}_0) G(\mathbf{X}_1) \rangle. \end{aligned}$$

■

Appendix B

Derivation of Linear Contribution to $\exp(\hat{A} + \hat{B})$

When \hat{B} is a small perturbation, expand the exponential of the sum of operators $e^{\hat{A} + \hat{B}}$ to the linear term $\hat{S} \sim O(\hat{B})$,

$$e^{\hat{A} + \hat{B}} = e^{\hat{A}} + \hat{S} + O(\hat{B}^2). \quad (\text{B.1})$$

Our task here is to find \hat{S} . By definition, this linear operator can be written as

$$\hat{S} = \frac{d}{d\lambda} \left(e^{\hat{A} + \lambda \hat{B}} \right)_{\lambda=0}, \quad (\text{B.2})$$

since

$$\hat{S}(\lambda) = \frac{d}{d\lambda} \sum_{n=0}^{\infty} \frac{1}{n!} (\hat{A} + \lambda \hat{B})^n \quad (\text{B.3})$$

$$= \sum_{n=1}^{\infty} \frac{1}{n!} \sum_p \overbrace{(\hat{A}, \hat{A}, \dots, \hat{A}, \hat{B})}^{n-1 \text{ times}} \quad (p \text{ means all permutations}) \quad (\text{B.4})$$

$$= \sum_{n=1}^{\infty} \frac{1}{n!} \hat{S}_n. \quad (\text{B.5})$$

Thus,

$$\hat{S}_0 = 0, \quad (\text{B.6})$$

$$\hat{S}_1 = \hat{B}, \quad (\text{B.7})$$

$$\hat{S}_2 = \hat{A}\hat{B} + \hat{B}\hat{A}, \quad (\text{B.8})$$

$$\hat{S}_3 = \hat{A}^2\hat{B} + \hat{A}\hat{B}\hat{A} + \hat{B}\hat{A}^2, \quad (\text{B.9})$$

$$\hat{S}_4 = \hat{A}^3\hat{B} + \hat{A}^2\hat{B}\hat{A} + \hat{A}\hat{B}\hat{A}^2 + \hat{B}\hat{A}^3, \quad (\text{B.10})$$

$$\therefore \hat{S}_{n+1} = \hat{A}^n\hat{B} + \hat{S}_n\hat{A}. \quad (\text{B.11})$$

Define auxiliary operator

$$\hat{T}(t) \equiv \sum_{n=0}^{\infty} \frac{t^n}{n!} \hat{S}_n, \quad (\text{B.12})$$

$$\hat{T}(1) = \hat{S}, \quad (\text{B.13})$$

$$\sum_{n=0}^{\infty} \frac{t^n}{n!} \hat{S}_{n+1} = \frac{d}{dt} \sum_{n=0}^{\infty} \frac{t^{n+1}}{(n+1)!} \hat{S}_{n+1} = \frac{d}{dt} \sum_{m=1}^{\infty} \frac{t^m}{m!} \hat{S}_m = \frac{d}{dt} \hat{T}(t), \quad (\text{B.14})$$

$$\sum_{n=0}^{\infty} \frac{t^n}{n!} (\hat{A}^n\hat{B} + \hat{S}_n\hat{A}) = \left(\sum_{n=0}^{\infty} \frac{t^n}{n!} \hat{A}^n \right) \hat{B} + \left(\sum_{n=0}^{\infty} \frac{t^n}{n!} \hat{S}_n \right) \hat{A} = e^{t\hat{A}}\hat{B} + \hat{T}(t)\hat{A}, \quad (\text{B.15})$$

$$\therefore \frac{d}{dt} \hat{T}(t) = e^{t\hat{A}}\hat{B} + \hat{T}(t)\hat{A}. \quad (\text{B.16})$$

Performing Laplace transform ($\tilde{T}(s) = \int_0^{\infty} e^{-st} \hat{T}(t) dt$), which preserves the order of opera-

tors) on both sides of above equation, we have

$$s\tilde{T}(s) = \frac{1}{s-\hat{A}}\hat{B} + \tilde{T}(s)\hat{A}, \quad (\text{B.17})$$

$$\tilde{T}(s)(s-\hat{A}) = \frac{1}{s-\hat{A}}\hat{B}, \quad (\text{B.18})$$

$$\tilde{T}(s) = \frac{1}{s-\hat{A}}\hat{B}\frac{1}{s-\hat{A}}. \quad (\text{B.19})$$

Then perform the inverse Laplace transform,

$$\hat{T}(t) = \int_0^t dt' e^{(t-t')\hat{A}} \hat{B} e^{t'\hat{A}}. \quad (\text{B.20})$$

Therefore,

$$\hat{S} = \hat{T}(t=1) = \int_0^1 d\lambda e^{(1-\lambda)\hat{A}} \hat{B} e^{\lambda\hat{A}} \quad (\text{B.21})$$

$$= e^{\hat{A}} \int_0^1 d\lambda e^{-\lambda\hat{A}} \hat{B} e^{\lambda\hat{A}}. \quad (\text{B.22})$$

■

Recall the similar Kubo transform is defined as (see McQuarrie¹² p.493)

$$\tilde{F} = \frac{1}{\beta} \int_0^\beta d\lambda e^{\lambda\hat{H}} F e^{-\lambda\hat{H}}. \quad (\text{B.23})$$

Appendix C

Rotational Average

In an isotropic medium, such as liquid or fluid, there is no preferential direction as the orientation is uniformly distributed. In other words, an isotropic fluid is invariant with respect to rotations about any axis. Our goal here is to derive the rotational average or the orientational average of products of elements of two tensors in an isotropic medium.

Before defining rotational average, we need the concept of rotational transformation between two coordinates. As shown in Figure C.1, the space-fixed XYZ frame and molecule-fixed xyz frame having a common origin, are transformed with direction cosine matrix (ref. Zare²³² chap. 3). The direction cosine matrix $\Phi(\phi, \theta, \chi)$ is the product of three successive rotations, $R_Z(\phi)$, then $R_N(\theta)$, and finally $R_z(\chi)$.

$$\begin{pmatrix} x \\ y \\ z \end{pmatrix} = R_z(\chi)R_N(\theta)R_Z(\phi) \begin{pmatrix} X \\ Y \\ Z \end{pmatrix} = \Phi(\phi, \theta, \chi) \begin{pmatrix} X \\ Y \\ Z \end{pmatrix}. \quad (\text{C.1})$$

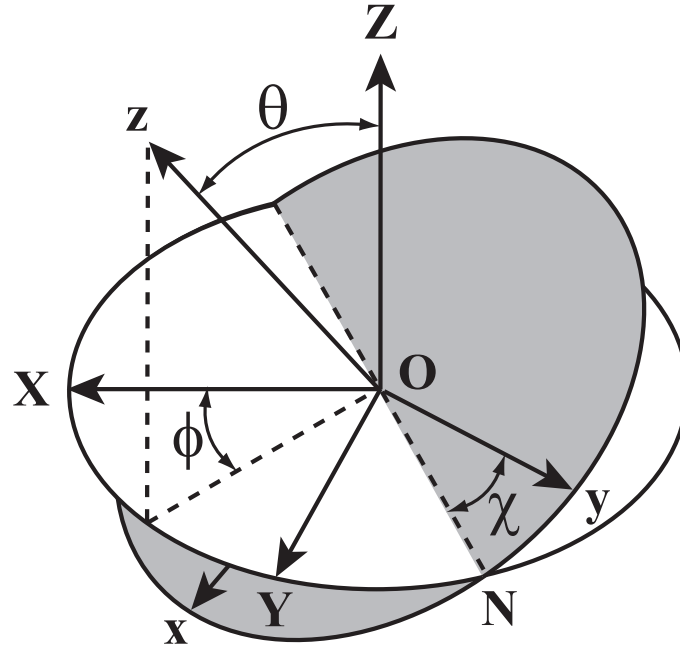


Figure C.1 Euler angle ϕ, θ, χ relating the space-fixed XYZ and molecule-fixed xyz frames. $\phi = 0 \sim 2\pi, \theta = 0 \sim \pi, \chi = 0 \sim 2\pi$.

$$R_Z(\phi) = \begin{pmatrix} \cos \phi & \sin \phi & 0 \\ -\sin \phi & \cos \phi & 0 \\ 0 & 0 & 1 \end{pmatrix}, \quad (\text{C.2})$$

$$R_N(\theta) = \begin{pmatrix} \cos \theta & 0 & -\sin \theta \\ 0 & 1 & 0 \\ \sin \theta & 0 & \cos \theta \end{pmatrix}, \quad (\text{C.3})$$

$$R_z(\chi) = \begin{pmatrix} \cos \chi & \sin \chi & 0 \\ -\sin \chi & \cos \chi & 0 \\ 0 & 0 & 1 \end{pmatrix}. \quad (\text{C.4})$$

$$\Phi(\phi, \theta, \chi) = \begin{pmatrix} c\phi c\theta c\chi - s\phi s\chi & s\phi c\theta c\chi + c\phi s\chi & -s\theta c\chi \\ -c\phi c\theta s\chi - s\phi c\chi & -s\phi c\theta s\chi + c\phi c\chi & s\theta s\chi \\ c\phi s\theta & s\phi s\theta & c\theta \end{pmatrix}. \quad (\text{C.5})$$

where c and s denote \cos and \sin respectively. The transformation matrix, or the direction cosine matrix is unitary, i.e. $\Phi^{-1} = \Phi^T$, for example $\Phi_{xZ} = (\Phi^{-1})_{Zx} = -\sin\theta \cos\chi$.

We use subscripts A, B, \dots as distinct Cartesian indices from XYZ frame, and i, j, \dots as distinct Cartesian indices from xyz frame. Now we can transform a matrix element in the XYZ frame into the xyz frame with any orientation (any value of Euler angles),

$$a_{ij} = \sum_{A,B} \Phi_{iA} \Phi_{jB} a_{AB}, \quad (\text{C.6})$$

$$\text{or vice versa, } a_{AB} = \sum_{A,B} \Phi_{iA} \Phi_{jB} a_{ij} = \sum_{A,B} (\Phi^{-1})_{Ai} (\Phi^{-1})_{Bj} a_{ij}. \quad (\text{C.7})$$

The rotational average or orientational average of any function $f(\phi, \theta, \chi)$ is simply integration over all possible Euler angles,

$$\begin{aligned} \overline{f(\phi, \theta, \chi)} &= \frac{1}{2\pi} \int_0^{2\pi} d\chi \cdot \frac{1}{2\pi} \int_0^{2\pi} d\phi \cdot \frac{1}{2} \int_0^\pi d\theta \sin\theta f(\phi, \theta, \chi) \\ &= \frac{1}{8\pi^2} \int_0^{2\pi} d\chi \int_0^{2\pi} d\phi \int_0^\pi d\theta \sin\theta f(\phi, \theta, \chi). \end{aligned} \quad (\text{C.8})$$

So the rotational average of the product of two tensor elements is²⁶⁷

$$\overline{a_{AB} b_{CD}} = \overline{\left(\sum_{i,j} \Phi_{iA} \Phi_{jB} a_{ij} \right) \left(\sum_{k,l} \Phi_{kC} \Phi_{lD} b_{kl} \right)} \quad (\text{C.9})$$

$$= \sum_{i,j} \sum_{k,l} \overline{\Phi_{iA} \Phi_{jB} \Phi_{kC} \Phi_{lD}} a_{ij} b_{kl}. \quad (\text{C.10})$$

Because of the symmetry, the only nonvanishing products of 4 direction cosine matrix

elements averaged over all directions are

$$\overline{\Phi_{iA}^4} = \frac{1}{5}, \quad (\text{C.11})$$

$$\overline{\Phi_{iA}^2 \Phi_{jB}^2} = \frac{2}{15}, \quad (\text{C.12})$$

$$\overline{\Phi_{iA}^2 \Phi_{jA}^2} = \overline{\Phi_{iA}^2 \Phi_{iB}^2} = \frac{1}{15}, \quad (\text{C.13})$$

$$\overline{\Phi_{iA} \Phi_{iB} \Phi_{jA} \Phi_{jB}} = \frac{1}{30}. \quad (\text{C.14})$$

For example, we test

$$\overline{\Phi_{zZ}^4} = \frac{1}{8\pi^2} \int_0^{2\pi} d\chi \int_0^{2\pi} d\phi \int_0^\pi d\theta \sin \theta \cdot \cos^4 \theta = \frac{1}{5},$$

$$\overline{\Phi_{zZ}^2 \Phi_{zY}^2} = \overline{\cos^2 \theta \sin^2 \theta \sin^2 \phi} = \frac{1}{15},$$

$$\begin{aligned} \overline{\Phi_{xZ} \Phi_{zZ} \Phi_{xY} \Phi_{zY}} &= \overline{-\sin \theta \cos \chi \cdot \cos \theta \cdot (\sin \phi \cos \theta \cos \chi + \cos \phi \sin \chi) \cdot \sin \phi \sin \theta} \\ &= -\frac{1}{30}. \end{aligned}$$

The summary on rotational average of direction cosines:³²⁸ any odd number direction cosine product vanishes, and for even numbers

$$\overline{\Phi_{iA} \Phi_{jA}} = \delta_{ij}/3, \quad (\text{C.15})$$

$$\overline{\Phi_{iA} \Phi_{jB}} = 0, \quad (\text{C.16})$$

$$\overline{\Phi_{iA} \Phi_{jA} \Phi_{kA} \Phi_{lA}} = \frac{\delta_{ij} \delta_{kl} + \delta_{ik} \delta_{jl} + \delta_{il} \delta_{jk}}{3 \times 5}, \quad (\text{C.17})$$

$$\overline{\Phi_{iA} \Phi_{jA} \Phi_{kB} \Phi_{lB}} = \frac{4\delta_{ij} \delta_{kl} - \delta_{ik} \delta_{jl} - \delta_{il} \delta_{jk}}{2 \times 3 \times 5}, \quad (\text{C.18})$$

$$\overline{\Phi_{iA}\Phi_{jA}\Phi_{kA}\Phi_{lA}\Phi_{mA}\Phi_{nA}} = \frac{\delta_{ij}\delta_{kl}\delta_{mn} + \delta_{ij}\delta_{km}\delta_{ln} + \dots (15 \text{ terms})}{3 \times 5 \times 7}, \quad (\text{C.19})$$

$$\overline{\Phi_{iA}\Phi_{jA}\Phi_{kB}\Phi_{lB}\Phi_{mB}\Phi_{nB}} = \frac{6\delta_{ij}(\delta_{kl}\delta_{mn} + \delta_{km}\delta_{ln} + \delta_{kn}\delta_{lm}) - \delta_{ik}\delta_{jl}\delta_{mn} - \dots (18 \text{ terms})}{2 \times 3 \times 5 \times 7}. \quad (\text{C.20})$$

As in an isotropic medium, tensor elements that are related by a reversal of indices are identical:²⁶⁷ $a_{ij} = a_{ji}$. Along with the nonvanishing direction cosine products, we can find the only nonzero averages are $ZZZZ, XXZZ, XZXZ$ and their permutation among the three spatial indices,

$$\overline{a_{ZZ}b_{ZZ}} = \frac{1}{15}\text{Tr}(a) \cdot \text{Tr}(b) + \frac{2}{15}\text{PP}(a, b), \quad (\text{C.21})$$

$$\overline{a_{XX}b_{ZZ}} = \frac{2}{15}\text{Tr}(a) \cdot \text{Tr}(b) - \frac{1}{15}\text{PP}(a, b), \quad (\text{C.22})$$

$$\overline{a_{XZ}b_{XZ}} = -\frac{1}{30}\text{Tr}(a) \cdot \text{Tr}(b) + \frac{1}{10}\text{PP}(a, b). \quad (\text{C.23})$$

where rotational invariants are used: (1) trace of a tensor $\text{Tr}(a) = \sum_i a_{ii}$, (2) pairwise product of two tensors $\text{PP}(a, b) = \sum_{i,j} a_{ij}b_{ij}$.

For example, we test the $XZXZ$ case,

$$\begin{aligned}
\overline{a_{XZ}b_{XZ}} &= \sum_{i,j} \sum_{k,l} \overline{\Phi_{iX}\Phi_{jZ}\Phi_{kX}\Phi_{lZ}} a_{ij}b_{kl} \\
&= \left(\overline{\Phi_{iX}\Phi_{jZ}\Phi_{iX}\Phi_{jZ}} = \frac{2}{15} \right) \cdot \sum_{i \neq j} a_{ij}b_{ij} \\
&+ \left(\overline{\Phi_{iX}\Phi_{iZ}\Phi_{iX}\Phi_{iZ}} = \frac{1}{15} \right) \cdot \sum_i a_{ii}b_{ii} \\
&+ \left(\overline{\Phi_{iX}\Phi_{iZ}\Phi_{jX}\Phi_{jZ}} = -\frac{1}{30} \right) \cdot \sum_{i \neq j} a_{ii}b_{jj} \\
&+ \left(\overline{\Phi_{jX}\Phi_{iZ}\Phi_{iX}\Phi_{jZ}} = -\frac{1}{30} \right) \cdot \sum_{i \neq j} a_{ji}b_{ij} \text{ (using } a_{ji} = a_{ij}) \\
&= \frac{1}{10} \sum_{i \neq j} a_{ij}b_{ij} + \frac{1}{15} \sum_i a_{ii}b_{ii} - \frac{1}{30} \sum_{i \neq j} a_{ii}b_{jj} \\
&= \frac{1}{10} \text{PP}(a, b) - \frac{1}{30} \text{Tr}(a) \cdot \text{Tr}(b).
\end{aligned}$$

For rotational average of the product of three tensor elements (related to the product of six direction cosines), see Murry and Fourkas²⁶⁷ for details.

Appendix D

Simulation Details

1. **MD propagation Algorithm:** velocity Verlet.⁵⁹

2. **Atomic liquid model.**

The Lennard-Jones potential is used to describe the interaction between solute and solvent atoms,

$$u(r_{ab}) = 4\epsilon_{ab} \left[\left(\frac{\sigma}{r_{ab}} \right)^{12} - \left(\frac{\sigma}{r_{ab}} \right)^6 \right]. \quad (\text{D.1})$$

System contains $N = 108$ or 256 atoms in total including 1 solute (u) atom and two kinds of solvent atoms — strong solvent (S) and weak solvent (W). On the solute's ground state, all pairs of atoms have the same interaction well depths $\epsilon_{ab} = \epsilon$; on the solute's excited state $\epsilon_{u-e,S} = 3\epsilon$, $\epsilon_{u-e,W} = 1.5\epsilon$, yet the solvent-solvent well depths remain the same as on the ground state. All particles have the same mass m and diameter σ .

3. **Lennard-Jones reduced unit**, let $m = \sigma = \epsilon = 1$, then

$$T^* = \frac{k_B T}{\epsilon}, \quad \rho^* = \rho \sigma^3, \quad t^* = \frac{t}{\sqrt{\frac{m\sigma^2}{\epsilon}}}, \quad r^* = \frac{r}{\sigma}. \quad (\text{D.2})$$

We assume liquid Argon parameters $m_{Ar} = 39.948$ a.m.u., $\sigma = 3.405\text{\AA}$, and $\frac{\epsilon}{k_B} = 119.8\text{K}$

to get real times and distances.

4. **Time step** $\delta t = 0.00250 \tau_{LJ} = 5.40$ fs ($1 \tau_{LJ} = \sqrt{\frac{m\sigma^2}{\epsilon}} = 2.16$ ps).
5. **Sampling rate** is 1 configuration every 10 MD steps. Other sampling rate will be specified if different from every 10 steps.
6. **Thermal condition.** Number density $\rho^* = \rho\sigma^3 = 0.80$, and reduced temperature $T^* = \frac{k_B T}{\epsilon} = 1.00 \pm 0.03$. It is a typical liquid Argon thermal condition.
7. **Computer cell length** is $L = 5.13 \sigma = 17.47 \text{ \AA}$ with cubic periodic boundary condition for $N = 256$ system.
8. **Getting equilibrated.**

(1) Ground state equilibrium configuration. Starting with *fcc* lattice and Gaussian distributed velocities with melting temperature $T^* = 5.00$ for $2 \times 10^3 \delta t = 10.8$ ps and relax for up to $1 \times 10^7 \delta t = 54$ ns, in the meantime, multiple temperature rescaling procedures are performed until the system temperature reaches $T^* = 1.00$. Then without rescaling temperature, the system relaxes for another $1 \times 10^6 \delta t = 5.4$ ns. Equilibrium ground state configuration is obtained and checked to be fully equilibrated by calculating the translational order parameter, radial distribution function, and comparing the fluctuation of kinetic energy with theoretical values:

Firstly, the translational order parameter is defined as follows.

$$\rho(\mathbf{k}) = \frac{1}{N} \sum_{i=1}^N \cos(\mathbf{k} \cdot \mathbf{r}_i), \quad \mathbf{k} = \frac{2\pi}{l}(-1, 1, -1) = \frac{(2N)^{\frac{1}{3}}\pi}{L}(-1, 1, -1), \quad (\text{D.3})$$

where \mathbf{k} is a reciprocal vector of the initial lattice, and l is the unit cell size, L in the computer cell size, N is the total number of atoms.³²⁹ The order parameter is recorded from the time when the temperature T^* is set to 5.0. After the system melts, the temperature T^* is rescaled to 1.0. However, after 167.4 ps has elapsed since the

heating, the temperature of system is never forcibly set to 1.0. The mean value of order parameter is -0.00215, which indicates that the system is in the liquid state and translational disordered.

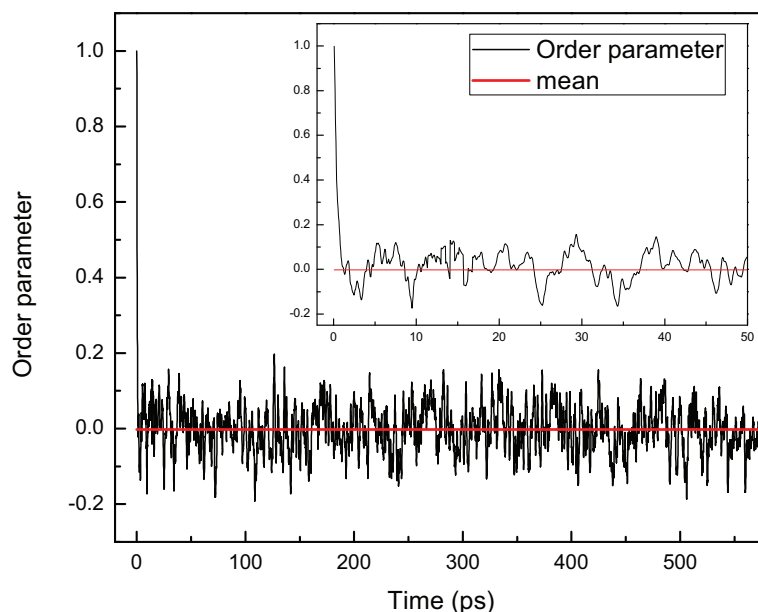


Figure D.1 Order parameter of the ground-state simulated Lennard-Jones liquid ($N = 256$).

Secondly, the radial distribution function or the pair distribution function of the equilibrium state is given by

$$g(r) = \frac{N(r)}{N_{ideal}(r)} = \frac{N(r)}{\rho 4\pi r^2 dr}, \quad (D.4)$$

which is plotted in Figure 3.1. Here the dr is 1/100 of half length of computer cell. $N(r)$ is the number of molecules located within the sphere shell whose radius is from r to $r + dr$. After equilibrium, MD simulation is run for 100 000 steps and accumulates the radial distribution every 10 steps. The total number of configurations used to calculate the radial distribution is 10 000.

Thirdly, I also checked the fluctuation of the kinetic energy(KE). The kinetic

energy is given by

$$KE = \sum_{j=1}^N \frac{1}{2} m \mathbf{v}_j^2. \quad (\text{D.5})$$

The temperature is defined as $T = \frac{2KE}{3Nk_B}$. So, for $N = 256$ system, the simulated fluctuation of the kinetic energy $\sigma(KE) = \sqrt{\langle KE^2 \rangle - \langle KE \rangle^2} = 12.10 \epsilon$, and the analytical result is $\sigma(KE) = \sqrt{\frac{3}{4} N k_B T} = 13.86 \epsilon$. The derivation of the fluctuation of kinetic energy in microcanonical ensemble is included in the next section.

Lastly, the velocity correlation function $C_{vv}(t)$ defined in Equation 3.2 is already shown in Figure 3.2, which is a typical one for a Lennard-Jones liquid.

(2) For the excited state, starting from equilibrium ground state configuration, after changing the well depth parameter, system is allowed to relax for $1 \times 10^7 \delta t = 54$ ns, and the equilibrium excited state configuration is obtained (and checked).

9. Solvation shell dimension.

For the atomic liquid system at the above-mentioned thermal condition, the cutoff radius for the first shell is $1.5561 \sigma = 5.2984 \text{ \AA}$, and the cutoff radius for the second shell is $2.4579 \sigma = 8.6755 \text{ \AA}$. The cutoff radii of the first and the second shells are the first and the second minimum of the solute–solvent radial distribution function as in Figure 3.1.

10. Choosing solute’s and strong and weak solvents’ polarizability

The isolated molecular polarizabilities $\alpha_u = 0.2 \sigma^3 = 7.90 \text{ \AA}^3$, $\alpha_S = 0.101 \sigma^3 = 3.99 \text{ \AA}^3$ (half of DMSO²⁷⁴), $\alpha_W = 0.0186 \sigma^3 = 0.73 \text{ \AA}^3$ (half of water²⁷⁵).

11. INM analysis parameters.

In INM analysis, the matrix diagonalization is performed by LAPACK library.²⁸⁵

Frequency range: -50 cm^{-1} to 200 cm^{-1} .

Histogram bin number = 200.

The influence spectrum $\rho_A(\omega) = \langle \sum_{\alpha} c_{\alpha}^2 \delta(\omega - \omega_{\alpha}) \rangle$ is subject to the normalization condition such that

$$\int_{\text{real}} d\omega \rho_A(\omega) = \left\langle \sum_{\text{real } \omega_{\alpha}} c_{\alpha}^2 \right\rangle. \quad (\text{D.6})$$

Similarly, for the 2D solute-pump/solvent-probe spectra, the response satisfies the following condition

$$\int_{\text{real}} R(\omega, T) \omega d\omega = \frac{\frac{\pi}{2} \left\langle e^{\beta \delta \Delta V(0)} \sum_{\text{real } \omega_{\alpha}} \Pi_{xz, \alpha}^2(T) \right\rangle_e}{\langle e^{\beta \Delta V} \rangle_e}. \quad (\text{D.7})$$

Derivation of kinetic energy fluctuation in microcanonical ensemble

For the canonical ensemble,

$$\sigma^2(KE) = \langle KE^2 \rangle - \langle KE \rangle^2 = -\frac{\partial \langle KE \rangle}{\partial \beta} = -\frac{\partial \left(\frac{3}{2} N \frac{1}{\beta} \right)}{\partial \beta} = \frac{3}{2} N (k_B T)^2.$$

Thus,

$$\sigma(KE) = \sqrt{\frac{2}{3N} \langle KE \rangle} = \sqrt{\frac{2}{n} \langle KE \rangle},$$

where n is the degrees of freedom.

For microcanonical ensemble, taking n -dimensional (n =degrees of freedom) SHO for example, the Hamiltonian is

$$\mathcal{H} = \sum_{j=1}^n \left(\frac{p_j^2}{2m} + \frac{1}{2} m \omega^2 x_j^2 \right) = KE(\vec{p}) + V(\vec{x}), \quad (\text{D.8})$$

and microcanonical partition function can be written as

$$\begin{aligned} \Omega(E, n) &= \frac{1}{h^n} \int d\vec{p} d\vec{x} \delta(E - \mathcal{H}(\vec{p}, \vec{x})) \\ &= \frac{f^2(n)}{h^n} \left(\frac{4m}{m\omega^2} \right)^{n/2} \int_0^{\infty} dt t^{n-1} \int_0^{\infty} du u^{n-1} \delta(E - t^2 - u^2). \end{aligned}$$

where

$$t^2 = \sum_{j=1}^n \frac{p_j^2}{2m} = \sum_{j=1}^n (p'_j)^2 = KE, \quad p'_j = \frac{1}{\sqrt{2m}} p_j,$$

$$u^2 = \sum_{j=1}^n \frac{1}{2} m \omega^2 x_j^2 = \sum_{j=1}^n (x'_j)^2 = V, \quad x'_j = \sqrt{\frac{1}{2} m \omega^2} x_j,$$

$$f(n) = \frac{2\pi^{n/2}}{\Gamma(\frac{n}{2})}.$$

This $f(n)$ is the Jacobian determinant in n -dimensional spherical coordinate.

$$d\vec{R} = dR R^{n-1} f(n), \quad (\text{see McQuarrie}^{12} \text{ p.28 } \mathbf{1-24.})$$

$$\text{so, } d\vec{p} = (2m)^{\frac{n}{2}} d\vec{p}' = (2m)^{\frac{n}{2}} dt t^{n-1} f(n),$$

$$\text{and } d\vec{x} = \frac{d\vec{x}'}{(m\omega^2/2)^{\frac{n}{2}}} = \frac{1}{(m\omega^2/2)^{\frac{n}{2}}} du u^{n-1} f(n).$$

Then,

$$\begin{aligned} \langle KE \rangle &= \frac{\frac{1}{h^n} \int d\vec{p} d\vec{x} KE \delta(E - \mathcal{H}(\vec{p}, \vec{x}))}{\frac{1}{h^n} \int d\vec{p} d\vec{x} \delta(E - \mathcal{H}(\vec{p}, \vec{x}))} \\ &= \frac{\int_0^\infty dt t^{n-1} \int_0^\infty du u^{n-1} t^2 \delta(E - t^2 - u^2)}{\int_0^\infty dt t^{n-1} \int_0^\infty du u^{n-1} \delta(E - t^2 - u^2)}, \end{aligned}$$

where

$$\int_0^\infty du u^{n-1} \delta(E - t^2 - u^2) = \left. \frac{u^{n-1}}{\left| \frac{\partial(E - T^2 - u^2)}{\partial u} \right|} \right|_{u=+\sqrt{E-t^2}} = \frac{1}{2} (E - t^2)^{\frac{n}{2}-1}.$$

Variable replacement: $x = \frac{t^2}{E} \Rightarrow dt = \frac{\sqrt{E} dx}{2\sqrt{x}}$, using the definition of Beta and Gamma

functions † , the average of KE and KE^2 become

$$\begin{aligned}
\langle KE \rangle &= E \cdot \frac{\int_0^1 (x)^{\frac{n}{2}} (1-x)^{\frac{n}{2}-1} dx}{\int_0^1 (x)^{\frac{n}{2}-1} (1-x)^{\frac{n}{2}-1} dx} \\
&= E \cdot \frac{B(\frac{n}{2}+1, \frac{n}{2})}{B(\frac{n}{2}, \frac{n}{2})} = E \cdot \frac{\Gamma(\frac{n}{2}+1)\Gamma(\frac{n}{2})}{\Gamma(n+1)} \cdot \frac{\Gamma(n)}{\Gamma(\frac{n}{2})\Gamma(\frac{n}{2})} \\
&= \frac{E}{2},
\end{aligned}$$

$$\begin{aligned}
\langle KE^2 \rangle &= E^2 \cdot \frac{\int_0^1 (x)^{\frac{n}{2}+1} (1-x)^{\frac{n}{2}-1} dx}{\int_0^1 (x)^{\frac{n}{2}-1} (1-x)^{\frac{n}{2}-1} dx} \\
&= E^2 \cdot \frac{B(\frac{n}{2}+2, \frac{n}{2})}{B(\frac{n}{2}, \frac{n}{2})} = E^2 \cdot \frac{\Gamma(\frac{n}{2}+2)\Gamma(\frac{n}{2})}{\Gamma(n+2)} \cdot \frac{\Gamma(n)}{\Gamma(\frac{n}{2})\Gamma(\frac{n}{2})} \\
&= \frac{E^2}{4} \frac{n+2}{n+1} = \langle KE \rangle^2 \frac{n+2}{n+1}.
\end{aligned}$$

So,

$$\frac{\langle KE^2 \rangle - \langle KE \rangle^2}{E^2} = \frac{1}{4(n+1)} \Rightarrow \frac{\sigma(KE)}{\langle KE \rangle} = \sqrt{\frac{1}{n+1}} \approx \sqrt{\frac{1}{n}}. \quad (\text{D.9})$$

Therefore, the fluctuation of the kinetic energy in the microcanonical ensemble is

$$\sigma_{KE}^{NVE} = \langle KE \rangle \cdot \sqrt{\frac{1}{n}} \quad (n \rightarrow \infty, \text{ where } n \text{ is the degrees of freedom}). \quad (\text{D.10})$$

For our system, the number of molecules $N = 256$ and degrees of freedom is $3N$, so the fluctuation of kinetic energy in microcanonical ensemble is connected to the fluctuation of kinetic energy in canonical ensemble as follows

$$\sigma_{KE}^{NVE} = \langle KE \rangle \sqrt{\frac{1}{3N}} = \sqrt{\frac{3}{4}} N k_B T = \frac{1}{\sqrt{2}} \sigma_{KE}^{NVT} = 13.86\epsilon. \quad (\text{D.11})$$

† Beta function is defined as $B(a, b) = \int_0^1 dx \cdot x^{a-1} \cdot (1-x)^{b-1} = B(b, a) = \frac{\Gamma(a)\Gamma(b)}{\Gamma(a+b)}$, where Gamma function $\Gamma(x) = \int_0^\infty t^{x-1} e^{-t} dt$, and use the relation $\Gamma(x+1) = x\Gamma(x)$.

Appendix E

Spatial Derivative of the Many-body

Polarizability

The spatial derivative is a key element to projection operator which is used to extract certain contributions out of the whole spectrum. This appendix includes formalism for the spatial derivative of the many-body polarizability along with tests with the atomic liquid model.

In dipole-induced dipole (DID) model (chapter 3), the many-body polarizability $\mathbf{\Pi}$ is the sum of all the effective molecular polarizabilities $\boldsymbol{\pi}_i$, ($i = 1, \dots, N$),

$$\mathbf{\Pi} = \sum_{i=1}^N \boldsymbol{\pi}_i, \quad (\text{E.1})$$

and

$$\boldsymbol{\pi}_i = \boldsymbol{\alpha}_i \cdot \left[\mathbf{1} + \sum_{j \neq i}^N \mathbf{T}_{ij} \cdot \boldsymbol{\pi}_j \right], \quad (\text{E.2})$$

where $\boldsymbol{\alpha}_i$ is the isolated-molecular polarizability tensor for molecule i and the dipole-dipole tensor between molecules i and j , \mathbf{T}_{ij} is given by

$$\mathbf{T}_{ij} \equiv \mathbf{T}(\vec{r}_{ij}) = \nabla \nabla \left(\frac{1}{r_{ij}} \right) = \left(\frac{3\hat{\mathbf{r}}\hat{\mathbf{r}} - \mathbf{1}}{r^3} \right)_{\mathbf{r}=\mathbf{r}_{ij}=\mathbf{r}_i-\mathbf{r}_j=(x,y,z), r=|\mathbf{r}|, \hat{\mathbf{r}}=\mathbf{r}/r}. \quad (\text{E.3})$$

Or in the tensor component form, the dipole-dipole tensor is (Greek letters without any subscript stand for Cartesian coordinates (x,y,z), and α_i is the isotropic isolated-molecular polarizability for molecule i . i, j, k are molecule indices.)

$$(T_{ij})_{\alpha\beta} = \nabla_\alpha \nabla_\beta \left(\frac{1}{r_{ij}} \right) = \left[\frac{\partial}{\partial r_\alpha} \frac{\partial}{\partial r_\beta} \frac{1}{(x^2 + y^2 + z^2)^{1/2}} \right]_{\mathbf{r}=\mathbf{r}_{ij}} = \left[\frac{3r_\alpha r_\beta - r^2 \delta_{\alpha\beta}}{r^5} \right]_{\mathbf{r}=\mathbf{r}_{ij}} \quad (\text{E.4})$$

Derivation of the spatial derivative

The spatial derivative of the many-body polarizability with respect to a particular k th Cartesian coordinate \mathbf{r}_k in compact tensor form, or molecule k 's component $\mu = (x, y, z)$, $r_{k\mu}$ in tensor component form are given by

$$\nabla_k \Pi = \sum_i \nabla_k \boldsymbol{\pi}_i \quad \text{or} \quad \frac{\partial}{\partial r_{k\mu}} (\Pi)_{\alpha\beta} = \sum_i \frac{\partial}{\partial r_{k\mu}} (\boldsymbol{\pi}_i)_{\alpha\beta} \quad (\text{E.5})$$

The spatial derivative of the effective molecular polarizability of molecule i is

$$\begin{aligned} \nabla_k \boldsymbol{\pi}_i &= \boldsymbol{\alpha}_i \sum_{j \neq i} [(\nabla_k \mathbf{T}_{ij}) \cdot \boldsymbol{\pi}_j + \mathbf{T}_{ij} \cdot (\nabla_k \boldsymbol{\pi}_j)] \\ &= \boldsymbol{\alpha}_i \cdot \begin{cases} \sum_{j \neq k} [(\nabla_k \mathbf{T}_{kj}) \cdot \boldsymbol{\pi}_j + \mathbf{T}_{kj} \cdot \nabla_k \boldsymbol{\pi}_j] & (i = k) \\ (\nabla_k \mathbf{T}_{ik}) \cdot \boldsymbol{\pi}_k + \sum_{j \neq i} \mathbf{T}_{ij} \cdot (\nabla_k \boldsymbol{\pi}_j) & (i \neq k) \end{cases} \end{aligned} \quad (\text{E.6})$$

Or in the component form (used in practice),

$$\begin{aligned} \frac{\partial}{\partial r_{k\mu}} (\boldsymbol{\pi}_i)_{\alpha\beta} &= \boldsymbol{\alpha}_i \cdot \sum_{j \neq i} \sum_{\gamma}^{x,y,z} \left[\frac{3 r_{ij}^2 (r_{ij\mu} \delta_{\alpha\gamma} + r_{ij\alpha} \delta_{\mu\gamma} + r_{ij\gamma} \delta_{\mu\alpha}) - 15 r_{ij\mu} r_{ij\alpha} r_{ij\gamma}}{r_{ij}^7} \right. \\ &\quad \left. \cdot (\delta_{ki} - \delta_{kj}) \cdot (\boldsymbol{\pi}_j)_{\gamma\beta} + \frac{3 r_{ij\alpha} r_{ij\gamma} - r_{ij}^2 \delta_{\alpha\gamma}}{r_{ij}^5} \cdot \frac{\partial}{\partial r_{k\mu}} (\boldsymbol{\pi}_j)_{\gamma\beta} \right], \end{aligned} \quad (\text{E.7})$$

where the spatial derivative of dipole–dipole tensor is \ddagger ,

$$(\nabla_k \mathbf{T}_{ij})_{\alpha\gamma}^{\mu} \equiv \frac{\partial}{\partial r_{k\mu}} (T_{ij})_{\alpha\gamma} = \frac{3r_{ij}^2 (r_{ij\mu} \delta_{\alpha\gamma} + r_{ij\alpha} \delta_{\mu\gamma} + r_{ij\gamma} \delta_{\mu\alpha}) - 15 r_{ij\mu} r_{ij\alpha} r_{ij\gamma}}{r_{ij}^7} (\delta_{ki} - \delta_{kj}). \quad (\text{E.8})$$

The derivation of the above relation is as follows:

$$\frac{\partial}{\partial r_{k\mu}} (T_{ij})_{\alpha\gamma} = \frac{\partial}{\partial r_{k\mu}} \left(\frac{3r_{ij\alpha} r_{ij\gamma} - r_{ij}^2 \delta_{\alpha\gamma}}{r_{ij}^5} \right) \quad (\text{E.9})$$

$$= \left\{ \frac{\partial}{\partial r_{k\mu}} [3(r_{i\alpha} - r_{j\alpha})(r_{i\gamma} - r_{j\gamma}) - r_{ij}^2 \delta_{\alpha\gamma}] \cdot r_{ij}^5 - \frac{\partial}{\partial r_{k\mu}} (r_{ij}^5) \cdot [3r_{ij\alpha} r_{ij\gamma} - r_{ij}^2 \delta_{\alpha\gamma}] \right\} / r_{ij}^{10}, \quad (\text{E.10})$$

where

$$\begin{aligned} & \frac{\partial}{\partial r_{k\mu}} [3(r_{i\alpha} - r_{j\alpha})(r_{i\gamma} - r_{j\gamma}) - r_{ij}^2 \delta_{\alpha\gamma}] \\ &= 3(r_{i\gamma} - r_{j\gamma}) \cdot \frac{\partial}{\partial r_{k\mu}} (r_{i\alpha} - r_{j\alpha}) + 3(r_{i\alpha} - r_{j\alpha}) \cdot \frac{\partial}{\partial r_{k\mu}} (r_{i\gamma} - r_{j\gamma}) \\ & \quad - \delta_{\alpha\gamma} \cdot \frac{\partial}{\partial r_{k\mu}} [(r_{ix} - r_{jx})^2 + (r_{iy} - r_{jy})^2 + (r_{iz} - r_{jz})^2] \\ &= 3(r_{i\gamma} - r_{j\gamma}) \cdot \delta_{\mu\alpha} (\delta_{ki} - \delta_{kj}) + 3(r_{i\alpha} - r_{j\alpha}) \cdot \delta_{\mu\gamma} (\delta_{ki} - \delta_{kj}) \\ & \quad - \delta_{\alpha\gamma} \cdot [2(r_{i\mu} - r_{j\mu}) \delta_{ki} - 2(r_{i\mu} - r_{j\mu}) \delta_{kj}] \\ &= (3r_{ij\gamma} \delta_{\mu\alpha} + 3r_{ij\alpha} \delta_{\mu\gamma} - 2r_{ij\mu} \delta_{\alpha\gamma}) \cdot (\delta_{ki} - \delta_{kj}), \quad (\text{E.11}) \end{aligned}$$

\ddagger Note that the upper and lower Greek letter indices are not related to contravariant and covariant tensor notation.

and

$$\begin{aligned}
\frac{\partial}{\partial r_{k\mu}} \left(r_{ij}^5 \right) &= \frac{\partial}{\partial r_{k\mu}} \left[(r_{ix} - r_{jx})^2 + (r_{iy} - r_{jy})^2 + (r_{iz} - r_{jz})^2 \right]^{5/2} \\
&= \frac{5}{2} [r_{ij}^2]^{3/2} \cdot [2(r_{i\mu} - r_{j\mu})\delta_{ki} - 2(r_{i\mu} - r_{j\mu})\delta_{kj}] \\
&= 5r_{ij}^3 r_{ij\mu} (\delta_{ki} - \delta_{kj}). \tag{E.12}
\end{aligned}$$

Substituting Equation E.11 and E.12 into Equation E.10, we have

$$\frac{\partial}{\partial r_{k\mu}} (T_{ij})_{\alpha\gamma} = \frac{3r_{ij}^2 (r_{ij\mu} \delta_{\alpha\gamma} + r_{ij\alpha} \delta_{\mu\gamma} + r_{ij\gamma} \delta_{\mu\alpha}) - 15 r_{ij\mu} r_{ij\alpha} r_{ij\gamma} (\delta_{ki} - \delta_{kj})}{r_{ij}^7}. \tag{E.13}$$

■

Properties of $\nabla_k \mathbf{T}_{ij}$:

- (1) $\nabla_k \mathbf{T}_{ij} \neq 0$ only if $i \neq j$ and $k = i$ or j .
- (2) $\nabla_k \mathbf{T}_{ik} = -\nabla_k \mathbf{T}_{ki} = -\nabla_i \mathbf{T}_{ik}$.

We can compute the spatial derivative of the many-body polarizability by iterative method. To the first order precision, the isolated molecular polarizabilities α_i ($i = 1, \dots, N$) is substituted into π_i in Equation E.7; and to the infinite order precision, the infinite order effective molecular polarizabilities π_i , ($i = 1, \dots, N$) is used in Equation E.7. For the first iteration, the initial guess of all the elements of $\nabla_k \pi_i$ ($i = 1, \dots, N$) are zero. The iteration is 1 cycle for the first order approximation, whereas for the infinite order the iteration terminates until tolerance is reached. The tolerance is

$$\sum_{i=1}^N \sum_{\alpha, \beta, \mu}^{x, y, z} \left| \frac{\partial}{\partial r_{k\mu}} (\pi_i)_{\alpha\beta}^{(n)} - \frac{\partial}{\partial r_{k\mu}} (\pi_i)_{\alpha\beta}^{(n-1)} \right| < 1 \times 10^{-6} \sigma^2. \tag{E.14}$$

Testing

In principle, any classical time autocorrelation function has a property that $-\frac{d}{dt} \langle A(0)A(t) \rangle =$

$\langle \dot{A}(0)A(t) \rangle$. In our case, one can compare the OKE response function $R(t) = -\frac{d}{dt} \langle \Pi_{xz}(0)\Pi_{xz}(t) \rangle$ calculated by numerical central difference method and OKE response function $R(t) = \langle \dot{\Pi}_{xz}(0)\Pi_{xz}(t) \rangle$ calculated by analytical spatial derivative method. The response functions calculated by two methods are expected to be the same within statistical error.

Numerical method

This is the way we used to calculate the OKE response function and its spectral density. Using the rotational invariance, the anisotropic OKE response function[§] can be written as

$$R(t) = -\frac{d}{dt} \langle \Pi_{xz}(0)\Pi_{xz}(t) \rangle = -\frac{d}{dt} \left\langle \frac{1}{10} \text{PP}(\mathbf{\Pi}(0), \mathbf{\Pi}(t)) - \frac{1}{30} \text{Tr}(\mathbf{\Pi}(0)) \cdot \text{Tr}(\mathbf{\Pi}(t)) \right\rangle. \quad (\text{E.15})$$

If we define the average as $C(t)$,

$$C(t) = \left\langle \frac{1}{10} \text{PP}(\mathbf{\Pi}(0), \mathbf{\Pi}(t)) - \frac{1}{30} \text{Tr}(\mathbf{\Pi}(0)) \cdot \text{Tr}(\mathbf{\Pi}(t)) \right\rangle. \quad (\text{E.16})$$

Then the response function $R(t) = -\frac{d}{dt} C(t)$, and in discrete circumstance, central difference is utilized to calculate the differentiation:

$$R(t) = -\frac{C(t + \delta t) - C(t - \delta t)}{2\delta t}. \quad (\text{E.17})$$

Analytical method

In this way, the OKE response function is a cross correlation between time derivative of polarizability and polarizability itself:

$$R(t) = \langle \dot{\Pi}_{xz}(0)\Pi_{xz}(t) \rangle = \left\langle \frac{1}{10} \text{PP}(\dot{\mathbf{\Pi}}(0), \mathbf{\Pi}(t)) - \frac{1}{30} \text{Tr}(\dot{\mathbf{\Pi}}(0)) \cdot \text{Tr}(\mathbf{\Pi}(t)) \right\rangle, \quad (\text{E.18})$$

[§]Here a constant factor $\beta = 1/k_B T$ is neglected for the current testing case.

where the time derivative of the many-body polarizability

$$\dot{\mathbf{\Pi}}(t) = \sum_{j=1}^N \sum_{\mu}^{x,y,z} \frac{\partial \mathbf{\Pi}(t)}{\partial r_{j\mu}} \cdot \frac{\partial r_{j\mu}}{\partial t} = \sum_{j=1}^N \sum_{\mu}^{x,y,z} \frac{\partial \mathbf{\Pi}(t)}{\partial r_{j\mu}} \cdot v_{j\mu}(t). \quad (\text{E.19})$$

From Equation E.7, we could get spatial derivative $\frac{\partial}{\partial r_{k\mu}} \mathbf{\Pi}(t)$ and $v_{j\mu}(t)$ is the velocity component μ of molecule j at time t that is available from molecular dynamics simulation.

The first order DID approximation is suitable for testing purpose, as first order method is not only time-saving but also has an exact analytical equivalent expression for both methods. Furthermore, previous study shows that first order DID is the main contribution to OKE spectra. Figure E.1 shows the comparison between analytical approach and numerical approach that confirms the equivalence between the two methods. Figure E.2 shows that the full order results have a greater difference in peak height than the first order ones, but the peak positions and shapes keep the same pattern as in first order results.

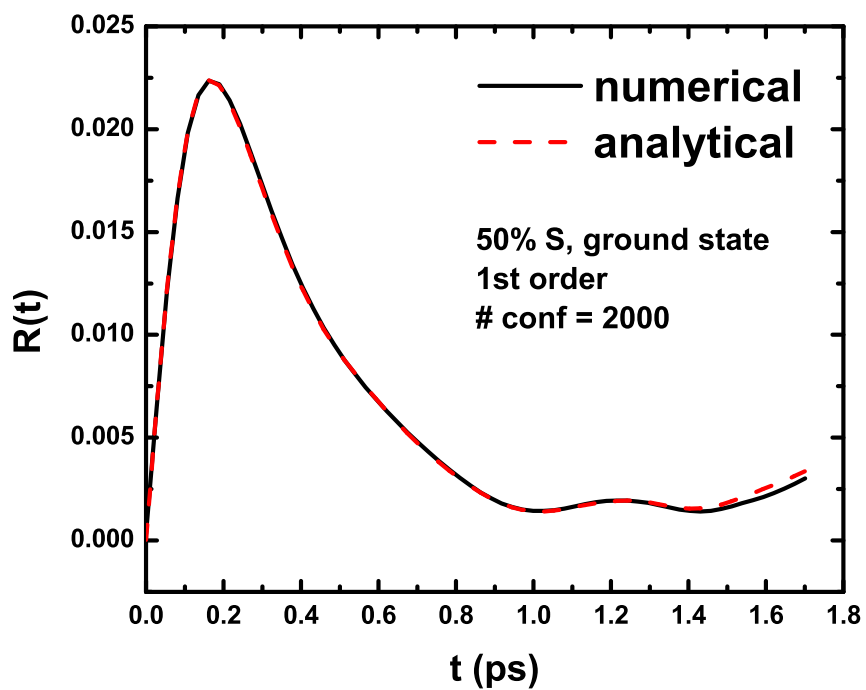


Figure E.1 Comparison of numerical and analytical OKE response functions (in units of $\sigma^5/(\epsilon m)^{1/2}$) for the ground-state 50% S mixture. First order DID approximation is used to calculate the many-body polarizability and the spatial derivative of the many-body polarizability. The response is computed through averaging over 2000 equilibrium liquid configurations.

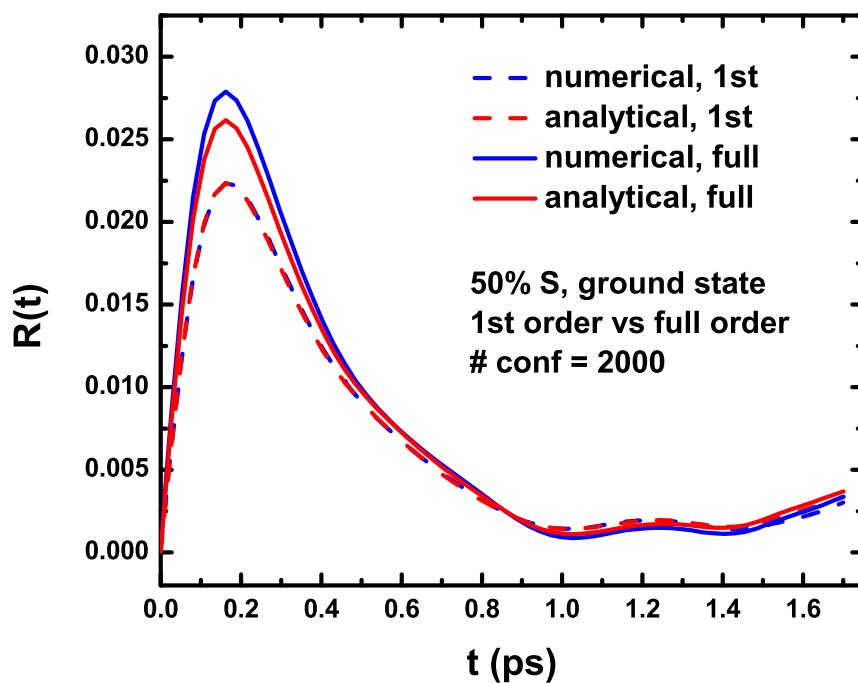


Figure E.2 Comparison of numerical and analytical OKE response functions (in units of $\sigma^5/(\epsilon m)^{1/2}$) for the ground-state 50% S mixture. Both first order and infinite order DID approximations used to calculate the many-body polarizability and the spatial derivative of the many-body polarizability are compared in the same plot. The response is computed through averaging over 2000 equilibrium liquid configurations.

Appendix F

Snapshot of Initial OKE Response

The largest 20 contributions to the initial OKE response $k_B TR(0) = \dot{\mathbf{\Pi}}(0) \otimes \mathbf{\Pi}(0)$ for a single configuration in 10% S and 50% S solvent mixtures. The ground-state configuration is identical for two mixtures, and the excited-state configurations are sampled from equilibrated excited-state 10% S and 50% S systems respectively. In the following result, u is the solute and v labels which solvent.

```
----- Parameters -----
DID approx to the 1st order.
Alpha_U=0.2,      Alpha_S=0.101,      Alpha_W=0.0186
-----

***** 10 % S, ground state *****
# of particles in first shell: 14
Pi_X_dot (times) Pi_X = -0.00404834

Pidot_uv (x) Pi_uv : 20 most important terms (value, v indices)
1      -0.000915218      8      8
2      0.000117151      106     8
3      -6.81886e-05      239     8
4      6.53074e-05      8      246
5      5.43596e-05      8      151
6      -4.55056e-05      246     8
7      4.51987e-05      8      209
8      4.21586e-05      8      106
9      4.20711e-05      8      98
10     3.82236e-05      8      74
11     -3.51783e-05      8      81
12     -3.33892e-05      98     8
13     3.01201e-05      8      201
14     2.13656e-05      8      99
15     1.72756e-05      246    239
16     1.66245e-05      99     8
17     -1.58519e-05      239    239
18     1.4579e-05      239    202
19     -1.41941e-05      8      127
20     1.26764e-05      239    246

Pidot_uv (x) Pi_vv : 20 most important terms (value, v indices)
1      4.19186e-05      8      81      8
2      4.19186e-05      8      8      81
3      -1.96562e-05      8      81     246
4      -1.96562e-05      8      246    81
5      1.92031e-05      8      8      98
6      1.92031e-05      8      98     8
7      -1.79914e-05      8      74     99
```

8	-1.79914e-05	8	99	74
9	-1.72519e-05	8	8	202
10	-1.72519e-05	8	202	8
11	1.48885e-05	8	202	239
12	1.48885e-05	8	239	202
13	1.31749e-05	8	209	246
14	1.31749e-05	8	246	209
15	1.18068e-05	8	8	74
16	1.18068e-05	8	74	8
17	-1.05778e-05	8	127	246
18	-1.05778e-05	8	246	127
19	-1.01758e-05	8	8	99
20	-1.01758e-05	8	99	8

Pidot_vv (x) Pi_uv : 20 most important terms (value, v indices)

1	4.79106e-05	8	81	8
2	4.79106e-05	81	8	8
3	1.74775e-05	151	8	8
4	1.74775e-05	8	151	8
5	-1.41322e-05	8	81	246
6	-1.41322e-05	81	8	246
7	1.18686e-05	209	246	8
8	1.18686e-05	246	209	8
9	1.15711e-05	127	246	8
10	1.15711e-05	246	127	8
11	-8.42463e-06	8	239	8
12	-8.42463e-06	239	8	8
13	8.19295e-06	8	201	8
14	8.19295e-06	201	8	8
15	7.8965e-06	74	99	8
16	7.8965e-06	99	74	8
17	-7.4149e-06	98	106	8
18	-7.4149e-06	106	98	8
19	-7.17485e-06	81	8	201
20	-7.17485e-06	8	81	201

Pidot_vv (x) Pi_vv : 20 most important terms (value, v indices)

1	-7.18398e-06	81	8	8	81
2	-7.18398e-06	8	81	8	81
3	-7.18398e-06	8	81	81	8
4	-7.18398e-06	81	8	81	8
5	2.47285e-06	8	81	8	74
6	2.47285e-06	8	81	74	8
7	2.47285e-06	81	8	8	74
8	2.47285e-06	81	8	74	8
9	1.67433e-06	8	81	8	98
10	1.67433e-06	81	8	8	98
11	1.67433e-06	8	81	98	8
12	1.67433e-06	81	8	98	8
13	-1.54602e-06	81	8	8	201
14	-1.54602e-06	81	8	201	8
15	-1.54602e-06	8	81	8	201
16	-1.54602e-06	8	81	201	8
17	-1.26287e-06	8	81	106	239
18	-1.26287e-06	8	81	239	106
19	-1.26287e-06	81	8	106	239
20	-1.26287e-06	81	8	239	106

***** 10 % S, excited state *****
of particles in first shell: 12
Pi_X_dot (times) Pi_X = -0.000845908

Pidot_uv (x) Pi_uv : 20 most important terms (value, v indices)

1	-0.000201255	10	10	
2	-0.000180299	20	20	
3	9.84748e-05	20	10	
4	5.64416e-05	250	20	
5	-5.54018e-05	208	20	
6	-5.36353e-05	20	87	
7	4.93313e-05	10	211	
8	4.41401e-05	10	208	
9	3.78741e-05	20	10	
10	-3.33983e-05	10	87	
11	-3.26399e-05	250	250	
12	3.09955e-05	250	10	
13	-2.66474e-05	208	208	
14	-2.64251e-05	211	10	
15	2.56098e-05	20	70	
16	-2.37834e-05	87	20	
17	2.28083e-05	179	10	
18	-2.2222e-05	10	179	
19	2.20871e-05	20	90	
20	-2.00774e-05	90	10	

```

Pidot_uv (x) Pi_vv : 20 most important terms (value, v indices)
1      -4.90587e-05      10      70      20
2      -4.90587e-05      10      20      70
3      -3.3093e-05       20      10      20
4      -3.3093e-05       20      20      10
5      -2.87138e-05      20      10      208
6      -2.87138e-05      20      208     10
7      2.46468e-05       20      238     10
8      2.46468e-05       20      10      238
9      -2.03616e-05      10      10      208
10     -2.03616e-05      10      208     10
11     1.89292e-05       10      87      10
12     1.89292e-05       10      10      87
13     -1.52437e-05      10      10      20
14     -1.52437e-05      10      20      10
15     1.41772e-05       20      20      179
16     1.41772e-05       20      179     20
17     1.38956e-05       10      20      208
18     1.38956e-05       10      208     20
19     -1.18946e-05      250     70      20
20     -1.18946e-05      250     20      70

```

```

Pidot_vv (x) Pi_uv : 20 most important terms (value, v indices)
1      -5.10345e-05      20      208     10
2      -5.10345e-05      208     20      10
3      4.48609e-05       70      20      10
4      4.48609e-05       20      70      10
5      3.88633e-05       10      238     20
6      3.88633e-05      238     10      20
7      -3.34628e-05      20      70      20
8      -3.34628e-05      70      20      20
9      -2.8369e-05       10      70      20
10     -2.8369e-05       70      10      20
11     -1.56348e-05      250     20      20
12     -1.56348e-05      20      250     20
13     -1.47646e-05      10      87      208
14     -1.47646e-05      87      10      208
15     1.26938e-05       20      208     250
16     1.26938e-05      208     20      250
17     -1.25805e-05      179     20      10
18     -1.25805e-05      20      179     10
19     1.16654e-05      250     20      10
20     1.16654e-05      20      250     10

```

```

Pidot_vv (x) Pi_vv : 20 most important terms (value, v indices)
1      -1.0157e-05       20      208     10      20
2      -1.0157e-05       20      208     20      10
3      -1.0157e-05      208     20      10      20
4      -1.0157e-05      208     20      20      10
5      -9.99789e-06      20      208     20      208
6      -9.99789e-06      20      208     208     20
7      -9.99789e-06      208     20      20      208
8      -9.99789e-06      208     20      208     20
9      8.4828e-06        20      70      20      70
10     8.4828e-06        20      70      70      20
11     8.4828e-06        70      20      20      70
12     8.4828e-06        70      20      70      20
13     7.30253e-06       10      238     238     10
14     7.30253e-06      238     10      238     10
15     7.30253e-06       10      238     10      238
16     7.30253e-06      238     10      10      238
17     6.65279e-06       20      208     238     10
18     6.65279e-06      208     20      238     10
19     6.65279e-06       20      208     10      238
20     6.65279e-06      208     20      10      238

```

```

***** 50 % S, ground state *****
# of particles in first shell: 14
Pi_X_dot (times) Pi_X = 0.00255942

```

```

Pidot_uv (x) Pi_uv : 20 most important terms (value, v indices)
1      -0.000915218      8      8
2      0.000636143      106     8
3      -0.000324912     106     98
4      0.000294003      106     106
5      0.000247979      98      98
6      0.000228926      8      106
7      0.000228451      8      98
8      0.000207558      8      74
9      -0.000191022      8      81
10     -0.000181307     98      8
11     -0.000138486     106     99
12     -0.000116589     98      81
13     0.000116017      8      99
14     -0.000115993     98      106

```

15	-0.000103047	99	98
16	-0.000102286	74	106
17	9.60324e-05	98	127
18	-9.47037e-05	74	74
19	9.02729e-05	99	8
20	8.39676e-05	98	99

Pidot_uv (x) Pi_vv : 20 most important terms (value, v indices)

1	-0.000530496	8	74	99
2	-0.000530496	8	99	74
3	-0.000266687	8	98	106
4	-0.000266687	8	106	98
5	0.000227622	8	8	81
6	0.000227622	8	81	8
7	0.000130083	98	8	74
8	0.000130083	98	74	8
9	0.000128477	8	99	127
10	0.000128477	8	127	99
11	0.000118487	106	98	106
12	0.000118487	106	106	98
13	-0.000114754	106	8	74
14	-0.000114754	106	74	8
15	-0.000113462	98	8	81
16	-0.000113462	98	81	8
17	-0.000106735	8	81	246
18	-0.000106735	8	246	81
19	0.000104275	8	8	98
20	0.000104275	8	98	8

Pidot_vv (x) Pi_uv : 20 most important terms (value, v indices)

1	0.00026016	8	81	8
2	0.00026016	81	8	8
3	0.000232837	74	99	8
4	0.000232837	99	74	8
5	-0.000218636	98	106	8
6	-0.000218636	106	98	8
7	0.000206031	8	81	98
8	0.000206031	81	8	98
9	0.00013307	99	127	106
10	0.00013307	127	99	106
11	9.79169e-05	8	81	74
12	9.79169e-05	81	8	74
13	9.45464e-05	106	127	98
14	9.45464e-05	127	106	98
15	8.93007e-05	8	81	106
16	8.93007e-05	81	8	106
17	-8.76136e-05	106	127	8
18	-8.76136e-05	127	106	8
19	8.25866e-05	8	81	99
20	8.25866e-05	81	8	99

Pidot_vv (x) Pi_vv : 20 most important terms (value, v indices)

1	-0.000211827	8	81	8	81
2	-0.000211827	8	81	81	8
3	-0.000211827	81	8	8	81
4	-0.000211827	81	8	81	8
5	8.40656e-05	74	99	98	106
6	8.40656e-05	74	99	106	98
7	8.40656e-05	99	74	98	106
8	8.40656e-05	99	74	106	98
9	8.33305e-05	8	81	74	99
10	8.33305e-05	8	81	99	74
11	8.33305e-05	81	8	74	99
12	8.33305e-05	81	8	99	74
13	-7.3099e-05	74	99	8	81
14	-7.3099e-05	74	99	81	8
15	-7.3099e-05	99	74	8	81
16	-7.3099e-05	99	74	81	8
17	7.29145e-05	8	81	8	74
18	7.29145e-05	8	81	74	8
19	7.29145e-05	81	8	8	74
20	7.29145e-05	81	8	74	8

***** 50 % S, excited state *****
 # of particles in first shell: 16
 Pi_X_dot (times) Pi_X = 0.00279396

Pidot_uv (x) Pi_uv : 20 most important terms (value, v indices)

1	0.00126255	26	26
2	-0.000738991	46	26
3	0.000642889	26	46
4	-0.000630301	46	46
5	0.000496723	26	111
6	-0.000453881	26	104

7	0.000325377	26	101
8	-0.000295651	101	101
9	-0.000292751	104	56
10	-0.000271673	104	46
11	-0.000265686	101	26
12	0.000252096	111	26
13	0.000251003	46	104
14	-0.000218356	26	56
15	-0.000214863	56	26
16	-0.00017522	26	29
17	0.000160376	46	25
18	-0.000152499	26	25
19	0.000151481	104	104
20	0.000150288	56	56

Pidot_uv (x) Pi_vv : 20 most important terms (value, v indices)

1	0.000611559	26	25	56
2	0.000611559	26	56	25
3	-0.00031796	26	46	101
4	-0.00031796	26	101	46
5	-0.00031222	26	101	111
6	-0.00031222	26	111	101
7	-0.000296455	46	25	56
8	-0.000296455	46	56	25
9	-0.000293822	46	104	111
10	-0.000293822	46	111	104
11	0.000240332	26	104	111
12	0.000240332	26	111	104
13	-0.000221257	26	46	111
14	-0.000221257	26	111	46
15	0.000213701	46	101	111
16	0.000213701	46	111	101
17	0.000206576	104	29	46
18	0.000206576	104	46	29
19	-0.000181261	101	25	111
20	-0.000181261	101	111	25

Pidot_vv (x) Pi_uv : 20 most important terms (value, v indices)

1	0.000339957	25	111	56
2	0.000339957	111	25	56
3	0.000269886	46	101	26
4	0.000269886	101	46	26
5	-0.000228723	101	111	25
6	-0.000228723	111	101	25
7	0.000203619	46	101	56
8	0.000203619	101	46	56
9	0.000171052	101	111	101
10	0.000171052	111	101	101
11	0.000163117	46	101	46
12	0.000163117	101	46	46
13	0.000155281	101	111	46
14	0.000155281	111	101	46
15	-0.000153218	25	111	111
16	-0.000153218	111	25	111
17	-0.00015177	25	111	26
18	-0.00015177	111	25	26
19	0.000138614	46	101	111
20	0.000138614	101	46	111

Pidot_vv (x) Pi_vv : 20 most important terms (value, v indices)

1	-0.000269424	46	101	46	101
2	-0.000269424	46	101	101	46
3	-0.000269424	101	46	46	101
4	-0.000269424	101	46	101	46
5	-0.000195955	101	111	26	56
6	-0.000195955	101	111	56	26
7	-0.000195955	111	101	26	56
8	-0.000195955	111	101	56	26
9	0.000191788	25	111	25	111
10	0.000191788	25	111	111	25
11	0.000191788	111	25	25	111
12	0.000191788	111	25	111	25
13	0.000173208	25	111	101	111
14	0.000173208	25	111	111	101
15	0.000173208	111	25	101	111
16	0.000173208	111	25	111	101
17	-0.000164815	101	111	101	111
18	-0.000164815	101	111	111	101
19	-0.000164815	111	101	101	111
20	-0.000164815	111	101	111	101

Bibliography

- [1] P. M. Chaikin, T. C. Lubensky, *Principles of condensed matter physics* (Cambridge University Press, New York, 1995), chapter 1.
- [2] R. M. Stratton, M. Maroncelli, *J. Phys. Chem.* **100**, 12981 (1996).
- [3] J. C. Owrutsky, D. Raftery, *Annu. Rev. Phys. Chem.* **45**, 519 (1994).
- [4] D. J. Nesbitt, R. W. Field, *J. Phys. Chem.* **100**, 12735 (1996).
- [5] B. C. Xu, R. M. Stratton, *J. Chem. Phys.* **92**, 1923 (1990).
- [6] J. E. Adams, R. M. Stratton, *J. Chem. Phys.* **93**, 1332 (1990).
- [7] M. Buchner, B. M. Ladanyi, R. M. Stratton, *J. Chem. Phys.* **97**, 8522 (1992).
- [8] Y. Wan, R. M. Stratton, *J. Chem. Phys.* **100**, 5123 (1994).
- [9] R. M. Stratton, *Acc. Chem. Res.* **28**, 201 (1995).
- [10] G. Seeley, T. Keyes, *J. Chem. Phys.* **91**, 5581 (1989).
- [11] T. Keyes, *J. Phys. Chem. A* **101**, 2921 (1997).
- [12] D. A. McQuarrie, *Statistical mechanics* (University Science Books, Sausalito, CA, 2000), chapter 21, 22.
- [13] R. Zwanzig, *Nonequilibrium Statistical Mechanics* (Oxford University Press, New York, 2001), chapter 2.
- [14] H. Goldstein, C. P. Poole, Jr, J. L. Safko, *Classical mechanics* (Addison-Wesley, Cambridge, MA, 2001), chapter 8, 3rd edition.
- [15] R. G. Gordon, *J. Chem. Phys.* **43**, 1307 (1965).
- [16] B. M. Ladanyi, R. M. Stratton, *J. Phys. Chem.* **100**, 1266 (1996).
- [17] B. M. Ladanyi, R. M. Stratton, *J. Phys. Chem. A* **102**, 1068 (1998).
- [18] R. M. Stratton, M. Cho, *J. Chem. Phys.* **100**, 6700 (1994).
- [19] G. Goodyear, R. E. Larsen, R. M. Stratton, *Phys. Rev. Lett.* **76**, 243 (1996).
- [20] S. Ryu, R. M. Stratton, *J. Phys. Chem. B* **108**, 6782 (2004).
- [21] U. Marconi, A. Puglisi, L. Rondoni, A. Vulpiani, *Phys. Rep.* **461**, 111 (2008).

- [22] G. L. Eyink, *Phys. Rev. E* **62**, 210 (2000).
- [23] J. T. Edward, *J. Chem. Educ.*, **47**, 261 (1970).
- [24] M. E. Tuckerman, B. J. Berne, *J. Chem. Phys.* **95**, 4389 (1991).
- [25] S. A. Adelman, *J. Chem. Phys.* **71**, 4471 (1979).
- [26] R. Zwanzig, *Nonequilibrium Statistical Mechanics* (Oxford University Press, New York, 2001), chapter 1, p. 21.
- [27] M. E. Tuckerman, *Statistical Mechanics: Theory and Molecular Simulation* (Oxford University Press, New York, 2010), chapter 15, p. 571.
- [28] R. M. Strat, in *Ultrafast Infrared and Raman Spectroscopy*, edited by M. D. Fayer (Marcel Dekker, New York, 2001).
- [29] M. E. Tuckerman, B. J. Berne, *J. Chem. Phys.* **98**, 7301 (1993).
- [30] J.-P. Hansen, I. R. McDonald, *Theory of Simple Liquids* (Academic Press, London, 2006), chapter 7, p. 193, 3rd edition.
- [31] Y. Q. Deng, B. M. Ladanyi, R. M. Strat, *J. Chem. Phys.* **117**, 10752 (2002).
- [32] D. E. Smith, C. B. Harris, *J. Chem. Phys.* **92**, 1312 (1990).
- [33] D. E. Smith, C. B. Harris, *J. Chem. Phys.* **92**, 1304 (1990).
- [34] R. Zwanzig, *Nonequilibrium Statistical Mechanics* (Oxford University Press, New York, 2001), chapter 8.
- [35] R. Zwanzig, in *Lectures in Theoretical Physics*, edited by W. E. Britton, B. W. Downs, J. Downs (Wiley, New York, 1961), p. 135.
- [36] H. Mori, *Prog. Theor. Phys.* **33**, 423 (1965).
- [37] H. Mori, *Prog. Theor. Phys.* **34**, 399 (1965).
- [38] R. Zwanzig, *J. Stat. Phys.* **9**, 215 (1973).
- [39] L. Onsager, *Phys. Rev.* **37**, 405 (1931).
- [40] L. Onsager, *Phys. Rev.* **38**, 2265 (1931).
- [41] H. B. Callen, T. A. Welton, *Phys. Rev.* **83**, 34 (1951).
- [42] D. Chandler, *Introduction to Modern Statistical Mechanics* (Oxford University Press, New York, 1987), chapter 8.
- [43] R. Jimenez, G. R. Fleming, P. V. Kumar, M. Maroncelli, *Nature* **369**, 471 (1994).
- [44] P. L. Geissler, D. Chandler, *J. Chem. Phys.* **113**, 9759 (2000).
- [45] B. B. Laird, W. H. Thompson, *J. Chem. Phys.* **126**, 211104 (2007).
- [46] E. A. Carter, J. T. Hynes, *J. Chem. Phys.* **94**, 5961 (1991).

- [47] J. S. Bader, D. Chandler, *Chem. Phys. Lett.* **157**, 501 (1989).
- [48] A. E. Bragg, M. C. Cavanagh, B. J. Schwartz, *Science* **321**, 1817 (2008).
- [49] M. J. Bedard-Hearn, R. E. Larsen, B. J. Schwartz, *J. Phys. Chem. A* **107**, 4773 (2003).
- [50] M. J. Bedard-Hearn, R. E. Larsen, B. J. Schwartz, *J. Phys. Chem. B* **107**, 14464 (2003).
- [51] G. Tao, R. M. Stratt, *J. Chem. Phys.* **125**, 114501 (2006).
- [52] B. Zhang, R. M. Stratt, *J. Chem. Phys.* **137**, 024506 (2012).
- [53] A. C. Moskun, A. E. Jailaubekov, S. E. Bradforth, G. H. Tao, R. M. Stratt, *Science* **311**, 1907 (2006).
- [54] L. Turi, P. Mináry, P. J. Rossky, *Chem. Phys. Lett.* **316**, 465 (2000).
- [55] T. Fonseca, B. M. Ladanyi, *J. Phys. Chem.* **95**, 2116 (1991).
- [56] T. Fonseca, B. Ladanyi, *J. Mol. Liq.* **60**, 1 (1994).
- [57] M. P. Allen, D. J. Tildesley, *Computer Simulation of Liquids* (Clarendon Press, Oxford, 1987), chapter 1, p. 4.
- [58] A. R. Leach, *Molecular Modelling: Principles And Applications* (Prentice Hall, New York, 2001), chapter 7, 2nd edition.
- [59] M. P. Allen, D. J. Tildesley, *Computer Simulation of Liquids* (Clarendon Press, Oxford, 1987), chapter 3, pp. 71–109.
- [60] D. Frenkel, B. Smit, *Understanding Molecular Simulation* (Academic Press, San Diego, 2002), chapter 3, p. 27, From Algorithms to Applications, 2nd edition.
- [61] M. P. Allen, D. J. Tildesley, *Computer Simulation of Liquids* (Clarendon Press, Oxford, 1987), chapter 4, p. 118.
- [62] P. G. Bolhuis, D. Chandler, C. Dellago, P. L. Geissler, *Annu. Rev. Phys. Chem.* **53**, 291 (2002).
- [63] K. Binder, D. W. Heermann, *Monte Carlo Simulation in Statistical Physics: An Introduction* (Springer Verlag, Berlin, 2010), chapter 5.
- [64] A. H. Zewail, *J. Phys. Chem. A* **104**, 5660 (2000).
- [65] A. Föhlisch, P. Feulner, F. Hennies, A. Fink, D. Menzel, D. Sanchez-Portal, P. M. Echenique, W. Wurth, *Nature* **436**, 373 (2005).
- [66] P. B. Corkum, F. Krausz, *Nat. Phys.* **3**, 381 (2007).
- [67] A. L. Cavalieri, N. Müller, T. Uphues, V. S. Yakovlev, A. Baltuška, B. Horvath, B. Schmidt, L. Blümel, R. Holzwarth, S. Hendel, M. Drescher, U. Kleineberg, P. M. Echenique, R. Kienberger, F. Krausz, U. Heinzmann, *Nature* **449**, 1029 (2007).

- [68] G. R. Fleming, *Chemical applications of ultrafast spectroscopy* (Oxford University Press, New York, 1986).
- [69] M. Maroncelli, G. R. Fleming, *J. Chem. Phys.* **89**, 875 (1988).
- [70] R. Karmakar, A. Samanta, *J. Phys. Chem. A* **106**, 4447 (2002).
- [71] A. Samanta, *J. Phys. Chem. B* **110**, 13704 (2006).
- [72] S. Arzhantsev, H. Jin, G. A. Baker, M. Maroncelli, *J. Phys. Chem. B* **111**, 4978 (2007).
- [73] M. Sajadi, N. P. Ernsting, *J. Phys. Chem. B* **117**, 7675 (2013).
- [74] L. Nilsson, B. Halle, *Proc. Natl. Acad. Sci. U.S.A.* **102**, 13867 (2005).
- [75] S. K. Pal, L. Zhao, A. H. Zewail, *Proc. Natl. Acad. Sci. U.S.A.* **100**, 8113 (2003).
- [76] S. D. Verma, N. Pal, M. K. Singh, S. Sen, *J. Phys. Chem. Lett.* **3**, 2621 (2012).
- [77] K. E. Furse, S. A. Corcelli, *J. Am. Chem. Soc.* **130**, 13103 (2008).
- [78] S. Sen, D. Andreatta, S. Y. Ponomarev, D. L. Beveridge, M. A. Berg, *J. Am. Chem. Soc.* **131**, 1724 (2009).
- [79] D. M. Willard, N. E. Levinger, *J. Phys. Chem. B* **104**, 11075 (2000).
- [80] J. Faeder, B. M. Ladanyi, *J. Phys. Chem. B* **104**, 10331046 (2000).
- [81] B. M. Ladanyi, R. M. Stratt, *J. Phys. Chem.* **99**, 2502 (1995).
- [82] M. Maroncelli, G. R. Fleming, *J. Chem. Phys.* **86**, 6221 (1987).
- [83] M. L. Horng, J. A. Gardecki, A. Papazyan, M. Maroncelli, *J. Phys. Chem.* **99**, 17311 (1995).
- [84] P. K. Chowdhury, M. Halder, L. Sanders, T. Calhoun, J. L. Anderson, D. W. Armstrong, X. Song, J. W. Petrich, *J. Phys. Chem. B* **108**, 10245 (2004).
- [85] B. M. Luther, J. R. Kimmel, N. E. Levinger, *J. Chem. Phys.* **116**, 3370 (2002).
- [86] N. Agmon, *J. Phys. Chem. A* **106**, 7256 (2002).
- [87] C. N. Nguyen, R. M. Stratt, *J. Chem. Phys.* **133**, 124503 (2010).
- [88] T. J. F. Day, G. N. Patey, *J. Chem. Phys.* **106**, 2782 (1997).
- [89] T. J. F. Day, G. N. Patey, *J. Chem. Phys.* **110**, 10937 (1999).
- [90] A. Yoshimori, T. J. F. Day, G. N. Patey, *J. Chem. Phys.* **109**, 3222 (1998).
- [91] D. Laria, M. S. Skaf, *J. Chem. Phys.* **111**, 300 (1999).
- [92] L. R. Martins, A. Tamashiro, D. Laria, M. S. Skaf, *J. Chem. Phys.* **118**, 5955 (2003).
- [93] K. Nishiyama, T. Okada, *J. Phys. Chem. A* **102**, 9729 (1998).

- [94] F. Cichos, R. Brown, U. Rempel, C. von Borczyskowski, *J. Phys. Chem. A* **103**, 2506 (1999).
- [95] B. M. Ladanyi, B. C. Perng, *J. Phys. Chem. A* **106**, 6922 (2002).
- [96] F. M. Floris, J. M. Martinez, J. Tomasi, *J. Chem. Phys.* **116**, 5460 (2002).
- [97] M. Sakurai, A. Yoshimori, *J. Chem. Phys.* **122**, 104509 (2005).
- [98] S. Murata, A. Yoshimori, *J. Chem. Phys.* **125**, 244501 (2006).
- [99] W. T. Pollard, R. A. Mathies, *Annu. Rev. Phys. Chem.* **43**, 497 (1992).
- [100] Y. Kimura, J. C. Alfano, P. K. Walhout, P. F. Barbara, *J. Phys. Chem.* **98**, 3450 (1994).
- [101] C. Silva, P. K. Walhout, K. Yokoyama, P. F. Barbara, *Phys. Rev. Lett.* **80**, 1086 (1998).
- [102] T. Q. Lian, Y. Kholodenko, R. M. Hochstrasser, *J. Phys. Chem.* **99**, 2546 (1995).
- [103] S. A. Kovalenko, N. Eilers-König, T. A. Senyushkina, N. P. Ernsting, *J. Phys. Chem. A* **105**, 4834 (2001).
- [104] J. T. M. Kennis, D. S. Larsen, K. Ohta, M. T. Facciotti, R. M. Glaeser, G. R. Fleming, *J. Phys. Chem. B* **106**, 6067 (2002).
- [105] O. F. Mohammed, *J. Phys. Chem. A* **114**, 11576 (2010).
- [106] C. R. Baiz, K. J. Kubarych, *J. Am. Chem. Soc.* **132**, 12784 (2010).
- [107] C. J. Fecko, J. D. Eaves, J. J. Loparo, A. Tokmakoff, P. L. Geissler, *Science* **301**, 1698 (2003).
- [108] C. J. Fecko, J. J. Loparo, S. T. Roberts, A. Tokmakoff, *J. Chem. Phys.* **122**, 054506 (2005).
- [109] T. Steinel, J. B. Asbury, J. Zheng, M. D. Fayer, *J. Phys. Chem. A* **108**, 10957 (2004).
- [110] C. Bressler, M. Saes, M. Chergui, D. Grolimund, R. Abela, P. Pattison, *J. Chem. Phys.* **116**, 2955 (2002).
- [111] C. Bressler, M. Chergui, *Chem. Rev.* **104**, 1781 (2004).
- [112] P. Wernet, D. Nordlund, U. Bergmann, M. Cavalleri, M. Odellius, H. Ogasawara, L. A. Näslund, T. K. Hirsch, L. Ojamäe, P. Glatzel, L. G. M. Pettersson, A. Nilsson, *Science* **304**, 995 (2004).
- [113] L. X. Chen, *Annu. Rev. Phys. Chem.* **56**, 221 (2005).
- [114] V.-T. Pham, W. Gawelda, Y. Zaushitsyn, M. Kaiser, D. Grolimund, S. L. Johnson, R. Abela, C. Bressler, M. Chergui, *J. Am. Chem. Soc.* **129**, 1530 (2007).
- [115] M. Chergui, A. H. Zewail, *ChemPhysChem* **10**, 28 (2009).

- [116] M. Chergui, *Acta Cryst* **A66**, 229 (2010).
- [117] C. Bressler, M. Chergui, *Annu. Rev. Phys. Chem.* **61**, 263 (2010).
- [118] B. Ahr, M. Chollet, B. Adams, E. M. Lunny, C. M. Laperle, C. Rose-Petruck, *Phys. Chem. Chem. Phys.* **13**, 5590 (2011).
- [119] C. Bressler, C. Milne, V. T. Pham, A. ElNahhas, R. M. van der Veen, W. Gawelda, S. Johnson, P. Beaud, D. Grolimund, M. Kaiser, C. N. Borca, G. Ingold, R. Abela, M. Chergui, *Science* **323**, 489 (2009).
- [120] A. Guinier, *X-Ray Diffraction: In Crystals, Imperfect Crystals, and Amorphous Bodies* (W. H. Freeman, San Francisco, 1963).
- [121] P. G. De Gennes, *Physica* **25**, 825 (1959).
- [122] J.-P. Hansen, I. R. McDonald, *Theory of Simple Liquids* (Academic Press, London, 2006), chapter 7, p. 201, 3rd edition.
- [123] H. Ihee, *Acc. Chem. Res.* **42**, 356 (2009).
- [124] T. K. Kim, J. H. Lee, M. Wulff, Q. Kong, H. Ihee, *ChemPhysChem* **10**, 1958 (2009).
- [125] C. Rischel, A. Rousse, I. Uschmann, P.-A. Albouy, J.-P. Geindre, P. Audebert, J.-C. Gauthier, E. Förster, J.-L. Martin, A. Antonetti, *Nature* **390**, 490 (1997).
- [126] C. Rose-Petruck, R. Jimenez, T. Guo, A. Cavalleri, C. W. Siders, F. Rksi, J. A. Squier, B. C. Walker, K. R. Wilson, C. P. J. Barty, *Nature* **398**, 310 (1999).
- [127] H. Ihee, M. Lorenc, T. K. Kim, Q. Y. Kong, M. Cammarata, J. H. Lee, S. Bratos, M. wulff, *Science* **309**, 1223 (2005).
- [128] A. Plech, M. Wulff, S. Bratos, F. Mirloup, R. Vuilleumier, F. Schotte, P. Anfinrud, *Phys. Rev. Lett.* **92**, 125505 (2004).
- [129] L. B. Skinner, C. J. Benmore, J. K. R. Weber, M. C. Wilding, S. K. Tumber, J. B. Parise, *Phys. Chem. Chem. Phys.* **15**, 8566 (2013).
- [130] R. W. Boyd, *Nonlinear Optics* (Academic Press, Burlington, MA, 2008), chapter 1, 3rd edition.
- [131] Y. R. Shen, *The principles of nonlinear optics* (Wiley, New York, 2003), chapter 6–8, reprint, illustrated edition.
- [132] S. Mukamel, *Principles of nonlinear optical spectroscopy* (Oxford University Press, New York, 1995), chapter 10, 11.
- [133] S. Mukamel, *Annu. Rev. Phys. Chem.* **51**, 691 (2000).
- [134] S. Mukamel, *Principles of nonlinear optical spectroscopy* (Oxford University Press, New York, 1995), chapter 5.
- [135] K. Blum, *Density Matrix Theory and Applications* (Springer Verlag, Berlin, 2012), chapter 2, Springer Series on Atomic, Optical and Plasma Physics, 3rd edition.

- [136] J. J. Sakurai, *Modern quantum mechanics* (Addison-Wesley, Reading, MA, 1994), chapter 3, p. 174, revised edition.
- [137] P. A. M. Dirac, *The Principles of Quantum Mechanics* (Clarendon Press, Oxford, 1958), chapter 21, pp. xii, 312 p., International series of monographs on physics, 4th edition.
- [138] S. Mukamel, *Principles of nonlinear optical spectroscopy* (Oxford University Press, New York, 1995), chapter 6.
- [139] B. I. Grimberg, V. V. Lozovoy, M. Dantus, S. Mukamel, *J. Phys. Chem. A* **106**, 697 (2002).
- [140] Y. J. Yan, S. Mukamel, *J. Chem. Phys.* **89**, 5160 (1988).
- [141] G. R. Fleming, M. Cho, *Annu. Rev. Phys. Chem.* **47**, 109 (1996).
- [142] Q. Zhong, J. T. Fourkas, *J. Phys. Chem. B* **112**, 15529 (2008).
- [143] D. Waldeck, A. J. Cross, D. B. McDonald, G. R. Fleming, *J. Chem. Phys.* **74**, 3381 (1981).
- [144] L. D. Ziegler, R. Fan, A. E. Desrosiers, N. F. Scherer, *J. Chem. Phys.* **100**, 1823 (1994).
- [145] D. Mcmorrow, W. T. Lotshaw, *J. Phys. Chem.* **95**, 10395 (1991).
- [146] M. Cho, S. J. Rosenthal, N. F. Scherer, L. D. Ziegler, G. R. Fleming, *J. Chem. Phys.* **96**, 5033 (1992).
- [147] M. Cho, M. Du, N. F. Scherer, G. R. Fleming, S. Mukamel, *J. Chem. Phys.* **99**, 2410 (1993).
- [148] M. Ricci, P. Bartolini, R. Chelli, G. Cardini, S. Califano, R. Righini, *Phys. Chem. Chem. Phys.* **3**, 2795 (2001).
- [149] J. T. Fourkas, in *Ultrafast Infrared and Raman Spectroscopy*, edited by M. D. Fayer (Marcel Dekker, New York, 2001).
- [150] N. A. Smith, S. R. Meech, *Int. Rev. Phys. Chem.* **21**, 75 (2002).
- [151] B. Ratajska-Gadomska, *J. Chem. Phys.* **116**, 4563 (2002).
- [152] C. J. Fecko, J. D. Eaves, A. Tokmakoff, *J. Chem. Phys.* **117**, 1139 (2002).
- [153] J. R. Rajian, B. R. Hyun, E. L. Quitevis, *J. Phys. Chem. A* **108**, 10107 (2004).
- [154] N. T. Hunt, A. A. Jaye, S. R. Meech, *Phys. Chem. Chem. Phys.* **9**, 2167 (2007).
- [155] E. W. Castner, J. F. Wishart, H. Shirota, *Acc. Chem. Res.* **40**, 1217 (2007).
- [156] I. A. Heisler, S. R. Meech, *J. Phys. Chem. B* **112**, 12976 (2008).
- [157] Q. Zhong, J. T. Fourkas, *J. Phys. Chem. B* **112**, 15342 (2008).

- [158] I. A. Heisler, S. R. Meech, *Science* **327**, 857 (2010).
- [159] I. A. Heisler, S. R. Meech, *J. Chem. Phys.* **132**, 174503 (2010).
- [160] E. W. Castner, Y. J. Chang, Y. C. Chu, G. E. Walrafen, *J. Chem. Phys.* **102**, 653 (1995).
- [161] Y. J. Chang, E. W. Castner, *J. Phys. Chem.* **100**, 3330 (1996).
- [162] C. W. Freudiger, M. B. J. Roeffaers, X. Zhang, B. G. Saar, W. Min, X. S. Xie, *J. Phys. Chem. B* **115**, 5574 (2011).
- [163] J. T. Fourkas, M. D. Fayer, *Acc. Chem. Res.* **25**, 227 (1992).
- [164] E. J. Brown, Q. Zhang, M. Dantus, *J. Chem. Phys.* **110**, 5772 (1999).
- [165] J.-C. Gummy, O. Nicolet, E. Vauthey, *J. Phys. Chem. A* **103**, 10737 (1999).
- [166] S. Park, J.-S. Park, T. Joo, *J. Phys. Chem. A* **115**, 3973 (2011).
- [167] T. Joo, Y. Jia, J.-Y. Yu, M. J. Lang, G. R. Fleming, *J. Chem. Phys.* **104**, 6089 (1996).
- [168] M. Cho, N. F. Scherer, G. R. Fleming, S. Mukamel, *J. Chem. Phys.* **96**, 5618 (1992).
- [169] M. Cho, G. R. Fleming, *J. Chem. Phys.* **98**, 2848 (1993).
- [170] A. Tokmakoff, M. D. Fayer, *J. Chem. Phys.* **103**, 2810 (1995).
- [171] M. C. Asplund, M. T. Zanni, R. M. Hochstrasser, *Proc. Natl. Acad. Sci. U.S.A.* **97**, 8219 (2000).
- [172] Y. Nagasawa, *J. Photochem. Photobiol., C* **12**, 31 (2011).
- [173] K. Ohta, J. Tayama, S. Saito, K. Tominaga, *Acc. Chem. Res.* **45**, 1982 (2012).
- [174] M. A. Schlosshauer, *Decoherence: And the Quantum-To-Classical Transition* (Springer, Berlin, 2007).
- [175] W. P. de Boeij, M. S. Pshenichnikov, D. A. Wiersma, *Annu. Rev. Phys. Chem.* **49**, 99 (1998).
- [176] M. Cho, J. Y. Yu, T. H. Joo, Y. Nagasawa, S. A. Passino, G. R. Fleming, *J. Phys. Chem.* **100**, 11944 (1996).
- [177] S. A. Passino, Y. Nagasawa, T. Joo, G. R. Fleming, *J. Phys. Chem. A* **101**, 725 (1997).
- [178] J.-Y. Yu, Y. Nagasawa, R. van Grondelle, G. R. Fleming, *Chem. Phys. Lett.* **280**, 404 (1997).
- [179] M. J. Lang, X. J. Jordanides, X. Song, G. R. Fleming, *J. Chem. Phys.* **110**, 5884 (1999).
- [180] X. J. Jordanides, M. J. Lang, X. Song, G. R. Fleming, *J. Phys. Chem. B* **103**, 7995 (1999).

- [181] D. S. Larsen, K. Ohta, Q. H. Xu, M. Cyrier, G. R. Fleming, *J. Chem. Phys.* **114**, 8008 (2001).
- [182] K. Ohta, D. S. Larsen, M. Yang, G. R. Fleming, *J. Chem. Phys.* **114**, 8020 (2001).
- [183] R. Agarwal, B. S. Prall, A. H. Rizvi, M. Yang, G. R. Fleming, *J. Chem. Phys.* **116**, 6243 (2002).
- [184] J. Stenger, D. Madsen, P. Hamm, E. T. J. Nibbering, T. Elsaesser, *J. Phys. Chem. A* **106**, 2341 (2002).
- [185] M. Cho, G. R. Fleming, *J. Chem. Phys.* **123**, 114506 (2005).
- [186] A. A. Oskouei, O. Bräm, A. Cannizzo, F. van Mourik, A. Tortschanoff, M. Chergui, *Chem. Phys.* **350**, 104 (2008).
- [187] M. H. J. Oh, M. R. Salvador, C. Y. Wong, G. D. Scholes, *ChemPhysChem* **12**, 88 (2010).
- [188] T. H. Joo, Y. W. Jia, J. Y. Yu, D. M. Jonas, G. R. Fleming, *J. Phys. Chem.* **100**, 2399 (1996).
- [189] P. Hamm, M. Zanni, *Concepts and Methods of 2D Infrared Spectroscopy* (Cambridge University Press, Cambridge, 2011), chapter 3.
- [190] M. Cho, *Two-Dimensional Optical Spectroscopy* (CRC Press, Boca Raton, 2009).
- [191] D. M. Jonas, *Annu. Rev. Phys. Chem.* **54**, 425 (2003).
- [192] M. D. Fayer, *Annu. Rev. Phys. Chem.* **60**, 21 (2009).
- [193] M. Khalil, N. Demirdöven, A. Tokmakoff, *J. Phys. Chem. A* **107**, 5258 (2003).
- [194] Z. Ganim, H. S. Chung, A. W. Smith, L. P. DeFlores, K. C. Jones, A. Tokmakoff, *Acc. Chem. Res.* **41**, 432441 (2008).
- [195] M. Cho, *Chem. Rev.* **108**, 1331 (2008).
- [196] A. Ma, R. M. Stratt, *Phys. Rev. Lett.* **85**, 1004 (2000).
- [197] A. Ma, R. M. Stratt, *J. Chem. Phys.* **116**, 4962 (2002).
- [198] A. Ma, R. M. Stratt, *J. Chem. Phys.* **116**, 4972 (2002).
- [199] A. Ma, R. M. Stratt, *J. Chem. Phys.* **119**, 8500 (2003).
- [200] A. Ma, R. M. Stratt, *Bull. Korean Chem. Soc.* **24**, 1126 (2003).
- [201] R. DeVane, C. Ridley, B. Space, T. Keyes, *J. Chem. Phys.* **119**, 6073 (2003).
- [202] R. DeVane, C. Ridley, B. Space, T. Keyes, *Phys. Rev. E Stat. Nonlin. Soft Matter Phys.* **70**, 050101 (2004).
- [203] R. DeVane, C. Ridley, B. Space, T. Keyes, *J. Chem. Phys.* **123**, 194507 (2005).

- [204] R. DeVane, C. Kasprzyk, B. Space, T. Keyes, *J. Phys. Chem. B* **110**, 3773 (2006).
- [205] R. DeVane, B. Space, T. I. Jansen, T. Keyes, *J. Chem. Phys.* **125**, 234501 (2006).
- [206] T. I. C. Jansen, J. G. Snijders, K. Duppen, *J. Chem. Phys.* **114**, 10910 (2001).
- [207] J. Cao, J. Wu, S. Yang, *J. Chem. Phys.* **116**, 3739 (2002).
- [208] T. Steffen, J. T. Fourkas, K. Duppen, *J. Chem. Phys.* **105**, 7364 (1996).
- [209] M. S. Lynch, K. M. Slenkamp, M. Cheng, M. Khalil, *J. Phys. Chem. A* **116**, 7023 (2012).
- [210] C. J. Milne, Y. L. Li, T. I. C. Jansen, L. Huang, R. J. D. Miller, *J. Phys. Chem. B* **110**, 19867 (2006).
- [211] Y. L. Li, L. Huang, R. J. Dwayne Miller, T. Hasegawa, Y. Tanimura, *J. Chem. Phys.* **128**, 234507 (2008).
- [212] R. A. Denny, D. R. Reichman, *J. Chem. Phys.* **116**, 1987 (2002).
- [213] T. Keyes, J. T. Fourkas, *J. Chem. Phys.* **112**, 287 (2000).
- [214] A. Tokmakoff, M. Lang, D. Larsen, G. Fleming, V. Chernyak, S. Mukamel, *Phys. Rev. Lett.* **79**, 2702 (1997).
- [215] A. Tokmakoff, G. R. Fleming, *J. Chem. Phys.* **106**, 2569 (1997).
- [216] T. Hasegawa, Y. Tanimura, *J. Chem. Phys.* **125**, 074512 (2006).
- [217] T. Hasegawa, Y. Tanimura, *J. Chem. Phys.* **128**, 064511 (2008).
- [218] M. Cho, *Two-Dimensional Optical Spectroscopy* (CRC Press, Boca Raton, 2009), chapter 3, p. 51.
- [219] G. Tao, R. M. Stratt, *J. Phys. Chem. B* **110**, 976 (2006).
- [220] X. Sun, R. M. Stratt, *Phys. Chem. Chem. Phys.* **14**, 6320 (2012).
- [221] X. Sun, R. M. Stratt, *J. Chem. Phys.* **139**, 044506 (2013).
- [222] S. Park, B. N. Flanders, X. M. Shang, R. A. Westervelt, J. Kim, N. F. Scherer, *J. Chem. Phys.* **118**, 3917 (2003).
- [223] A. M. Moran, S. Park, N. F. Scherer, *J. Phys. Chem. B* **110**, 19771 (2006).
- [224] A. M. Moran, S. Park, N. F. Scherer, *Chem. Phys.* **341**, 344 (2007).
- [225] A. M. Moran, R. A. Nome, N. F. Scherer, *J. Chem. Phys.* **127**, 184505 (2007).
- [226] S. Park, J. Kim, A. M. Moran, N. F. Scherer, *Phys. Chem. Chem. Phys.* **13**, 214 (2011).
- [227] S. Park, J. Kim, N. F. Scherer, *Phys. Chem. Chem. Phys.* **14**, 8116 (2012).
- [228] D. F. Underwood, D. A. Blank, *J. Phys. Chem. A* **107**, 956 (2003).

- [229] D. F. Underwood, D. A. Blank, *J. Phys. Chem. A* **109**, 3295 (2005).
- [230] S. J. Schmidtke, D. F. Underwood, D. A. Blank, *J. Am. Chem. Soc.* **126**, 8620 (2004).
- [231] S. J. Schmidtke, D. F. Underwood, D. A. Blank, *J. Phys. Chem. A* **109**, 7033 (2005).
- [232] R. N. Zare, *Angular Momentum: Understanding spatial aspects in chemistry and physics* (Wiley, New York, 1988), chapter 3, Wiley-Interscience publication.
- [233] B. B. Laird, W. H. Thompson, *J. Chem. Phys.* **135**, 084511 (2011).
- [234] C. Dellago, S. Mukamel, *J. Chem. Phys.* **119**, 9344 (2003).
- [235] Y. Nagata, Y. Tanimura, *J. Chem. Phys.* **124**, 024508 (2006).
- [236] C. Dellago, S. Mukamel, *Phys. Rev. E* **67**, 035205 (2003).
- [237] M. Kryvohuz, J. S. Cao, *Phys. Rev. Lett.* **96**, 030403 (2006).
- [238] S. V. Malinin, V. Y. Chernyak, *Phys. Rev. E* **77**, 056201 (2008).
- [239] B. J. Ka, E. Geva, *J. Chem. Phys.* **125**, 214501 (2006).
- [240] J. Kim, T. Keyes, *Phys. Rev. E* **65**, 061102 (2002).
- [241] T. Keyes, J. Kim, *J. Chem. Phys.* **122**, 244502 (2005).
- [242] R. A. Denny, D. Reichman, *Phys. Rev. E* **63**, 065101 (2001).
- [243] R. A. Denny, D. R. Reichman, *J. Chem. Phys.* **116**, 1979 (2002).
- [244] J. Cao, S. Yang, J. Wu, *J. Chem. Phys.* **116**, 3760 (2002).
- [245] T. I. C. Jansen, S. Mukamel, *J. Chem. Phys.* **119**, 7979 (2003).
- [246] M. Maroncelli, *J. Mol. Liq.* **57**, 1 (1993).
- [247] P. J. Rossky, J. D. Simon, *Nature* **370**, 263 (1994).
- [248] M. Maroncelli, *J. Chem. Phys.* **94**, 2084 (1991).
- [249] A. Luzar, D. Chandler, *J. Chem. Phys.* **98**, 8160 (1993).
- [250] G. M. Sando, K. Dahl, J. C. Owrutsky, *J. Phys. Chem. B* **111**, 4901 (2007).
- [251] T. A. Özal, N. F. A. van der Vegt, *J. Phys. Chem. B* **110**, 12104 (2006).
- [252] S. H. Mushrif, S. Caratzoulas, D. G. Vlachos, *Phys. Chem. Chem. Phys.* **14**, 2637 (2012).
- [253] M. G. Ortore, P. Mariani, F. Carsughi, S. Cinelli, G. Onori, J. Teixeira, F. Spinozzi, *J. Chem. Phys.* **135**, 245103 (2011).
- [254] F. Cichos, A. Willert, U. Rempel, C. von Borczyskowski, *J. Phys. Chem. A* **101**, 8179 (1997).

- [255] A. E. Bragg, G. U. Kanu, B. J. Schwartz, *J. Phys. Chem. Lett.* **2**, 2797 (2011).
- [256] A. K. Laha, P. K. Das, S. Bagchi, *J. Phys. Chem. A* **106**, 3230 (2002).
- [257] J. Zielkiewicz, *Phys. Chem. Chem. Phys.* **2**, 2925 (2000).
- [258] M. Basilevsky, A. Odinkov, E. Nikitina, F. Grigoriev, N. Petrov, M. Alfimov, *J. Chem. Phys.* **130**, 024504 (2009).
- [259] M. Basilevsky, A. Odinkov, E. Nikitina, F. Grigoriev, N. Petrov, M. Alfimov, *J. Chem. Phys.* **130**, 024505 (2009).
- [260] H. Li, S. Arzhantsev, M. Maroncelli, *J. Phys. Chem. B* **111**, 3208 (2007).
- [261] C. Swalina, S. Arzhantsev, H. Li, M. Maroncelli, *J. Phys. Chem. B* **112**, 14959 (2008).
- [262] C. Wang, R. M. Stratt, *J. Chem. Phys.* **127**, 224503 (2007).
- [263] C. Wang, R. M. Stratt, *J. Chem. Phys.* **127**, 224504 (2007).
- [264] C. N. Nguyen, J. I. Isaacson, K. B. Shimmyo, A. Chen, R. M. Stratt, *J. Chem. Phys.* **136**, 184504 (2012).
- [265] R. Righini, *Science* **262**, 1386 (1993).
- [266] A. Tokmakoff, *J. Chem. Phys.* **105**, 1 (1996).
- [267] R. L. Murry, J. T. Fourkas, *J. Chem. Phys.* **107**, 9726 (1997).
- [268] D. McMorro, W. T. Lotshaw, G. A. Kenney-Wallace, *IEEE J. Quantum Electron.* **24**, 443 (1988).
- [269] S. Pales, L. Schilling, R. J. D. Miller, P. R. Staver, W. T. Lotshaw, *J. Phys. Chem.* **98**, 6308 (1994).
- [270] A. K. Burnham, G. R. Alms, W. H. Flygare, *J. Chem. Phys.* **62**, 3289 (1975).
- [271] L. C. Geiger, B. M. Ladanyi, *J. Chem. Phys.* **89**, 6588 (1988).
- [272] B. M. Ladanyi, *Chem. Phys. Lett.* **121**, 351 (1985).
- [273] J. Applequist, J. R. Carl, K.-K. Fung, *J. Am. Chem. Soc.* **94**, 2952 (1972).
- [274] K. J. Miller, *J. Am. Chem. Soc.* **112**, 8533 (1990).
- [275] W. F. Murphy, *J. Chem. Phys.* **67**, 5877 (1977).
- [276] W. S. Xie, J. Z. Pu, J. L. Gao, *J. Phys. Chem. A* **113**, 2109 (2009).
- [277] B. T. Thole, *Chem. Phys.* **59**, 341 (1981).
- [278] P. T. van Duijnen, M. Swart, *J. Phys. Chem. A* **102**, 2390 (1998).
- [279] L. Lupi, L. Comez, M. Paolantoni, D. Fioretto, B. M. Ladanyi, *J. Phys. Chem. B* **116**, 7499 (2012).

- [280] T. I. C. Jansen, M. Swart, L. Jensen, P. T. van Duijnen, J. G. Snijders, K. Duppen, *J. Chem. Phys.* **116**, 3277 (2002).
- [281] M. Paolantoni, B. M. Ladanyi, *J. Chem. Phys.* **117**, 3856 (2002).
- [282] G. R. Fleming, S. A. Passino, Y. Nagasawa, *Phil. Trans. R. Soc. Lond. A* **356**, 389 (1998).
- [283] M. Cho, G. R. Fleming, S. Saito, I. Ohmine, R. M. Stratt, *J. Chem. Phys.* **100**, 6672 (1994).
- [284] M. P. Allen, D. J. Tildesley, *Computer Simulation of Liquids* (Clarendon Press, Oxford, 1987).
- [285] E. Anderson, Z. Bai, C. Bischof, S. Blackford, J. Demmel, J. Dongarra, J. Du Croz, A. Greenbaum, S. Hammarling, A. McKenney, D. Sorensen, *LAPACK Users' Guide* (Society for Industrial and Applied Mathematics, Philadelphia, PA, 1999), 3rd edition.
- [286] R. E. Larsen, E. F. David, G. Goodyear, R. M. Stratt, *J. Chem. Phys.* **107**, 524 (1997).
- [287] S. Mukamel, V. Khidekel, V. Chernyak, *Phys. Rev. E* **53**, R1 (1996).
- [288] H. Goldstein, C. P. Poole, Jr, J. L. Safko, *Classical mechanics* (Addison-Wesley, Cambridge, MA, 2001), 3rd edition.
- [289] B. J. Berne, G. D. Harp, *Adv. Chem. Phys.* **17**, 63 (1970).
- [290] U. Balucani, R. Vallauri, *Chem. Phys. Lett.* **166**, 77 (1990).
- [291] M. Canales, J. A. Padro, *Mol. Simul.* **8**, 335 (1992).
- [292] A. D. J. Haymet, *Chem. Phys. Lett.* **107**, 77 (1984).
- [293] B. M. Ladanyi, S. Klein, *J. Chem. Phys.* **105**, 1552 (1996).
- [294] F. Cichos, R. Brown, P. A. Bopp, *J. Chem. Phys.* **114**, 6834 (2001).
- [295] F. Ingrosso, B. M. Ladanyi, B. Mennucci, M. D. Elola, J. Tomasi, *J. Phys. Chem. B* **109**, 3553 (2005).
- [296] M. A. Schlosshauer, *Decoherence: And the Quantum-To-Classical Transition* (Springer, Berlin, 2007), chapter 1-3.
- [297] O. V. Prezhdo, P. J. Rossky, *Phys. Rev. Lett.* **81**, 5294 (1998).
- [298] E. R. Bittner, P. J. Rossky, *J. Chem. Phys.* **103**, 8130 (1995).
- [299] E. R. Bittner, P. J. Rossky, *J. Chem. Phys.* **107**, 8611 (1997).
- [300] B. J. Schwartz, E. R. Bittner, O. V. Prezhdo, P. J. Rossky, *J. Chem. Phys.* **104**, 5942 (1996).
- [301] H. Hwang, P. J. Rossky, *J. Phys. Chem. B* **108**, 6723 (2004).

- [302] G. S. Engel, T. R. Calhoun, E. L. Read, T.-K. Ahn, T. Mančal, Y.-C. Cheng, R. E. Blankenship, G. R. Fleming, *Nature* **446**, 782 (2007).
- [303] T. Brixner, J. Stenger, H. M. Vaswani, M. Cho, R. E. B. G. R. Fleming, *Nature* **434**, 625 (2005).
- [304] T. R. Calhoun, N. S. Ginsberg, G. S. Schlau-Cohen, Y.-C. Cheng, M. Ballottari, R. Bassi, G. R. Fleming, *J. Phys. Chem. B* **113**, 16291 (2009).
- [305] A. Ishizaki, G. R. Fleming, *Annu. Rev. Condens. Matter Phys.* **3**, 333 (2012).
- [306] C. Meier, J. A. Beswick, *J. Chem. Phys.* **121**, 4550 (2004).
- [307] C. Meier, *Phys. Rev. Lett.* **93**, 173003 (2004).
- [308] L. Chuntunov, D. G. Kuroda, A. Ghosh, J. Ma, R. M. Hochstrasser, *J. Phys. Chem. Lett.* **4**, 1866 (2013).
- [309] M. Karavitis, V. A. Apkarian, *J. Chem. Phys.* **120**, 292 (2004).
- [310] Z. Bihary, M. Karavitis, V. A. Apkarian, *J. Chem. Phys.* **120**, 8144 (2004).
- [311] W. H. Miller, *J. Phys. Chem. A* **105**, 2942 (2001).
- [312] W. H. Miller, *J. Chem. Phys.* **136**, 210901 (2012).
- [313] B. J. Schwartz, P. J. Rossky, *J. Chem. Phys.* **101**, 6902 (1994).
- [314] P. Mináry, L. Turi, P. J. Rossky, *J. Chem. Phys.* **110**, 10953 (1999).
- [315] L. Mones, P. J. Rossky, L. Turi, *J. Chem. Phys.* **135**, 084501 (2011).
- [316] F. Messina, O. Bräm, A. Cannizzo, M. Chergui, *Nat. Commun.* **4**, 2119 (2013).
- [317] W.-S. Sheu, P. J. Rossky, *J. Am. Chem. Soc.* **115**, 7729 (1993).
- [318] W.-S. Sheu, P. J. Rossky, *J. Phys. Chem.* **100**, 1295 (1996).
- [319] A. Staib, D. Borgis, *J. Chem. Phys.* **104**, 9027 (1996).
- [320] S. E. Bradforth, P. Jungwirth, *J. Phys. Chem. A* **106**, 1286 (2002).
- [321] V. T. Pham, I. Tavernelli, C. J. Milne, R. M. van der Veen, P. D'Angelo, C. Bressler, M. Chergui, *Chem. Phys.* **371**, 24 (2010).
- [322] S. Mukamel, *Principles of nonlinear optical spectroscopy* (Oxford University Press, New York, 1995), chapter 8.
- [323] V. Chernyak, W. M. Zhang, S. Mukamel, *J. Chem. Phys.* **109**, 9587 (1998).
- [324] W. M. Zhang, V. Chernyak, S. Mukamel, *J. Chem. Phys.* **110**, 5011 (1999).
- [325] T.-S. Yang, P. Vöhringer, D. C. Arnett, N. F. Scherer, *J. Chem. Phys.* **103**, 8346 (1995).
- [326] G. Goodyear, R. M. Stratt, *J. Chem. Phys.* **105**, 10050 (1996).

- [327] V. I. Arnold, *Mathematical Methods of Classical Mechanics* (Springer Verlag, New York, 1989), p. 216, 2nd edition.
- [328] S. S. Andrews, *J. Chem. Educ.* **81**, 877 (2004).
- [329] M. P. Allen, D. J. Tildesley, *Computer Simulation of Liquids* (Clarendon Press, Oxford, 1987), chapter 5, p. 171.

Index

- 3-pulse photon echo peak shift, 38, 140, 229
- anisotropic OKE response, 100
- attosecond laser, 21
- bond-angle distribution, 196
- breakdown of linear response theory, 18
- Brownian motion, 9
- charge-transfer-to-solvent, 233
- close-packed lattices, 211
- coherent nonlinear spectroscopy, 29
- computer simulation, 19
- coumarin 153, 23, 45, 97, 232
- density matrix, 31
- density operator, 32
- dipole operator, 31
- dipole-induced-dipole model, 94
- dispersive birefringence, 36
- double-sided Feynmann diagram, 33, 34
- dynamical variable, 6, 49
- Einstein frequency, 151
- energetic dynamics of solvents, 194, 230
- ensemble dephasing, 35
- ergodicity, 7
- femtosecond laser, 21
- fifth-order Raman spectroscopy, 41, 75
- fluctuation–dissipation theorem, 10, 11, 13, 18
- four-wave mixing, 30, 33, 60
- four-wave-mixing, 37
- Fourier transform, 8
- Fourier-transform deconvolution technique, 90
- Gaussian statistics, 18, 62
- generalized Langevin equation, 11, 76
- generating function, 64
- Heisenberg picture, 58
- homodyne detection, 86
- homogeneity, 1
- homogeneous broadening, 12
- hybrid INM/MD method, 169
- imaginary-frequency INMs, 5
- influence spectra, 155
- influence spectrum, 8

infrared spectroscopy, 8
inhomogeneous broadening, 35
instantaneous normal mode, 3, 40, 141
instantaneous-pair theory, 12
instantaneous-normal-mode theory, 3
Intramolecular Vibrational-energy Redistri-
bution, 2
isotropic OKE response, 100
isotropy, 1, 29

Landau-Teller relation, 11
Langevin equation, 9
Laplace transform, 56
Lennard-Jones potential, 80
light-matter interaction, 29, 31, 33, 40
linear INM theory, 154, 184, 234
linear response theory, 9, 13, 17, 48
Liouville equation, 49
Liouville operator, 50
Liouville-space pathway, 33
local oscillator, 89, 228
many-body polarizability, 42, 95, 226, 254
Markovian process, 9
memory function, 12
mode-coupling theory, 76
molecular dynamics, 20
molecular dynamics simulation, 80
Monte Carlo, 20, 21

non-Markovian process, 11
non-rephasing pathways, 35
nonlinear optical effects, 29
nonlinear susceptibility, 29

OKE influence spectra, 158
Onsager's regression hypothesis, 13
optical heterodyne detection, 36, 88, 89
optical Kerr effect, 30, 35, 60, 86, 100
order parameter, 248

phase matching condition, 30, 33
phase space, 6, 49
phase space distribution, 49
phonons, 1
photon echo, 38
photons, 26, 29
Poisson bracket, 32, 50, 75, 169, 235
polarizability-velocity correlation function,
114
polarizability operator, 42
population, 32, 33
preferential solvation, 78
projection operator, 112
pump-probe configuration, 24, 86
pure dephasing, 12

quantum coherence, 32, 33, 232
quantum commutator, 32

quantum Liouville equation, 32
 radial distribution function, 82
 Raman-induced Kerr effect spectroscopy, 37
 reduced spectral density, 91, 100
 rephasing pathways, 35, 38
 resonant-pump polarizability response spectroscopy, 44, 140
 resonant-pump polarizability response spectroscopy, 227
 resonant-pump third-order Raman spectra, 228
 rotational average, 62, 241
 scattering experiments, 26
 Schrödinger picture, 55
 simple harmonic oscillator, 173
 solute-pump/solvent-probe spectroscopy, 42, 68, 187
 solvated electron, 233
 solvation, 2, 77
 solvation influence spectra, 167
 solvent mixtures, 78
 spectral density, 7, 91, 100, 159
 spectral diffusion, 38
 Stokes–Einstein relation, 11
 structural dynamics of solvents, 194, 230
 terahertz, 8
 time correlation function, 6
 time-dependent fluorescence, 38
 time-dependent fluorescence spectroscopy, 15, 23
 time-resolved X-ray diffraction, 28
 time-resolved X-ray liquidography, 28
 transient absorption, 24
 transient birefringence, 36
 transient dichroism, 36
 transient grating, 30, 37
 transient solvation polarizability, 45
 two-dimensional infrared spectroscopy, 41
 ultrafast X-ray absorption spectroscopy, 26
 velocity autocorrelation function, 82
 vibrational population relaxation time, 12
 vibrational relaxation, 2
 X-ray diffraction, 26
 Zwanzig–Mori projection operator, 13